MBE-grown ZnO-based nanostructures for electronics applications

Oscar W. Kennedy

A thesis presented for the degree of

Doctor of Philosophy

Department of Electronic and Electrical Engineering

University College London

UK

2018

Contents

Dedication

To Mum and Dad.

Declaration

I, Oscar Kennedy, confirm that the work presented here in this thesis is my own. Where information has been derived from other sources I can confirm that this has been indicated in the thesis.

Acknowledgements

As with any PhD, almost none of this work would have been possible without those who have taught, collaborated with, supervised, had lunch with, traveled with, discussed science with, laughed with, cooked dinner for, drank with and lived with me over the last ∼four years.

First thanks have to go to Professor Paul Warburton, my supervisor, who has has freely given me his time and generously supported my cleanroom habit. He has allowed me freedom to pursue my research interests and supported me even when this has led me away from areas directly relating to the title of this document. Without this freedom I would have undoubtedly not have enjoyed this PhD as much as I have.

Next I have to thank everyone who has taught me over the course of my PhD. Drs Maddison Coke, Jonathan Burnett, Nic Constantino, James Sagar, James Aldous, Jon Fenton, Marion Sourribes, Ivan Isakov, Edward Romans, and Mr Marios Hadjimichael - you took a new PhD student liable to break equipment just by looking at it and turned him into a walking talking experimentalist. He is even allowed a key to the lab. This bye line seems hopelessly inadequate in the way of thanks for what must have been cumulatively hundreds of hours spent looking over my shoulder, training and helping me along the way.

Thanks has to go to a new generation of PhD students, in particular Matthew Sparks and Jamie Potter. You have both become indispensable running labs, making sure there are gloves, tissues, RHEED screens, liquid helium and whatever else may be needed when I want to do science. Without willing hands to help fix equipment it would probably stay broken.

I have been really lucky to work with some wonderful collaborators. In particular sustained collaboration with Dr. Edward White and Professor Milo Shaffer has been fantastic and led to some really interesting work. Thanks also go to Maximillian Zapf for the cryogenic photoluminescence data.

I have to thank the wonderful technical staff at UCL who have maintained a lot of the equipment which I have used throuhout this PhD. The cleanroom staff of Steve Etienne,

Vijay Krishnan, Suguo Huo, Lorella Rossi and Rohit Khanna as well as Dr. Steve Firth.

Thanks to all the wonderful housemates who have made the last four years a treat - Charlotte, Alexa, Suhan, Izzy, Zoë, Fed, Jack, Cam. Thanks also to all my other friends, especially PWDC.

Mum, Dad, Izzy - thanks and love as always.

Abstract

Low-dimensional semiconductors have properties different from their bulk counterparts and are thus attractive components for future electronic devices. This thesis presents work on ZnO nanostructures and ZnO/ZnMgO nano-heterostructures grown by molecular beam epitaxy (MBE) for electronics applications.

ZnO nanostructures are grown by gold-catalysed MBE. We show that the cut of sapphire used as a substrate determines the orientation of one-dimensional nanostructure growth. On C-plane sapphire we grow ZnO nanowires and on R-plane sapphire we grow ZnO nanobelts. The morphology of nanobelts is shown to depend on temperature with tapering reduced at higher temperatures. Field-effect transistors based on ZnO nanobelts are fabricated to characterize the electronic properties of single nanobelts.

ZnO/ZnMgO heterostructure nanowires and nanobelts are grown and characterized. We show abrupt ZnO/ZnMgO interfaces and demonstrate that the core-shell structures in nanowires increase the luminescence intensity of nanowires. Nanobelt heterostructures are characterized optically at both room temperature and cryogenic temperatures showing evidence of quantum confinement in these structures.

Scanning transmission electron microscope cathodoluminescence (CL) is performed on single ZnO nanowires. We perform hyperspectral mapping of CL, in which a single nanowire is spatially mapped with full CL spectra collected at each spatial co-ordinate on the nanowire. We achieve record resolution for hyperspectral mapping and deconvolve full spectra into constituent components. This allows us to distinguish surface and defect peaks as well as CL from inter-band processes in ZnO.

We perform proof-of-principle studies combining high quality RF superconducting circuits with epitaxial ZnO layers on single sapphire substrates. Such chips can be used for future experiments coupling mechanical degrees of freedom to superconducting qubits for quantum opto-mechanical experiments.

Impact Statement

In this thesis we present experimental research on ZnO thin films and nanostructures. This work has already been published in academic journals (see publications 10.2) and additional publications are currently under review. This work has already had impact by adding to the literature canon.

Of the publications under review, one details scanning transmission electron microscopy cathodoluminescence of ZnO nanowires. As well as presenting new scientific results, we presented a detailed methodology, which we believe will be implemented by groups performing such experiments in the future. As an early paper on this area there will be an impact on future work using this technique. This thesis details work aiming to control the electrical properties of ZnO nanowires by forming heterostructures with ZnMgO. Zn, Mg and O are all earth abundant, non-toxic materials. Technologies based on compounds of these elements are therefore attractive for future applications from both a materials security and sustainability point of view. The results we present, showing the growth of these heterostructures, may contribute to future work creating these new electronics.

Over the course of this PhD I have been a part of a significant amount of public engagement through the #challengemartha project. We attended numerous festivals (including Cheltenham Science Festival and Greenman Festival) and developed interactive public engagement where we explained molecular beam epitaxy, semiconductor electronics, and materials characterization to a broad audience (4 year olds 80 year olds).

The work presented in this thesis is often collaborative and a number of new collaborations have been started, including collaborations initiated by me independently. These include collaborations with Jena University (where the cryogenic PL in chapter 7 was performed) and others with Chalmers University, Hitachi Cambridge and The University of Sherbrooke to name a few. These new collaborations will sustain after my PhD and make an impact to future science allowing the exchange of expertise.

List of Figures

List of Tables

Chapter 1

Introduction

Semiconductor electronics have changed the world we live in. The computer used to write this thesis uses a silicon central processing unit with 22 nm transistors. The screen on the computer is made of light emitting diodes (LEDs) which can produce rich colours, mimicking the whole visible spectrum, which are made of AlInGaP, GaN and InGaN. It has an in-built camera which has a semiconducting charge-coupled device. If a picture is taken on that camera it can be sent anywhere in the world by fibre-optic internet whereby information is transmitted as pulses of light which are produced and re-amplified on its journey by semiconductors. Semiconducting lasers, chemical sensors, and electronic amplifiers each facilitate further applications and this paragraph is far from an exhaustive account of the applications of semiconductors.

A semiconducting technological revolution began in Bell Laboratories when they made the first semiconducting transistor in 1947 for which the Nobel prize for physics was awarded. Work on semiconducting electronics has not stopped since and developments have been driven by an increasing control over semiconductor growth and an increase in the ability to process the resultant materials. Significant recent research has focused on the use of nanoscale semiconductors.

Semiconducting devices have reached the nanoscale for two reasons. The first is a direct consequence of Moores Law [1]. As the number of transistors on an integrated circuit increases, the size of the transistor decreases. If the number of transistors doubles every two years, then, given a two-dimensional integrated circuit, this implies that the in-plane dimensions of the transistors halves every four years. Exponential growth in transistor number therefore very rapidly leads to very small transistors and hence nanoscale semiconductors. Given 71 years since the first transistor was made, and scaling in accordance with Moore's law, in plane dimensions of transistors should be $2^{-71/4} = 4.5 \times 10^{-6}$ of

the size of the first transistor. The electrically active region in the first transistor was $\sim 2.5 \times 10^{-4}$ m [2] which implies that transistor dimensions should be $\sim$1 nm today. In 2017 IBM revealed 5 nm transistor technology not significantly larger than the estimated transistor size assuming only Moore's law. However nanoscale semiconductors are not only interesting just because they dont occupy much space. The properties of semiconductors (and indeed many other classes of materials) change when they reach the nanoscale.

The birth of nanotechnology is attributed, with some controversy, to Richard Feynman and his 1959 talk titled 'There is plenty of room at the bottom' [3]. As materials become smaller, their properties change. In some cases, this is due to how they interact with external fields e.g. semiconductor nanowires can act as optical waveguides [4]. The properties of nanomagnets can be controlled by varying their shape on the nanoscale [5]. Nano-structured catalysts are highly efficient (for example in water splitting [6]) due to the increased surface area. Nanostructuring materials provides the engineer with a new tool-box which can be used to create materials with new functional properties.

Moore's law is approaching physical limits set by silicon technology since transistors are now at length scales where quantum tunneling is important and further reductions in size increase such effects. Instead of maintaining exponential growth in transistor number, developments in computing hardware have started to also focus on new horizons, one of which is referred to as 'More than Moore' (MTM) computing [7]. In MTM computing, rather than increasing the transistor number, new functionality is interfaced directly with silicon. This includes interfacing optical sensors and emitters with silicon technology allowing new optical computing paradigms or interfacing directly with chemical and biological signals.

For a number of MTM components, silicon is not a suitable material. For example, silicon has an indirect band-gap and is thus not suitable for many types of optical device. Materials other than silicon have a number of desirable properties beyond silicon including direct band gaps, large piezoelectric coefficients and surface states with energies suitable for water splitting to name a few such properties.

This thesis details work performed using semiconducting ZnO in thin films (one dimension at the nanoscale) and in nanowires and nanobelts (two or three dimensions on the nanoscale). We grow and characterize ZnO nanostructures with the aim of modifying functional properties of ZnO for electronic or opto-electronic applications.

1.1 ZnO Material Properties

ZnO is a wide band-gap (3.37 eV), natively n-type, polar semiconductor composed of earth abundant, non-toxic elements [8]. It has been claimed that it forms the largest variety of nanostructures of any material [9]. It can be alloyed with Mg to form $Zn_{1-x}Mg_xO$ where the band gap and polarization are tuned by the fractional Mg content (x) [10]. It is piezoelectronic allowing for coupling between electrical and mechanical degrees of freedom in ZnO based devices [11]. It has a high-energy exciton (63 meV) [12] which is stable at room temperature and increases the optical efficiency of ZnO. The combination of these properties make ZnO an extremely attractive material system with which to work.

The promise of p-type doping caused intensive research into ZnO in the late 2000s but despite this intensive research, stable p-type doping with significant carrier concentration has not been realised. This limits the possible applications of ZnO and derived materials excluding the possibility of e.g. electrically pumped semiconductor UV lasers in all-ZnO-devices. The intensive research programme, despite not achieving reliable p-type doping, resulted in a large body of work on ZnO (building on the initial work performed in the 1960s). It also resulted in significant investment in ZnO related technologies. Based on this investment, ZnO seed crystals for hydrothermal growth have been grown and increased in size so that very recently 2“ wafers became commercially available [13].

ZnO is an ionic crystal and is made up of a regular arrangement of Zn^{2+} cations and O^{2-} anions in the wurtzite structure. The wurtzite structure consists of interlocking tetrahedra of anions and cations. This means that the unit cell has a small dipole. When tiling the unit cell, the dipole of neighbouring unit cells cancel meaning that no net-polarization occurs. However, when applying an electric field, all positive cations move in one direction whilst the negative anions move another - i.e. ZnO is polarizable.

The polarization of ZnO has a number of interesting, and useful, consequences. When the ions move the ZnO crystal deforms since it is piezoelectric and the electric field in the ZnO is coupled to its mechanical deformation. The formation energy of polar and non-polar faces differ due to different unscreened electric fields at the different surfaces. This determines how ZnO nanostructures grow and results in a number of different nanostructures.

The piezoelectricity intrinsic to the polar ZnO crystal structure makes ZnO a suitable material for piezoelectric devices. There is a huge class of devices which make use of the coupling between electric field and mechanical motion. ZnO is not ideally suited to all of these applications. Energy scavenging devices which translate mechanical energy

into a current are an attractive proposal but require p-type material which is not readily achieved in ZnO. Piezoelectric materials are also used for precise electrically controlled motion for example in atomic force microscope stages. However, as ZnO is natively n-type (and therefore conductive) applying a large voltage across ZnO at room temperature will induce a current to flow.

One area which may exploit the piezoelectric properties of ZnO is as a layer for surface acoustic wave (SAW) devices. A SAW device typically contains two interdigitated electrodes, one of which is connected to an RF voltage. The RF voltage creates a periodic deformation of the ZnO beneath it which creates an acoustic wave in the surface of the ZnO. These waves travel at the speed of sound in the material. These electrodes have a resonant frequency when the spacing of electrode fingers is equal to the wavelength of SAWs. SAW transducers are used to add time delays into RF circuits for example in mobile phones. They have also comparatively recently been used in quantum circuits where qubits have been read out by SAWs rather than by coupling to electronic degrees of freedom [14]. ZnO single crystal films have been used as piezoelectric substrates for cryogenic SAW generation [11]. Thin film ZnO offers an attractive alternative as they may be grown on different substrates including silicon and sapphire (neither of which are piezoelectric).

1.2 ZnO Nanostructures

ZnO is likely the material system with the largest variety of derivative nanostructures. These nanostructures include nanoparticles, nanowires, nanobelts, nanospirals, nanotetrapods, nanorings and hollow nanocylinders, to give a non-exhaustive list [9]. The most common nanostructure in ZnO is the nanowire, a quasi one-dimensional object which grows along the [0001] crystal axis. ZnO nanowires have been synthesized by a number of techniques including MBE [15, 16], chemical vapour deposition[17], solution processes[18] and metalorganic vapour phase epitaxy (MOVPE)[19].

As already mentioned, the polarization of ZnO allows for a number of promising engineering applications. Therefore, combining the advantages of nanostructuring with polarization engineering may allow for novel devices to be realized. However, in order to exploit the polarization of ZnO in nanostructures the direction of polarization relative to the nanostructure must be considered. In nanowires the long axis is the same as the polar axis which allows for applications such as piezoelectric energy harvesting [20]. However, other classes of polarization engineered nanostructures are possible and may require different relative orientations such as ZnO nanobelts where the polarization axis may be

perpendicular to the growth axis [21].

1.3 Structure of this Thesis

In this thesis we use molecular beam epitaxy (MBE) to grow high quality ZnO thin films and nanostructures. We perform structural, optical and chemical analysis on these structures using a variety of analytical techniques. We then fabricate devices from the nanostructures and thin films, characterizing their electronic properties and demonstrating proof-of-principle devices.

Chapters 2-5 provide a background on semiconductor nanowires (chapter 2), ZnO/ZnMgO interfaces in thin films and nanowires (chapter 3), techniques used to characterize nanostructures and thin films (chapter 4) and details on cleanroom fabrication techniques and fabrication protocols used to fabricated devices (chapter 5).

Chapter 6 details experimental results growing ZnO nanostructures. It starts by demonstrating some new characterization on ZnO nanowires grown by MBE. It then details work demonstrating the first reported growth of ZnO nanobelts by MBE. These nanobelts are characterized structurally, optically and electronically having been fabricated into field effect transistor devices.

The growth and characterization of ZnO/ZnMgO heterostructure nanostructures are reported in chapter 7 with energy dispersive X-ray spectroscopy measurements on core shell nanowires and optical characterization (both cryogenic and room temperature) of single, and ensembles of, core-shell nanobelts.

Chapter 8 presents work performed on MBE grown ZnO nanowires in which a scanning-transmission-electron-microscope (STEM) is used to generate a cathodoluminescence (CL) signal which is then mapped with 10 nm resolution across the nanowire. We spatially resolve CL across a nanowire showing distinct signals from the nanowire core, surface and defects.

Chapter 9 is a proof of principle experiment. We aim to show the compatibility of high quality microwave superconducting devices (ubiquitous in circuit quantum electrodynamics) with epitaxial thin film ZnO on sapphire substrates. This experiment will pave the way to have (on a single chip) high quality superconducting electronics for quantum information processing as well as quantum devices based on SAWs and phonons which may, for example, present opportunities building time delays into quantum circuits.

In Chapter 10 we summarize the conclusions from this work and suggest future work which may be of particular interest in furthering this field.

Chapter 2

Semiconductor Nanowires

Despite their first synthesis over 50 years ago [22], semiconductor nanowires have only been subject to intensive research for the last 10-15 years. This is due to the difficulties in their rational synthesis where progress has been made only comparatively recently. In this section an overview on semiconductor nanowires and other one dimensional nanostructures is given including their growth and the growth of derivative heterostructures and their possible applications. Many review articles have been written on this topic [23, 24, 25, 26] although this is not an exhaustive list. As semiconductor nanowire research has matured, distinct research areas have emerged and more current reviews tend to focus more specifically on these research areas.

2.1 Why Nanowires?

Semiconductor nanostructures are a class of matter where interesting, novel physics can be found and exploited for technological advantage. By nanostructuring a material the physical properties change. These changes occur as one or more of the dimensions of the nanostructure drop below characteristic lengths in the bulk semiconductor. As the dimensions of nanowires change, it is therefore possible to alter the properties of nanowires (and how they grow) relative to the bulk materials depending on the relative cross sectional dimensions of nanowire and the pertinent lengthscales in question.

2.1.1 Synthesis

Inherent in the small dimension of nanowires is a small contact area between nanowire material and the substrate which the nanowire grows upon. When growing high quality thin film semiconductors it is necessary to use an appropriately lattice matched substrate.

This means that it has only been possible to interface specific materials in thin film geometry. Heteroepitaxial films are almost always not perfectly lattice matched and this places constraints on the thickness of the film which may grow whilst being coherently strained. Above critical thicknesses the film relaxes and defects are introduced to the film. It is sometimes possible to subsequently reduce the number of defects by growing a thicker film since when defects meet they can mutually terminate. These types of constraints mean that the growth of thin films and complex thin film structures can be challenging.

On the other hand, as nanowires have such a small contact area to the substrate, nanowires may grow on substrates which are not lattice matched to the nanowire material. This allows, in principle, the combination of a number of different materials together on a single sample and offers an obvious advantage of nanowires over thin film geometries. For example ZnO nanowires have been synthesized on silicon [27], c-plane sapphire [28, 29], a-plane sapphire [29], m-plane sapphire [30], GaN [31], carbon fibre cloth [32] and even paper [33], to give a non-exhaustive list. Furthermore, nanowires may be synthesized without a substrate, either in solution [34] or from an aerosol of nanoparticles in precursor gases called aerotaxy [35], a process being commercialised by Solvotaics, a spinout from Lund university.

Not only can nanowires be synthesized on a number of substrates or without substrates, but once synthesized nanowires may be removed from their substrate and rationally contacted by nanofabrication processes for further application. These processes are often used for research purposes, but since they take a significant amount of time (from humans and equipment) this approach is not likely to be useful outside a laboratory for applications requiring many nanowires, such as energy harvesting. However, for high value, low-nanowire-number applications, this may be a suitable strategy which allows the physics of nanowires to be introduced to different material systems. This strategy has been successfully employed to generate on-chip masers by interfacing the properties of a III/V nanowire with high quality superconducting circuits on a silicon substrate for quantum information applications [36].

A particularly interesting example application of interfacing different classes of material is the integration of nanophotonic structures directly into silicon processors. Traditional computing is based on silicon, the material at the heart of practically all modern computers and all PCs. However, silicon has an indirect band gap. This makes it unsuitable for optical applications. When interfacing with light (such as fibre-optic broadband) additional semiconductor materials are required, typically III/V semiconductors which can

form light sources and detectors. Nanowires allow the on-chip combination of III/V technology and silicon computing for enhanced optical capabilities. The on-chip combination of silicon and III/V materials has been realised in a CMOS-compatible process named template assisted selective epitaxy (TASE) pioneered by IBM [37].

2.1.2 Material Properties

As the dimensions of nanowires change, so can the physical properties of the nanowire. A good example of this is how, as the nanowire cross-sectional dimensions drop below the mean-free-path of phonons in the bulk material, phonon scattering at the edge of nanostructures increases. This means that, for example, the thermal conductivity in silicon nanowires decreases with nanowire diameter [38]. The mean-free-path of electrical carriers in these materials is typically much shorter than that of phonons, and so surface scattering of electrons is not increased as much as that of phonons [39]. This allows the relative thermal and electrical conductivities to be engineered by changing the dimensions of the nanostructures. This is of great importance for applications such as thermoelectrics where waste heat is scavenged and converted into electricity. For a good thermoelectric figure of merit a large electrical conductivity and small thermal conductivity are desirable. Additionally quantum confinement in low-dimensional systems may further increase the electrical conductivity without increasing thermal conductivity [39, 40].

Nanowires are ideally suited to any application where a large surface area is required due to the large surface:volume ratio inherent in nanowire geometry. Obvious examples where this is advantageous are (photo)catalysis (where reactions occur at the surface of the catalyst) or for chemical and biological sensing (where the state of the nanowire surface will change its properties in a way which may be readily read out). Additionally, the surface of nanowires necessarily breaks translational symmetry of the underlying crystal lattice. This causes a number of surface states which are often involved in catalysis and sensing. These applications have been demonstrated in nanowires: ZnO nanowires have been fabricated into ethanol sensors [41]; GaN nanowires have been used as photocatalysts [42]; and TiO_2 nanowires have been used for water splitting [43].

Semiconductor nanowire lasers are enabled by the geometry of the nanowire combined with the semiconducting properties of the nanowire. In a nanowire laser, the nanowire acts as an optical cavity confining light due to reflections at the ends of the nanowire from refractive index contrast (this is despite the lateral dimensions of the nanowire being smaller than the wavelength of light generated by the laser). The nanowire also acts

as a gain medium where coherent radiative recombination across the band gap of the semiconductor provides the gain mechanism for the laser. This was first demonstrated with ultraviolet (UV) nanowire lasers using ZnO nanowires which were optically pumped [44]. Since that first demonstration, nanowire lasers operating at a variety of different wavelengths have been realised. Importantly, electro-luminescence has been realised in nanowire lasers [45] allowing, in principle, integration and operation of nanowire lasers. These nanolasers are promising as low footprint sources of coherent light on chips or for low-power sensing applications. This application is enabled due to the shape and size of the nanowire meaning that it couples to external fields and allows waveguiding, which would not be the case in a bulk material.

2.2 Why not nanowires?

Despite the positive attributes of nanowires highlighted in the previous section, nanowires have been slow to be commercially exploited. Clearly there are significant obstacles which are hindering the transition from lab-based technologies to on-the-shelf technologies. There are many challenges relating to the production of nanowire-based hardware due to the cost and consistency of their synthesis and the ease of integration with existing fabrication technologies.

There are two strategies for synthesizing nanowires: bottom up and top down approaches [46], both of which face challenges. In a bottom up approach nanowires self assemble. A good example of this is self-catalysed GaAs nanowires, where nanowire growth occurs spontaneously often from a Ga droplet which forms on the substrate [47]. ZnO nanowires grown by self-assembled gold nanoparticles are also good examples of bottom up synthesis in ZnO [15]. Bottom up approaches allow very fine nanowires with high yields to grow over large areas. These approaches do not allow the rational placement of nanowires and often results in a spread in nanowire properties. Top down approaches such as TASE [37] allow rational placement and design of nanowires. They struggle to achieve the ultra-small dimensions of the finest nanowires grown by bottom up processes and are inherently expensive, requiring an extra stage of lithography to define where the nanowires are to grow. A strategy which has had significant success and become widespread is rational deposition of a periodic array of catalyst particles [48] or the etching of an array of periodic holes through a surface layer on the substrate [49]. This defines where nanowires grow (setting their spacing) so that each nanowire nominally grows in the same environment thereby reducing the variation in nanowire properties.

Additionally, when discussing more than Moore technologies, it is essential that nanowire growth be CMOS compatible. This provides an additional challenge since if nanowires are to be directly synthesized onto silicon chips, significant constraints are imposed on the nanowire growth (e.g. limits on temperature and materials used). If nanowires are not grown directly onto silicon, there are challenges in deterministically combining them with an existing chip in a relatively low cost process.

The challenges of growing nanowires, with good properties and small nanowire-to-nanowire variation and making them into functional devices are significant. No perfect strategy has yet emerged and nanowires remain an expensive technology to commercialise. Current commercial ventures include the Swedish company 'glo' which manufactures GaN nanowire LEDs and another Swedish company, Solvotaics, which makes nanowire photovoltaics. Anecdotally, nanowire photovoltaics have been targeted at specific markets where high efficiency products can justify higher costs. These are applications such as photovoltaics for space missions or focusing on the Japanese market where the high population density and mountainous geography mean that the availability of land suitable for solar is limited and thus efficiency more important.

2.3 Nanowire Heterostructures

Combining different materials in a single nanowire to form a heterostructure allows the functional properties of nanowires to be further enhanced beyond the bulk properties [50]. The dopant density can be varied within a single nanowire to embed devices into single nanowires [51] or this can be done by the addition of an entirely new material. Sometimes the new material enhances the existing properties of the nanowire – for example if a new material is grown as a shell layer around the nanowire, surface traps are passivated thereby improving the carrier mobility [47]. Sometimes the interface between different material allows entirely new properties to be achieved such as the formation of quantum wells or dots inside the nanowire [52]. Sometimes heterostructures are used to grow poorly lattice-matched crystals where an intermediate, nanowire stub with a better lattice match is used to start growth before subsequent growth of the required material [53]

Given the geometry of nanowires there are two distinct types of heterostructure which may be formed in a nanowire. Axial heterostructures result when the chemistry of the nanowire is modulated along the length of the nanowire. A nanowire-embedded axial heterostructure is shown schematically in Figure 2.1 (a). Radial heterostructures, on the other hand, result when the chemistry of the nanowire is modulated along the radius of the

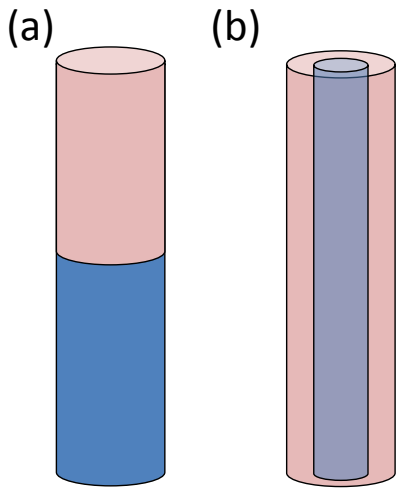

Figure 2.1: Schematics of (a) axial and (b) radial heterostructure nanowires with cylindrical geometry. The two materials are indicated by the two colours.

nanowire. A nanowire-embedded radial heterostructure is shown schematically in Figure 2.1 (b). Simple heterostructures involve only two materials with a single interface such as those shown in Figure 2.1. However, more complicated heterostructures may be grown which incorporate more than two chemistries or where the chemistry changes multiple times.

Radial heterostructures of semiconductor nanowires coated by epitaxial superconductors have been grown [54]. The superconducting layer proximitises the semiconductor and these materials have been used for experiments on Majorana Fermions. Additional radial structures include radial p-i-n junctions where doping profiles are modulated in the radial direction for possible photovoltaic applications [55, 56].

By translating heterostructures, typically used in thin films, into the nanowire geometry, the mobility of electrons has been significantly enhanced above the mobility in the bare nanowire. This has been done with GaAs/AlGaAs core shell nanowires where the chemistry and doping profile is radially modulated [57] resulting in mobilities of 2200 $cm^2V^{-1}s^{-1}$ at room temperature. In Ge/Si heterostructure nanowires, 77 K mobility increases from 100–280 $cm^2V^{-1}s^{-1}$ in bare nanowires to 700–1,800 $cm^2V^{-1}s^{-1}$ in heterostructure nanowires [58]. Polarization induced 2DEGs have been shown in GaN/AlN/AlGaN triangular-nanowire core-shell heterostructures [59] with mobilities of 3,100 $cm^2V^{-1}s^{-1}$ at room temperature and 21,000 $cm^2V^{-1}s^{-1}$ at 5 K. Therefore the heterostructures traditionally used in thin films can be successfully translated into nanowires to modify the electron mobility with record mobilities arising due to polarization induced 2DEGs.

Chapter 3

ZnO/ZnMgO Heterointerfaces

3.1 ZnO Ternary Compounds

There are multiple ternary and quarternary compounds based on ZnO. These compounds allow the properties of the material to be tuned for specific applications. Notable ternary compounds are ZnMgO where the band gap increases with Mg concentration [60] and ZnCdO where the band gap drops with Cd concentration [61]. The quarternary compound ZnBeMgO allows the band gap to be increased whilst countering some of the strain that arises due to in-plane lattice mismatch at high Mg concentrations in ZnMgO [62].

In addition to modifying the band gap, these compounds have different polarization from the virgin ZnO. For instance, in ZnMgO the Mg atomic radius is smaller than Zn. This means the lattice parameter of ZnMgO is smaller than ZnO so the same charge imbalance is maintained over smaller distance resulting in a larger polarization. In this work we focus on ZnMgO as a ternary compound. A large body of work studying ZnMgO heterostructures has been published. At small Mg concentrations the in-plane lattice mismatch between ZnO and ZnMgO is sufficiently small to allow coherent epitaxial growth with little strain. Coherent growth has also been demonstrated with much higher Mg concentrations in strained films [63].

In $Zn_{1-x}Mg_xO$ the band gap and the polarization change with the fractional Mg concentration x. A review of the literature on ZnMgO luminescence[64] found the relationship between fractional Mg content in $Zn_{1-x}Mg_xO$ and the band gap to be

$$E_{Zn_{1-x}Mg_xO} = (3.38 + 1.55x)\text{eV} \tag{3.1}$$

where x is the fractional Mg content. The polarization in $Zn_{1-x}Mg_xO$ is given for epitaxial samples by

$$P_{Zn_{1-x}Mg_xO} = (0.0322 + 0.024x)\text{Cm}^{-2} \tag{3.2}$$

[65]. These equations are valid for fractional Mg concentrations up to 0.2.

The crystallographic orientation of the heterointerface is important in determining how the heterointerface forms and its properties. There are three different types of heterointerface between ZnO and ZnMgO. The interface can be non-polar (i.e. the normal to the face is perpendicular to [0001]) or polar. If the heterointerface is polar it may there are two non-equivalent polar faces of ZnO, the Zn-polar and O-polar faces. These faces can are sometimes referred to as n-type (Zn-polar) and p-type (O-polar) faces due to the type of carriers required at the interface to compensate for the polarization mismatch.

3.1.1 Band Structure at Interfaces

The band profile at the different interfaces is influenced by the band mismatch, the polarization mismatch and also the free carriers in the material which may flow to screen electric fields. Using a 1d Poisson-Schrödinger equation solver [66] we calculate example band profiles (Figure 3.1 a) and corresponding free charge distributions (Figure 3.1 b). The simplest interface is the non-polar interface, at which there is a band misalignment between the ZnO and the ZnMgO and the carrier density of the respective materials.

At the Zn-polar interface the effects of band misalignment and polarization mismatch are additive. A triangular quantum well forms and the abundant free electrons from native shallow donors fall into the quantum well and become confined a shown in the blue line in Figure 3.1. The accumulation of electrons at this interface is why it is referred to as n-type. At low temperatures electrons are confined in the lowest energy level in this quantum well. The structures are similar in band structure to those found at GaAs/AlGaAs modulation doped interfaces where, in addition to the heterointerface, a series of layers with carefully controlled doping profile are used to create electric fields due to the separation of ionised donors and the free carriers [67].

At the O-polar interface the effects of band misalignment and polarization oppose each other. In the calculated profiles here electrons flow away from the p-type interface and redistribute (green line in Figure 3.1). This process in reality is quite complex and will also depend on the density of free electrons which varies from sample to sample. However, schematically the band profile shows that at this interface there is a very shallow quantum well in the valence band rather than the conduction band.

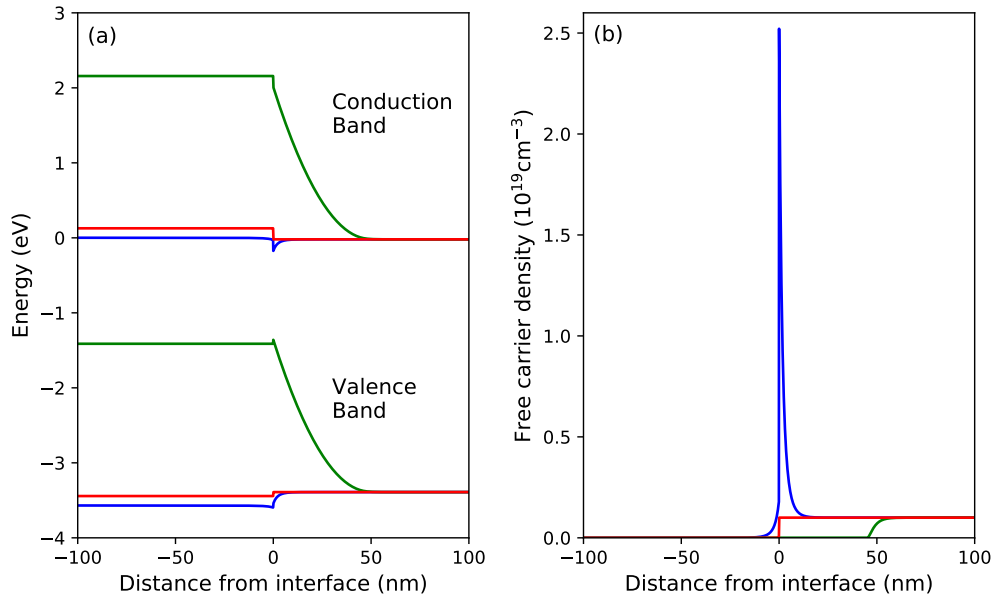

Figure 3.1: Solutions to self-consistent 1D Poisson-Schrödinger Equation showing (a) band profiles and (b) free carrier density of non-polar (red), Zn-polar (blue) and O-polar (green) heterostructures at 4K as a function of the distance from the abrupt ZnO/ZnMgO interface. ZnMgO (ZnO) is on the left (right) hand side.

3.1.2 Optical Properties of Interfaces and Heterostructures

ZnO is a wide band semiconductor which has rich optical properties including non-linear optical properties, a number of defect-related luminescence peaks from native defects and impurity atoms, phonon replica peaks and excitonic and biexcitonic recombination. The combination of band mismatch and polarization mismatch at heterointerfaces allows for structures which modify the optical properties of the ZnO in a number of manners based on the band alignment at these interfaces. Here we consider how these heterostructures may modify the luminescence spectra of ZnO.

The simplest modification of luminescence is the addition of peaks from ZnMgO. ZnMgO is a wider band-gap material and so if ZnMgO is present it may contribute higher energy luminescence. This has nothing to do with the heterointerface and is simply due to the presence of different materials with different band gaps.

At heterointerfaces quantum wells may form either due to electric fields at polar interfaces caused by a polarization mismatch or from rationally designed quantum wells where ZnO wells are placed between ZnMgO barriers. In a quantum well, the energy levels of electrons are quantized. Radiative transitions starting and/or ending in quantum wells will therefore have different energy based on the extra energy from quantum confinement

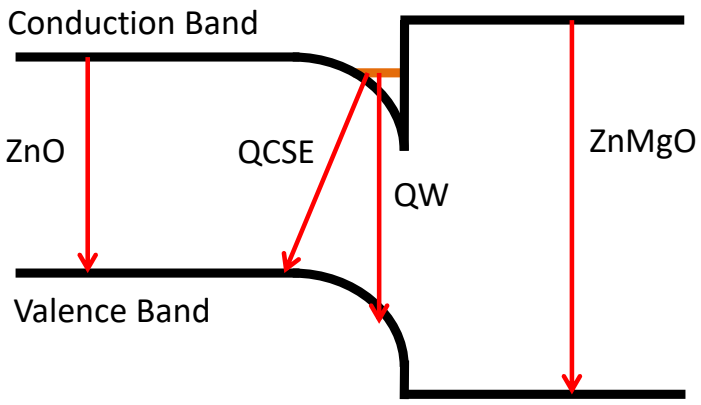

Figure 3.2: Schematic showing optical transitions which may occur at a Zn polar heterostructure. ZnO and ZnMgO refers to transitions between conduction and valence band in the respective materials. QW refers to optical transitions with higher energy due to quantum confinement in wells and QCSE refers to optical transitions at lower energy due to the quantum confined Stark Effect.

[68].

At polar interfaces it is also possible that the quantum confined Stark effect (QCSE) occurs [69]. Due to the finite size of electron and hole wave functions, there is an overlap between electrons confined within a polar quantum well and holes in the valence band of the narrow band material. In polarization-induced quantum wells the quantum well is at lower energies than the conduction band of ZnO and so transitions from the well into the valence band will be at lower energy than transitions from conduction band to valence band away from the quantum well. This means that peaks in luminescence from QCSE occur at energies below the band gap of ZnO. All of these processes are shown schematically in Figure 3.2.

3.2 ZnO/ZnMgO Thin Film Heterostructures

Thin film heterostructures of ZnO/ZnMgO have been grown by MBE [70], MOVPE [71], PLD [72], CVD [73] on many different substrates including c-plane [74] and a-plane [75] sapphire, $ScAlMgO_4$ (SCAM) [76] and single crystal ZnO [70]. The band mismatch and polarization mismatch at the heterointerface allows for the formation of quantum wells which spatially confine carriers and excitons and thus modifies the optical and transport properties at the interface.

The growth method and the substrate both have important effects for the resulting het-

erostructures. For example, high quality ZnMgO with donor concentration $< 10^{15}$ cm^{-3} can be grown by MBE [77]. Typically MBE allows for the highest quality interfaces and best control over the materials grown and in ZnO it has allowed the growth of interfaces with the highest electron mobility by several orders of magnitude with electron mobilities exceeding 10^6 in MBE [70] with values of a few hundred to a few thousand typically reported by other techniques. The choice of substrate has important effects on the film that grows. Substrates with poor lattice matching will strain the film which will, at certain thicknesses, relax forming defects. The substrate also controls the orientation of ZnO which grows, including the polarity of the ZnO. Different cuts of sapphire have different lattice matching with ZnO. C-plane sapphire is poorly lattice matched but oxygen polar $(000\bar{1})$ ZnO grows on c-plane sapphire. By growing a thin MgO buffer on the c-plane sapphire polarity can be inverted to Zn-polar (0001) ZnO [78]. ZnO grows oxygen-polar on a-plane sapphire [79]. On single crystal ZnO substrates ZnO and ZnMgO layers grow with the same orientation as the substrate and therefore their orientation may be controlled by using substrates with different cuts. ZnO substrates are commercially available with Zn and O-polar faces as well as with non-polar faces.

3.2.1 Non-polar Heterostructures

In non-polar ZnO/ZnMgO heterostructures, there is a band-gap mismatch at the interface but no polarity mismatch. The band mismatch allows ZnO quantum wells to form between ZnMgO barriers. There are internal electric fields at polarization mismatched interfaces which tilt bands in ZnO. The band profiles of such an interface are shown in red in Figure 3.1. In cases where this is not desirable, non-polar interfaces are used. Quantum well structures have been grown on a-plane ZnO with excellent structural properties and controllable quantum well widths [80]. Recently abrupt wells have also been demonstrated on m-plane ZnO substrates [81, 82].

These non-polar heterostructures have been thoroughly structurally characterized by a combination of x-ray diffraction [82], transmission electron microscopy [80, 81] and atom probe tomography [81] showing abrupt interfaces between materials and consistent well width but also elemental segregation at interfaces. As well as structural characterization, the optical properties of such heterostructures are typically measured by techniques such as photoluminescence which show transitions between levels in the quantum well with increased energy in accordance with 'particle in a box' models. Due to the lack of polarization in these heterostructures there is no luminescence from the QCSE [80].

Polarization tilts the bands of the quantum wells which isolates electrons on one side of the quantum well and holes on the other. This reduces the electron-hole wave-function overlap and thus reduces the chance they recombine. These properties have meant that a number of groups are seeking to exploit non-polar heterostructures in which there is no band-tilting, for optical applications.

ZnO is a particularly attractive material for some optical applications, such as quantum cascade lasers (QCLs) and photodetectors, as the 72 meV optical phonon in ZnO is stable at room temperature. Empirically, many QCLs only operated at temperatures such that $\hbar\omega/k_B < T$. This is because thermal broadening of quantum well levels means that it electrons do not selectively tunnel into the upper energy level for lasing and thus a population inversion can not be generated at temperature above this temperature. This can be circumvented by using LO phonons to assist the tunneling across barriers in the QCL and allows operation at temperatures greater than $\hbar\omega$ [83]. This however limits the operating temperature so that $\hbar\omega_{phonon}/k_B < T$. The large LO phonon energy in ZnO therefore could allow room temperature operation of QCLs. Groups are therefore aiming to develop cascade lasers based on ZnO for room temperature THz emission [84].

3.2.2 Polar Heterostructures

In polar heterostructures very narrow triangular wells form due to the electric field from the polarization mismatch. These heterostructures have typically been used to form two dimensional electron gases (2DEGs) which have been achieved at both O-polar [85] and Zn-polar interfaces [86] although with much lower mobilities at O-polar interfaces. The polarity of the interface not only effects the electronic properties, but can also effect the Mg distibution at the interface. Abrupt compositional changes at O-polar interfaces would cause a region of p-type ZnO due to the polarization mismatch. This can drive Mg redistribution at these interfaces to avoid the formation of these p-type regions [87].

The polarization mismatch at the heterointerface causes sufficient quantum confinement that 2DEGs are present even at room temperature [88]. The room temperature mobility is typically a few hundred $cm^2V^{-1}s^{-1}$ and depends on the Mg concentration showing an increasing mobility with higher Mg concentration in the ZnMgO layer. This is promising for devices operating at room temperature based upon this 2DEG. At lower temperature mobilities in excess of one million $cm^2V^{-1}s^{-1}$ have been reported [70]. These high mobility heterostructures typically have lower Mg concentration mismatches since at lower temperatures the depth of the quantum well is not important. At these tempera-

tures an optimal Mg concentration of $x \sim 0.01$ was found. Below this value scattering charge impurity limited and increasing the Mg content and hence the depth of the well improved the screening from these charged impurities. For $x \geq 0.01$, an increase in surface roughness due to the epitaxial mismatch between ZnO and ZnMgO was found to limit the mobility [89].

At these interfaces the high mobility and correspondingly long electron scattering times have allowed low-temperature experiments on these interfaces to probe new, fundamental physics. The first demonstration of the quantum Hall effect in oxide materials [86] was at the ZnO/ZnMgO heterointerface. Even-denominator fractional quantum Hall states have been observed at the ZnO/ZnMgO heterointerface, including a number of states previously never observed [90] and new spin-dependent transport at the interfaces not well understood by current models [91].

As well as transport measurements, these interfaces have been extensively studied by using optical techniques. These heterostructures show luminescence from ZnO and ZnMgO as well as more complex peaks due to recombination between states induced by band bending and electron confinement at the heterointerface. As in non-polar heterostructures there is luminescence from transitions between quantum well levels. At these interfaces there is also a polarization-induced quantum well and corresponding QCSE [92]. There are also more complex transitions between quantum well levels and different valence sub-bands which can be resolved at low temperatures [93].

3.3 ZnO/ZnMgO Nanostructure Heterostructures

Experiments on heterostructures in nanostructures face further complexities, both in their growth and their subsequent characterization. Nanostructures, particularly quasi 1d nanostructures are highly anisotropic and have a number of different exposed faces. When growing nano-heterostructures, there are distinct types of heterostructure which will modify the nanostructure's properties in different ways and will typically grow in tandem.

For nanoheterostructures based on ZnO/ZnMgO all previous work has been on heterostructures in ZnO nanowires which grow along [0001]. This has implications for the different functionalities which may be achieved by these heterostructures. Axial nanowire heterostructures will have polar quantum wells where 2DEGs may form since the modulation in chemistry occurs along [0001]. The 2DEG will be perpendicular to the axis of the nanowire and thus will not increase the mobility of carriers along the length of

the nanowire (the typical device geometry). Such a heterostructure may act as a barrier for carriers moving along the nanowire. These 2DEGs will have corresponding optical emission including QCSE. Radial nanowire heterostructures will be along non-polar axes and thus no polarization-induced quantum wells will form. However, non-polar quantum wells may still confine electrons and modify transport properties. Quantum wells may also confine electrons and modify the optical properties of the nanowires, or simply passivate the nanowire surface increasing the optical efficiency of such nanowires [94].

To complicate matters further, in nanostructures, the electronic bands typically bend at the semiconductor/vacuum interface. In ZnO, due to the n-type conductivity and surface trap states, the bands bend upwards. When interfaces are close to the nanowire surface, band bending can therefore further modify the band structure across these interfaces.

ZnO/ZnMgO heterostructures have been previously been embedded into nanostructures. In all reports this has been in ZnO nanowires. Both axial [95, 96, 97] and radial [96, 97] ZnO/ZnMgO heterostructures have been grown, where often both occur simultaneously. These heterostructures have typically been characterized by transmission electron microscopy (TEM) where in scanning TEM (STEM) it is possible to generate atomic number contrast so that ZnMgO and ZnO give different contrast [95, 97]. An example of such TEM characterization showing axial heterostructures in a nanowire is shown in Figure 3.3. In these images Z-contrast and constrast in TEM images are used to distinguish ZnO and ZnMgO regions.

Once grown, the heterostructure nanowires are then typically characterized by optical techniques with either cathodoluminescence or photoluminescence measurements of emission with reports of transitions in both ZnO and ZnMgO. In axial quantum wells the QCSE is reported whereas it is absent in radial wells. This shows that polarization induced 2DEGs do occur within these nanowires in the axial direction [97].

Additionally peaks at energies above the band gap of ZnO, caused by quantum well levels, have been reported in axial [95] and radial [97, 96] quantum wells. In figure 3.4 we show CL spectra acquired on a single core-shell nanowire showing CL emission at increased energy due to carrier confinement by radial quantum wells.

ZnO/MgO core-shell nanostructures show increased external quantum efficiency above plain ZnO nanowires grown by the same technique [98]. ZnO/ZnMgO core-shell nanowires show increased integrated PL signals above plain ZnO nanowires [99]. A high quantum efficiency has been shown for core-shell ZnO/ZnMgO nanowires, where the quantum efficiency drops above a critical Mg concentration due to the introduction of misfit dislocations

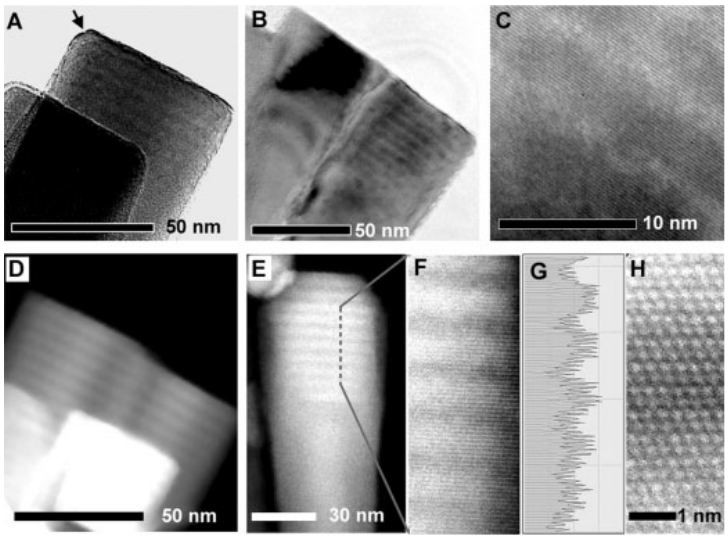

Figure 3.3: TEM characterization of axial ZnO/ZnMgO heterostructures reproduced from [95]. Low (a, b, d, e) and high (c, f, h) resolution images are shown in both TEM (a-c) and STEM (d-h) imaging modes. (g) Shows analysis of the STEM image in (f) resolving the crystal planes.

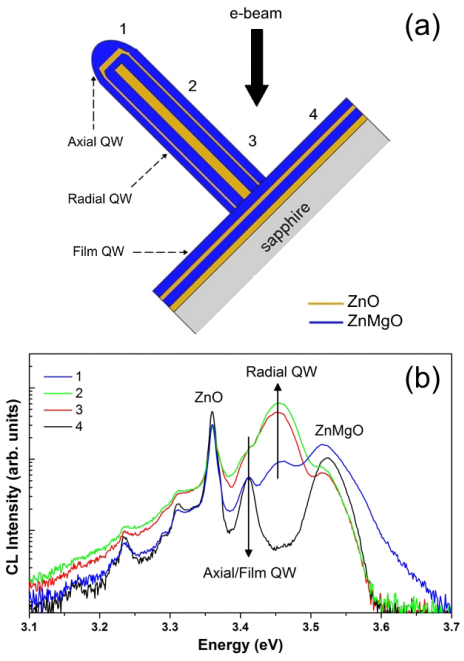

Figure 3.4: Cathodoluminescence spectra acquired on a single core-shell nanostructure reproduced from [96]. CL spectra are acquired at a series of locations indicated in (a) and shown in (b). This shows CL components from quantum wells, ZnMgO and the ZnO.

[97].

3.4 Summary and Outlook

As only n-type doping has reliably been achieved in ZnO, any future ZnO devices must be unipolar devices or composite devices where p-type channels made of a different material are used in combination with n-type ZnO.

Unipolar devices include sensors [100] and amplifiers [101]. Miniaturizing such devices is desirable, for instance nano-amplifiers could be placed on-chip to amplify signals close to their generation before any attenuation occurs. And nano-scale force sensors could be used to measure small forces on the nanoscale such as in nanoscale biological systems. ZnO and especially heterostructured ZnO could potentially offer benefits in both of these applications. In order to understand why it is instructive to consider how heterostructures may grow at the nanoscale.

In ZnO there are mutliple pertinent crystal directions. When forming heterointerfaces along these directions the properties of the interface depends on the crystallographic face in which the interface occurs. In order to modify the transport properties by heterostructuring, the 'best' face to use for the heterointerface is the Zn-polar (0001) face. At this face a band mismatch and a polarization mismatch act together to create a quantum well which confines electrons to two dimensions forming a 2DEG. These 2DEGs have exceptional low temperature mobilities at low Mg concentrations and also show significant increases in mobility relative to ZnO, even at room temperature, allowing both fundamental physics experiments and possible room temperature device applications.

Embedding this into a 1D nanostructure would be particularly interesting for higher temperature applications. This is because the depth of the quantum well which forms at this interface is determined by the Mg concentration in the ZnMgO layer a deeper quantum well is achieved with a larger Mg concentration. In the planar geometry there is a trade-off between the depth of the quantum well and the strain at the interface. The interfaces hosting the highest mobility 2DEGs have been achieved using very low Mg doping concentrations [ref] as these interfaces have small lattice mismatches and therefore little strain or defects due to relaxation of the films. However, the small Mg concentration means that the quantum well is shallow and therefore in order to ensure that the electrons remain confined in these quantum wells, low temperatures are required. This is to ensure that the thermal energy is small compared to the well depth and that electrons are confined at the interface. However, in 1D nanostructures there are different strain relief mechanisms

and strain may be relieved at the nanowire surface. This, in principle, allows higher Mg concentrations in ZnMgO layers without hampering the mobility due to scattering from defects.

In ZnO nanowires and other 1D nanostructures, the directions of crystal planes and the long, growth axis of the nanowire are important for determining which different heterostructures can be grown. As the Zn-polar (0001) face is the face where transport properties are most modified by heterostructuring, the mutual direction of the growth axis and [0001] will be important determining how the transport properties are modified. If, as is normal for device applications, transport occurs along the axis of the nanostructure, then to form a heterostructure which modifies the transport properties of the nanostructure it is important that [0001] is perpendicular to the growth axis. For nanowires, the most common of ZnO nanostructures, this is not the case as they grow along [0001]. A different nanostructure is required as the basis of these heterostructures in order to modify the transport properties.

If such an interface were embedded within a nanostructure and realised high mobilities electrons within a nanowire this could form the channel of a field effect transistor for applications as a high electron mobility transistor used for amplifying microwave signals or for fast switches with low power consumption [59].

Electrons at these interfaces are confined due to the polarization mismatch at an interface which creates a quantum well. ZnO is piezoelectric and so the mechanical deformation of the ZnO couples to the internal electric fields. Therefore deforming such a quantum well would affect the band structure at the quantum well and affect the resistance of the 2DEG channel.

Piezoelectronic force sensors based on ZnO nanowires have previously been realised [20] where piezoelectric effects in the nanowire induce depletion regions and affect the resistance. These nanowires were highly resistive meaning that drain-source currents were small affecting the sensitivity of these sensors. Heterostructure nanostructures with embedded 2DEG channels could be more conductive, allow higher currents and therefore offer a potential improvement in sensitivity.

Chapter 4

Experimental Methods - Sample Growth and Characterization

The growth, characterization and subsequent device fabrication and measurement of thin film ZnO and 1D ZnO nanostructures involves a number of experimental techniques which are detailed in this chapter.

4.1 MBE Growth

ZnO nanostructures and thin films discussed in this thesis have been grown in a II/VI SVTA Oxide MBE system at UCL. A schematic of the MBE used is shown in figure 4.1. The main MBE chamber operates at ultra-high vacuum (UHV) with base pressures typically of order of magnitude 10^{-10} Torr. Beams of reactants are provided by Knudsen effusion cells (metals) and an RF plasma source (oxygen). Whilst growing, the sample is radiatively heated to temperatures up to a maximum nominal temperature of 900 °C.

The main chamber is pumped by an ion pump and a cryo-pump in order to achieve the base pressure. To achieve UHV it is necessary to bake the chamber after the internal surfaces of the chamber have been exposed to atmosphere. When baking the chamber, it is wrapped in insulating blankets and heated to ∼160°C for 2-4 days. In this time gases adsorbed to surfaces in the chamber when it was exposed to atmosphere are desorbed comparatively rapidly. If a bake is not performed adsorbed gases desorb slowly into the chamber and act as a 'virtual leak', limiting the vacuum to 10^{-8} to 10^{-9} Torr. The load lock is pumped by a combination of scroll and turbo pumps. Rough pumping the load lock by the scroll pump before fine pumping on the turbo allows a rapid pump down from atmosphere to a base pressure of order of magnitude 10^{-8} Torr in less than an hour.

This allows the main chamber to be kept at UHV whilst samples are rapidly loaded and unloaded. UHV in the main growth chamber ensures that beams of reactants are ballistic (i.e. collide with no gas molecules before hitting the sample) and that there is a very low level of impurity atoms which become incorporated into the sample.

Liquid nitrogen is flowed through a cryo-shield on the main chamber during growth. This cools the surfaces of the chamber which provides some additional cryo-pumping during growth when pressures are increased. Cooling the chamber walls with liquid nitrogen also decreases the rate of desorption from the chamber walls of any remaining adsorbed gases. More importantly, it also increases the sticking coefficient of any incident reactants on the chamber walls. This means that they stick to the walls rather than being mobile within the chamber. Mobile reactants in the chamber may interfere with growth as reactants not in the primary molecular beams may be incident on the sample. Additionally, if reactants do not always stick to chamber walls then metals may collide with a number of surfaces before being deposited elsewhere within the MBE chamber. This means that surfaces such as vacuum windows may be coated by a layer of metal meaning they cannot be seen through and require removal to clean. More harmful to the smooth operation of the MBE are short circuits which may build up between internal electrical connections e.g. between filaments on ion gauges. Whilst the MBE may be operated when certain windows are partially obscured, inoperational ion gauges require fixing which in turn requires venting the MBE and may be avoided by the use of liquid nitrogen.

Knudsen effusion cells are used to provide beams of elemental zinc and magnesium at beam equivalent pressures (BEP) 10^{-8} to 10^{-6} Torr. The pressure of these beams is controlled by the temperature of the cells. The cells are dual filament meaning there are two proportionalintegralderivative (PID) controlled heaters in each cell. One heater is positioned around the crucible holding the material, the body of the effusion cell, and the other at the tip of crucible. If the material becomes molten and then solidifies upon cooling, then the hot tip stops re-crystallisation around the opening of the cell. If such recrystallization were to occur it would block the desired beams of reactants in future growth and may require venting or significant heating to unblock. The tip is therefore always operated 50°C hotter than the body of the cell. In figure 4.2 we show the relationship between tip temperature and the beam equivalent pressure (BEP) of the cells.

Oxygen is supplied as RF plasma at powers 100 - 500 W and is leaked into the chamber at a rate of 1 - 3 standard cubic centimetres per minute (SCCM) as controlled by a mass flow controller. This results in a pressure of $\sim 5 \times 10^{-5}$ Torr in the chamber.

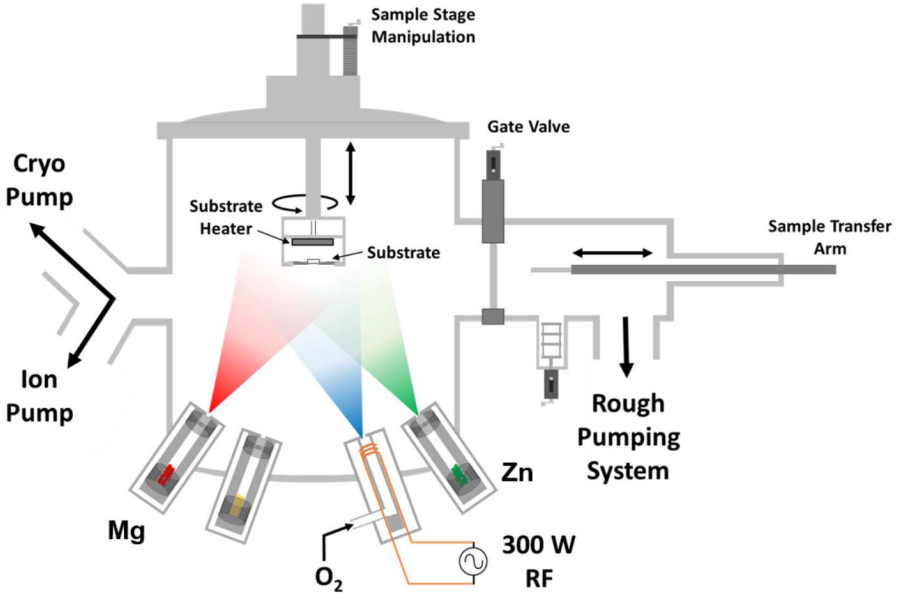

Figure 4.1: Schematic of the UCL Oxide MBE provided courtesy of Dr. James Sagar.

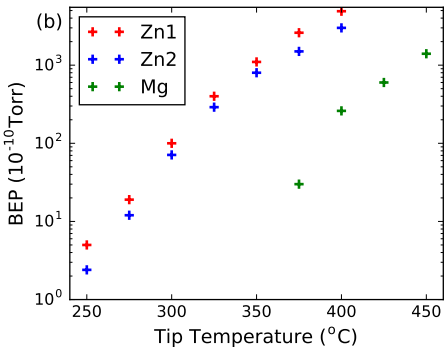

Figure 4.2: Calibration curves showing the beam equivalent pressure against the tip temperature of the effusion cells (two Zn cells and one Mg cell). The body of the effusion cells is always run 50°C colder than the tip.

During growth the samples are held at elevated temperatures as the sample temperature affects growth dynamics. Measuring the temperature of a sample in UHV MBE is known to be technically challenging due to the rotating sample stages meaning that electrically contacting a thermocouple physically on the sample holder is difficult [102]. A schematic diagram of the sample heating and thermometry in the MBE is shown in figure 4.3. Samples are back heated using a radiative heater - a graphite coil which is Joule heated. The temperature of the sample is measured in two ways: by using a thermocouple and by measuring the radiation emitted by the sample. A thermocouple is placed the same distance from the heater as the sample and measures temperature. As the heating is radiative and the heater is equidistant from the sample and thermocouple, it is supposed that the temperature of the thermocouple is the same as the sample temperature. This is not necessarily true and the thermocouple temperature does not necessarily provide a true reading of sample temperature although it does provide a good run-to-run comparison of the true sample temperature. The output of the thermocouple is fed into a PID loop which controls the power to the graphite heater and allows stable temperatures to be achieved.

In addition to the thermocouple there is a pyrometer which measures the black body spectrum of the sample and thus calculates its temperature. This is a primary measure of the sample temperature although it has limitations. Firstly, it is only capable of measuring the sample temperature when above some threshold when the sample emits sufficient black body radiation. Pyrometry is also very sensitive to the material which it measures as these samples will have different emissivities at specific wavelengths. Two notable effects of this are that when rotating the sample the temperature (as measured by the pyrometer) oscillates at the rotation frequency. This is due to sampling more of the sample or the Molybdenum sample holder which have different emissivities. When switching from growing ZnO to ZnMgO the apparent temperature jumps since Mg increases the emissivity at wavelengths pertinent for the pyrometer. The pyrometer reading is very sensitive to the cleanliness of the window shown in Figure 4.3. If this window becomes coated (which may happen during growth or from small pieces of debris) then this affects the reading of the pyrometer. This changes over time but very little between consecutive growths and is a good way to compare growths performed within a short time frame of each other. Using these two methods together allows for better run-to-run consistency of sample temperature.

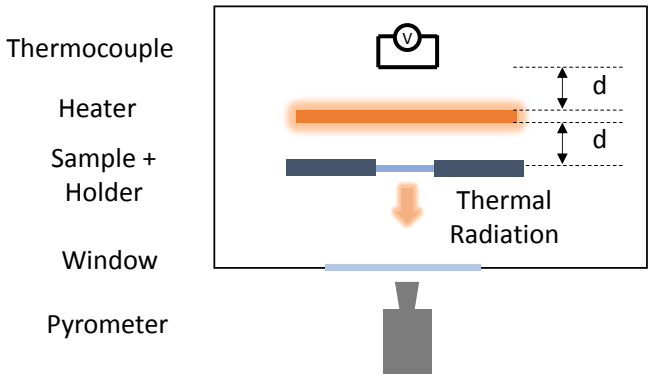

Figure 4.3: A schematic of the sample heating and thermometry in the MBE. A thermocouple is placed equidistant from a heating element as the sample to be heated and acts as a thermometer active over a large temperature range which is used for feedback in PID loops. A pyrometer measures the black body spectrum of the sample and provides the primary measure of the sample temperature. The black box indicates the boundary between vacuum and atmospheric pressure.

4.1.1 Substrate Preparation

In this thesis nanostructures have been grown on sapphire substrates and thin films on sapphire and silicon substrates. Sapphire substrates of various planes are bought as 2" wafers and silicon wafers in a variety of sizes (2"-6"). Wafers are diced into 10 mm × 10 mm samples. The diced samples are then cleaned by subsequently being subjected to 5 minutes sonication in acetone, 5 minutes sonication in 2-propanol and 5 minutes sonication in deionized (DI) water. They are then baked at ∼200° C to drive off residual moisture. For nanostructure growth a thin film of gold is deposited on the surface to act as a catalyst. This film is deposited in a thermal evaporator where a 3-5 nm thin film (as determined by a quartz-crystal microbalance) of gold is thermally evaporated onto the substrates.

4.1.2 Nanostructure Growth Procedure

Typically when growing nanostructures, a sapphire substrate coated with a thin film of gold is loaded into the loadlock and the flow of ∼ 3 litres/hour liquid nitrogen around the cryo-shield is begun. The loadlock is then pumped (first roughing on the scroll then fine pumping using the turbo) to its base pressure whilst a radiative heater heats the sample to 200 °C in order to outgas any adsorbed gas species (in particular water) on the sample and sample holder. During this pump down time the Knudsen effusion cells are heated to the temperature set points corresponding to desired pressures from determined

from calibration measurements shown in Figure **??**. Once the set point temperatures are achieved, and have been held for at least ten minutes allowing the temperature (and consequent flux) to stabilize, the Zn and Mg pressures are measured using a beam flux monitor (BFM). The BFM is a Bayard Alpert ion gauge similar to those described in [103]. If the pressures are not the desired values the temperature of the cells is adjusted and left to reach their new set point and settle before being measured again. After the cells have been left to stabilize for another 30 minutes the pressures are measured again. Once pressures are stable and at the desired values then the sample is loaded into the main chamber. An oxygen plasma is then struck by introducing a flow of oxygen and tuning a variable capacitor (which connects the UHV RF electrode via a vacuum feed-through to the ground of the chamber) to minimise the reflected power to the RF generator. Oxygen flow is 'burst' into the chamber by shutting the mass flow controller (MFC), allowing chamber pressure to drop as pressure builds up behind the MFC, before re-opening the MFC allowing a sudden 'burst' of pressure which causes the ignition of the plasma. The sample is heated to its desired temperature (as determined using the thermocouple and the pyrometer) at which point the zinc cell and oxygen plasma shutters are opened and growth starts. Once growth is completed (typically after two hours) the cells are shut and the sample is cooled. The sample may either be cooled to room temperature and unloaded from the MBE or it may be cooled to a new temperature at which heterostructures are grown. At this temperature the zinc, magnesium and oxygen shutters are opened and closed in a sequence determined by the desired heterostructure. Once the heterostructure growth is complete all shutters are shut, the oxygen plasma is turned off and the sample is cooled. Once at $T \leq 150°\text{C}$ the sample is unloaded from the chamber. When the residual pressure in the chamber is lower than the zinc and magnesium beam equivalent pressures, their respective fluxes are re-measured using the beam flux monitor to ensure that they have been constant throughout growth.

4.1.3 Nanostructure Growth Mechanisms

The growth of one dimensional nanostructures is described by the vapor-liquid-solid (VLS) growth mechanism which allows for exchange of materials between vapor, liquid and solid phases resulting in an enhanced growth rate in one dimension. The VLS model was first proposed in 1964 [22] as a mechanism to explain the growth of Si whiskers. Comparatively recently more general models which unify a family of three phase growth models [104] have been proposed which focus on the underlying mechanisms behind enhanced one

dimensional growth in three-phase systems.

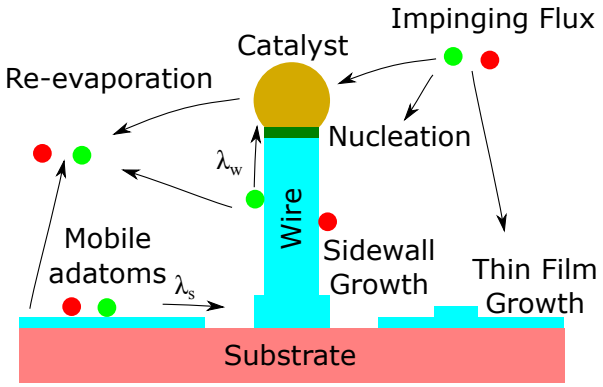

Figure 4.4: Schematic showing the different processes occurring during VLS nanowire growth. The catalyst, wire, substrate and thin films are labeled along with the processes occuring during VLS growth. λ_w and λ_s refer to the mean free path of adatoms on the walls of the wire and substrate respectively. In general these may be different for different species.

In one-dimensional VLS growth a liquid catalyst particle (often gold) acts as a reservoir of reactants. As the liquid catalyst dissolves the incident reactants, the liquid becomes super-saturated with one of the reactants. It then becomes energetically favourable for some of the dissolved reactants to crystallize and form a solid reducing the concentration of reactants within the liquid particle. When 1D nanostructures grow there is a smaller energy cost for this crystallization to happen epitaxially at the interface between the liquid droplet and the top of the nanowire meaning that this deposition lengthens the nanostructure in one direction resulting in the growth of a 1D nanostructure. Deposition may occur where an entire monolayer at the interface between the droplet and the nanostructure is simultaneously deposited or the deposition of an island covering a small fraction of the interface which subsequently grows into a monolayer. When deposited as an island, there is a number of places where the island may nucleate; importantly it may nucleate at the three-phase boundary or a two-phase liquid/solid boundary [104].

A schematic highlighting a number of the important processes occurring in VLS growth is shown in figure 4.4. Here a flux of reactants is directed at the substrate where they are adsorbed as adatoms. The flux also impinges directly upon the liquid catalyst where it may be directly absorbed. Adatoms are mobile on the substrate and have characteristic mean free paths λ which may be different on different parts of the sample so we define λ_w and λ_s where the mean free path of adatoms on the wire is λ_w and on the substrate is λ_s. This may be different for different species of adatom, and, on a faceted nanostructure, λ_w

may depend on the nanowire facet. The mean free path of adatoms characterizes the rate at which adatoms either re-evaporate or transition directly to the solid phase without first being absorbed by the liquid catalyst. Vapour to adsorbed reactant to solid transitions can occur and result in sidewall growth on nanowires or thin film/boulder growth on the substrate which does not result in 1D nanostructures.

In addition to mechanisms described by the VLS model relating to growth there may be other processes which occur whilst a sample is being grown. For example when growing a ZnO/ZnMgO heterostructure it is possible that Mg migrates into the ZnO as a thermally activated process. When growing nanowires on a substrate of different chemistry there may also be epitaxial effects to consider where the epitaxial relationship of nanowires and substrate causes non-vertical growth of nanostructures.

Due to the many processes which may occur and are all interdependent, it is difficult to use VLS growth to *a priori* predict how nanostructures will grow. However, the VLS model provides a very successful model of nanostructure growth which can aid understanding of what processes have occurred during nanowire growth. Once understood in terms of VLS growth, the growth of future nanowires can in some cases be tailored in order to control the rate of different processes and thus control the growth of nanowires. Detailed analyses of VLS growth for GaAs nanowires grown in MBE have allowed the explanation of a number of phenomena observed in nanowire growth including switches of crystal structure, variations in dimensions and growth rates [105, 106].

4.1.4 Sample holders

Two generations of sample holders were used in this thesis. The way the sample is mounted within the system will affect the transport of heat into the sample. This affects the temperature of the sample surface for a given temperature reading of the thermocouple/power supplied by the radiative heater shown in Figure 4.3. The steady state solution to transport of heat into and out of the sample will also affect the uniformity of temperature across the sample. The first generation of sample holders was a disc of molybdenum with a 10 mm $\times$ 10 mm beveled hole cut into it (Figure 4.5 a, b). A 10 mm $\times$ 10 mm sample sits in this hole, supported by the lip and is the left hand sample holder in figure 4.5. The back of samples were coated with a thick film of titanium in order to better absorb electromagnetic radiation from the radiative heater. (This is particularly important when growing onto transparent substrates.)

The first generation of sample holder resulted in large thermal gradients across the

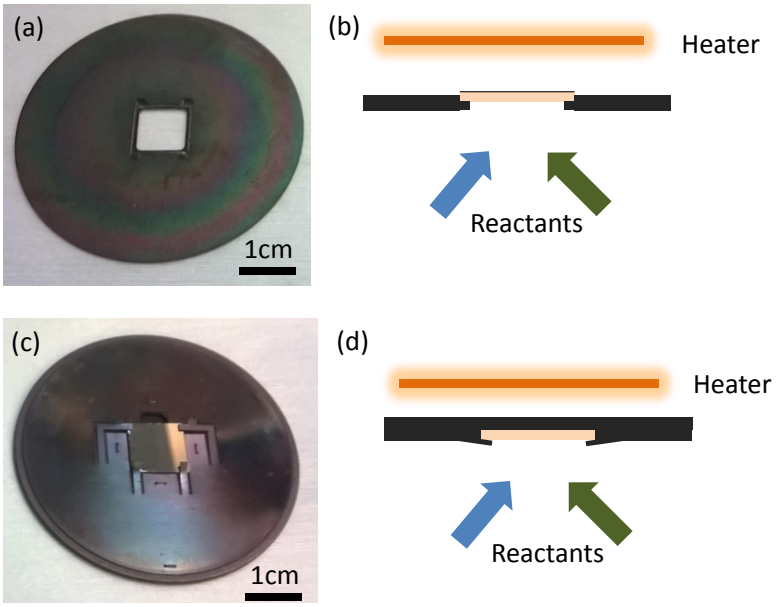

Figure 4.5: Two generations of sample holder. (a) The first generation of sample holder with the beveled lip which holds the sample in place. (c) The second generation of sample holder which has molybdenum clips to hold the sample and a thick molybdenum back plate. (b, d) respectively show schematic cross sections of the old and new sample holders with the radiative heater.

sample. The first clue to these thermal gradients was visible to the naked eye since the apparent colour of the sample depends upon the local density of nanostructures - a high density of nanostructures results in an apparent darkening of the substrate due to scattering of incoming light. Samples grown in this sample holder had a dark ring around the edge close to where the sample was in physical contact to the sample holder showing a systematic variation in nanostructure density which is shown schematically in 4.6 (a). This is verified by SEM images at the edge of the sample, where there is a high density of nanostructures (Figure 4.6 d), and at the centre, where there is not (Figure 4.6 e).

The uneven growth across the sample was demonstrated to be an effect due to temperature variations across the sample by a simple experiment in which a sheet of molybdenum foil was placed behind the sample holder and held in place using a second sample holder - a 'sandwich structure' as shown in Figure 4.7. This sandwich structure meant that the top sample holder was radiatively heated. This heat was then conducted into the sample through the molybdenum foil. When samples were when mounted in this sandwich structure for growth the samples were seen to be evenly coloured (schematically shown in Figure 4.6 (b) indicative of even nanostructure growth. This was demonstrated by SEM images taken at a number of sites across the sample all showing similar densities of

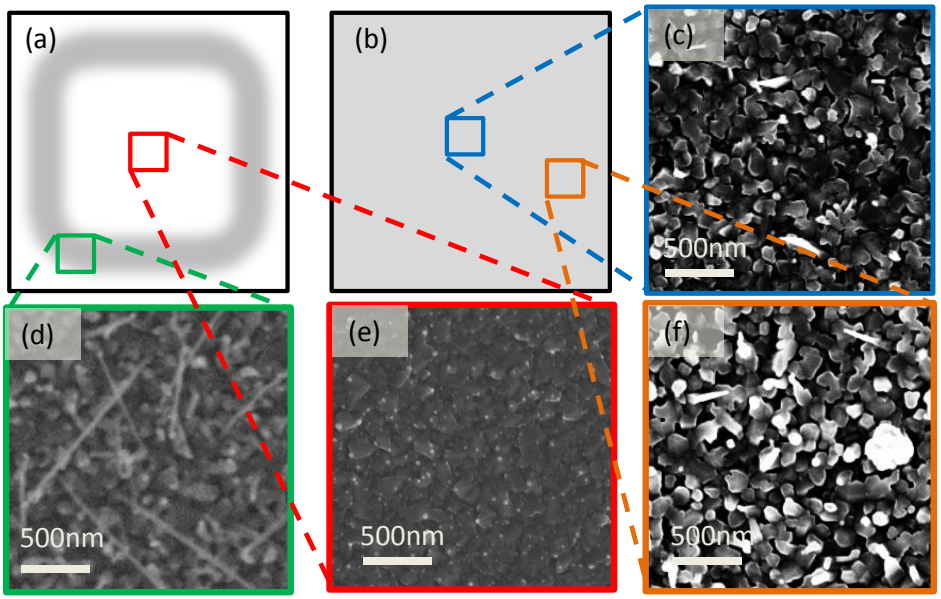

Figure 4.6: Schematic showing the distribution of nanowires (darker regions) on (a) samples grown in the old sample holder and (b) the new sample holder and when performing proof of principle tests using sandwich structures with molybdenum foil (see main text for details). (d, e) show SEM images taken at two points on a nanowire sample grown using the old sample holder showing the significantly different sample morphology. (c, f) show SEMs of two similar areas taken on a sample grown using a molybdenum sandwich structure with similar morphology.

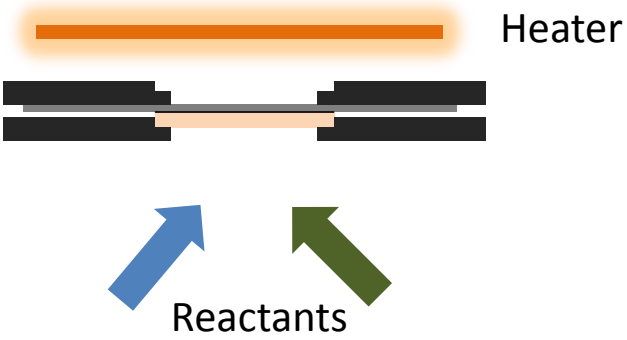

Figure 4.7: The 'sandwich' holder, where a piece of molybdenum foil is placed behind a substrate which is then held in place by a second sample holder. This improves heat transfer across the sample although drops the absolute temperature at the sample growth face due to increased reflection and radiative losses.

nanostructures and sample morphologies such as those in Figure 4.6 (c, f).

The non-uniform heating was a significant problem for a number of reasons. Firstly it meant that the number of nanowires in a single sample was significantly reduced as they only grow in a ∼1 mm strip around the edge of the sample. There were therefore fewer nanowires for subsequent experiments and processing. More importantly it made it challenging to relate nanowire properties to growth temperature. For instance, SEMs of nanowire samples (measuring the local morphology) could vary significantly depending where on the sample the SEM is taken due to temperature variations. When performing ensemble measurements, depending on the area averaged by the ensemble measurement, there is either systematic variation depending on where on the nanowire sample is measured, or the ensemble measurement averages over a number of different local growth temperatures. When nanostructures are removed from the substrate there is not any evidence where they originally came from meaning there is no information on the temperature the individual nanostructure grew at.

Based upon the experiment using sandwich structures a new sample holder was made which could provide uniform heating across the sample. The new sample holder consists of two pieces of molybdenum; a back and front piece. The back piece is a 2“ disk which has a 10 mm × 10 mm groove cut into the disk. The front piece is attached to the bottom and has clips and openings cut into it. The sample sits in the groove in the front piece and the clips push it down onto the back piece so that there is Molybdenum in contact with the back side of the sample. This sample holder heats from the back rather than from the sides generating a uniform temperature across the sample. The sample holder is shown in Figure 4.5 (c, d). There is still a small amount of extra heating in the very local vicinity of the clips but this is a small effect when compared to the previous sample holder.

4.2 Sample Characterization

Following growth, samples are subsequently characterized using a number of techniques. These techniques give us information about the morphology of nanostructures and films, their crystallographic growth directions and orientations with respect to the substrate as well as information about their band structure and defect states.

4.2.1 Scanning Electron Microscopy and Helium Ion Microscopy

Scanning Electron Microscopes (SEMs) and Helium Ion Microscopes (HIMs) allow high resolution (both < 10 nm) imaging of as-grown nanostructures. Both techniques use a

primary beam of charged particles (electrons for SEM and helium ions for HIM) which rasters across a sample. When these charged particles collide with the sample they generate secondary electrons the intensity of which is measured. A SEM/HIM image is a map of secondary electron (SE) yield, and as SE yield depends on the sample morphology, it shows the morphology of nanostructures, their local density and what directions they grow in.

HIM allows for higher resolution imaging particularly on insulating substrates. HIM gives higher resolution images since the beam of helium ions remains very narrow even when it enters the sample. Therefore SEs are generated from a small area of the sample. In SEM the electrons scatter and even a narrow beam of primary electrons can excite SEs from a large area. HIM is particularly good for insulating samples since when performing charged particle microscopy an electric current is delivered to the sample by the primary beam. If this charge cannot dissipate then it repels the like charge in the primary beam causing deformation in the image. Typically HIM uses beams with a lower current than SEM which means that charge builds up more slowly. Additionally as He ions are positively charged the charging effects can be neutralised by negative electrons. A flood gun is used to spray low energy electrons across a sample neutralising the charge built up by the He ions allowing for the compensation of charging.

In this work a Carl Zeiss 1540 Cross beam SEM was used. In order to image semiconductors often grown on insulating samples a lower accelaration voltage of $\sim$2 kV was used. The HIM was a Carl Zeiss Orion Nanofab which has a dual gas system so that either He or Ne may be used as the ion species.

The HIM uses an atomically sharp tungsten needle in an electric field as a gas ionisation source. The needle is made from a single tungsten crystal which is then cut to a sharp tip by Ga^+ FIB. This needle is installed in the microscope and is then further sharpened by heating in an electric field. This is then further sharpened by the user who pulses an electric field in steps up to 50 kV pulling single atoms off of the tip to leave a trimer, a tip which is only three atoms. The user then chooses one of these atoms and aligns it to the optical axis of the microscope.

4.2.2 Transmission Electron Microscopy

Transmission electron microscopes (TEMs) are different from SEMs as the electrons which generate the signal used to create the final image are electrons from the primary beam. This is possible since the electrons pass through the sample and are incident on detectors further down the column, hence the 'transmission' in TEM. TEM is a broad field of

research and a full description beyond the scope of this thesis. Williams and Carter is an excellent textbook describing a number of TEM imaging techniques [107].

In order to be suitable for TEM, samples must be electron transparent ($\lesssim$100 nm) as otherwise the sample will block out the electron beam and no image will be generated. Fortunately the individual nanostructures considered in this thesis are of dimensions sufficiently small that they are electron transparent. However in order to image these samples in TEM it is necessary to remove the nanostructures from the substrate upon which they are grown. This is done by placing a piece of as-grown nanostructure sample in a small amount of 2-propanol. The solution is then placed in an ultra-sonic bath for 1-3 minutes. Nanostructures break off from the substrate during sonication and become suspended in solution. This solution is then pipetted on to TEM grids and allowed to dry. TEM grids used in this thesis are meshes of copper or gold covered with a thin carbon film which supports the nanostructures and is also electron transparent.

There are two modes in which a TEM can be operated. The traditional broad-beam operation involves a wide beam of electrons traveling down the optical axis. The electron beam passes through the sample, and electrons in the beam pick up additional phase as they pass through the sample, this extra phase allows the electron beam to be refocused showing an image of the sample. In this mode the image generated is a projection of the sample into the 2-dimensional imaging plane. Using a high voltage primary electron beam (100 - 300 kV) and high quality focusing optics in this mode it is possible to resolve individual lattice planes in high resolution TEM (HRTEM). HRTEM is TEM performed at higher magnifications and typically made possible by higher quality electron-optics. In order to resolve lattice planes, in addition to high quality optics, the sample must be tilted so that a zone axis (or crystallographic axis) is aligned with the optical axis of the microscope. Columns of atoms are then projected in the TEM image.

Alternatively the electron beam can be focused into a narrow divergent beam with the narrowest spot size at the sample which is rastered across the sample which is called scanning-transmission-electron-microscopy (STEM). With STEM a number of different signals can be collected (and where appropriate spectrally analysed) each of which gives information local to the primary electron beam. Notably for this thesis these signals include: high angle incoherently scattered electrons; characteristic x-rays; the spectrum of electrons which have interacted with the sample; and photons produced in electron-hole pair recombination.

High angle ($> 3^\circ$ [107]) incoherently scattered electrons are used in high angle annular

dark field imaging (HAADF). The amount of electrons which are scattered incoherently to these angles depends on the thickness of the sample and the atomic number of the material [108]. If there is more material then there are more scattering centres and thus more scattered electrons. As these electrons are Rutherford scattered (scattering of electrons due to Coulomb potential of the nucleus) the scattering cross section depends on the atomic number of the elements giving more scattered electrons from higher atomic number elements. Together these effects give thickness and atomic number contrast in HAADF images.

High energy electron beams knock electrons out of low lying energy levels. When an electron is emitted there is an empty electronic state at lower energy in the atomic nucleus and a higher energy electron will fall into the lower lying energy level. These electronic transitions emit x-rays dependent on the difference in energy between the higher and lower levels. The energies of the x-rays are characteristic of the element and so their spectrum can give information on elemental composition. In energy-dispersive x-ray spectroscopy (EDS), x-rays emitted under electron-beam-irradiation are analysed giving information about elemental composition coincident with the electron beam. As the electron beam rasters the sample this information can be mapped providing elemental composition maps.

After interacting with the sample, electrons will lose some energy which is transferred to the sample. By spectral analysis of the electrons which have passed through the sample we can find out how much energy electrons have lost by interacting with the sample. This is called electron energy loss spectroscopy (EELS) [109]. A highly monochromatic electron beam is required to perform EELS as the initial energy of the electrons must be well known to determine how much energy the electrons lose. EELS can be performed either in the high loss or low loss regime both of which give different pieces of information. High loss EELS allows measurement of elemental composition by looking at the losses associated with core electron transitions which produce the x-rays measured in EDS. Low loss EELS focuses on energy regimes below that of characteristic x-rays. It can give some limited information on band gap but also on plasmonic resonances in the sample. These techniques are limited in resolution by probe size and collector efficiency but state-of-the-art EELS measurements have allowed atomic resolution elemental mapping - see for example [110].

Energetic electrons in the primary electron beam can excite a number of quasiparticles in the sample. Some of these quasiparticles will be excitons or electron hole pairs which can recombine radiatively and emit photons. Collecting and spectroscopically analysing the photons generated in electron hole pair recombination is known as cathodoluminescence

(CL). It gives local information about band gap and defect states. It is typically limited in spatial resolution by the minority carrier diffusion length in the material being studied.

A number of TEMs have been used for data in this thesis including a JEOL 2100 at Brunel University London (CL maps) and an abberation corrected FEI TITAN 80/300 at Imperial College London (HRTEM and EDX).

4.2.3 X-Ray Diffraction

In x-ray diffraction (XRD) a beam of x-rays of fixed wavelength are shone on to a sample. The x-rays then scatter off of crystal planes in the sample in accordance with Bragg's law

$$2d\sin(\theta) = n\lambda \tag{4.1}$$

where λ is the wavelength of the incident x-rays, d the spacing between crystal planes and θ the angle between the incident beam and the sample surface as shown in Figure 4.8. In XRD there are a number of measurements which may be performed. These measurements give different information about the samples and may be more or less useful characterizing different samples. In this thesis $\theta - 2\theta$, $2\theta - \omega$, x-ray reflectivity and pole figure measurements are used to characterize nanostructures and thin films. A brief overview of these different techniques is given here. These techniques are applied to thin films and nanostructures grown on single crystal substrates. A Rigaku Smartlab x-ray diffractometer which uses Cu K_α x-rays with a wavelength of 1.5406 Åwas used to perform measurements.

The basic configuration of an XRD set up is shown in figure 4.8. The simplest XRD measurement which can be performed is a $\theta - 2\theta[111]$ scan. In this measurement the sample and detector are moved (changing θ and 2θ) and the intensity of scattered x-rays is collected. When the angles of source, collector and sample satisfy Bragg's law for crystal planes in the sample the scattered x-ray signal is intense, otherwise it is weak. This allows a measurement of the spacing of crystal planes in the sample and (given knowledge of the crystal structure) the lattice parameters of the sample. It is, however, only sensitive to crystal planes oriented such that their normal points vertically upwards in this geometry.

In order to measure $\theta - 2\theta$ scans it is necessary to carefully align the sample. We first align to the flat surface of the sample. This is done by aligning the x-ray source so that it shines directly into the detector ($\theta = 0$) and moving the sample up and down so that it cuts the x-ray beam. As the sample cuts the x-ray beam the intensity of x-rays drops and the surface of the sample is found at half the maximum intensity. The sample is then

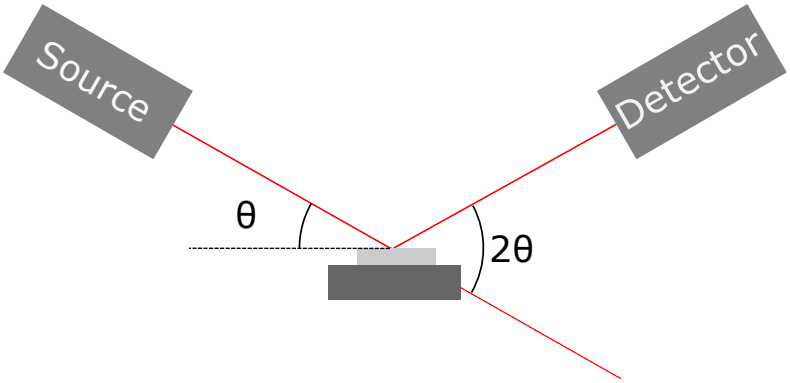

Figure 4.8: Schematic configuration of XRD measurement setup.

tilted so that so that more or less of the beam is cut by the sample. At the maximum intensity the sample is determined to be flat. These steps are iterated to align the sample. Additional alignment can be achieved by moving the x-ray source and detector to a small value of θ so that x-rays are reflected from the surface of the sample. The sample is then tilted so that x-rays are reflected into the detector (when the surface is flat) and misses the x-ray detector otherwise. The position of maximum reflected intensity is the aligned position.

When using crystalline substrates of high quality, it is best to align the single crystal substrate to the XRD. This is done by referencing one of the diffraction peaks of the single crystal substrate. As the substrate is typically a high quality, bulk sample the location of diffraction peaks is known. Therefore any errors in alignment can be accounted for by aligning to the diffraction peak of the crystal. This allows for better comparisons between samples as measurement is aligned to a known value, the substrate peak, and is called a $2\theta - \omega$ measurement [112].

A related measurement is x-ray reflectivity [113], where shallow angle x-rays (small θ) are reflected off of the surface of the sample. When reflected off a thin film, reflections occur at the film/air interface and the film/substrate interface meaning that there are two reflected beams with some phase difference. These beams interfere with each other and constructive/destructive interference will occur depending on the incident angle, the film thickness and the film density. Therefore, with a thin film, when scanning the incident angle of x-rays, the intensity of reflected x-rays will oscillate as a function of the angle the x-rays make to the sample. Additionally, x-rays will be lost due to surface roughness where x-rays are reflected but not towards the x-ray detector, resulting in a drop in intensity. By fitting to these oscillations the surface roughness and the thickness of these films can be characterized.

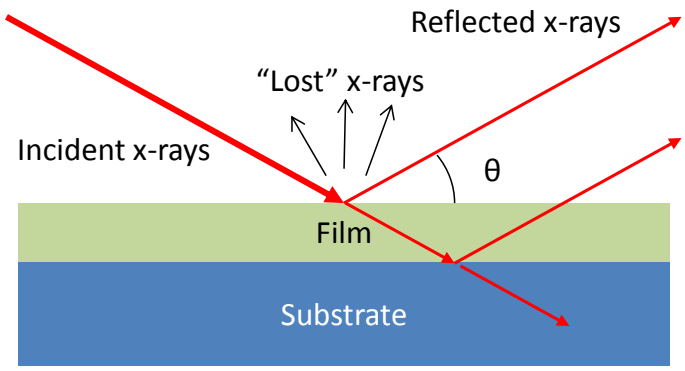

Figure 4.9: Schematic of x-ray reflectivity measurement. Incident x-rays are reflected by the surface of the film and at the interface between film and substrate. X-rays are also 'lost' to specular reflection and diffuse scattering or by propagating into the substrate.

As $\theta - 2\theta$ or $2\theta - \omega$ scans give information about crystal planes which are oriented in the plane of the substrate, they are of limited use for the analysis of nanostructures since they often grow with crystal planes not parallel to the substrate surface meaning they do not contribute to diffracted intensity in these geometries. Nanostructures do not form a film which can be coherently reflected off and so x-ray reflectivity is also of little use. Additional XRD techniques can however provide extensive information about samples. One such technique is the pole plot.

In a pole plot [114] the x-ray source and detector are fixed at a value of θ corresponding to a known Bragg reflection in the material. The sample is then tilted and rotated and as the sample moves an intensity map is collected. The sample rotates around the normal to the sample (ϕ) and is tilted (χ) as shown in figure 4.10. In a single pole figure we look at a single set of equivalent crystal planes that we choose when selecting the Bragg peak when setting up the experiment. When the normal to the crystal planes points vertically within the XRD set up they will satisfy the Bragg condition and contribute to the scattered x-ray intensity.

This technique is a powerful tool when determining how nanostructures grow on a substrate. When growing 1D nanostructures then if we align the XRD to the Bragg peak corresponding to the growth axis of the nanostructures a pole figure is a map of nanostructure growth directions. We can also use pole figures or partial pole figures to align the sample so that nanostructures are pointing vertically in the XRD before performing a $\theta - 2\theta$ scan so that in the subsequent measurement scattered x-ray intensity comes from the nanostructures rather than secondary growths on the sample.

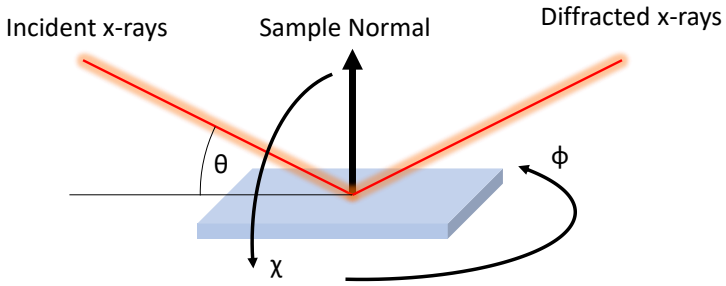

Figure 4.10: A schematic diagram showing the sample orientation during the acquisition of a pole-plot. The red lines shows the x-ray beam aligned to a Bragg peak. Rotations in ϕ are about the normal to the sample. Rotations in χ are about the a vector in the plane of the sample and also the plane of the x-ray beams (i.e. the x-ray beam at $\theta = 0$).

4.2.4 Photoluminescence

Photoluminescence (PL) is a technique used to characterize the band structure of semiconductors. Electron-hole pairs are generated in the sample using a light source (typically with energy above the band gap of the semiconductor). These electron hole pairs then recombine; either directly across the band gap, across the band gap but mediated by an exciton, or via defect states. Recombination may be radiative (giving out photons) or non-radiative (no photons emitted). The photons emitted by radiative recombination are collected and spectrally analysed. These spectra have peaks at different energies associated with these different emission processes. A schematic of these different recombination mechanisms is shown in Figure 4.11 (b). The PL spectrum contains information about the band gap, excitonic structure and defect states present in a semiconductor material.

PL spectra are temperature dependent - at high temperature thermal energy may wash out fine structure in PL spectra meaning that features, such as exciton peaks, cannot be resolved. PL at cryogenic temperatures allows for this structure to be better resolved.

A Renishaw fluorescence microscope was used to perform room temperature PL. The PL setup uses UV light at 325 nm (3.81 eV) produced by a HeCd laser. The laser power is 2-3 mW and is focused to a spot 1-2μm wide although no power-meter operating at 325 nm is available meaning this is not well calibrated. The full power density of the laser is therefore 600-4,000 Wcm^{-2} although probably in the lower end of this window as the beam is likely 2μm wide. The intensity of the incident light may be controlled as may collection times. A filter may be used to cut out a portion the laser light dropping the power density of the laser beam. A schematic of the confocal PL set-up is shown in Figure 4.11 (a). By increasing the collection time we improve signal to noise in the measurements.

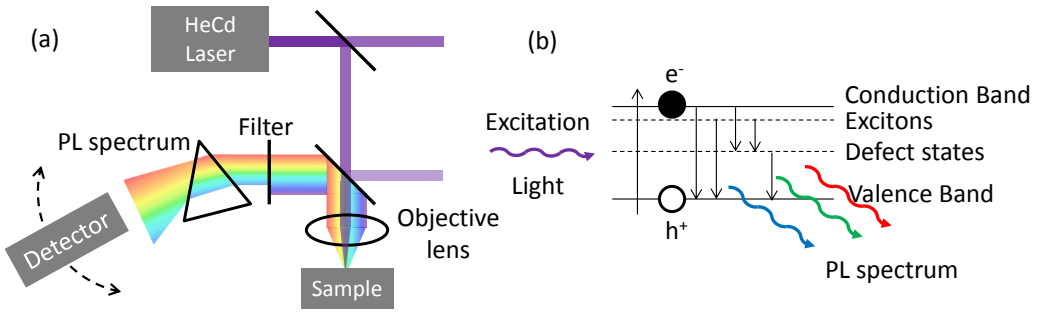

Figure 4.11: (a) Schematic diagram showing the Renishaw confocal PL microscope. A HeCd laser is used to generate light which excites carriers. This is then focused onto the sample. The PL spectrum is collected by the same objective lens that focuses the light onto the sample. This then passes through a filter which cuts out parts of the spectrum (typically the wavelengths of excitation light). This passes through a prism and the detector moves collecting counts from different parts of the spectrum. (b) Schematic of the PL process showing how incident light excites electron hole pairs which recombine via different defect/exciton states and give off a PL spectrum.

However, the CCD used to count the PL intensity is also sensitive to cosmic rays so we increase the number of cosmic rays within each spectrum. Increasing the intensity of pump light increases the signal, but may also change the PL spectrum as defects are saturated.

The excitation beam can be focussed into a small spot by the powerful objective in the Renishaw confocal system so that PL spectra may be collected from small regions of the sample. We use the narrow beam to perform single nanostructure PL after having dispersed nanowires on a pre-patterned substrate. The substrate has a labelled array of crosses which are large enough to resolve in the confocal microscope on the Renishaw. Imaging the dispersed nanowires by SEM/HeFIB allows us to determine where (relative to the markers) nanostructures are distributed on the substrate. Care is taken to minimise exposure to electron/helium beams in case they cause damage to the samples. Therefore few images (at low magnifications) are taken.

Once the nanostructures are located on the sample, the PL laser is aligned to the region where we know there is a nanostructure and a luminescence spectrum is collected. An example SEM image used to locate nanostructures is shown in Figure 4.12. 1D nanostructures can act as waveguides for light and therefore depending on the precise orientation of the nanostructures on the sample there may be variations in the amount of light that is emitted towards the objective lens and thus reaches the detector. This means that mak-

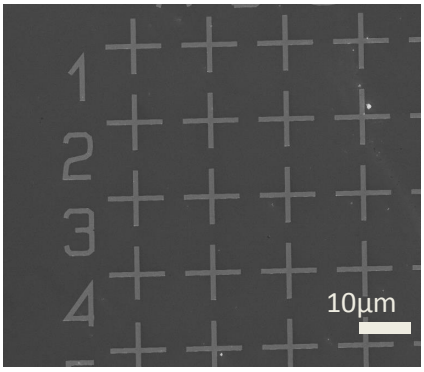

Figure 4.12: SEM image of a Cr/Au grid on Si which is used to locate nanostructures in PL.

ing inferences based on the absolute intensity of PL spectra from single nanowires must be made with care. Once room temperature PL measurements are performed on these nanowires, further analytical techniques may be performed, such as cryogenic PL, higher resolution imaging or SEM-EDS.

4.2.5 Cathodoluminescence

Cathodoluminescence (CL) is a similar technique to PL except an energetic electron beam is used to excite electrons from valence to conduction band rather than photons in PL. The electron beam is typically the beam from an electron microscope. CL allows for the collection of spatially resolved luminescence data even on the nanoscale. This is difficult to achieve with PL as beams of light cannot readily be focused to spots below the Abbe limit of $\lambda/2$ (hundreds of nanometres for UV wavelengths). Electron beams typically have spot sizes which are $\approx$10 nm in SEM and $\approx$1 nm in STEM. This means that even within single nanowires it is possible to get spatially resolved luminescence measurements. In this thesis we present data which have been collected by STEM CL which is a recently developed technique which allows ultra-high resolution luminescence maps to be collected from nanostructures. In STEM CL, the electron beam from a scanning transmission electron microscope is used to excited carriers highly locally. An optical fibre is fed into the STEM column and used to collect the CL spectrum which is fed to a spectrometer. This is discussed further in chapter 8.

4.2.6 X-ray Photoelectron Spectroscopy

In x-ray photoelectron spectroscopy (XPS) a sample is irradiated by monochromated x-rays which cause electrons to be ejected from the sample. The spectrum of kinetic energy of

the ejected electrons is measured and thus the binding energy of the electron is determined by the difference between the kinetic energy of the electron and the energy of the x-rays which caused it to be ejected, less the work function of the material. As the binding energy of electrons depends on the element then the energy of emitted electrons gives information about the elemental composition of the sample. XPS is (in a crude manner) EDS backwards. In XPS monochromated x-rays come in and the spectrum of electrons gives information on elemental composition whereas in EDS monochromated electrons come in and the spectrum of x-rays gives information on elemental composition.

XPS is a surface sensitive technique since only the electrons that escape the sample are detected. If an x-ray collides with an electron deep within the sample it will likely undergo some form of collision and consequent re-trapping before being ejected from the sample. The chance of an electron escaping decays exponentially with distance from the sample surface making XPS highly surface sensitive (only the top few nanometres although this is sample dependent). Adding an angle between the normal to the surface and the x-ray detector increases the surface sensitivity of the measurement as electrons excited at the same depth traveling towards the detector must travel through more material to reach the surface than when being ejected at the normal to the surface.

The XPS system used for measurements in this thesis is a Thermo Scientic K-Alpha instrument using a monochromated x-ray source of Al K_α radiation at 1486.6 eV. The measurements were performed by Matthew Sparks of UCL.

Chapter 5

Experimental Methods - Device Fabrication and Characterization

In this thesis electrical devices have been fabricated from MBE grown ZnO nanowires and films. These devices allow the properties of ZnO nanowires to be measured in the nanowire field-effect transistor (FET) geometry. We also explore the use of ZnO films for future piezoelectric devices. This chapter details the fabrication and analysis of these devices.

5.1 Cleanroom Fabrication Techniques

Nanodevices are fabricated using a variety of lithography techniques in which layers of metal contacts or dielectrics are selectively deposited or etched. Aligning these layers to each other and nanomaterials deposited on substrates allows the fabrication of nanodevices out of these active layers or nanomaterials. This occurs in a cleanroom at the London Centre for Nanotechnology.

5.1.1 Electron-Beam- and Photo- lithography

In both electron beam lithography (EBL) and photolithography a resist material is selectively irradiated and consequently undergoes some physical change. This physical change allows the irradiated regions of resist to be selectively developed thereby transferring patterns into a resist layer. In EBL the irradiation is done by a beam of high energy electrons. A combination of precise sample movements and electron beam rastering allows comparatively large areas to be exposed selectively defining patterns in the resist. In photolithography UV light is used to irradiate the resist. The UV light is either shone uniformly over the sample and then selectively blocked by a photo-mask (typically a chrome pattern

printed on glass) or focused into a fine beam which is then rastered across the sample. All of the photolithography discussed in this thesis is performed using a photo-mask.

In EBL the electron beam is precisely rastered by deflecting the beam using electric fields in the fixed electron beam column. Electrons may be deflected by a maximum distance and so when the sample is stationary only a certain area directly underneath the column may be exposed. In order to expose patterns larger than the distance which the electron beam may be deflected the stage must move. The pattern to be exposed is therefore split up into a series of 'write fields'. Each write field is exposed with the sample stationary and the electron beam rastering within the write field. Once the write field exposure is complete, the stage moves, centering the next write field within the area the electron beam may raster. The next write field is then exposed. A write-field alignment procedure allows the deflection of the beam to be calibrated to the stage motion. This can either be done using any random feature on the sample which gives SEM contrast or using pre-fabricated arrays of alignment markers, patterned for this specific purpose. Write-field alignment with patterned alignment markers will typically result in smaller misalignments than that using random markers as they are designed to interface with image recognition software allowing computer aided alignment and arrays of markers allow for corrections to rotational misalignement.

In both EBL and photolithography positive and negative tone resists may be used, schematics of which are shown in Figure 5.1. The same patterns can be made in positive and negative resists by inverting the exposed patterns. This is straightforward in mask based photolithography where the negative of the image is simply printed onto the mask. In EBL inverting the pattern can result in significant increases in exposure times. A positive tone resist is one which becomes more soluble in developer after exposure and so the exposed regions are washed away. In a negative tone resist the opposite is true and the exposed resist remains after development. Resists consist of a chemical which interacts with the radiation which is dissolved in a solvent. The liquid resist can be spun onto substrates forming a uniform thin layer of resist. In spinning a sample is coated in the liquid resist and then rotated at speeds typically exceeding 1000 rpm for approximately one minute.

Positive tone resists are selectively developed due to the breaking of chemical bonds in a polymer under irradiation. A typical example of positive tone resist is polymethyl methacrylate (PMMA), a long chain polymer and widely used EBL resist. Long chain PMMA dissolved in anisole is used as a resist. In this thesis PMMA with molecular

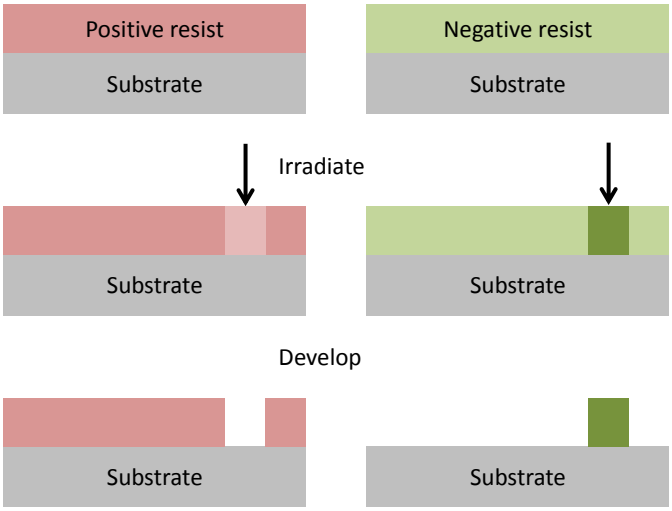

Figure 5.1: Schematic showing exposure and development of positive and negative resists. The arrow indicates the incident radiation which exposes the resist.

weights 950,000 and 495,000 are used where the 950,000 is composed of longer chain polymers. When electron beams irradiate the sample, it breaks the long chain molecules into monomers which are then removed by a developer which is a mix of methyl isobutyl ketone (MIBK) and 2-propanol (IPA) in the ratio 1:3. In a negative tone resist the irradiation cross-links monomers in the resist resulting in something with lower solubility than the unexposed resist. An example of negative tone resist is hydrogen silsesquioxane (HSQ) - often referred to as liquid glass. When exposed to electron irradiation silicon in the HSQ cross links and a silicon oxide layer forms.

Typically functional devices are not composed of resists and instead the resist is used to transfer a pattern to active layers. This can be done by lift-off or etching. In lift-off a resist is exposed and developed before an active layer is deposited uniformly over the sample. Where the resist has been removed the active layer is deposited directly onto the sample and elsewhere remains on top of a resist layer. The resist layer is then dissolved (in, for example, acetone) and anything deposited on top of it floats away leaving behind the pattern defined by the resist. When etching the resist layer acts to protect an active layer beneath the resist layer, transferring the resist pattern into the active layer.

Lift-off is typically performed with a positive tone resist, shown schematically in Figure 5.2, meaning wherever the resist is exposed to radiation the deposited layer will remain. Often when performing lift-off, bi-layer resists are used, where the bottom layer of the resist is more sensitive to the radiation than the top. Due to back scattering of electrons or diffraction of light, regions around the intentionally exposed area will receive a smaller

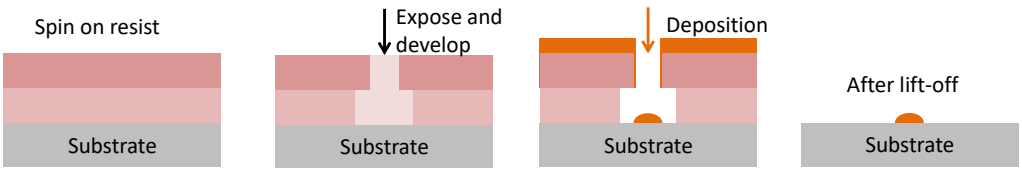

Figure 5.2: Schematic of deposition using bi-layer resist for lift-off.

dose of radiation than the intentionally exposed regions. The lower dose is sufficient to expose the more sensitive bottom layer of resist and so, when developing, the region around the exposed area will also be removed in the bottom layer. This results in an undercut which can be advantageous when performing lift-off. The undercut means that any of the deposited layer which coats the side walls of the resist are not physically connected to the material intended to remain. This means that when performing lift-off the solvent which dissolves the resist can access the resist rather than having a protective layer which stops access. It also prevents 'lily-padding', where the deposited layer coats the sidewall of the resist and results in a lip which remains after lift-off.

In work presented in this this thesis one EBL system (Raith150Two) and two mask aligners (a Karl Suss MJB3 and a Quintel mask aligner) were used. The EBL system can be operated with acceleration voltages up to 30 kV and an aperture ranging from 10 to 120 μm diameter. Increasing the diameter of the aperture increases the spot size which decreases the resolution but also increases the current which decreases the exposure time. A tradeoff between the finesse of features required and a reasonable exposure time must therefore be made when determining the EBL operation parameters. For optical lithography, the Karl Suss is better suited for precise alignment to small samples due to better contrast in the optical microscope (making alignment easier) and a better controlled stage where fine x, y, z and rotational alignments can be made to align to the sample. The Quintel mask aligner can be used with larger wafers and up to 6" wafers can be exposed (up to 4" were processed for work presented in this thesis).

5.1.2 Magnetron Sputtering

Magnetron sputtering is a thin film deposition technique which, for devices discussed in this thesis, has been used to deposit metallic layers. An SVS 6000 DC magnetron sputterer with a number of metallic targets has been used. In magnetron sputtering a sample is loaded into a vacuum chamber. Once pumped to sufficient vacuum, a gas of argon, nitrogen or a mixture of the two is leaked into the chamber to reach a set point

pressure. A voltage is applied between two electrodes, the cathode of which is the metallic contact to be sputtered. The voltage causes the ignition of a plasma and the positive ions in the plasma are accelerated towards the cathode and collide with it. In these energetic collisions small pieces of material are knocked off (or sputtered) from the metallic anode which forms a broad beam within the chamber. When these sputtered particles collide with a solid surface (the sample or chamber sides) they are deposited. However, as the pressure of the carrier gas is a few mBar the mean free path of gas atoms is significantly smaller than the size of the chamber and sputtered material will collide a number of times with gas atoms before reaching a solid surface and being deposited. This means that atoms in the beam of sputtered material are not highly directional which can have effects when performing lift-off. As the sputtered material is not in a directional beam it will coat resist side-walls as well as exposed regions. Side-wall coating may stop lift-off chemicals from reaching the side-walls to dissolve resist and thus hamper lift-off.

In the SVS 6000 there is additionally an *in-situ* ion gun. The ion gun has a cathode and an accelerator plate. Gas atoms have outer electrons stripped by the cathode and are accelerated towards the sample. This is typically done using argon - an inert, massive gas - which bombards the surface of the sample, milling away the top layer. Controlling the accelerator voltage and beam current changes the rate at which this happens. This can be useful to perform before depositing films by sputtering as it cleans the surface and any contaminants before metallization which may help to minimise the contact resistance between the sample and metal layers or adhesion of layers.

5.1.3 Thermal Evaporation

Thermal evaporation is conceptually simple - a source of material (often a metal) is heated and, as it approaches its boiling point the vapour pressure of the material increases evaporating the metal. This is done in a vacuum (typically $< 10^{-6}$ mBar) so the evaporated metal is transported ballistically to the sample which is placed above the source. When colliding with the sample the evaporated metal loses thermal energy and re-solidifies coating the sample. As this is all done at high vacuum the mean free path of the evaporated metal molecules is typically longer than the dimensions of the vacuum chamber meaning that they do not collide (and react) with other molecules and that the evaporation is highly directional. Directional evaporation can be advantageous when performing lift-off as there is less sidewall covering of resist by metal.

In order to evaporate a metal it is necessary to heat it. This may be done in a

number of configurations. In this thesis the most common is by loading the material to be evaporated onto a piece of a different material with a melting point significantly above the evaporated material - often tungsten - and Joule heating this second material. The heated material may be formed either into a dimple boat, a coil or a rod. A dimple boat is a flat narrow piece of material which has a dimple in its centre. Rods are cylinders of metal which are electroplated with the material to be evaporated. Rods are typically used for chrome evaporation as chrome sublimes and therefore is not raised to a temperature where it melts. Coils are spirals of the high melting point material which has wire of the evaporated material hung off the spiral. When the material melts the surface tension of the liquid material means that it coats the wire. In addition to Joule heating it is possible to directly heat the material with radiation such as an electron beam. The material must be placed in a crucible with high melting point and then heated. Thermal evaporation is used to deposit catalyst materials for nanowire growth.

5.1.4 Reactive Ion Etching

Reactive ion etching (RIE) is a dry etching technique in which a sample is etched using a chemically reactive plasma. A sample is placed in a vacuum chamber which is pumped to base pressure ($< 1 \times 10^{-5}$ mBar) before a mixture of gases is leaked in to a pressure set point. A plasma with controllable power is struck by applying an RF potential difference between the sample plate and a plate at the top of the chamber. Ions in the plasma collide with the sample which etches the surface of the sample where the collisions occur.

RIE is different to ion beam milling (such as that performed in the SVS) as the gases typically used in RIE are chemically reactive. For example, a gas used to fabricate devices discussed in this thesis is SF_6. When a plasma of SF_6 is excited, fluorine radicals are generated. These fluorine radicals are highly reactive with some materials and therefore etch the material much more quickly than physical ion bombardment alone. By choosing the gas chemistry for the material it is possible to optimize the relative etch rates of different materials - we can perform selective etching. This is useful when, for example, PMMA patterned by EBL is used as an etch mask. PMMA layers are < 300 nm thick and are rapidly milled through in a physical etch (such as argon milling). However, PMMA is comparatively resistant to chemical etching by fluorine radicals (especially relative to metals such as niobium) meaning that in RIE using fluorine chemistries it is possible to etch niobium films at a sufficiently high rate that a PMMA mask allows a $\approx$100 nm film to be etched through before the PMMA layer. This would not be possible using ion

milling. The RIE used to fabricated devices discussed in this thesis is an Oxford Instrument PlasmaProNGP80 RIE which has a number of gas chemistries available including SF_6 and CHF_3 which are used for Niobium and Niobium Nitride etching recipes.

5.2 Nanowire Devices

In order to determine the electrical properties of nanostructures, they must be electrically contacted and thus incorporated into electrical devices. In order to characterize semiconductor nanostructures they are fabricated into a field effect transistor (FET). FETs are three-terminal devices in which a current flows from a source electrode to a drain electrode through the nanostructure. An electrical field may be applied by a gate electrode. The electrical properties of the nanostructure are measured as a function of both drain-source voltage and applied gate voltage.

5.2.1 Fabrication

In order to fabricate single nanostructure FETs we use a procedure established by a previous PhD student, Dr. Marion Sourribes [115].

FETs are fabricated on a carrier chip which has macroscopic electrodes patterned onto it allowing contact to be made to the FET. Making the carrier chips is a multi-stage process which is shown schematically in Figure 5.3. It starts with a highly doped Si wafer. A thermal oxide is grown on this silicon wafer which ultimately separates the nanowire (on top of the oxide) from the highly doped Si which acts as a universal back gate in the final device. Macroscopic contact pads for wire bonding (or contacting via probe needles) and alignment markers are then patterned by photolithography using a bi-layer resist (LOR 10B and S1805). The 2-layer resist results in an undercut in the resist sidewall giving improved liftoff. A Cr/Au (5/50nm) layer is then thermally evaporated, before lift-off is performed in 1165 microposit remover.

Next a layer of thick photoresist (S1818) is spun onto the whole wafer. Tweezers are used to carefully scratch away a small piece of resist on each chip exposing the underlying substrate. The wafer is then submerged in hydrofluoric acid (HF) to etch any exposed SiO_2 which was thermally grown on the top of the wafer, exposing the highly doped substrate. The wafer is then rapidly (< 10 minutes exposure to atmosphere) loaded into a thermal evaporator where another Cr/Au (5/50nm) layer is thermally evaporated. This is then lifted off and the remaining metal acts as a good electrical contact to the highly-doped back gate.

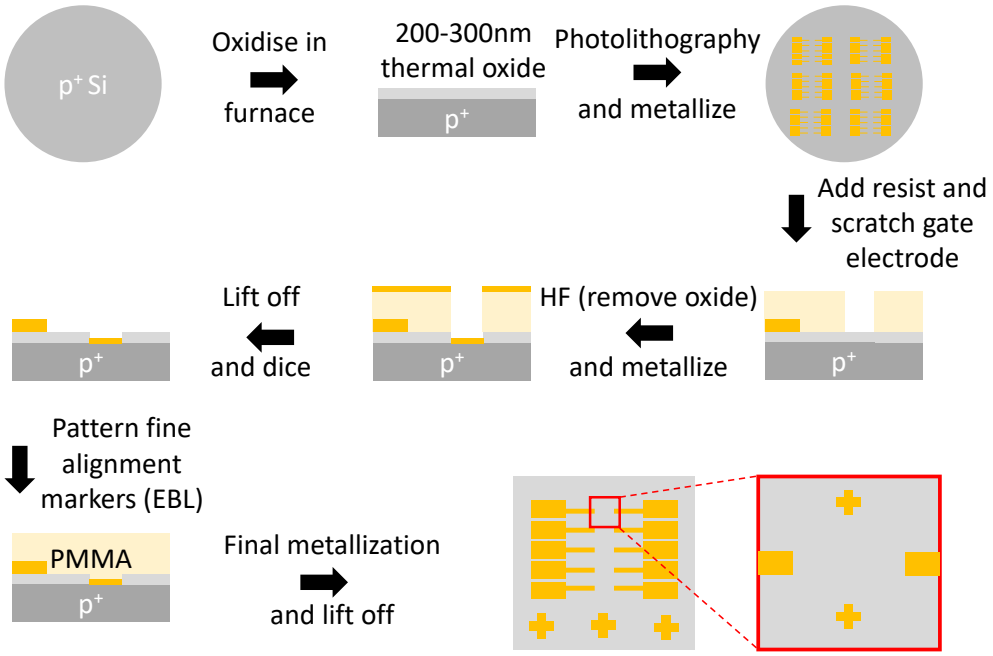

Figure 5.3: Schematic of step by step fabrication of pre-patterned carrier chips for nanowire devices.

The wafer is then diced into 10x10mm chips and further processing occurs by EBL. After aligning to large alignment markers deposited in the photolithography stage, finer alignment markers are patterned by EBL. This allows the alignment necessary in order to make contact to single nanowires in subsequent processing steps. A final thermal evaporation deposits the alignment markers and after lift-off the chip is ready for nanowire devices to be fabricated upon it.

As shown schematically in Figure 5.4 we start with a pre-patterned chip. Nanowire devices are then made by taking a piece of as-grown nanowire substrate and sonicating it in a small amount (∼2 ml) 2-propanol (IPA). This causes nanowires to break off the substrate and enter suspension in the IPA similar to the process for preparing nanowires for TEM section 4.2.2. This nanowire solution is then pipetted onto the pre-patterned chip and the IPA allowed to evaporate leaving behind nanowires randomly deposited upon the substrate.

The nanowire-covered chip is then loaded into the EBL where SEM micrographs are taken of the surface. These show the location of nanowires relative to EBL patterned alignment markers which allows patterns to be designed which will connect the nanowire to the contact pad. These patterns are automatically generated using a piece of software developed by Dr. Marion Sourribes, a previous PhD student within the group [115].

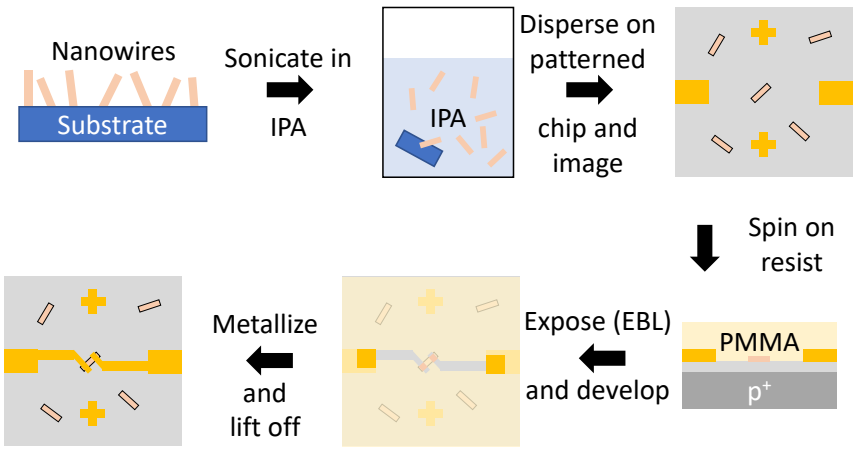

Figure 5.4: Schematic of step by step fabrication of nanowire devices.

Once the nanowires are imaged the sample is unloaded and a layer of PMMA is spun onto the device (PMMA 950 A4 $\approx$ 300nm thick). By aligning to the chip (first to the large alignment markers made by photolithograpy and subsequently to the small EBL alignment markers close to the nanostructure) we ensure that the pattern overlays the nanowire and macroscopic alignment markers. After EBL exposure (using a dose of 150nC/μm^2) the chips are developed in a mixture of MIBK and IPA (1:3) for 60s.

The developed sample is loaded into a DC magnetron sputter with an in-situ argon ion mill (SVS 6000). After $\approx$ 2 hours of pumping the ion gun is switched on and the nanowires are milled for 60 s with an acceleration voltage of 390 V resulting in an ion current of 10 mA. This cleans the surface of the nanowire in preparation for metallization and improves contact resistance [116]. After the ion mill step the chamber is allowed to pump briefly before metallization. A 10 nm Ti film is sputtered first after a $\sim$5 minute pre-sputter/getter stage. This is followed by a 50 nm Au film being sputtered in situ. Ti/Au contacts have previously been used to create ohmic contacts to ZnO [117, 118]. The titanium layer aids adhesion and also makes the contacts ohmic as a thin layer of titanium dioxide forms at the Ti/ZnO interface due to the greater electron affinity of Ti than Zn. This leaves some oxygen vacancies (donors) at the interface between the contact and ZnO. Increasing the free electron density at the contact promotes ohmic behaviour.

A final stage of lift-off is performed using 1165 microposit remover before a rinse in acetone followed by IPA (to remove 1165 residues). The chip is blowed dry using a dry nitrogen gun. At this point the device is ready for measurement.

5.2.2 Field Effect Transistors

Having fabricated single nanostructure FETs we perform electrical measurements on the device in order to infer properties of the nanostructure. We initially characterize the resistance of nanowires without the application of a gate voltage typically in a two-point configuration. We then apply a gate voltage at fixed drain-source voltage and measure the current flowing through the nanostructure. We keep the subsequent analysis, where possible, sufficiently generic that the geometry of the nanostructure only becomes relevant when calculating the capacitance between the nanostructure and the gate electrode.

Within a nanostructure the net charge is zero. For n-type nanostructures such as ZnO, there is positive charge associated with ionized shallow donors, surface states and charge on the back gate capacitor. Negative charges are free electrons in the nanowire which may carry current. We may therefore write

$$Q_{electrons} = qL \int n(\vec{x})dS = Q_{SS} + CV_G + qLn_dA \tag{5.1}$$

where $Q_{electrons}$ is the charge associated with free carriers, $n(\vec{x})$ is the charge carrier number density at the position $\vec{x}$ allowing for variations across the nanostructure cross section, Q_{SS} is the charge of surface states on the nanowire, C is the capacitance between the nanostructure and the gate electrode, L is the length of the conduction channel, A is the cross sectional area of the nanostructure, n_d is the donor density and q the charge of the carriers.

We may write, in general, the drain source current through the nanostructure

$$I_{ds} = \frac{qV_{ds}}{L} \int \mu(\vec{x})n(\vec{x})dS \tag{5.2}$$

where V_{ds} is the drain source voltage and $\mu(\vec{x})$ is the position dependent mobility across the nanostructure cross section. If there is significant contact resistance then the voltage across the nanowire will be smaller than the drain source voltage which will modify these results. Previous measurements [64] on ZnO nanowires using the same contact materials have shown negligible contact resistances relative to nanowire resistance by electrical measurements in four-point configurations and thus we neglect contact resistance in subsequent analysis.

We introduce the effective mobility

$$\mu_{eff} = \frac{\int \mu(\vec{x})n(\vec{x})dS}{\int n(\vec{x})dS} \tag{5.3}$$

which is the mobility averaged across carriers. By substituting equation 5.3 into 5.2 we

may write

$$I_{ds} = \frac{\mu_{eff} V_{ds}}{L} q \int n(\vec{x}) dS \tag{5.4}$$

which we may substitute into equation 5.1 into to get

$$I_{ds} = \frac{\mu_{eff} V_{ds}}{L^2} [Q_{SS} + CV_G + qLn_d A] \tag{5.5}$$

which we may write as

$$I_{ds} = \frac{\mu_{eff} C}{L^2} [V_G + V_T] V_{ds} \tag{5.6}$$

where V_T is a threshold voltage. This means that when plotting I_{ds} against gate voltage, the threshold voltage is the magnitude of the gate voltage intercept. We have therefore written the equation for current through the nanostructure in the form of an FET, allowing standard FET analysis to be applied. The threshold voltage V_T is given by

$$V_T = \frac{Q_{SS}}{C} + \frac{n_d q A L}{C} \tag{5.7}$$

There is a region of transistor operation where the drain source current I_{ds} is linear with gate voltage. By fitting a line to this region we may extract the threshold voltage and the transconductance from the x intercept and the gradient of the line respectively. The transconductance, g_m is defined as

$$g_m = \frac{\partial I_{ds}}{\partial V_G} \tag{5.8}$$

From the transconductance the mobility may be calculated as

$$\mu_{eff} = \frac{g_m L^2}{C V_{ds}} \tag{5.9}$$

The calculated mobility is not affected by the presence (or lack of) surface charge on the nanostructure. This means that the experimentally extracted field-effect-mobility does not require any assumptions about surface states.

We may calculate the number density of charge carriers in the nanowire in two manners. The threshold voltage gives a measure of the number of shallow donors in the nanostructure

$$n_d = \frac{CV_T}{qAL} - \frac{Q_{ss}}{qAL} \tag{5.10}$$

In the limit that there are few surface states the second term can be neglected and we may determine the number of shallow donors from the threshold voltage. In this calculation the threshold voltage is the voltage applied to one plate of the capacitor (the substrate back gate) in order to deplete the nanowire or add charge to the ground plane equal the free charges in the nanowire.

Alternatively the resistance of the nanostructure at zero applied gate voltage and its dimensions can be used to compute the conductivity σ as

$$\sigma = n_{carriers} e \mu_{eff} \tag{5.11}$$

Having calculated the effective mobility from the transconductance we can compute the free carrier density at zero applied gate voltage. This is related to, but different from, the number of shallow donors in the nanowire. When the surface state density is small these two values should be equal. When there the surface state density is high these numbers will differ as the number of free carriers at zero applied gate voltage will be significantly lower than the number of shallow ionized donors since the electrons from these donors will be trapped at surfaces.

Once fabricated transistors are measured using a Keithley SCS 4200, a system which contains a number of precision voltage and current sources and meters designed to characterize the electrical properties of semiconductors. It has a ground connection as well as four versatile ports which may be configured to source or measure voltage or current over a wide range of values. The SCS is used to simultaneously apply a gate voltage as well as measure the drain-source channel. Preamplifiers on the input to the SCS mean that it is able to measure currents as small as a few picoamps. The SCS is connected to the nanowire chip using a probe station. In the probe station probe tips (metallic needles) are positioned using three-axis positioner and touched onto the nanowire sample contact pads.

5.2.3 Capacitance Models

In order to infer material properties from gate-dependent transport measurements we need to know the capacitance between the nanostructure and the back gate. The capacitance is geometry dependent and will depend on the nanostructure being measured, as well as the thickness and permittivity of the oxide coating of the Si wafers. These capacitances are very small and hard to measure and are therefore estimated numerically. Calculating the capacitance between the nanostructure and the gate electrode is a routine problem for nanowire and other 1D nanostructure device measurements. However, there are a number of different gate geometries and nanostructure shapes and dimensions. Depending on the gate geometry and relative dimensions in the device, different models of capacitance are appropriate.

The most common model used for calculating the capacitance in 1D nanostructures is that used for nanowires. Assuming an approximately circular cross section of a nanowire

we may write the capacitance of the nanowire as [119]

$$C_{nanowire} = \frac{2\pi\epsilon_0\epsilon_r L}{cosh^{-1}\left(\frac{r+t_{ox}}{r}\right)} \tag{5.12}$$

where r is the radius of the nanowire, ϵ_0 and ϵ_r are the permittivity of free space and the relative permittivity of the oxide respectively, L is the length of the nanowire channel and t_{ox} is the oxide thickness which is the capacitance for an infinite metallic cylinder above a plane. This model, whilst widely used, has a number of limitations: it assumes the nanowire is metallic where it is typically semiconducting, causing an over-estimation in capacitance [120]. It also assumes that the material is uniformly encased within a dielectric. In the back-gate geometry there is an asymmetry to the device; beneath the nanostructure is one dielectric (SiO_2) and above and around the nanostructure another (air). These two materials have different relative permittivity which, again, affects the calculated capacitance where the assumption that it is surrounded by SiO_2 over-estimates the value of capacitance relative to finite element models [121]. A detailed discussion of these issues is presented in a previous PhD thesis by Dr. Marion Sourribes [115].

In addition to these issues, some nanostructures have geometry significantly different to nanowires with a circular cross section considered to arrive at equation 5.12. Nanobelts have an approximately rectangular cross section. The simplest models for these is to consider them as parallel plate capacitors with the gate electrode.

$$C_{nanobelt} = \frac{\epsilon_0\epsilon_r wL}{t_{ox} + t_{nanobelt}/2} \tag{5.13}$$

where w is the width of the nanobelt, L the length of the conduction channel and $t_{nanobelt}$ the thickness of the nanobelt. As the nanobelt is semiconducting, the Thomas-Fermi screening length is long compared to typical nanobelt thicknesses, meaning that we model the electrode as being half-way through the nanobelt.

This simple model doesn't account for any fringing fields which may occur in the device and assumes that the nanobelt is quasi-infinite in both width and length (which is typically not true). Therefore, this model of capacitance may be improved to incorporate the geometry better. Firstly, the highly doped back-gate is effectively infinite in comparison to the nanobelt. Therefore, using the method of image charges, we may compute the capacitance between the nanobelt and back gate as the capacitance between the nanobelt and an identical virtual nanobelt spaced the same distance behind the surface of the back gate. Still using the equation for parallel plate capacitors, this doubles the separation between the the plates of the capacitor from equation 5.13 giving

$$C_{nanobelt} = \frac{\epsilon_0\epsilon_r wL}{2t_{ox} + t_{nanobelt}} \tag{5.14}$$

This equation still assumes that the two nanobelts may be treated as quasi-infinite plates in a parallel plate capacitor and does not account for any fringing fields. Fringing fields are important when the dimensions of the nanobelt in the plane of the oxide are small compared to the thickness of the oxide layer. There are two limits which we may consider this in: (i) the oxide layer is much thicker than the width of the nanobelt but shorter than the length of the conducting channel (ii) the length and the width of the nanowire are shorter than the channel. As the length of the nanobelt conductive channel drops the importance of fringing fields (which increase the capacitance) increases. This has been investigated numerically in [122] where it has been found that, for radially symmetric nanowires, as the length to radius ratio drops Equation 5.12 becomes less accurate and significantly over-estimates the capacitance of the nanowire.

We consider the limit where both dimensions are small relative to the thickness of the oxide layer since this is the case for devices discussed later in this thesis. As the oxide layer is thick compared to the dimensions of the nanobelt (width, length and consequently also thickness), the nanobelt and its image will be separated by a large distance compared to the dimensions of the nanobelt. It therefore cannot be modeled as two plates in a parallel plate capacitor. Nevertheless, the precise shape of the nanobelt becomes less important. We therefore may use a higher symmetry model and approximate the geometry of the nanobelt as spherical where the capacitance of two spheres is known analytically [119] to be

$$C_{Sphere} = 4\pi\epsilon_0\epsilon_r r \sinh(\beta) \sum_{n=1}^{\infty} \mathrm{cosech}(2n\beta) \tag{5.15}$$

where $\beta = \cosh^{-1}(d/2r)$, d is the separation of the centres of the two spheres and r is the radius of the two spheres. We set r to preserve the volume of the nanobelt (i.e. $w \times t \times l = \frac{4}{3}\pi r^3$. When $d \gg r$ this may be expanded in powers of r/d to be [123]

$$C_{Sphere} = 4\pi\epsilon_0\epsilon_r r \left[\frac{r}{d} + \frac{r^3}{d^3} + \frac{3r^5}{d^5} + ...\right] \tag{5.16}$$

to give an expression for the capacitance between the two spheres. This will better account for fringing fields when the oxide thickness is large compared to the nanobelt dimensions.

We use a relative permittivity of SiO_2 $\epsilon_r = 3.9$ [124]. As the oxide layer is thick compared to the nanobelt dimensions we approximate that the electric field will mostly be confined to the oxide dielectric rather than in air although this is an approximation.

5.2.4 Surface States

We may use Equation 5.10 to determine the number of shallow donors if there are few surface states on the nanostructure, however, the anisotropy inherent in surface states means that their effect on the electrostatics of a nanostructure is more complicated than uniformly depleting the density of carriers. This effect depends on the nature of the surface states and the dominant carrier type. In ZnO, surface defects act as locations for chemisorption of oxygen where O_2 molecules bond to a conduction band electron becoming negatively charged and adsorbed to the surface [125].

This adsorbed layer changes the distribution of charge within the nanostructure causing band-bending. Qualitatively, oxygen adsorbed to the surface takes electrons from the conduction band, depleting the free carriers in the nanostructure and forming a negative surface charge Q_{SS}. There is then a residual positive charge (from the shallow donors) in the core of the nanostructure which is balanced by a negative surface charge from the surface states. The charge distribution causes an electric field which causes the electronic bands to bend upwards at the nanostructure surface. This means that it is energetically costly for the remaining free electrons to be at the surface (i.e. close to a negative surface layer) and they move towards the centre of the nanostructure leaving a depletion region at the nanostructure surface. The band profiles of such a nanobelt are shown schematically in Figure 5.5.

Carriers flow within a region which is smaller than the physical dimensions of the nanostructure due to the surface depletion region. The shape and size of the depletion region will depend on the respective shape and size of the nanostructure. In addition the surface charge may change depending on the exposed facet of ZnO. This complicates analysis of transport properties of nanostructures where the approach detailed above assumes a uniform transport channel, the dimensions of which are the same as the nanobelt dimensions. Band bending may also affect luminescence, particularly in heterostructures where the heterointerface occurs in a region of band bending.

5.3 Superconducting Resonators

Superconducting resonators are high quality-factor circuit elements made from thin film superconductors (typically Nb, Al or related compounds). They are ubiquitous in circuit quantum electrodynamics (cQED) and are often used to read out and address superconducting [126], and other [127, 128], qubits.

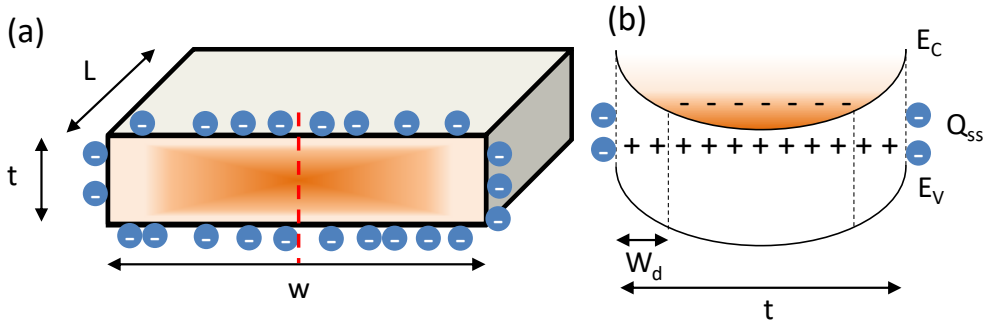

Figure 5.5: (a) Schematic of negatively-charged surface-adsorbed oxygen on a nanobelt with dimensions thickness t, width w, and length L. The shading indicates the free electron density in the nanobelt cross section. The dashed red line indicates where a band profile cross section has been taken in (b). (b) Schematic of the band profile of a cross section across a nanobelt with negative surface charges Q_{SS}, a depletion region with ionised shallow donors of thickness W_d and a core with negatively charged free electrons and positive ionised donors.

Superconducting resonators have been fabricated as part of a proof of principle experiment demonstrating the compatibility between high quality cQED elements on-chip with piezoelectric ZnO for future quantum devices where both photons and phonons interact. This work is detailed in chapter 9.

Superconductivity is a rich field of fundamental and applied physics. As it is not the focus of this thesis, only a brief introduction focusing on the aspects of superconductivity pertinent to the devices discussed in this thesis will be given here. There are many textbooks which cover the theory of superconductivity [129, 130] and a number of excellent PhD theses which summarise (and add valuable contributions to) work on applied superconductivity in particular, superconducting resonators [131, 132].

5.3.1 Brief introduction to superconductivity

Superconductivity is a phase of matter. It is characterized by zero DC resistance and the expulsion of magnetic fields. When a superconductor is cooled through its superconducting transition temperature (T_c) it under goes a phase transition, its DC. resistivity drops to zero and any magnetic flux which penetrates the superconductor is expelled.

In 1957 Bardeen, Cooper and Schrieffer proposed BCS theory to explain superconductivity [133]. In BCS theory an attractive potential emerges between pairs of electrons due to the exchange of virtual particles (e.g. phonons as initially proposed). Due to the at-

tractive potential electrons bond together and form Cooper pairs. Cooper pairs are bosons as opposed to electrons which are fermions. As bosons have integer spin, the exclusion principle does not apply to them and they may form a condensate. Electrons condense into a Cooper pair condensate where an energy gap separates Cooper pair states from unpaired electronic states. In this condensate oscillations of atomic potential do not have enough energy to affect the condensate as a whole, nor break apart electrons. Current may therefore flow without dissipation as carriers are not scattered. In BCS superconductors the energy gap, Δ is related to the critical temperature of the superconductor and at zero temperature is given by [129]

$$\Delta(T = 0) = 1.764 k_B T_c \tag{5.17}$$

Higher critical temperature BCS superconductors therefore have larger superconducting gaps. It is worth mentioning that 'High Tc' superconductors have a complicated anisotropic band structure and that these statements about superconducting gaps are significantly more complicated for these systems and well beyond the scope of this thesis. At finite temperature Cooper pairs can be broken and these broken Cooper pairs form quasiparticles. Using a higher Tc BCS superconductor means that the superconducting gap is larger and consequently at a given temperature there will be fewer quasiparticles.

5.3.2 Theory of superconducting resonators

Superconducting microwave resonators are RF superconducting elements which support standing electronic waves which oscillate at microwave frequencies. The low dissipation of superconductors allows for high quality elements.

The simplest superconducting resonator is an LC tank circuit which is a lumped element resonator. This is an inductor of inductance L which connects the two plates of a capacitor of capacitance C. Energy oscillates from being stored in an electrical field on the plates of the capacitor to the magnetic field around an inductor. This occurs at a frequency $\omega = 2\pi f = \frac{1}{\sqrt{LC}}$.

Often superconducting resonators are made in a distributed geometry. A distributed resonator is a strip of a superconductor in the proximity of a superconducting ground plane. The strip of superconductor has an inductance per unit length, l, and capacitance to ground per unit length, c. The resonator can be modeled as a transmission line where microwave radiation travels along a transmission line with a phase velocity

$$v_{phase} = \frac{1}{\sqrt{lc}} \tag{5.18}$$

There are two geometries of distributed resonator, quarter-wave and half-wave resonators. In a quarter-wave resonator one side of the transmission line is open circuit and the other end is shorted to ground. In a half-wave resonator both ends of the resonator are open circuit. These different geometries impose different boundary conditions on the resonator. At open circuit ends of the resonator no current may flow but a voltage between ground may be sustained - i.e. the open circuit is a voltage antinode and current node. The converse is true at grounded ends of resonators - a current may flow but no voltage may be sustained i.e. is a voltage node and current antinode. The resonant frequency of the resonator is determined by the time it takes for a wave of microwave radiation to travel the length of the transmission line at the phase velocity above in accordance with the boundary conditions imposed by the geometry of the resonator.

Although at DC superconductors have no dissipation, at microwave frequencies superconducting resonators do dissipate energy. This occurs due to a complex surface resistance as described by Mattis-Bardeen theory and will limit the quality factor of a resonator. The Mattis-Bardeen limited quality factor (Q_{MB}) depends on temperature (higher Q_{MB} at lower temperature). Resonators should be operated at a small fraction of critical temperature in order to exhibit high internal quality factors.

The quality factor will saturate with decreasing temperature as other mechanisms become the limiting factor. In particular at low resonator power (the regime pertinent for quantum applications) resonators couple to two level fluctuators on or in the substrate. These two level fluctuators are random quantum systems due to imperfections in the substrate or on the surface of the substrate. On sapphire substrates these have been identified as physisorbed hydrogen [134]. When the resonator (in the low power limit) couples to these random quantum systems it loses energy to these quantum systems. This acts as a dissipation mechanism whch reduces the internal quality factor of the resonator.

The coupling between superconducting resonators and their electronic environment also affects their resonant frequency and quality factor. A typical geometry to read out resonators is to capacitively couple the resonators to a 50Ω feedline. The capacitive coupling between the resonator and feedline means that the resonator can absorb energy from the feedline and also means that, having absorbed energy, it can be fed back into the feedline. This provides another route for resonators to lose energy and reduces the quality factor. The loaded quality, Q_l, factor of a resonator is related to the coupling quality factor, Q_c and the internal quality factor Q_i by

$$\frac{1}{Q_l} = \frac{1}{Q_i} + \frac{1}{Q_c} \tag{5.19}$$

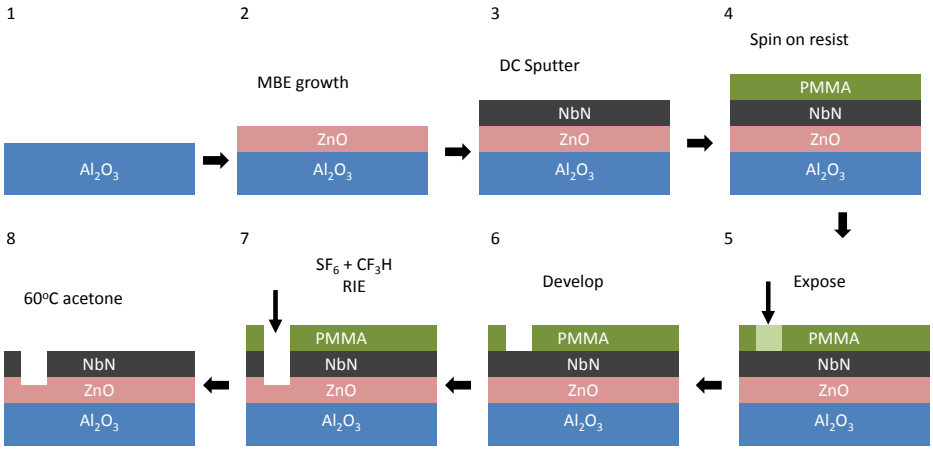

Figure 5.6: Schematic of steps (1) - (8) required to fabricate superconducting resonators on ZnO epitaxial films.

5.3.3 Superconducting resonator fabrication

Fabricating superconducting resonators is a multistage process which is shown schematically in Figure 5.6.

In order to fabricate superconducting resonators a superconducting film must first be deposited on top of the substrate (either ZnO overgrown or bare). This is done by DC magnetron sputtering. Substrates are initially cleaned by three stages of 5 minutes of sonication in acetone then 2-propanol and finally deionised water before being blown dry by dry nitrogen.

Once cleaned the samples are loaded into the sputter system on a Si carrier wafer. The chamber is pumped overnight achieving a pressure $< 8 \times 10^{-7}$ mBar. At this pressure argon and nitrogen (50:50 mix) are flowed into the chamber to a pressure of 3 mBar the relative flows being controlled by a mass flow controller and a 200 W plasma is struck on a niobium target. The sample shutter remains closed and the target is sputtered for $\sim$ 10 minutes before the gases are turned off and pumping continues. This getter stage reduces the final pressure achieved as Nb reacts with residual gases in the chamber.

Once the final pressure of 6×10^{-7} mBar is achieved the same process as the getter stage begins. The 50:50 Ar:N gas mix flows into the chamber and a plasma is struck. The target is pre-sputtered for 5 minutes to remove any contamination on the top of the Nb target and present a clean surface. The sample shutter is then opened and sputtering occurs for a time set by the target film thickness. A NbN film is deposited on the surface of the substrate. Once the film is deposited the plasma is turned off and the gas flow stops. The chamber is subsequently vented.

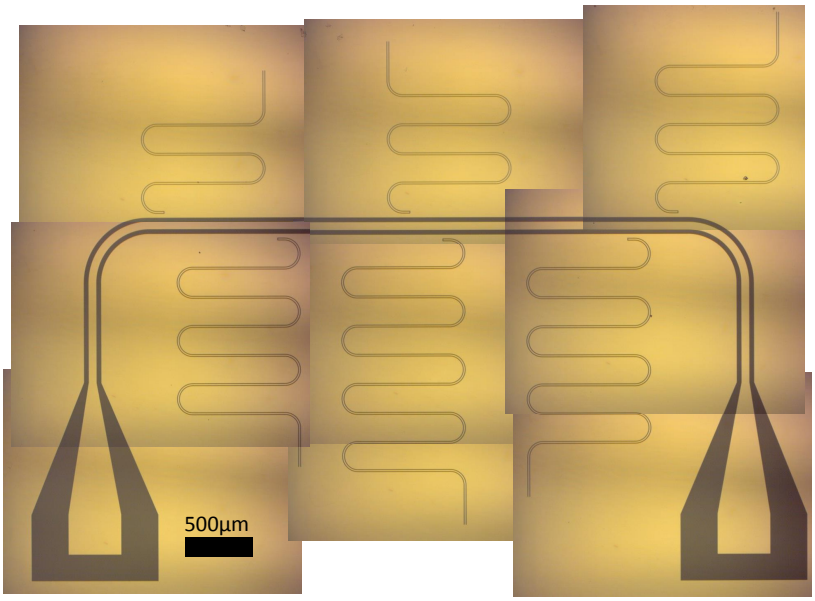

Figure 5.7: A series of optical micrographs stitched together showing the NbN superconducting resonator device. A feed line is used as a microwave through. The superconducting resonators are the meandering structures and are capacitively coupled to the feedline.

The samples are then covered in PMMA A4 950 resist with a resist spinner. The speed of the spinner is optimized to achieve a 300 nm thick resist layer. The samples are then loaded into an electron beam lithography system where the resist is exposed with the desired pattern. The sample is unloaded and developed with exposed resist being removed.

Once the pattern is transferred into the resist the sample is loaded into a reactive ion etcher (RIE). A 100 W plasma composed of 14 SCCM SF_6 and 35 SCCM CHF_3 at a pressure of 100 mTorr is struck. Radicals in the plasma attack the NbN and etch away any exposed NbN. This transfers the pattern made in the resist to the superconducting film. Etching is done in 1 minute steps with 1 minute wait between etches. This prevents the sample overheating and the resist hard baking. This is also important as at high temperature other plasma processes such as deposition or reactions between the resist and radicals may occur. The total mill time depends on the total thickness to be etched through. The recipe has a typical etch rate of ∼50 nm/min It is possible to vent the system, check that etching has completed, and if not reload the system and continue the process.

Samples are then placed in a 60 °C acetone bath which dissolves remaining resist leaving the finished sample. An optical micrograph of a finished device is shown in Figure 5.7.

5.4 Cryogenic Measurement

In order to perform measurements at cryogenic temperatures we use a ^{3}He system with a base temperature of 300 mK. In order to achieve a base temperature of 300 mK a number of cooling stages are required. First, the sample is mounted on the end of the probe inside a vacuum jacket. The vacuum jacket is then pumped using a scroll pump to a base pressure of ≈2 mBar. Once the vacuum jacket is evacuated a controlled amount of ^{4}He is put into the vacuum jacket. This He is gaseous and provides a heat leak between the sample (at the centre of the vacuum jacket) and the walls of the jacket.

The ^{3}He system is a 'wet' system where a probe is slowly lowered into a dewar of liquid ^{4}He. The boiling point of ^{4}He is 4.2 K and so this provides a comparatively straightforward route to achieve 4.2 K where the gaseous ^{4}He provides a heat leak between the liquid ^{4}He and the sample. As the probe cools down the gaseous ^{4}He in the vacuum jacket is pumped by the sorb inside the vacuum jacket. The sorb is a piece of charcoal which acts as a sorption pump where at low temperatures He gas is adsorbed to the surface of the sorb. Once the sample has cooled to ∼5 K the heat link between between the sample and the liquid ^{4}He bath is removed as the exchange gas is pumped out which allows further cooling.

The needle valve is then opened allowing some liquid ^{4}He to be sucked into the 1 K pot. The scroll pump is opened onto the 1 K pot and the relative positions of the needle valve and the valve connecting the 1 K pot to the scroll are adjusted to control the vapour pressure of the ^{4}He in the 1 K pot. A schematic of the phase diagram is shown in Figure 5.8. By pumping on the ^{4}He and driving the vapour pressure down, the boiling point of the ^{4}He is also driven downwards. This allows the 1 K pot to be cooled to ≈2 K. The ^{3}He provides a heat link between the sample and the 1 K pot so the sample is also cooled to this temperature.

At 2K ^{3}He will liquefy. When the 1 K pot is at temperatures below the boiling point of ^{3}He, the gaseous ^{3}He condenses on the 1 K pot and collects above the sample. Once all of the ^{3}He is condensed then the heat link between the 1 K pot and the sample is broken. In order to cool further we need to pump on the ^{3}He.

The ^{3}He is extremely expensive and therefore must form a closed cycle. We therefore use a sorption pump in the ^{3}He chamber to pump on the ^{3}He. The rate of sorption onto the surface of the charcoal depends on the temperature with the sorption rate increasing at lower temperatures. Therefore by cooling the sorb we can start to pump on the ^{3}He. Just as when cooling the 1 K pot, by driving down the vapour pressure of the ^{3}He we drive down its boiling point and cool to ≈300 mK.

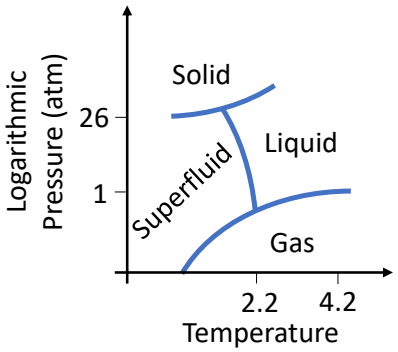

Figure 5.8: Schematic of the phase diagram of ^{4}He showing gaseous, liquid, solid and superfluid phases following London 1954. The boiling point of He at atmospheric pressure is shown on the axis as is the temperature of the triple point of gas, liquid and superfluid helium.

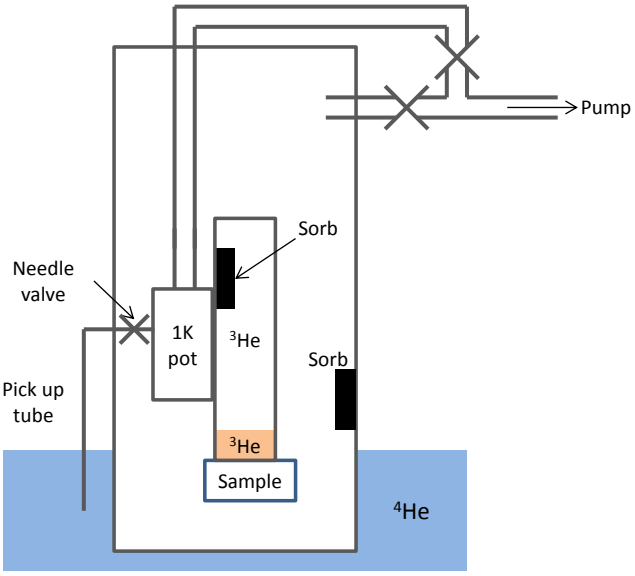

Figure 5.9: Schematic of the ^{3}He system showing components important for reaching the base temperature of ≈300 mK.

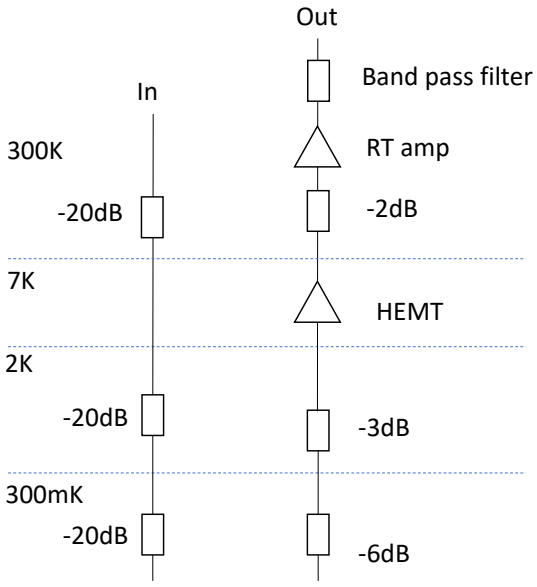

Figure 5.10: Cryogenic and room temperature microwave circuitry used for the measurement of superconducting resonators.

The microwave circuitry schematic of the cryostat is shown in Figure 5.10. There is 60dB of attenuation on the in-line to thermalize inbound signals. The outline consists of small attenuators before a cryogenic HEMT. The constraints that the probe must fit inside a dewar neck imposed significant restraints on space and precluded circulators as isolators and the 9dB of attenuation between sample and HEMT is used to thermalize these lines.

The signal is further amplified and filtered to improve the signal to noise ratio. Samples are mounted onto the probe by wirebonding the resonator to a PCB which is connected to the probe using SMPM push connectors.

Chapter 6

Zinc Oxide Nanostructure Growth

Understanding and controlling the growth of ZnO nanostructures is an important step in tailoring these nanostructures for functional properties. Despite the VLS model of 1d nanostructure growth, the number of competing processes in VLS means that *a priori* understanding of how nanowires will grow is not practical and the growth of nanowires must be characterized and optimized by experimental feedback.

There is a number of properties of 1d nanostructures which it is desirable to control at the point of growth. The properties will depend on ultimate application but will often include morphological properties (length, width, tapering, sidewall roughness), crystallographic properties (crystallographic growth axis and side faces, orientation with respect to substrate) and properties relating more directly to the intended function of the nanowires such as electrical properties (resistivity, mobility, freeze out temperature).

Control of growth dynamics and kinetics, in principle, allows some degree of control over these different properties and is detailed in this chapter. When growing nanostructures by metal-catalysed plasma-assisted molecular beam epitaxy (PAMBE) there are some obvious methods by which nanostructures may be tailored:

- substrate choice and preparation;
- catalyst chemistry and preparation;
- sample temperature;
- incident fluxes of reactants.

The parameter space of growth optimization is consequently large given the number of inter-related parameters which may be adjusted in order to control the numerous properties we may want to tailor. It is therefore necessary to have a rational way to test this

parameter space. This typically involves correlating one property (or type of property such as morphology) to a growth condition which we can change experimentally (e.g. growth temperature) and performing a series of growths changing one parameter to determine the effect of the growth condition on the property in question.

In this thesis sapphire substrates were predominately used as substrates for nanostructure growth. This is due to the abundance of high-quality sapphire substrates. Epitaxial relationships between ZnO and sapphire at nucleation will determine the mutual crystallographic orientations of the ZnO grown upon the different cuts of sapphire, and will affect growth directions of nanowires. Sapphire has the space group $R\bar{3}c$ and has the corundum crystal structure. Substrates with a number of crystalline cuts are commercially available. Growth on two cuts of sapphire (c- and r-plane sapphire) is investigated.

6.1 Growth on c-plane sapphire

Prior research has established a technique for growing ZnO nanowires on c-plane sapphire[64, 15]. These nanowires grow along the [0001] direction of ZnO. A TEM image of an example nanowire is shown in Figure 6.1. This nanowire is typical of nanowires grown by Au-catalysed PAMBE. They are quasi-one dimensional, 500nm-2μm long, and slightly tapered. Due to the 'forest' growth of nanowires there is often substantial spread in nanowire dimensions and electrical properties [64]. A high resolution TEM inset is shown in Figure 6.1. This shows the highly crystalline structure common to these nanowires and previously reported. The overlay to the high resolution inset shows the atomic reconstruction of the ZnO crystal structure from the centre of the nanowire.

In this section we present some new analysis on ensembles of ZnO nanowires grown on c-plane sapphire to complement previous work. This work was made possible by the new generation of sample holder where the growth temperature was constant across a large area of the sample (excepting corners close to clips). This allowed the precise investigation of the effect of growth temperature on samples and combining this with ensemble measurement techniques which sample a large region of the sample. Previously ensemble measurement techniques would average over a large growth temperature range which makes it more challenging to assign changes in these measurements to temperature changes.

In order to determine how growth temperature affects the growth modes of nanowires, XRD pole plots of nanowires grown at different temperatures are collected. In Figure 6.2 we present XRD pole plots of nanowires grown on c-axis sapphire at three different temperatures. As described in 4.2.3, XRD pole plots can allow the determination of the

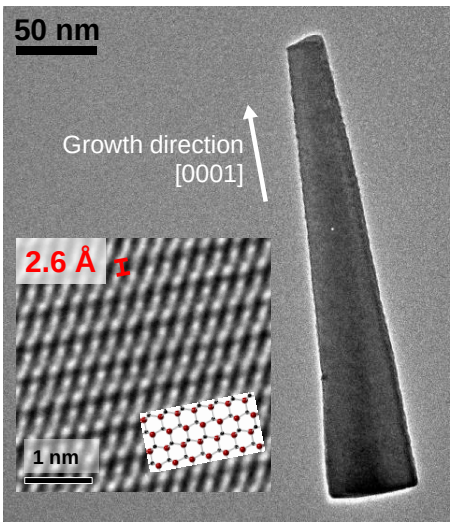

Figure 6.1: TEM of a single ZnO nanowire grown on c-plane sapphire. The gold nanoparticle has likely fallen off during sonication for TEM sample preparation. The inset shows a HRTEM section of ZnO nanowire showing the [0001] growth direction of the nanowire with an atomic reconstruction superimposed above the TEM image. TEM is perfomed by Dr. Edward White of Imperial College London.

growth directions of nanostructures. We know that nanowires grown on c-plane sapphire grow along [0001]. This is shown by HRTEM of nanostructures grown on c-plane sapphire shown in figure 6.1 and widely reported in the literature. Therefore, when the diffractometer is aligned to the (0002) diffraction peak of ZnO, a pole figure will be a map of the growth direction of these nanowires.

The XRD pole figures in Figure 6.2 have some common features: they all have three-fold symmetry, the most intense peaks are at χ=39° and there are six much weaker peaks at $\chi \approx 70°$. One such peak is circled in Figure 6.2 (b). The common intense peaks at $\chi = 39°$ are due to diffraction from the dominant growth mode of nanowires on c-plane sapphire and are present with the same symmetry in samples grown at all shown temperatures. It is instructive to plot, in combination with polar contour plots, intensity plots at specific χ and ϕ values as well as the maximum intensity integrated across all ϕ values at given χ. Such plots are shown in Figure 6.3. The dominant nanowire growth mode is seen as the intense peak at $\chi = 39°$ in Figure 6.3 (a) and the three intense peaks in (b) and is present at approximately the same intensity in all samples. The breadth of the dominant nanowire growth mode in Figure 6.3 (a) shows that there is a spread in orientations which nanowires may point w.r.t. the substrate. The FWHM of the peak related to the dominant growth mode is $\sim 6°$ for all growth temperatures. This is consistent with nanowires being able

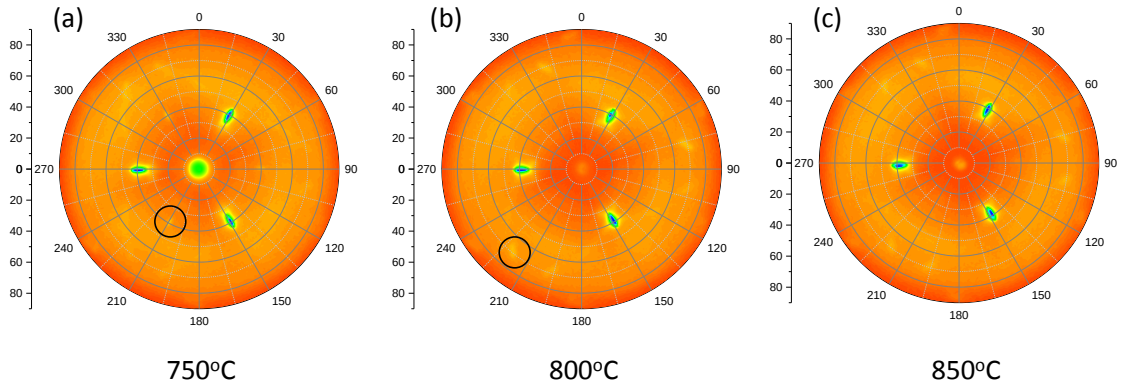

Figure 6.2: Pole figures of ZnO nanowires grown on c-axis sapphire at (a) 750°C (b) 800°C and (c) 850°C. These are plots of diffracted intensity as a function of ϕ (increases around the circle) and χ (increases out along the radius of the circle). The figures are collected with the diffractometer aligned to the (0002) diffraction peak of ZnO. Low intensity satellite peaks are circled at $\chi = 39°$ in (a) and $\chi = 70°$ in (b).

to relieve epitaxial strain on their sidewalls and thus being less constrained by epitaxial relations than their thin film counterparts. The low intensity satellite peaks at $\chi = 70°$ are also more readily visible in Figure 6.3 (a). We attribute this additional peak to another epitaxial relationship between ZnO and the sapphire substrate allowing ZnO to grow in additional configuration.

There is variation between pole figures of samples grown at different temperatures. At the lowest growth temperature (750°C) there is a comparatively intense peak at the centre of the pole figure (Figure 6.2 a). This central peak is approximately one order of magnitude more intense in this sample than in samples grown at higher temperature and is the peak at $\chi = 0$ in Figure 6.3 (a). This peak indicates that there is growth with (0001) of the ZnO parallel to (0001) of the Sapphire. As well as the three intense peaks at $\chi = 29°$ which we assign to the dominant nanowire growth there are three additional weak peaks which also occur at $\chi = 39°$ and 60° misaligned in ϕ from the dominant nanowire growth mode. These peaks are only present in the sample grown at 750°C but not for samples grown at higher temperature. One of these weak peaks is circled in Figure 6.2 (a) and are the three low intensity peaks in the line for the sample grown at 750°C in Figure 6.3 (b) at $\phi = 90°$, 210° and 330°. As these satellites have the same χ value as the dominant nanowire growth mode it is likely that they also relate to nanowire growth. These additional growth modes ($\chi = 0°$ and $\chi = 39°$) are suppressed at higher temperature as, although these orientations of ZnO are local minima in potential energy for adsorbed reactants, at higher temperature

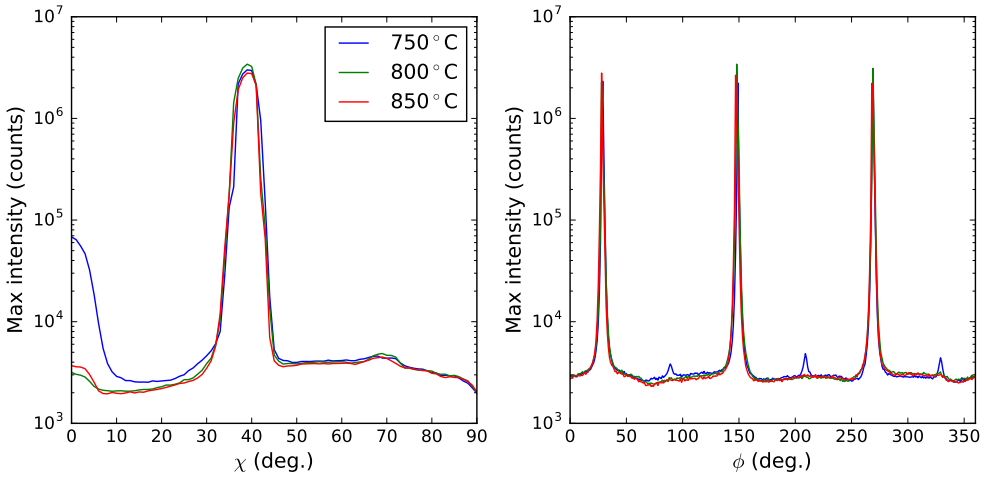

Figure 6.3: (a) the maximum intensity value for all ϕ values against χ. (b) The XRD intensity as ϕ is swept from 0 to 360° and χ is held at 39°.

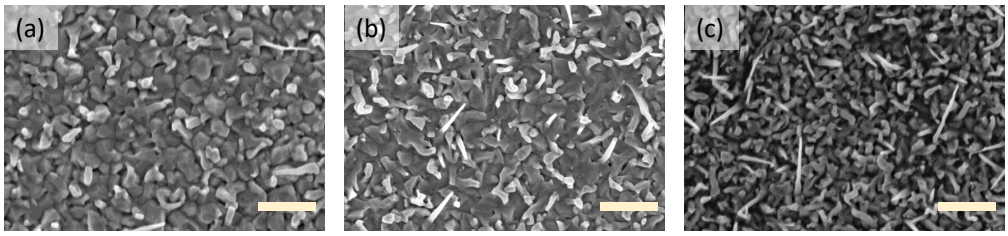

Figure 6.4: SEM micrographs of nanowires grown at (a) 750°C , (b) 800°C, (c) 850°C. Samples are the same samples for which pole figures are collected in Figure 6.2. Scale bar is 500nm.

there is sufficient thermal energy to escape these local minimum and reach a more stable configuration (i.e. the dominant nanowire growth).

XRD pole figures are a measure of the amount of crystalline substance with crystal axes in different orientations. They do not contain any information about what the morphology of the material is. For instance a polycrystalline film with different preferred epitaxial relations may look identical in a pole figure to nanowires. We therefore collect a series of electron micrographs of these samples (figure 6.4) allowing us to relate the XRD peaks to different growth modes.

The SEMs of these samples show that although the pole figures of these samples have the same dominant peaks, these peaks are caused by ZnO with different morphology. At lower temperature (Figure 6.4 a) very few nanowires grow, and those that do are relatively short (typically <500 nm). The dominant growth morphology is 'boulder' growth. The dominant peaks in the XRD are the same for low and high temperature so we can determine

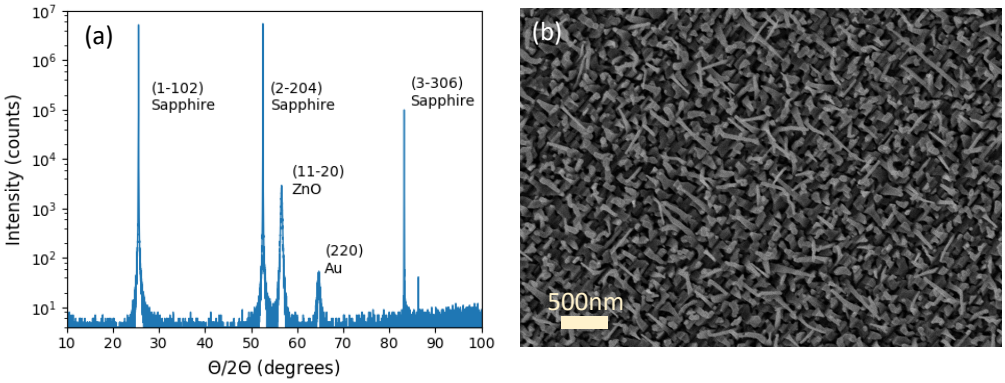

Figure 6.5: (a) $\Theta - 2\Theta$ scan of nanowires grown on r-plane sapphire at 800°C with peaks labeled. (b) SEM of the sample showing a high density of oriented nanostrutures.

that the boulders are growing with the same epitaxial relationships as the nanowires. This may indicate that nucleation is identical in samples grown at different temperatures but that the temperature is not high enough to ensure continued VLS growth. This may be because catalysts solidify or that adsorbed reactants mean free path drops meaning that they are deposited on the nanowire sidewall before reaching the catalyst for nanowire growth. At higher temperatures (Figure 6.4 b, c) there are a significantly more nanowires and those nanowires are longer. The growth direction of these nanowires has the same three-fold symmetry as that seen in the pole figures.

It is hard to relate features in the SEMs to secondary growth modes. The quantitative analysis of pole figures presented in Figure 6.3 shows that even when secondary growth modes are relatively abundant (compared to sampled grown at lower temperature) the intensity of their corresponding XRD peaks are significantly lower (orders of magnitude) than the dominant growth mode. Therefore there is significantly less ZnO growing with this configuration and identifying it from a SEM reliably is impracticable. It is likely that the increase in ZnO growing with [0001] normal to the substrate at lower temperature is part of the boulder growth seen on the substrate.

6.2 Growth on r-plane sapphire

Changing the cut of the substrate changes the epitaxial relationship between the nanostructures and the substrate. The cut of substrate therefore plays an important role determining the nanostructures that grow. In order to study this we grow ZnO nanostructures (using an identical growth procedure) on r-plane sapphire.

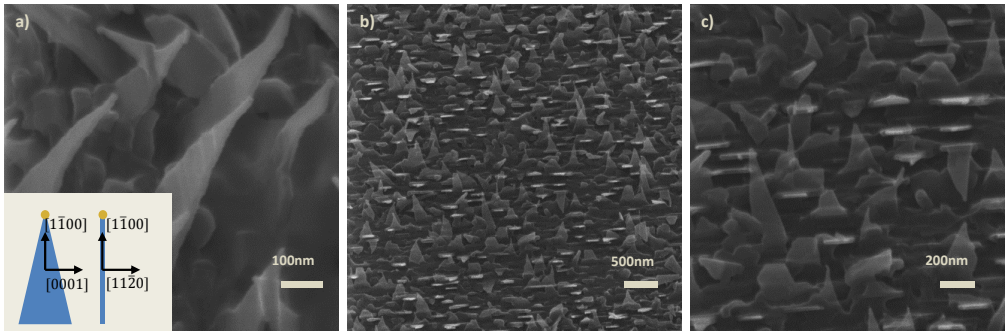

Figure 6.6: HeFIB microraphs of a sample grown at 750°C. Images are taken at (a) 40° and (b,c) 31° tilt. The tilt axis in (a) is perpendicular to that in (b,c). Inset to (a) are cartoons of nanostructures showing crystallographic orientations determined by HRTEM (Figure 6.9) and XRD pole figures (Figure 6.8).

Samples are initially grown for 90 minutes at 800°C. We perform a $\Theta - 2\Theta$ scan on the sample for initial characterization (Figure 6.5 a). This confirms that the substrate is r-plane sapphire and that the ZnO grows with [11$\bar{2}$0] pointing vertically out of the substrate (aligned with [1$\bar{1}$02] of sapphire). SEM micrographs (Figure 6.5 b) show that quasi-1d nanostructures grow with high density with specific growth directions. In order to characterize these nanostructures further we use a combination of high resolution TEM, XRD pole figures and He FIB micrographs.

6.2.1 Characterizing nanostructures grown on r-plane sapphire

Initially we collect high magnification HeFIB micrographs. These high resolution images allow us to better understand the nanostructure morphology and growth orientaion with respect to the substrate. By tilting the samples as they are imaged we can measure the growth direction with respect to the substrate. As nanostructures grow predominately along one axis we tilt along this axis and another axis perpendicular to this to investigate their growth directions.

In Figure 6.6 (a) the sample is tilted about an axis perpendicular to the wide base of the nanostructures. This shows the 2d triangular lamellar shape of these nanostructures. In Figure 6.6 (b) we tilt the sample along an axis 90° misaligned to the first axis until the nanostructures growing with one of the two dominant orientations align with the primary ion beam. When the nanostructures are aligned with the ion beam they appear brighter than their surroundings. This is because ions penetrate an appreciable depth into the nanostructure and therefore the secondary electron emission occurs along the length of

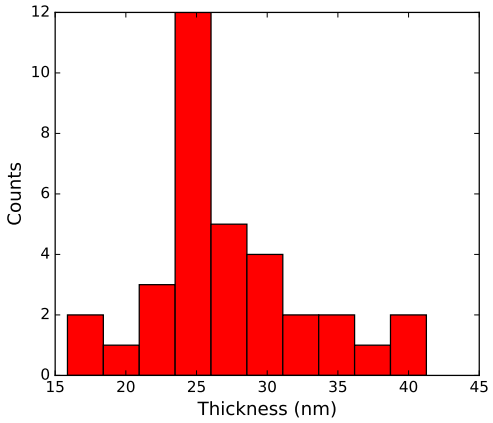

Figure 6.7: Histogram of nanostructure thickness measured from HeFIB image shown in Figure 6.6 (b). The resolution on the HeFIB image is ∼1 nm pixels meaning error bars are small relative to bin widths.

the nanowire rather than just at the surface. This image is taken at a tilt of 31°, the angle these nanostructures make to the normal of the substrate.

When the nanostructures are aligned to the primary ion beam we may also measure the thickness. The thickness of a number of nanostructures shown in Figure 6.6 (b) are measured using freeware ImageJ and a histogram of nanostructure thicknesses is shown in Figure 6.7. As 1d nanostructures can relieve strain at the surface there is a spread in growth directions (shown by breadth of peaks in Figure 6.8) and so this may systematically increase the measured thickness. This shows that most of these nanostructures have a thickness of $\sim$ 25 nm but with some significant variation in thicknesses of nanostructures. The rectangular cross section, tapered lamellae have a very different morphology from the nanowires which were grown on c-axis sapphire and this may be indicative that these nanostructures grow with different crystallographic orientation.

We collect pole figures on a sample grown at 800°C with the diffractometer aligned to two different reflections of ZnO. This allows us to map different crystallographic orientations across the substrate. In the pole figure with the diffractometer aligned to $(1\bar{1}00)$ (Figure 6.8 a) there are two peaks. These peaks are at $\chi = 31°$ and separated by 180° in ϕ. This matches the dominant nanostructure growth direction seen by HeFIB. We therefore conclude that these nanostructures grow along $[1\bar{1}00]$. In Figure 6.8 (c) we show a schematic of the nanostructures as the x-ray beam diffracts off them causing the peak in the pole figure. There are two additional peaks in this pole figure at $\chi = 90°$ which we attribute to a different growth mode.

When the diffractometer is aligned to (0002) planes there are a number of peaks. Two

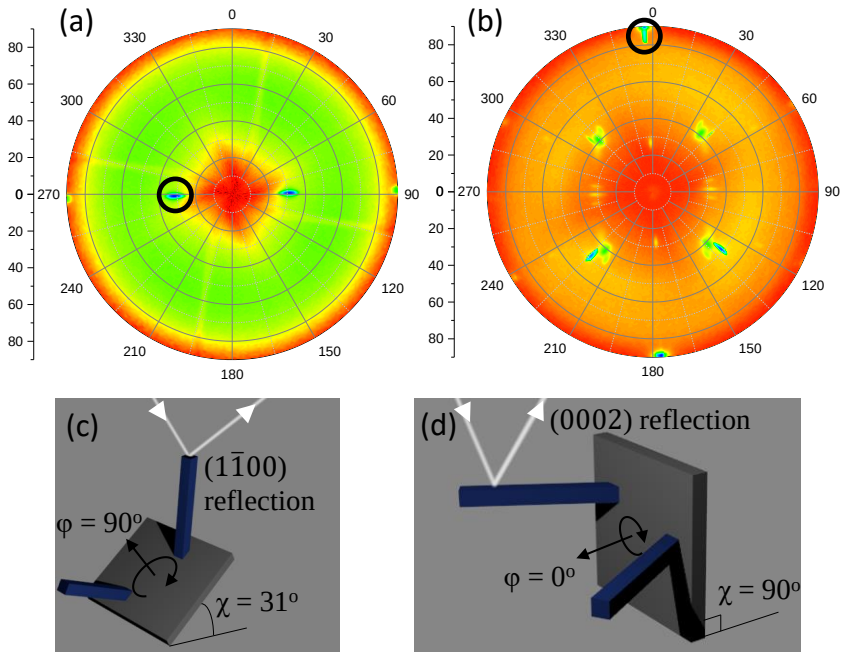

Figure 6.8: Pole figures collected on nanostructures grown on r-plane sapphire with the diffractometer aligned to the (a) $(1\bar{1}00)$ and (b) (0002) reflections of ZnO. (c) and (d) show cartoons of the nanobelt orientation at the peaks in diffraction circled in (a) and (b) respectively.

peaks are located at χ=90° and are separated from each other in ϕ by 180° and from the peaks in the $(1\bar{1}00)$ pole figure by 90°. If [0001] is in the plane of the lamellae then this peak in the (0002) pole figure 90° misaligned from the dominant peak in $(1\bar{1}00)$ pole figures would also be caused by diffraction from nanostructures growing in the dominant growth mode. This seems likely and may be confirmed by TEM of such nanostructures.

From these pole figures we infer that the dominant growth mode is nanostructures growing along $[1\bar{1}00]$, a different crystallographic orientation from the nanowires which grow on c-axis sapphire. Nanostructures which grow along this axis are referred to as nanobelts [135, 21, 136]. There are additional peaks in the XRD pole figures which have not been accounted for. We attribute these to secondary growths of either nanowires, nanobelts or thin film ZnO.

We perform HRTEM on these nanostructures in order to confirm the crystallographic orientation which has been inferred from a combination of HeFIB and pole figures. A sample of nanostructures grown at 750°C is prepared for TEM as described in 4.2.2. First a low resolution TEM (inset to Figure 6.9) shows that this is one of the approximately triangular nanostructures which we have identified as nanobelts. Subsequent HRTEM of the nanostructure (Figure 6.9) confirms its crystallographic orientation. By Fourier transforming the lattice fringes (inset) in the TEM it is possible to determine the crystallographic orientation of the nanobelt. This shows that it grows along $[1\bar{1}00]$ and that [0001] is perpendicular to this direction and in the plane of the nanobelt lamella.

HRTEM (Figure 6.9) shows extended defects within the nanobelt. These have been widely reported in these ZnO non-polar nanostructures [137, 21, 138] and have been identified as Wurtzite I_2 basal plane stacking faults [138].

In addition to the dominant nanostructures growing on r-plane sapphire ($[1\bar{1}00]$ nanobelts, a number of other nanostructures also grow on these substrates including nanowires which grow along [0001] and nanobelts growing along $[11\bar{2}0]$. These nanostructures all grow in specific directions with respect to the substrate determined by the epitaxial relationships between ZnO and sapphire.

These nanobelts are candidates for subsequent heterostructure growth. 'Radial' heterostructures where ZnMgO is grown around a ZnO nanobelt would result in a ZnO/ZnMgO interface which (i) has a component of the polar vector perpendicular to the interface and (ii) extends along the length of the nanowire. As two dimensional electron gases (2DEGs) form at ZnO/ZnMgO heterointerfaces due to a mismatch in polarization, (i) means that a 2DEG may in principle form at these interfaces. As these interfaces would extend the

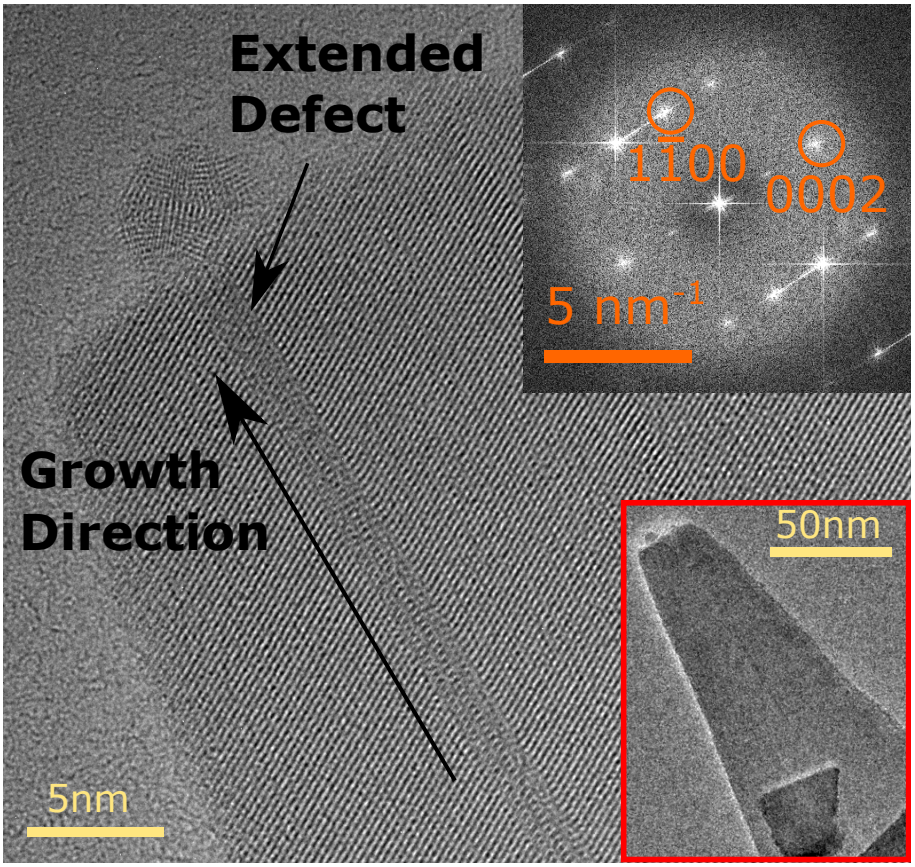

Figure 6.9: HRTEM of a nanobelt grown at 750°C collected by Dr. Edward White of Imperial College. The growth direction is labelled and a small gold catalyst nanoparticle is visible at the top of the nanobelt. Also labelled is an extended defect along the growth direction of the nanobelt. Inset is an FFT of the HRTEM showing that the nanobelt grows along $[1\bar{1}00]$ and perpendicular to that (in the plane of the nanobelt) is [0002]. Another inset shows a low resolution TEM of the same nanobelt showing its morphology.

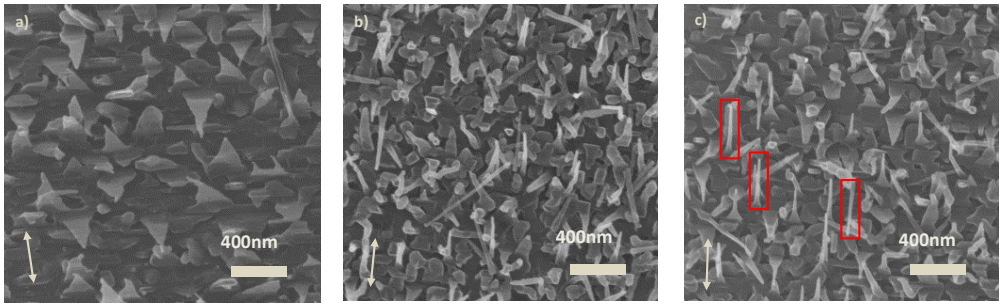

Figure 6.10: Top down He FIB micrographs of nanobelts grown at (a) 750°C, (b) 800°C and (c) 900°C. The arrows show the in plane direction of the dominant growth direction of nanobelts and red boxes in (c) indicate nanobelts with virtually no tapering.

length of the nanowire this possible confined electron space may meaningfully modify the transport properties of such nanowires.

6.2.2 Morphology control of ZnO nanobelts

It is desirable to be able to control the morphology of nanobelts at the point of growth. The nanobelts grown often exhibit significant tapering in one plane. This means that the side faces of these nanowires are not the polar (0001) face but instead are at some oblique angle to the polar face. For future heterostructure applications this is not desirable.

Samples are grown for 90 minutes at a number of temperatures. We present He FIB images of these samples in Figure 6.10. The sample with the lowest growth temperature (Figure 6.10 a) shows significant tapering. The nanobelts are triangular.

At an intermediate temperature of 800°C (Figure 6.10 b) the tapering has significantly decreased. At the highest achieveable growth temperature of $\approx$ 900°C (Figure 6.10 c) several nanowires show virtually no tapering and are rectangular in shape.

By adjusting the growth temperature of nanobelt samples we can tailor their morphology. At high temperature we achieve approximately rectangular nanowires which have side faces of either the polar (0001) facet or a face only marginally misaligned from this facet. This means that the polar vector is approximately normal to these faces, ideal for subsequent heterostructure growth.

Tapering in quasi one-dimensional nanostructures occurs due to sidewall growth[139]. As the tapering is reduced at higher temperatures we take this as evidence that we suppress sidewall growth at elevated growth temperatures. We believe this is due to a reduction in surface adsorption due to elevated growth temperatures.

The triangular lamellar shape of samples grown at lower temperature shows that side-

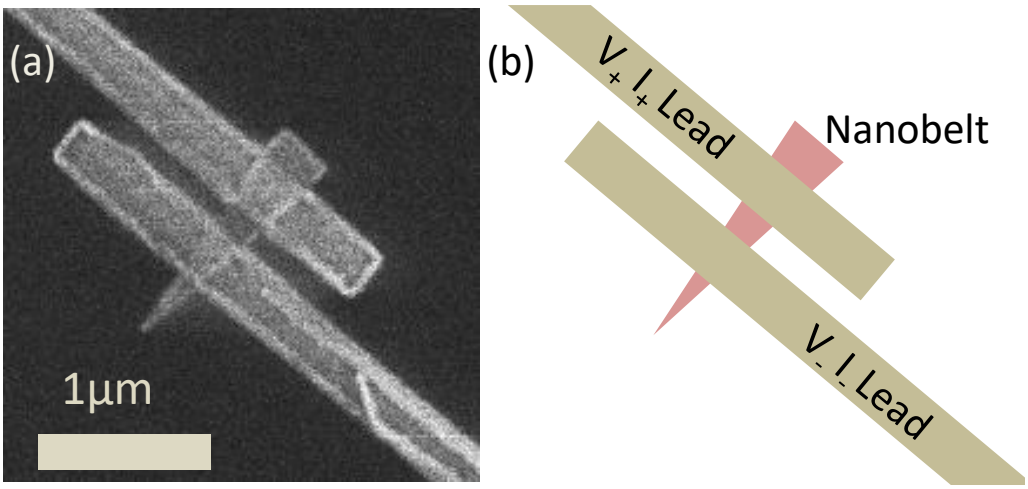

Figure 6.11: (a) He FIB micrograph of a two terminal nanobelt device. Some 'lily-padding' has occured on the bottom electrode and results in an increase in contrast on this sample. (b) Schematic showing the same device where two Ti/Au leads contact a nanobelt (pink). The highly doped Si substrate acts as a universal back gate.

wall growth occurs preferentially on the polar side face of the nanobelt. This occurs as the surface energy of the polar face is larger than that of non-polar faces [140]. When an island nucleates on the polar sidewall the total area of exposed polar face does not increase as the new polar face of the island has the same area as the polar face the island overgrows. If an island nucleates on the non-polar face, two of the sidewalls of the island are polar. The energy of the polar surfaces is greater than non-polar surfaces which gives rise to preferential sidewall growth on polar surfaces. It therefore costs more energy to nucleate onto non-polar sidewalls. Results pertaining to growth of these nanobelts has been published [141].

6.2.3 Electrical characterization of nanobelts

Nanobelts were fabricated into transistors using the method described in subsection 5.2.1. A nanobelt sample was grown for four hours at 850°C to create long nanostructures which are easier to use in subsequent fabrication.[1] An example FET device is shown in Figure 6.11 where a gate voltage is uniformly applied by a back gate.

Ti/Au contacts are used to make ohmic contact to ZnO nanobelts. Titanium contacts have previously been shown to make ohmic contacts to ZnO nanowires [142, 64]. In

[1] 850°C is a best guess temperature based on power supplied to the sample by radiative heating and the heating profile below 800°C as there were technical issues with the thermocouple meaning that it cut out at temperatures above 800°C.

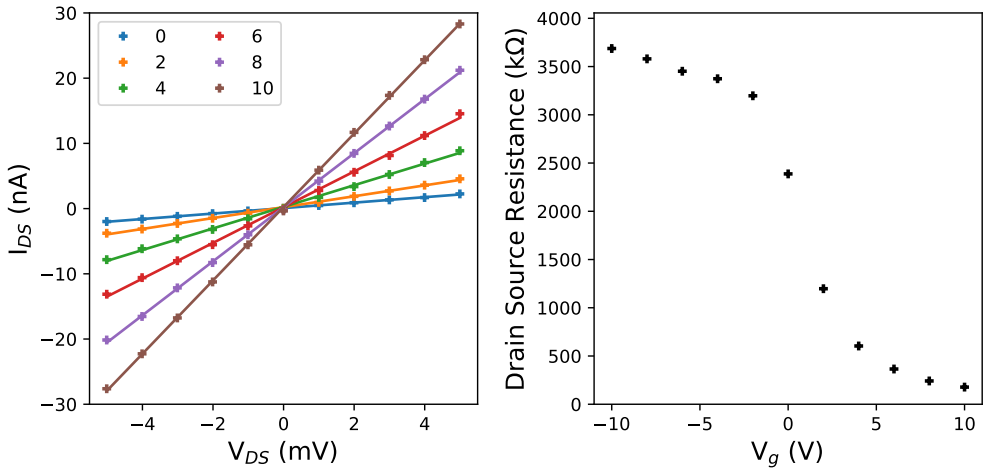

Figure 6.12: Room temperature electrical characterization of a ZnO nanobelt. (a) Two terminal IVs of the NBFET with a gate voltage ranging from 0 to 10V. Gate voltages of -10V were applied but lines overlie each other on these axes. (b) The resistance as calculated by fitting a line to the IVs in (a) as a function of applied gate voltage. Colors match those in (a).

particular in [64] nanowires grown by the same MBE technique are fabricated into four terminal devices. These devices allow the contact resistance to be measured and it was found to be a small fraction of the nanowire resistance ($< 5\%$) in room temperature measurements. We therefore neglect contact resistance effects in the subsequent analysis of room temperature electrical measurements.

This is shown by the linear IVs in Figure 6.12 (a). By applying a gate voltage to the nanobelt the resistance of the nanobelt may be tuned. The resistance of the nanobelt is fit as a function of applied gate voltage and is shown in Figure 6.12 (b). The resistance changes by a factor of 20 when the gate voltage changes from -10V (R=3.69MΩ) to 10V (R=178kΩ). The steepest change in resistance occurs around $V_G = 0$V where by a change in gate voltage of 4V can switch the resistance from 3.2MΩ to 1.2MΩ.

In order to determine the mobility of electrons in these nanostructures we measure the transconductance by fixing the drain source voltage and measuring the drain source current as a function of gate voltage. This is shown in Figure 6.13 where a line is fit to the linear portion of the graph to extract the transconductance (gradient) and threshold voltage (x-intercept). The increase in conductance with a positive gate voltage shows that these are n-type semiconducting nanobelts (as expected for ZnO).

The physical dimensions of the nanobelt must be measured to determine the the mo-

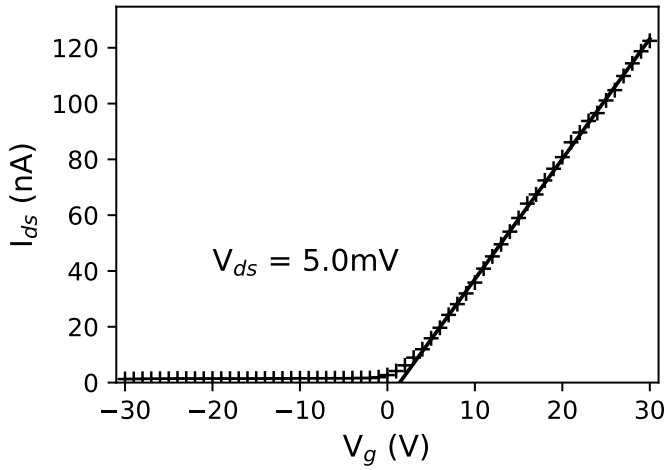

Figure 6.13: Room temperature drain-source current across the nanobelt FET as a function of applied gate voltage in ambient conditions. A line is fit to the linear portion of the curve. The gradient of this line is the transconductance (4.31nA/V) and the x intercept is the threshold voltage (-1.40V).

bility and number density of nanostructures. The length of the conduction channel and the width can be rapidly measured by He FIB/SEM. However these techniques do not give information on the thickness of the nanobelt. In order to determine this AFM was performed on the nanobelts (e.g. Figure 6.14) and height profiles collected. A spread of nanobelt thicknesses from 30 - 45 nm was found. These nanobelts are thicker than measurements by tilted He FIB (Figure 6.7), likely as these nanobelts have been grown for longer than those measured by He FIB. Sidewall growth during this longer growth time is likely the cause of this increased thickness. With physical dimensions of the nanobelt we can model the capacitance between the nanobelt and the back gate as described in 5.2.2. As the oxide layer is thick (400 nm) compared to the nanobelts, we use Equation 5.15 for the capacitance.

The physical and room temperature electrical properties of the nanobelt devices measured are summarised in table 6.1. Of six devices measured the average mobility is $20\text{cm}^2\text{V}^{-1}\text{s}^{-1}$. The un-gated resistance of nanobelts shows substantial variation from 180 kΩ to 45 MΩ. These are two terminal measurements of the nanobelts and so will include contact resistance between the metal electrodes and the semiconductor nanowire. The resistance in each of these nanobelts is significantly reduced by the application of positive gate voltages (which does not strongly affect the contact resistance). Measurements on nanowire FETs fabricated by the same technique found contact resistance to

be negligible in comparison to nanowire resistance [64]. We therefore believe that the variation in ungated resistance to be a genuine measurement of nanobelt properties rather than simply a measurement of nanobelt contact resistance.

We compute two values of electron density n_1 and n_2 as described in 5.2.2, where n_1 is calculated considering the threshold voltage (Equation 5.10) and n_2 the conductivity and mobility (Equation 5.11). For these devices we find that n_1 varies significantly (including negative values of electron density). Previous PhD students have previously found that in MBE grown nanowires, electrical properties exhibit order of magntitude nanowire to nanowire variation [64]. Therefore variation in electron density between different nanobelts is not in and of itself troubling. However, negative electron densities are non-physical (in an n-type material) and this shows that there is a problem with this method of measuring electron density. In order to derive Equation 5.10 (the equation used to determine n_1 from the threshold voltage) we have assumed that the total charge on the nanowire from surface states is negligible. Due to the large surface to volume ratio of the thin nanobelts, the charge from surface states will be significant. We therefore attribute the significant variation in n_1 to surface states. This suggests that this is not a suitable method for extracting the electron density in these nanobelts. The presence of surface states should only effect the intercept of the line fit to the transconductance (Figure 6.13). The electron mobility is extracted from the gradient to this line and we therefore believe the values extracted here to be genuine. The mobilities extracted are similar to nanowires grown by this technique further supporting that the genuine electron mobility is extracted here. This is supported by observations on ZnO nanowire FETs in the literature where a change in sign in threshold voltage based on different environmental conditions has been demonstrated [143]. Here in the presence of oxygen the threshold voltage switched from negative (air and vacuum) to positive in the presence of oxygen due to the increased adsorbed surface oxygen acting as surface traps for electrons.

There is less variation between nanowires in n_2 (and no negative values of electron density). However the values found for n_2 are significantly lower than values often found for electron density in ZnO. This is likely again due to surface states. When calculating n_2 we consider a uniform channel where electrons, with the mobility already determined from the transconductance, flow. This does not allow for a non-uniform channel where surface states have caused band bending and carriers are confined to flow in a region at the nanobelt core much smaller than the nanobelt dimensions. As pointed out in 5.2.2 n_2 is also not a measure of the donor density, rather it is a measure of the free carriers in

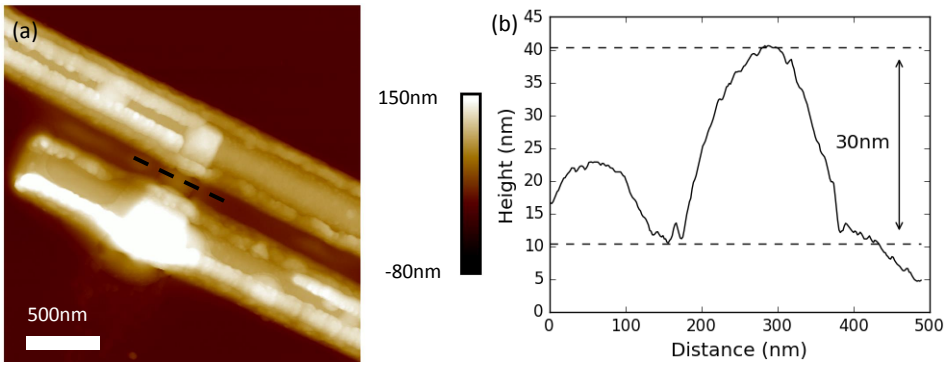

Figure 6.14: (a)AFM image of a nanobelt FET device. The dashed line indicates where a height profile has been taken allowing the thickness of the nanobelt to be measured as 30nm. (b) The height profile along the dashed line. AFM is performed by Mr Adrian Hodel.

the nanowire at zero gate voltage. Therefore, significant numbers of surface states may deplete the nanowire of carriers so that, even given 'normal' doping levels in intrinsic ZnO ($\approx 10^{17}\text{cm}^{-3}$) the total free carriers at zero gate voltage may be smaller.

6.3 Conclusion

In this chapter we study the growth of ZnO nanowires and nanobelts. We provide some new characterization of nanowire growth and secondary growth modes for nanowires before focussing on ZnO nanobelts - the growth of which we demonstrate by MBE for the first time [141]. We characterize the structural properties of these nanobelts and demonstrate morphology control with growth temperature. By changing the temperature we reduce tapering in the nanobelts which means that the polar direction of ZnO is closer to perpendicular to the side face of the nanobelt. This is important for heterostructures based on these nanobelts which exploit the polarization mismatch at heterointerfaces. As these polarization mismatched interfaces would run along the length of the nanostructure they may modify the transport properties of nanobelts.

We characterize the electrical properties of ZnO nanobelts by fabricating single nanobelt FET devices. Nanobelts show signifcant variation in electrical properties showing order-of-magnitude variations in ungated resistance and significant mobility variations between nanobelts. The donor and carrier densities extracted from gated measurements on the nanobelts demonstrate the significant effect of surface states on the nanobelt's electrical properties. Passivating the nanowire surfaces may be one route to achieving more reliable

Length (nm)	Width (nm)	Thickness (nm)	g_m (nA/V)	V_{th} (V)	R($V_g = 0$) (MΩ)	μ ($cm^2V^{-1}s^{-1}$)	n_1 (cm^{-3})	n_2 (cm^{-3})
134	191	30	4.29	-1.34	1.85	29.9	-5.6×10^{16}	$2.65\pm0.52\times10^{12}$
145	235	40^+	4.05	0.13	1.16	20.7	4.9×10^{15}	$4.03\pm0.80\times10^{12}$
124	184	45*	3.40	8.48	0.18	19.1	2.8×10^{17}	$2.76\pm0.56\times10^{13}$
161	212	35	1.08	0.08	0.71	33.8	3.3×10^{15}	$5.67\pm1.1\times10^{12}$
158	187	40	17.23	-2.19	12.1	12.1	-8.3×10^{16}	$2.42\pm0.48\times10^{11}$
129	257	40	1.34	-1.93	5.6	5.6	-7.29×10^{16}	$5.82\pm1.1\times10^{11}$

Table 6.1: Summary of electrical properties of nanobelt devices measured. Length, width and thickness are all dimensions of the nanobelt channel. Length and width are measured from He FIB images. Thicknesses are measured by AFM. At the time of AFM some devices were damaged making some measurements impossible. Thicknesses marked $^+$ are inferred from other nanobelts as they could not be measured. Thicknesses marked * use an inference between the height profile measured when the nanobelt is covered in gold to an uncovered profile (subtract 10nm) based on other nanobelts. As the oxide layer is 409nm (significantly larger than nanobelt dimensions) we use the approximation of Equation 5.16. g_m is the transconductance and V_{th} is the threshold voltage, both found by fitting to the drain-source current at fixed bias whilst varying the gate voltage (Figure 6.13. R($V_g = 0$) is the resistance at zero gate voltage. μ is the electron mobility. n_1 and n_2 are measures of the donor density and free electron density at zero applied gate voltage respectively. Errors in n_2 are predominately due to uncertainty in the thickness of the nanobelt as determined by AFM.

nanobelt electrical properties [143].

The nanobelt FETs have an on/off current of ≈ 20 which is not very large when compared to other FETs. However, these devices are not designed to have a large on/off current and are instead fabricated to measure the electronic properties of these nanostructures. Passivating ZnO nanowires has been shown to improve FET properties (such as subthreshold swing) and would be interesting to do in future devices. Additionally different FET geometries (such as wrap gates or top gates) can lead to much improved FET properties should this be desired.

Chapter 7

Nanowire and Nanobelt Heterostructures

In this chapter we study the growth and characterization of nanowire and nanobelt heterostructures using a combination of transmission electron microscopy and photoluminescence performed on nanostructure ensembles as well as single nanostructures.

7.1 Nanowire Heterostructures

We first investigate the growth of heterostructures in nanowires grown on c-plane sapphire focusing on simple axial and radial heterostructures.

7.1.1 Axial heterostructures

To grow an axial heterostructure the chemistry must change during growth of the nanostructure. For ZnO/ZnMgO heterostructures grown by molecular beam epitaxy this means that Mg flux must be introduced part way through the growth of the nanostructure. In order to achieve an axial heterostructure axial growth must continue after the Mg flux is introduced. In order to continue axial growth it is necessary to maintain a high growth temperature so that gold catalysts do not solidify and we continue VLS growth.

Using the 'old' sample holder shown in Figure 4.5 we grow nanowires on c-axis sapphire at 750°C. Nanowires were grown with Zn BEP of 3.7×10^{-7} Torr and an oxygen plasma with a flow rate of 3SCCM and a power of 300W. After one hour of growth a low Mg flux was introduced with a BEP of 5.9×10^{-9} Torr and growth continues for another hour. Note that temperatures with different sample holders are not directly comparable and for the same thermocouple reading, samples in the old sample holder are hotter than in the

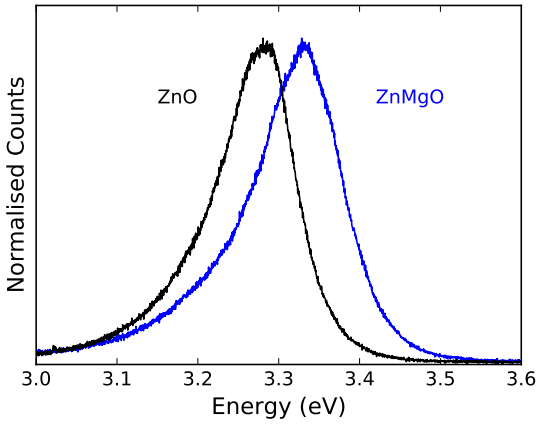

Figure 7.1: Photoluminescence spectrum of attempted axial heterostructures (blue labelled ZnMgO) with plain ZnO nanowires for reference (black labelled ZnO).

new sample holder by $\sim$ 100 °C.

PL on these nanowires (blue line in Figure 7.1) shows emission centered at 3.33eV. There are no distinct peaks from ZnO and ZnMgO indicating that heterostructures may not have been formed. The PL emission of the intended axial heterostructures is 30meV above PL emission from ZnO nanowires grown in similar conditions without the addition of Mg which is shown in Figure 7.1 for reference. The energy difference between the PL peaks can be translated into a Mg concentration of $\sim$1% which is close to the 1.6 % of the fractional Mg flux during the second phase of growth.

We collect STEM-EDS maps of the nanowires grown using this technique (Figure 7.2). These EDS maps show no variation in elemental concentration, rather a uniform Mg incorporation throughout the nanowire consistent with PL analysis showing only a single luminescence peak. This is seen for a number of nanostructures from the same batch. At the elevated growth temperature Mg is mobile and may diffuse into the nanostructures. This means that as well as being incorporated by VLS growth Mg diffuses into the ZnO nanowire bases which were grown initially. This does demonstrate how annealing under a Mg flux allows for retroactive nanowire doping and band gap control.

An obvious solution to stop Mg diffusing into nanowires is to drop the growth temperature as this is a thermally activated process. However, at lower growth temperature gold catalysts solidify stopping axial VLS growth. Using the 'old' sample holder nanowires did not grow very efficiently (short nanowires with a low yield [64]) at temperatures below 700 °C. Given that Mg diffuses throughout the nanostructure at this temperature we conclude that it is not possible to grow axial heterostructures by this technique (gold-

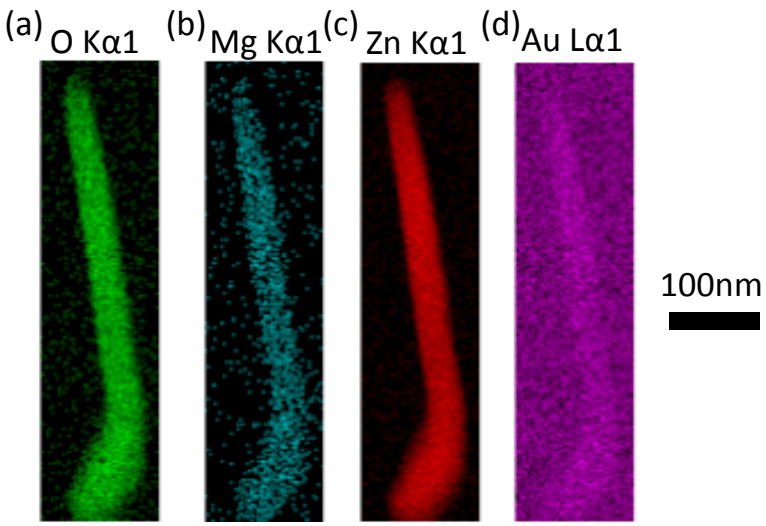

Figure 7.2: Maps of (a) Oxygen (b) Magnesium (c) Zinc K edge intensity and (d) Gold L edge collected by STEM EDS. STEM EDS was performed by Edward R. White of Imperial College London. The kink at the base of the nanowire is a defect introduced during the initial growth of the ZnO nanowire.

catalysed PAMBE on sapphire) and a lower temperature growth technique is required. This could, for example, be nanowire growth catalysed by silver which has a lower melting point than gold and can thus be used to grow at lower temperatures [144, 145].

7.1.2 Radial heterostructures

In order to grow radial heterostructures a core must be grown with one chemistry before a shell is subsequently grown around the core with a different chemistry. In PAMBE when the growth temperature drops we cease axial growth as the catalyst particles solidify and instead promote sidewall growth. We should therefore be able to achieve core-shell heterostructures by first growing 1d nanostructures as discussed in Chapter 6 before dropping the growth temperature and changing the chemistry of the reactants. In order to grow core-shell ZnO/ZnMgO nanowires we introduce a flux of Mg during the shell growth. It is important that temperatures are sufficiently low as to ensure that there is no Mg diffusion into the nanowires as seen at high temperatures e.g. Figure 7.2.

We investigate two samples where shells are grown for different times. The first sample with shorter shell growth (630s) is grown with a Zn flux of 2.9×10^{-7} Torr and Mg flux 2.9×10^{-8} Torr. For the second sample shells are grown for longer (9000s) with a Zn flux of 2.0×10^{-7} Torr and Mg flux 2.3×10^{-8} Torr (both samples have a Zn:Mg ratio of $\approx$10:1).

PL spectra of both samples are shown in Figure 7.3. The sample with short shell growth

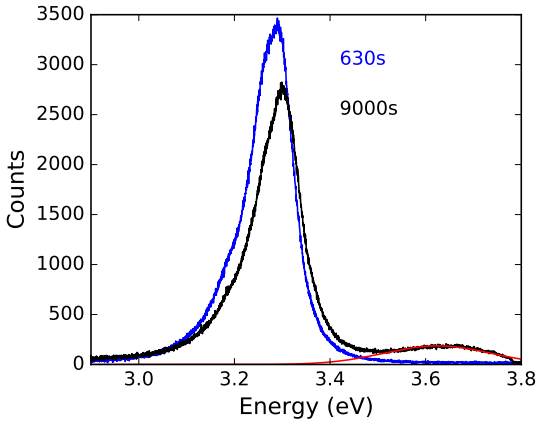

Figure 7.3: Photoluminescence on two nanowire heterostructure samples with shells grown for 630s (blue) and 9000s (black). A Gaussian profile is fit (red) to the ZnMgO peak after a Jacobian transformation is performed giving a central energy of 3.62 eV and $\sigma = 0.11$ eV.

shows an peak from excitonic emission in ZnO but no higher energy ZnMgO peaks. The sample with the long shell growth also shows a peak associated with excitonic emission with slightly higher central energy. This slightly higher energy is within the range commonly observed for nanowire samples where there is some small sample to sample variation and therefore is not taken as evidence of Mg diffusing into the nanowires. The PL spectra for nanowires with long shell growths also shows a ZnMgO peak at higher energies. The distinct luminescence peaks indicates that ZnO and ZnMgO co-exist on the sample.

Equation 3.1 allows us to determine the Mg content of the ZnMgO shell from the PL peak energy. Fitting to the ZnMgO peak we extract the central energy to be 3.62 eV which gives a fractional Mg concentration of 16%.

In order to investigate these heterostructures further we perform STEM EDS on nanowires from both samples (Figure 7.4). The EDS maps show that both samples have nanowires with core-shell geometry despite there being no PL signal from the shell in the sample with the shorter shell growth.

The nanowire from the sample with the shorter shell growth has a ZnMgO shell which is ≈3nm thick (Figure 7.4 a-c). These shells may be too thin to give a luminescent response as carriers may diffuse out of the shell either, into the ZnO core or, to the surface where they recombine via surface states, faster than they recombine in the shell.

The sample with shells grown for 9000s also shows ZnMgO shells (Figure 7.4 d-f) and these are substantially thicker. Although there are a significant number of counts at the centre of the nanowire, this does not indicate diffusion but is due to the projection of the

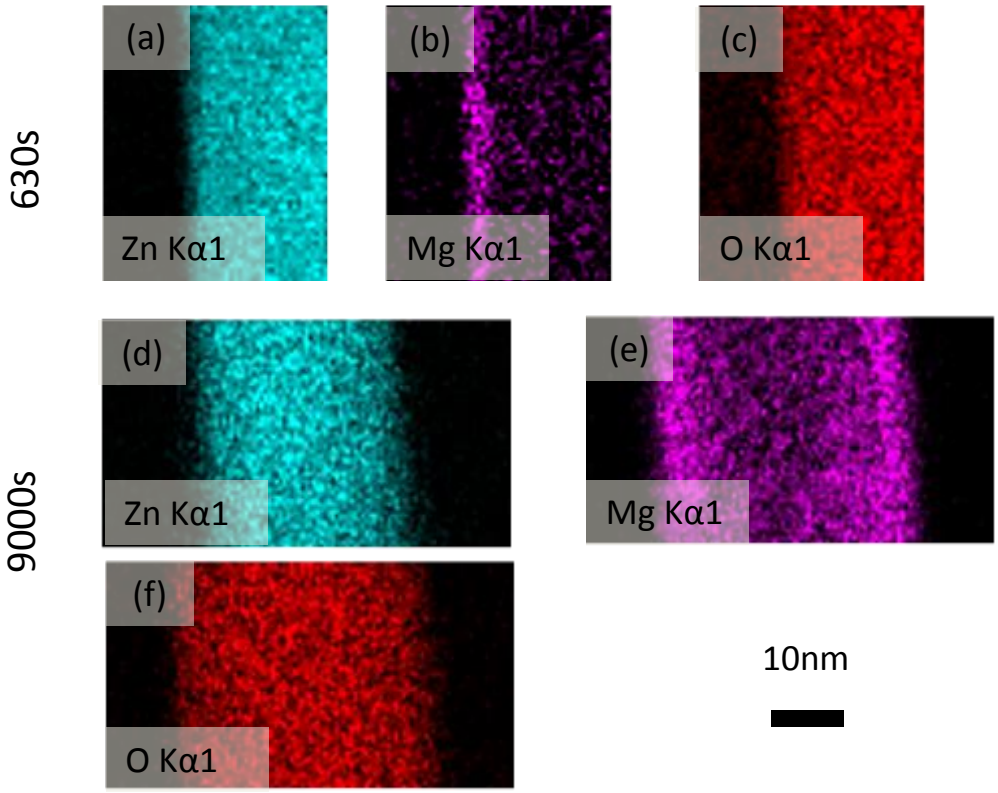

Figure 7.4: STEM EDS maps of the amplitude of the (a,d) Zn and (b,e) Mg K edge and (c,f) the Oxygen L edge of a core shell nanowire where shell growth occurred at 550°C occurred over a 630s (a-c) and 9000s (d-f). STEM EDS was performed by Edward R. White of Imperial College London.

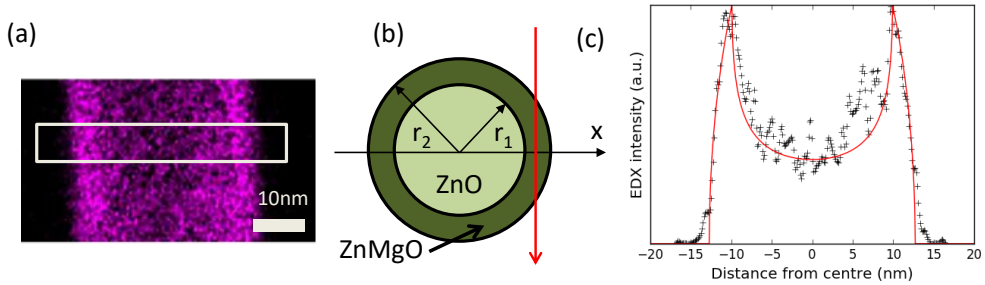

Figure 7.5: (a) EDS map shown in Figure 7.4 (e) with a region marked where an intensity profile has been extracted using ImageJ. (b) Schematic of model where a ZnMgO shell (thickness = r_2 - r_1) coats a circular ZnO core (radius = r_1). Assuming a point like electron beam (shown in red) the intersection of the beam and the shell can be calculated analytically. (c) The line scan of Mg counts from (a) (black crosses) and a plot of equation 7.1 using $r_2 = 12.7$ nm $r_1 = 9.9$ nm in red.

core-shell into two dimensions meaning that the shell wraps the whole nanowire. This can be confirmed by taking an intensity profile of EDS maps such as is done in Figure 7.5 (the area mapped is shown in (a) and the results in (c)). We can calculate the intersection of the electron beam with a ring shell surrounding a circular core. Assuming a point-like beam (the beam has minimal physical width) the intersection between the beam and the shell layer is given by

$$I(x) = \begin{cases} 0, & \text{if } |x| > r_2. \\ \sqrt{r_1^2 - x^2}, & \text{if } r_2 > |x| > r_1. \\ \sqrt{r_1^2 - x^2} - \sqrt{r_2^2 - x^2}, & \text{if } x < r_1. \end{cases} \tag{7.1}$$

where r_1 and r_2 are the radii of the core and the whole nanowire respectively. This geometry is shown schematically in Fiure 7.5 (b). We plot the measured intensity and the model using a nanowire radius of 13.2nm and a core radius of 10 nm in Figure 7.5 (c) and show excellent agreement between the model and results showing that these structures are indeed core-shell nanowires with abrupt heterointerfaces and a shell thickness of 3.2 nm ± 0.5 nm. These thicker shells from the nanowires with longer shell growth do provide luminescent signatures as shown in Figure 7.3.

EDS maps were performed on a number of nanowires from the sample with longer shell growth. The thickness of the ZnMgO shell for each nanowire is extracted as above, considering the intensity of EDS counts across a line-scan and using the model in Equation 7.1. The shell thickness is plotted as a function of nanowire diameter in Figure 7.6 and shows

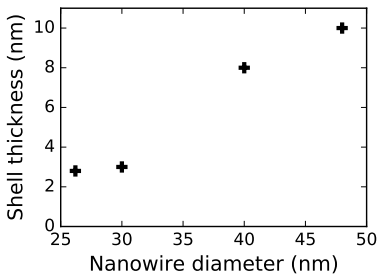

Figure 7.6: The thickness of ZnMgO shells as a function of nanowire diameter measured from EDS maps of nanowires with shells grown for 9000s. The thickness of shells is measured from EDS maps such as those presented in Figure 7.4 by modeling EDS line-scan profiles according to Equation 7.1. Error bars are approximately the same size as markers.

that in this sample the shell thickness increases with nanowire diameter. Assuming that the same flux of reactants were present to each nanowire then more material would be required to make a shell of the same thickness on a nanowire with larger diameter and we would expect the converse - thinner shells for larger diameter nanowires. A simple explanation for variation between nanowire diameters is that there is significant variation in catalyst size as the nanoparticles are formed randomly by de-wetting an evaporated film. However, the observation that we have thicker shells on larger diameter nanowires indicates that thicker nanowires may form due to a greater local flux of adsorbed reactants to the nanowire and that nanowire growth is influenced significantly by the local environment and not the catalyst. Using Mg shells as markers we may therefore explore the growth dynamics of nanowires.

7.1.3 Passivation

We perform PL measurements from 1.6 - 3.6 eV on the heterostructure sample with a 600s shell growth (thin shells) and some ZnO nanowires grown under similar conditions with no heterostructures and present this data in Figure 7.7. The heterostructure sample has a significantly more intense near band edge (NBE) emission at 3.3 eV than the plain nanowires. Despite the increased NBE intensity of the heterostructures the absolute intensity of the defect peaks is decreased relative to the plain nanowires. Despite the thin ZnMgO layer not contributing an independent PL peak, clearly the capping layer of ZnMgO significantly affects the PL spectrum of the nanowires. This is due to the passivation of the nanowire surfaces.

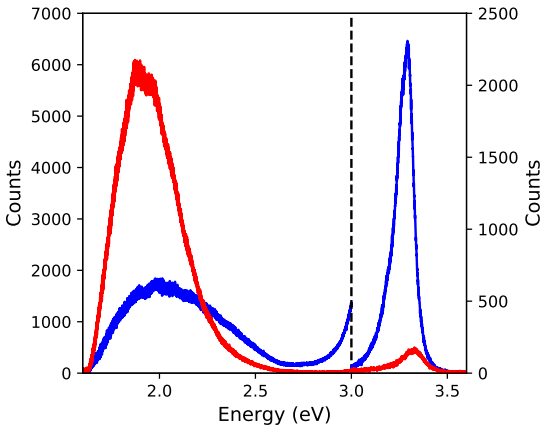

Figure 7.7: Ensemble PL measurements on a heterostructure nanowire sample with 600 s shell growth (blue) and a plain nanowire sample (red). The PL is collected in two measurements as different filters are required to access different regions of the electromagnetic spectrum and are both acquired at room temperature. The dashed line indicates the spectral regions in each acquisition.

7.2 Nanobelt Heterostructures

Core-shell nanobelt heterostructures are particularly interesting due to the polar mismatch at the heterointerface which would extend the length of these nanostructures. Schematics of such nanobelts are shown in Figure 7.8 with a 3d image in (a) and a cross section showing crystallographic orientations in (b). Using lessons from nanowire heterostructure growth, we attempt to grow nanobelt heterostructures. It is important to note that the sample holders used changed between the nanowire heterostructure growth and the nanobelt growth. This has the benefit of more uniform growth across the sample but means that it is necessary to recalibrate the sample temperature. For the same temperature reading of the MBE thermocouple the sample surface temperature is systematically lower in the new sample holder than in the old by approximately 100°C.

The mechanism for sidewall growth may be different between nanowires and nanobelts. ZnO nanowires have sidewalls which are non-polar. Therefore uniform sidewall coverage is expected. However, ZnO nanobelts have distinct sidewall faces - a polar and a non-polar face. Indeed, as shown by the tapering of ZnO nanobelts grown at lower temperatures, sidewall growth occurs predominately on the polar face due to the different energy costs of island formation on polar and non-polar surfaces. The two polar faces are also not identical with a Zn- and an O-polar face and ZnO grows differently along the two polar directions. In thin films the two polarities of ZnO grow on different substrates and in

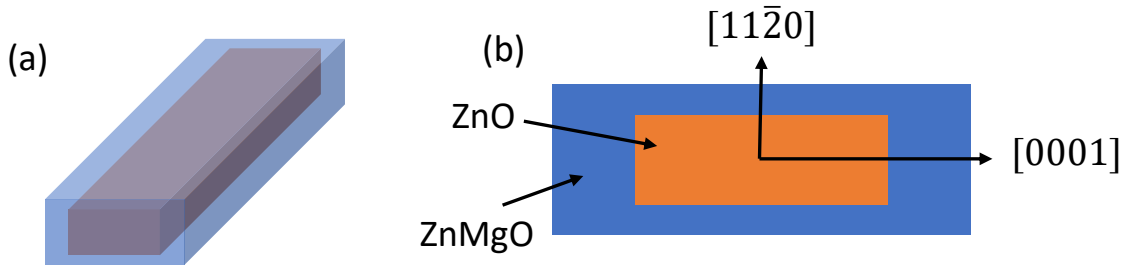

Figure 7.8: Schematics of nanobelt heterostructures with (a) 3d image of the heterostructure and (b) cross section showing crystallographic directions in the nanobelt.

bulk crystals the growth on O-polar faces results in a higher defect density [13]. The difference in energy associated with island nucleation on the different faces means that we may expect correspondingly different sidewall growth for different ZnO faces with less sidewall growth on faces with higher nucleation energy. This means when growing heterostructure nanobelts we expect more ZnMgO growth on the polar sidewalls than the non-polar sidewalls.

We grow ZnO nanobelts as described in section 6.2.1 for 5400 seconds. The target growth temperature is 900°C. The growth temperature is then reduced and a ZnMgO shell is grown for 1800 seconds with a Zn:Mg flux ratio of ≈12:1. There is some variation between flux ratios based on drift in fluxes across the day resulting in fluctuations in fractional Mg flux of a few percent.

7.2.1 Ensemble Photoluminescence

To initially characterize the samples we perform ensemble photoluminescence on the samples which is presented in Figure 7.9. Since ZnMgO has a larger band gap than ZnO, PL from the ZnMgO will occur at higher energies.

Each of the nanobelt samples has a peak in PL corresponding to exciton emission from ZnO (≈3.3eV). Samples grown at 600°C or lower have distinct ZnMgO peaks in addition to the ZnO exciton emission. This shows that there is ZnMgO on the sample in addition to the ZnO but, as this is an ensemble average, it does not confirm that the ZnMgO is in the core/shell configuration intended.

Three samples show ZnMgO emission at similar energies (those with shells grown at 500°C, 550°C and 600°C with a Zn:Mg ratio of 16:1). In these samples there is a trend where the ZnMgO peak becomes more intense at higher growth temperatures up to 600°C although the peak energy doesn't change. This may be indicative of higher quality ZnMgO

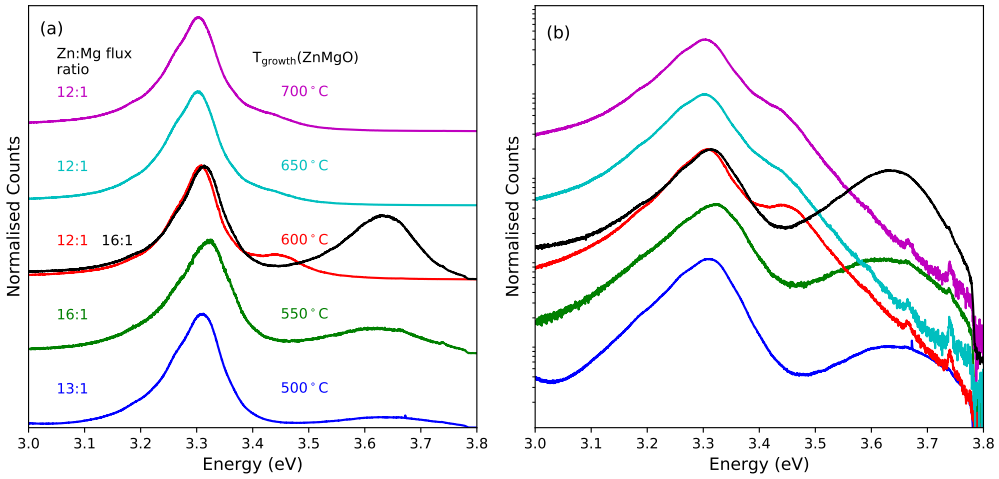

Figure 7.9: Photoluminescence spectra of ZnO/ZnMgO heterostructure nanobelts with the ZnMgO shell grown at different temperatures and slightly different Zn:Mg flux ratios. Temperatures and beam flux ratios are listed in the figure. Each curve is offset vertically for clarity. Data are plot on (a) a linear scale and (b) a logarithmic scale.

due to the higher growth temperature.

Of the two samples with ZnMgO grown at 600°C, both show well resolved ZnMgO peaks which have different central energies for the ZnMgO peak (red and black lines in Figure 7.9). Additionally the sample with the higher Mg flux (red) gives off lower energy emission and hence has a lower band gap presumably resulting from less Mg being incorporated. As temperatures are controlled by a PID controller taking as its input the temperature measured by a thermocouple not located on the sample surface, temperatures are not perfectly controlled. In the sample which has a lower energy ZnMgO peak the temperature (as read out by the pyrometer) increased slightly during growth and so the true growth temperature may be slightly higher than the other sample by 2–5 °C.

For samples with ZnMgO grown above 600°C, a PL signal corresponding to the ZnMgO band gap is not obvious when plotted on a linear scale. When PL for these samples with shells grown at higher temperature is plotted on a logarithmic scale (Figure 7.9 b) a shoulder on the high energy portion of the ZnO PL peak is apparent which is not present for samples with shells grown at lower temperatures. This shoulder we attribute to the presence of ZnMgO either directly due to luminescence of the wide band material or indirectly due to luminescence processes allowed by the heterointerface. We confirm that Mg is present on the surface by performing XPS on the samples with shells grown at high temperature where Mg XPS peaks are found as discussed in section 7.2.2.

Whilst the central energy and intensity of the ZnO peak remains approximately con-

stant, the ZnMgO peak shows non-monotonic behaviour in intensity with temperature, increasing with shell growth temperature up to 600 °C before reducing. The central energy of the peak is constant at ∼3.65 eV with temperature up to shell growth temperatures of ∼600 °C when it falls to become a shoulder to the ZnO peak.

One explanation of the trend in PL with ZnMgO growth temperature is that at higher temperature the shell growth rate falls. As the growth rate falls, the shell thickness decreases. From nanowires we have seen that thinner shells do not provide a PL peak (e.g. Figure 7.3) and this would likely be the same for nanobelts. This doesn't explain the change in central energy but does explain the non-monotonic change in intensity. The change in central energy could relate to the epitaxial quality of the ZnMgO. At higher temperatures we expect higher quality, more epitaxial ZnMgO to grow. If ZnMgO shells are strained by the ZnO core then this may reduce the incorporation of Mg in the shell, leading to a reduction of the central energy of the luminescence.

We perform PL as a function of the pump laser excitation power on the sample with shells grown at 550 °C and compare this with a reference spectrum of ZnO nanobelts in Figure 7.10. The reference ZnO nanobelts only showed a change in absolute intensity with pump power with the normalised spectra remaining the same up to changes in signal to noise ratio. For the heterostructure nanobelts, at 100% power (∼600 Wmm^{-2}) the PL spectrum has a low number of counts at low energies, a ZnO peak and a higher energy ZnMgO peak. The ZnO peak from the heterostructure nanobelts and the plain nanobelts look qualitatively similar, although there are fewer counts for the ZnO nanobelt sample at energies below the band gap of ZnO.

As the pump power decreases from its maximum power of ∼2mW the PL spectra of the heterostructure nanobelts change. The absolute counts of the spectra are shown in Figure 7.10 (a). All spectra are acquired with the same acquisition time and averaging meaning that the PL spectra are non-monotonic with pump power.

The PL spectra are acquired by shining laser light at the sample and then measuring the emitted light. We measure the PL properties of the sample when illuminated by light of a given fluence. Continuous illumination can change the properties of the sample, for instance, under intense illumination surface traps may on average be empty as photons free electrons from the traps faster than they are re-trapped. This can affect the band structure of the nanostructures and the consequent PL spectra acquired. The power dependent PL spectra are therefore capturing luminescence features due to carrier dynamics in the nanostructures.

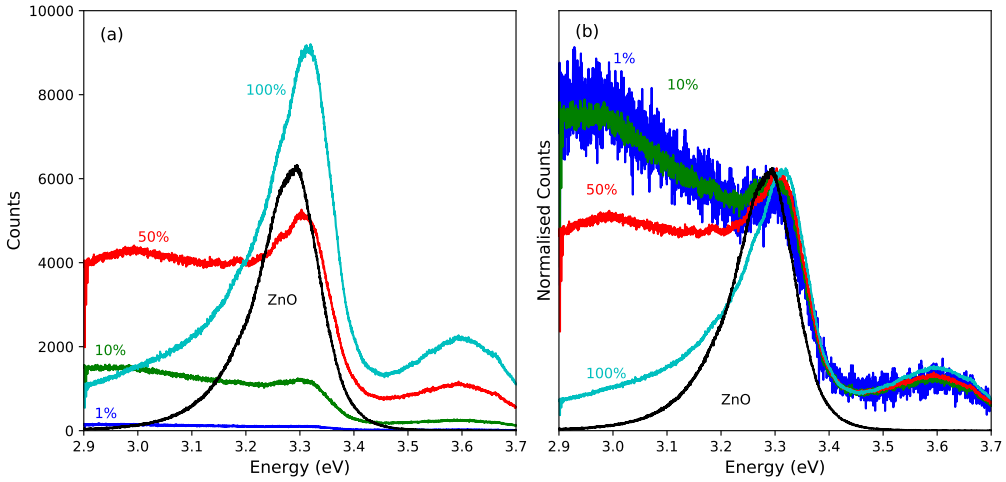

Figure 7.10: Power dependent PL spectra taken of a heterostructure nanobelt ensemble and a plain ZnO nanobelt sample (black line) at room temperature. The percentage of the maximum applied laser power (2 mW laser power 2 μm spot) is indicated on the graph. The plain ZnO nanobelt is taken at 10% power; the normalised spectrum showed no measurable power dependence between 100 and 0.1% power except for a change in signal to noise ratio. We plot (a) the absolute number of counts and (b) the counts normalised to the ZnO peak.

In 7.9 (b) we show the PL spectra normalised by the ZnO peak at 3.3 eV. The normalised counts show that the relative intensity of the ZnO peak and the ZnMgO peak remain roughly constant. However, the counts at lower energies of 2.9–3.2 eV become more intense relative to the ZnO peak before saturating with decreasing laser pump power at 10% of the maximum applied power. There is therefore some luminescence process at energies below the band gap of ZnO which does not occur in plain ZnO nanobelts and also does not occur under intense excitation. A potential candidate for this luminescence process is the quantum confined stark effect.

QCSE occurs when electrons (holes) confined in a quantum well recombine with holes (electrons) from the narrow-gap material on one side of the well. QCSE luminescence occurs at energies below the band gap of the narrow gap material and may only occur when a quantum well forms. This luminescence process is qualitatively at the correct energy (<3.3 eV) and occurs in heterostructures but not plain nanobelts supporting the suggestion that it arises due to QCSE.

If the luminescence is due to QCSE then this is suppressed at high power. This cannot be due to saturation of the QCSE (i.e. the maximum intensity due to QCSE emission is reached) as Figure 7.10 (a) shows non-monotonicity. Therefore it must be due to a

change in the band structure under intense illumination. This could include screening of potentials due to large numbers of charge carriers affecting the band structure and confining potentials resulting in the lack of a quantum well.

QCSE emission was measured in polar quantum wells at the tips of nanowires by CL at 5 K with peak energies ∼140meV below the main ZnO peak [97]. The measurements presented here are performed on ensemble nanobelts at room temperature meaning broader peaks are to be expected. The luminescence peak here is 300meV below the band gap of ZnO although the details of QCSE will depend on the exact band-misalignment. We discuss QCSE related PL later in the thesis where cryogenic PL and single-nanostructure PL are reported.

7.2.2 X-ray Photoelectron Spectroscopy

In order to test whether Mg is present on these samples XPS measurements are performed on the nanobelt samples where only low intensity shoulders are seen on the ZnO peak in ensemble PL and also upon the sample grown at 600°C with a 12:1 Zn:Mg ratio for reference. As XPS is an ensemble measurement when performed on nanostructures it will average over many nanostructures as well as any material on the surface that is not part of a nanostructure (e.g. thin film or boulder growth). We show the Mg peaks in the XPS spectra (Figure 7.11 a) and the whole XPS spectrum (Figure 7.11 b). XPS is performed by Matthew Sparks.

The significant counts from surface carbon contamination and adsorbed oxygen make extracting a true Zn:Mg ratio difficult. These XPS measurements do confirm that there is surface Mg present in all of the samples, even when there is a low intensity PL peak from ZnMgO. We may also fit the peaks and find the ratio between the area under the Zn and Mg XPS peaks as shown in Table 7.1. Whilst there is variation in this ratio between samples, the variation is not monotonic and likely due to significant surface contamination. However, the ratios are comparable in magnitude.

7.2.3 Single Nanobelt PL

Ensemble PL measurements of the nanobelts show distinct ZnO and ZnMgO peaks (Figure 7.9) indicating that there may be heterostructures present. However this is far from conclusive. Alternatively there could be ZnMgO in close proximity to the ZnO but not in the heterostructure geometry. This ZnMgO could possibly be in the form of boulder growth on the substrate. A better measurement indicating nanobelt heterostructures would be

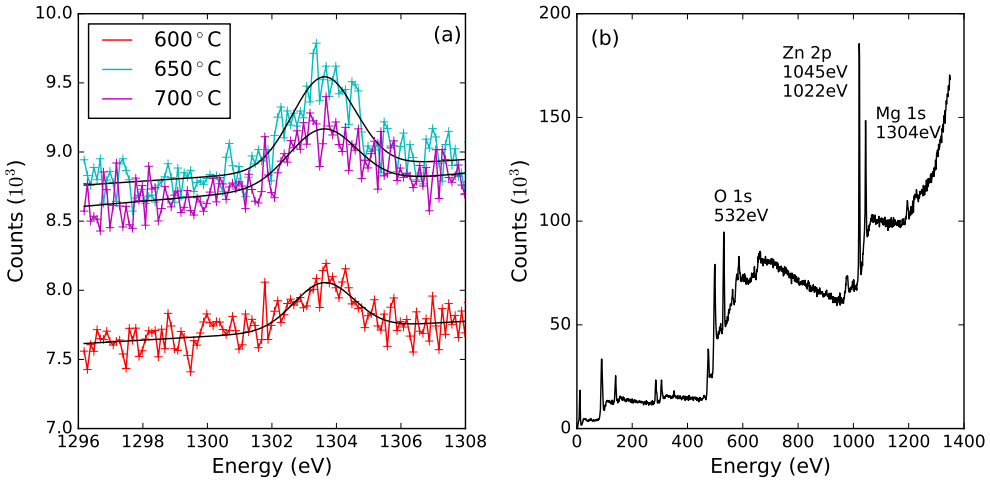

Figure 7.11: XPS spectra of nanobelt heterostructures. (a) Zoom on Mg 1s peak in the XPS spectrum for samples grown at three temperatures. A small Mg peak is present in all samples measured. A Gaussian is fitted to each of the magnesium peaks after first subtracting a linear background. Fit parameters are shown in table 7.1. (b) A full XPS spectrum of the sample grown at 700°C with pertinent peaks labeled. XPS is performed by Matthew Sparks of UCL.

Shell Growth Temperature (°C)	Mg A fit	Mg σ fit	Mg $A\sigma\sqrt{2\pi}$	Zn (1022 eV) $A\sigma\sqrt{2\pi}$	Zn:Mg peak ratios
600	340±30	0.93±0.09	790	36,400	46.1
650	670±35	0.99±0.06	1650	41,300	25.0
700	410±33	1.05±0.1	1080	41,400	38.3

Table 7.1: Table summarizing XPS results for samples with shells grown at 600, 650 and 700 °C. The fit parameters for Mg peaks are given as well as the ratio of areas under the Zn and Mg peaks for all samples showing similar values for all samples. The fits are shown in Figure 7.11. An exact quantification is more difficult and includes equipment-specific parameters.

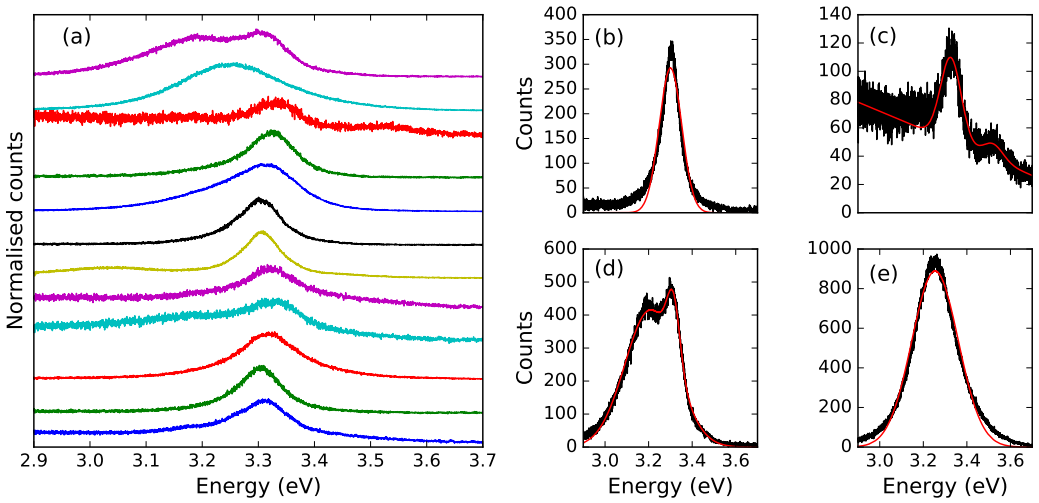

Figure 7.12: Room temperature PL measurements on single nanobelt samples grown at 600°C with a Zn:Mg ratio of 12:1 (a) A number of normalised PL spectra offset for clarity (b-e) several characteristic spectra. (b) A PL peak at 3.3eV as expected for ZnO. (c) A PL peak from both ZnO (3.3eV) and ZnMgO (∼3.5eV) (d) One peak at ∼3.3eV from ZnO and another peak at lower energies. (∼3.2eV). (e) A single, lower energy peak. Due to a less intense signal the spectrum in (c) is collected for a longer a time. this improves the signal to noise ratio allowing the peaks to be resolved but also results in the higher intensity background. Red lines show fits to the spectra where (b, e) are fit using a single Gaussian, (c) has a linear background subtracted before being fit by the linear sum of two Gaussians and (d) is fit by the linear sum of two Gaussians.

PL spectra from single nanobelts containing ZnO and ZnMgO peaks. This would show that there is ZnO and ZnMgO in a single nanobelt showing that at least the different chemistries coexist within single nanobelts, meaning that some form of heterostructure is formed. There are additionally luminescence signatures which are characteristic of quantum confinement of the heterointerface such as quantum confined stark effect (QCSE) and quantum well luminescence. At room temperature these spectra may be broad (or not present) due to thermal broadening.

We perform PL on single nanobelts as described in section 4.2.4. We disperse nanobelts from two of samples whose ensemble measurements are shown in Figure 7.9. One sample has shells grown at 550°C (green curve in Figure 7.9) with a Zn:Mg ratio of 16:1; and the other at 600°C with a Zn:Mg ratio of 12:1 (red curve in Figure 7.9). Spectra from single nanobelts grown at 600°C collected at room temperature are shown in Figure 7.12.

Spectra from different nanobelts (Figure 7.12 a) show substantial variation despite all

coming from the same growth run with shells grown at 600 °C. This is likely due to a combination of factors: Firstly, we know that there is nanostructure to nanostructure variation in the shape and size of the nanobelt. Probably more important than variations in shape and size for luminescence properties are variations in the heterostructure, including the thickness of shell growth and Mg concentration of the shell. Variation in heterostructure dimensions was shown for nanowires in Figure 7.6 and therefore likely occurs for nanobelts as these heterostructures are grown by the same technique.

In Figure 7.12 (b-e) we present a series of archetypal spectra collected on single nanobelts. Figure 7.12 (b) shows a PL spectrum with a single peak which is characteristic of excitonic emission from ZnO. It is fit by a single Gaussian which has a central energy of 3.30eV and a standard deviation, $\sigma = 0.05$eV. The fit is not perfect and does not capture tails in the spectrum, nor the maximum intensity. This may be due to small levels of additional luminescence processes also occuring.

Figure 7.12 (c) shows a PL spectrum with a low intensity. Due to the low intensity the spectrum has been measured with an integration time five times longer than the other spectra. There is a comparatively large background which is characteristic of these PL measurements when low intensity sources are measured for longer times. This spectrum shows two peaks, one characteristic of excitonic emission from ZnO and another which has an energy associated with ZnMgO with lower intensity. This spectrum looks very similar to ensemble measurements once the background is disregarded. We take these two peaks as evidence that this is a spectrum from a heterostructure where both the ZnO and ZnMgO are luminescing. We subtract a linear background from the spectrum and then fit it by the sum of two Gaussians. The Gaussian which fits the ZnO peak has a central energy of 3.32 eV and $\sigma = 0.05$ eV (similar to the excitonic spectrum in Figure 7.12 b). The ZnMgO peak has a central energy of 3.52 eV and $\sigma = 0.05$ eV. Based on the difference in central energies of the two peaks (0.19 eV) and Equation 3.1 this gives a fractional magnesium concentration of the shell of x=0.12.

Figure 7.12 (d) shows a spectrum which clearly also has two peaks. One of the peaks, as expected, is characteristic of excitonic emission from ZnO with central energy 3.31eV and $\sigma = 0.03$eV. The second peak is, however, at lower energy than the ZnO peak. It has central energy 3.20eV and $\sigma = 0.12$eV. This is significantly broader than any of the excitonic peaks in the other spectra. The different central energy and width indicate that this peak is caused by a different mechanism. This second peak at lower energies is seen in a number of spectra. These peaks are separated by 110meV meaning that the low energy

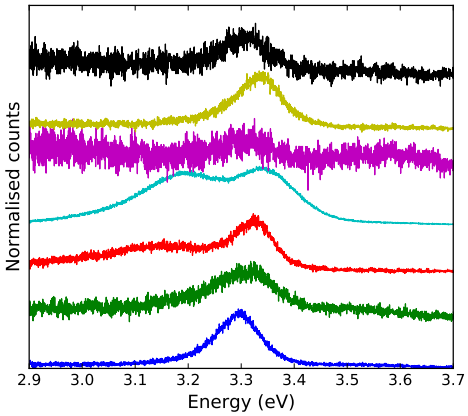

Figure 7.13: Normalised single nanobelt PL spectra taken from a different sample (grown at 550°C with a Zn:Mg ratio of 16:1 - green curve in Figure 7.9. Lines offset vertically for clarity.

peak is not a phonon replica of the main peak since the LO phonon in ZnO is 72 meV.

Figure 7.12 (e) is fit by a single Gaussian. This peak however resembles the lower energy peak seen in Figure 7.12 (d) more than excitonic emission from ZnO – the central energy is lower(3.25 eV) and the peak is broad (σ =0.11 eV).

The variety of PL spectra which we find in nominally similar nanobelts is intriguing. These different spectra are also found when performing single nanobelt PL on nanobelts from a different sample (Figure 7.13). Spectra with two peaks with the second peak being at either higher or lower energy, are seen as well as nanobelts giving only excitonic ZnO emission. The variation in PL spectra between nanostructures shows that ensemble measurements alone are insufficient in order to determine the optical properties of single nanostructures.

7.2.4 Low Temperature Nanobelt Photoluminescence

At room temperature, features in photoluminescence spectra are blurred out by the significant thermal energy (300 K $\times k_B$ = 26meV). By cooling the sample to lower temperature and reducing the thermal energy of carriers in the sample, we may resolve features which are obscured at room temperature. Maximillian Zapf, a collaborator at Jena University, Germany, performed cryogenic photoluminescence on the single nanobelts discussed in the previous section. These measurements are performed using a HeCd laser at 4.2 K and are performed both on single nanobelts using a narrow (∼0.5 μm) excitation beam and also on ensembles of as-grown heterostructure nanobelts using a broad (∼1 mm) excitation beam.

The ensemble measurements will average over millions of nanobelts as there are many nanobelts per square micron. Together these measurements give a better understanding of the luminescence processes occurring in nanostructures.

Ensemble Measurements

We first perform ensemble PL measurements on two samples which have previously been discussed: the sample with shells grown at 600 °C and a Zn:Mg ratio of 12:1 (Figure 7.14 a, b) and the sample with shells grown at 550 °C with a Zn:Mg ratio of 16:1 (Figure 7.14 c, d). These samples have distinct room temperature ensemble PL spectra which are representative of different samples. The sample with shells grown at 600 °C has a narrow PL peak associated with the ZnMgO which at room temperature is a shoulder to the main peak. The sample with shells grown at 550 °C has a much broader ZnMgO peak which is centred at higher energy (Figure 7.9). The PL spectra in Figure 7.14 are collected with an excitation power of 0.3W cm^{-2}, over 1000 times lower excitation power than the room temperature measurements.

At 300 K both samples have a PL peak from ZnO at 3.32 eV which arises due to transitions across the band gap of ZnO. As the samples cool this peak narrows and moves to higher energies and at 4K is centred at 3.37 eV. The narrowing of peaks with decreasing temperature is a normal feature of PL as the carriers have less thermal energy to broaden transitions. The increase in energy of the ZnO PL peak is something that has been reported upon previously [146] and is due to a temperature dependent band-gap. As the temperature drops the main broad PL peak from ZnO narrows, revealing a family of peaks.

The emission from ZnO is known to have a number of components from free excitons (FX), neutral donor bound excitons (D^0X) and the phonon replicas of these excitonic peaks [147]. At high temperatures the FX peaks dominate the zero-phonon line and at low temperatures the D^0X peaks become dominant. This occurs as at higher temperatures the donors become thermally activated. Therefore FX emission freezes out with the intrinsic carriers in ZnO which occurs at ∼100 K. In Figure 7.14 (a, b) the zero-phonon peak at 100K shows split peaks since at this temperature both the FX and D^0X peak occur with significant intensity. The FX peak is at slightly higher energy than the D^0X.

At energies lower than the ZnO zero-phonon line there are further peaks which are well resolved at lower temperatures. These peaks are phonon replicas – i.e. when electrons and holes recombine they emit a phonon as well as a photon. The phonons generated here are linear optical (LO) phonons which have energies in the range 70–72 meV [148, 147].

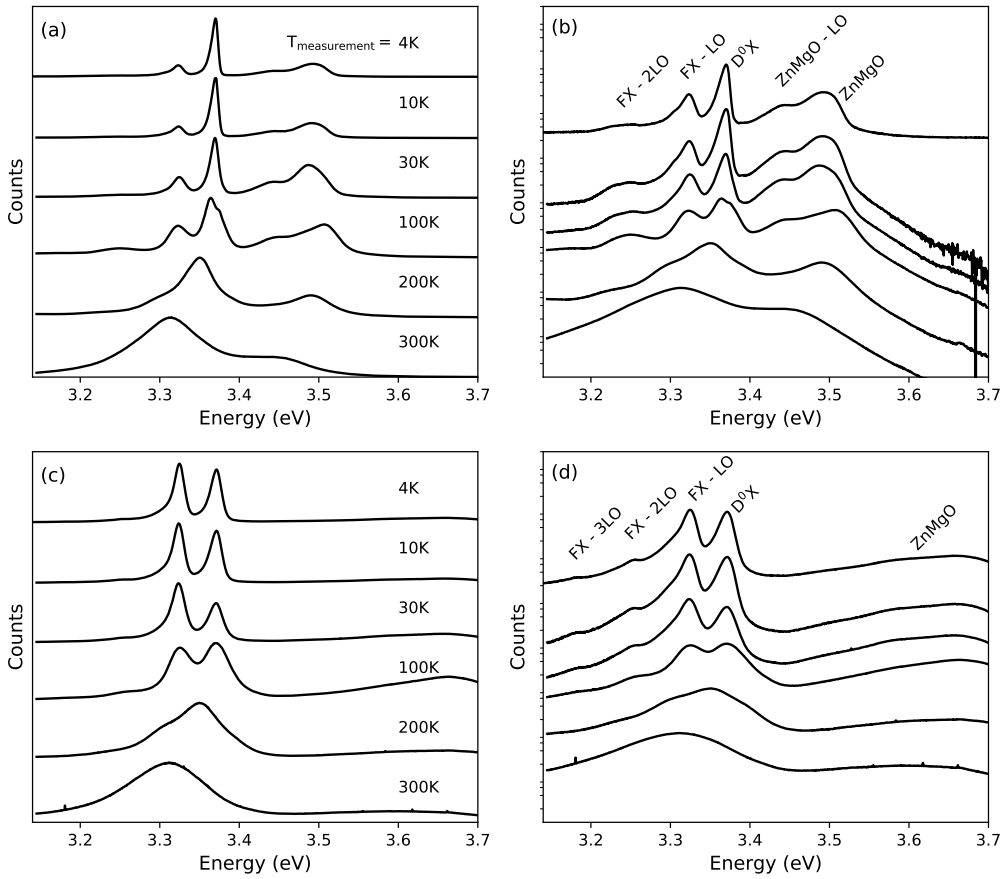

Figure 7.14: Temperature dependent photoluminescence measurements performed with a broad ∼1 mm excitation beam on an ensemble of ZnO/ZnMgO nanobelt heterostructures with (a, b) shells are grown at 600 °C and (c, d) shells grown at 550 °C. The spectra are off-set for clarity and plotted on (a, c) linear (b, d) logarithmic intensity scales. Each spectrum is normalised to the most intense point within the spectrum. Measurement temperatures are labeled. Spectra are collected with a pump power density of 0.3 Wcm^{-2}

The LO-phonon coupling is much greater for the FX than D^0X, meaning that the phonon replicas are of the free exciton peak, which is entirely suppressed by D^0X at cryogenic temperatures in these nanobelts. When closely expecting the FX-LO peak on logarithmic scales there appears to be a shoulder to the peak at lower energies. This much lower intensity peak is ∼70 meV below the D^0X peak indicating that it is likely a phonon replica of the donor-bound exciton peak and is labelled D^0X - LO. It is at much lower intensity due to the weaker phonon-exciton coupling for the donor bound exciton.

The two samples differ predominately in the central energy, and width of the ZnMgO peak from the shell luminescence. For the sample with shells grown at 600 °C (Figure 7.14 a, b), at room temperature the shell luminescence is at energies just above the broad ZnO peak and is a shoulder to the peak. At lower temperatures the peaks split and become well resolved. At temperatures of 100 K and below the ZnMgO peak splits into two peaks, a main peak and a lower energy shoulder separated by ∼50 meV. This is similar to the 47meV separation between the D^0X peak and FX-LO peak. We therefore think it reasonable to suggest that this peak is an LO-phonon replica of the ZnMgO peak. The broad ZnMgO peak has no obvious structure. The broad luminescence band may indicate a spread in ZnMgO concentrations between samples and thus any fine structure will be washed out by averaging over millions of nanostructures. The narrower peak and LO phonon replica indicates that the ZnMgO has higher crystal quality in the sample where shell growth occurs at 600 °C.

The LO-phonon replicas of the FX peak give information about the ZnO crystal quality and tell a different story about crystal quality from that indicated by the ZnMgO peak. The sample where the shell is grown at 550°C has three LO-phonon replicas which can be resolved as opposed to the two LO phonon replicas seen in the sample with shell growth at 600 °C. As these are ensemble measurements interpreting this is challenging. One suggestion is that the shells grow more epitaxially at higher temperature – i.e. the heterointerface is more extended, higher quality and the materials on either side are epitaxially related for larger regions. Epitaxial shells with different lattice constants would strain the core and strain broadens LO phonon replicas. The shorter lattice constant of the ZnMgO will compressively strain the ZnO core. Whilst epitaxial matching improves the quality of the ZnMgO layers, it strains the ZnO layers reducing the crystalline quality of the core.

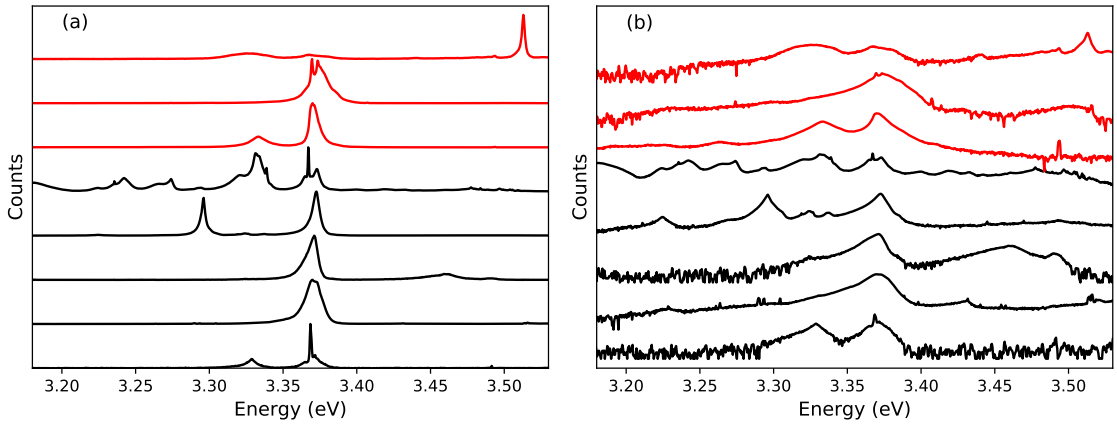

Figure 7.15: Single nanowire photoluminescence performed at 4 K on (a) linear and (b) logarithmic scales. Features from cosmic rays are removed and spectra are offset for clarity. Spectra in black are of nanowires where the shell growth was performed at 600 °C and the shells were grown at 550 °C for spectra in red. All spectra were collected using a pump power of 95 Wcm^{-2}. Spectra are processed before plotting on a logarithmic axis since noise in the CCD can cause counts below the noise floor to be recorded as a negative value which cannot be plotted on a logarithmic scale. Therefore the absolute value of the counts is plotted (i.e. no negative values) with a small offset of 1 extra count (i.e. no zero counts).

Single Nanobelt Measurements

We present cryogenic PL measurements on a number of single nanowires from both batches of nanowires in Figure 7.15. These spectra show a rich variation in features which deviate significantly from the ensemble measurements, as they do at room temperature. Common to all PL spectra is a ZnO peak centred at 3.37 eV. In three of the measured nanobelts this 3.37 eV peak has fine structure with a very narrow, very intense peak. Most nanobelts have PL from energies higher than the ZnO band gap showing that in the single nanostructures there are heterostructures i.e. both ZnO and ZnMgO are present in the same nanobelt. More importantly these spectra have fine structure which cannot be straightforwardly explained by a combination of emission from different excitons and phonon replicas. Together the fine structure and the emission from ZnO and ZnMgO from the same nanostructure indicate that there is complex luminescence arising from quantum confinement and complex band profiles at heterointerfaces in these single nanostructures.

At 4.2 K we acquire PL spectra using different excitation powers which we show for three nanobelts in Figure 7.16 on linear and logarithmic scales. In addition to showing

power dependence, these higher magnification spectra more clearly show the features of spectra characteristic of different nanobelts. These nanowires are all from the sample where shells are grown at 600 °C. These spectra all show luminescence from ZnO. The D^0X peak for the ensemble measurement has an FWHM of ∼10 meV at a pump power of 0.27 Wcm^{-2}. Even at substantially higher pump powers of 95Wcm^{-2} the nanobelt which shows no fine structure (Figure 7.16 c, d) has an FWHM of ∼6 meV. The nanobelts are high quality single elements with some scatter in properties and so averaging over many nanobelts broadens the spectrum and explains why single nanobelts have a narrower PL peak than ensemble measurements. Two of the nanobelts have ZnO PL peaks with not only a narrower FWHM but also very sharp, intense components and additional fine structure (Figure 7.16 a, b and e, f). The most intense peak for the nanowire with spectra shown in Figure 7.16 (a, b) has a FWHM of ∼1 meV ±0.5 meV where errors arise due to the spectral resolution of this measurement and the existence of overlapping peaks. This is similar to the 0.7 meV FWHM of the most intense excitonic peaks measured on high quality single crystal substrates [149] indicating that the ZnO which composes the core of these nanobelts is of high quality.

The nanobelt spectrum shown in Figure 7.16 (c, d) has a series of peaks separated by ∼70 meV which are therefore attributed to LO phonon replicas. These peaks are marked by a dot-dashed line in red. However, these spectra are replicas of the D^0X peak rather than the FX peak. This shows that in this nanobelt there is significant coupling between the linear optical phonon and the donor bound exciton. For single crystal ZnO and ensemble measurements on the same sample this is not the case.

There are many features in these spectra which aren't well described by phonon replicas of different excitons in just ZnO. Each of the spectra show significant PL intensity at energies above the band gap of ZnO. Some of these peaks are due to the presence of the wider band ZnMgO. These ZnMgO peaks confirm that we have heterostructure nanobelts - where there is ZnO and ZnMgO in a single nanobelt. As well as containing a ZnMgO peak, the spectra collected at 95 Wcm^{-2} shown in Figure 7.16 (b, f) both show fine structure at energies above the ZnO peak. The fine structure is not well explained by the presence phonon replicas of the main ZnMgO peak as they are not separated by constant energy, nor periodic and are narrower than the ZnMgO peak. We interpret the emission peaks at energies above the ZnO peak and below the ZnMgO peak as being due to transitions between quantum-well-levels where the energy of the transition is increased due to the quantum confinement.

There are also features in the luminescence at energies lower than the D^0X transition which are not well explained by the phonon replicas of the D^0X or FX excitons. Examples of these peaks badly explained by ZnO, ZnMgO and phonon replicas are the peak in the PL at 3.337eV in Figure 7.16 (d) and many peaks in 7.16 (f). These we attribute to quantum confined stark effect (QCSE) allowing transitions at energies lower than the band gap of ZnO.

As the excitation power is increased the spectra qualitatively change. Peaks, as expected, broaden due to the more intense pumping populating the valence band with holes of a spread of different energies. The relative intensity of different peaks is highly power dependent. For instance when pump power density increases from 95 to 3183 Wcm^{-2} the intensity of the D^0X - LO peak increases relative to the D^0X peak by $\sim$50% whereas the FX - LO peak increases by $\sim$2000% for the nanobelt shown in Figure 7.16 (c, d). This may be due to the saturation of donors with increased pump power. Many of the features attributed to quantum-well luminescence and QCSE are washed out with increasing pump power. This is likely due to the saturation of transitions associated with quantum well levels.

These spectra are complex, and vary significantly between nanobelts. It is important to consider why this is the case. Firstly, as already discussed, even single crystal ZnO has a rich family of luminescence peaks which may be resolved at low temperatures. This includes a series of excitonic peaks and phonon replicas of the peaks. Whilst the central energy of these peaks is determined by the structure of ZnO, it is known that the band gap of ZnO nanowires can be modulated by, for instance, strain [150]. Therefore, even knowing the nominal energy of these excitons and transitions, the central energies of these peaks can vary slightly between nanowires. As demonstrated by EDS maps of nanowire heterostructures in section 7.1.2, the thickness of heterostructures varies between nanostructures when grown using this technique. The fractional Mg content of shells also varies between nanobelts as shown by the low temperature PL measurements on single nanobelts presented in Figure 7.15 where the central energy of ZnMgO peaks varies between nanobelts.

As well as transitions occurring solely in the ZnO or solely in the ZnMgO there are multiple luminescence processes which occur due to the interface between the ZnO and the ZnMgO where there is both a polarization mismatch and a band-gap mismatch. These are transitions between quantum well levels (i.e. at energies above ZnO) and QCSE emission (i.e. at energies below ZnO).

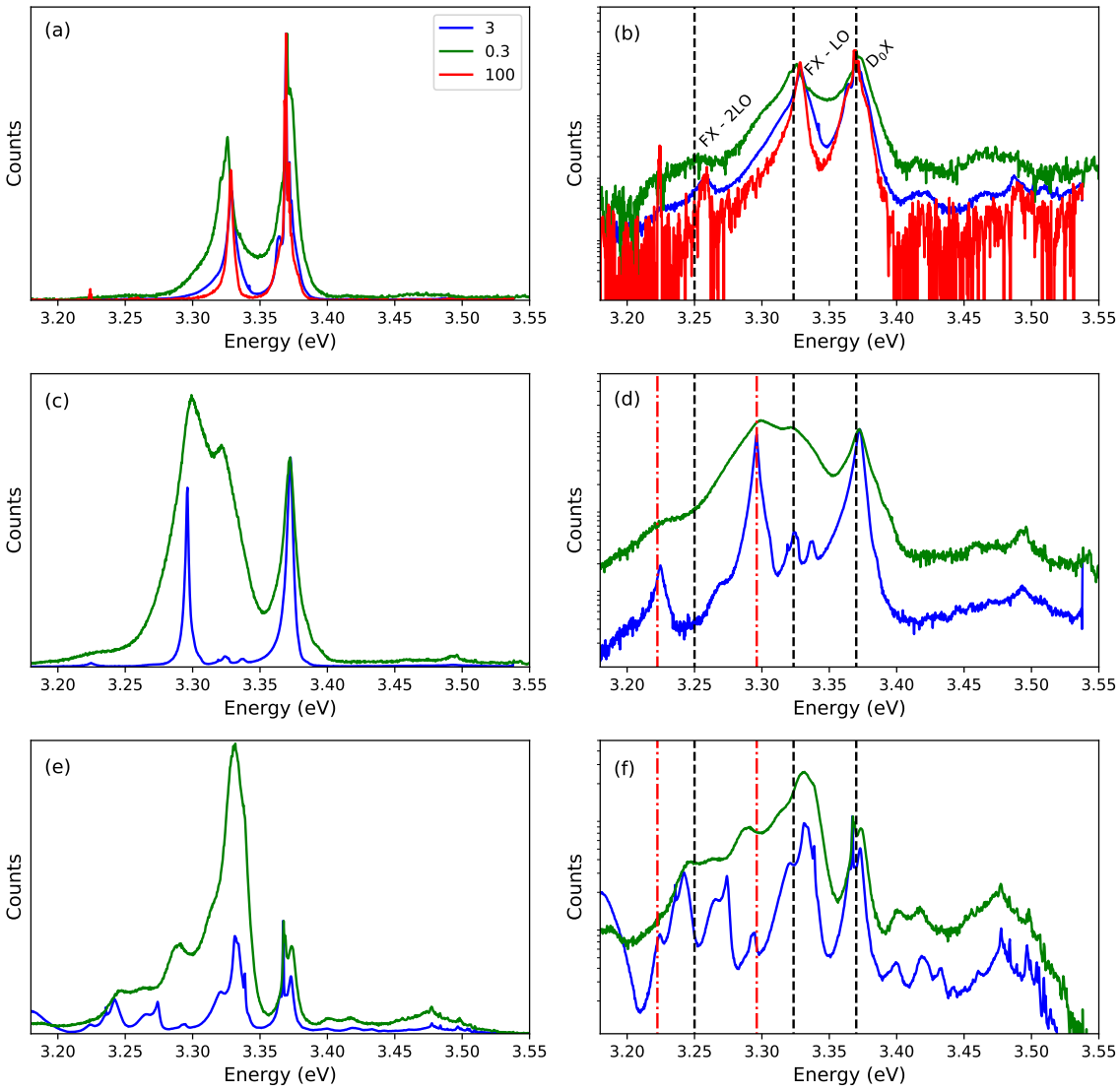

Figure 7.16: Power dependent PL spectra of three nanobelts where each pair (a, b), (c, d) and (e, f) show the same spectra on linear and logarithmic scales. Spectra are collectred with 100, 3 and 0.3 μW excitation beams corresponding to power densities of 3183, 95 and 9.5Wcm^{-2} which are shown in green, blue and red respectively. Spectra are recorded at 4.2 K. Black lines indicate the position of D^{0}X, FX - LO and FX - 2LO as determined from ensemble measurements on the same sample. Red dot-dashed lines mark the position of D^{0}X - LO and D^{0}X - 2LO as determined from the spectrum in (b).

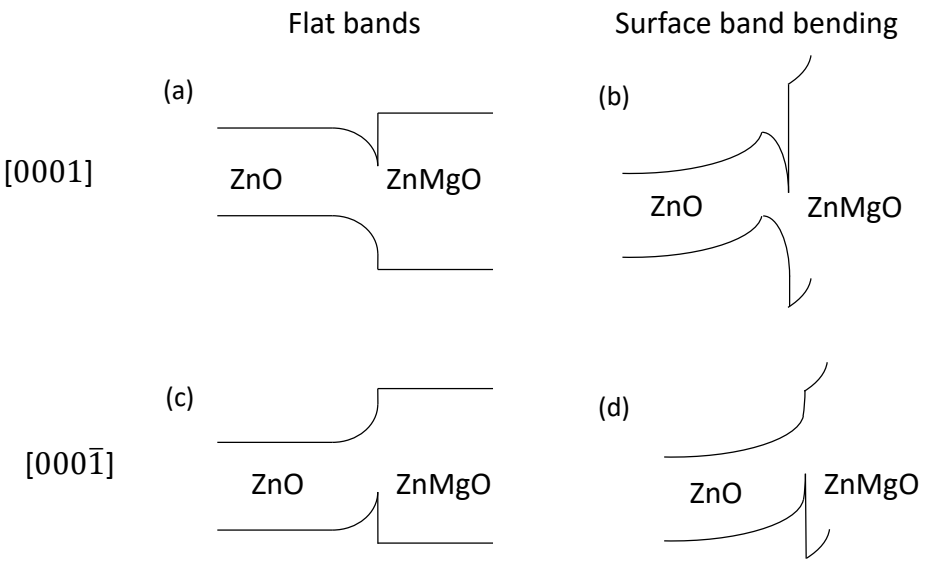

Figure 7.17: Schematics of band profiles at polar interfaces including the effects of band bending. (a, b) show the Zn-polar interface and (b, d) show the O-polar interface. (a, c) show the band profile with flat bands and (b, d) show schematically the addition of band bending.

Due to the crystallography of these nanobelts there are at least three qualitatively different faces in the nanostructure as shown in the schematic in Figure 7.8. The two side faces of the lamella are both polar, one is Zn polar and the other O-polar. The top and bottom faces of the lamella are non-polar. The band structure at each of these interfaces is different due to the combination of polarization and band gap mismatch at these different interfaces. Given that the luminescence processes depend on the local band structure, this means each of these faces may have a different luminescence characteristic. The Mg content of shells also varies between nanostructures meaning the polarization and band offset at these three distinct faces will vary between nanostructures. Furthermore, electronic bands bend upwards at the surface of ZnO nanostructures due to the n-type conductivity and negative surface traps. Band bending may further influence the band structure at these interfaces. In Figure 7.17 we show schematic band profiles at both Zn and O-polar interfaces between ZnO and ZnMgO in the presence and absence of surface band bending. Given all this, we expect that interfaces with a number of different band structures are present in each nanostructure and that there is variation between the nanostructures. More complex processes such as QCSE or quantum-well luminescence depend sensitively on the depth of the quantum well (which affects the energy of luminescence) and the spatial overlap of electron and hole wave functions (which affects the intensity of the transitions).

Therefore, it is not surprising that we see such variation between nanostructures and that single heterostructure nanobelt PL spectra may be hard to interpret.

There have been previous reports of luminesce arising due to QCSE at polar ZnO/ZnMgO interfaces. In [97] CL is recorded at polar ZnO/ZnMgO interfaces within nanowires At the polar interface in these nanowires there is QCSE luminesce at 3.24 eV (140 meV below the band gap) with approximately 1/7th of the intensity the ZnO peak. In [92] the same interface is investigated in thin film geometry. At 5 K QCSE is observed 40-50meV below the ZnO luminescence and the peaks here are also approx. 1/7th of the intensity of the ZnO peak. In the nanostructures investigated here there are un-explained peaks in Figure 7.16 at 100 meV below the ZnO peak with intensity $\sim$1/7th of the ZnO peak, in Figure 7.16 30 meV below the ZnO peak with intensity 1/25th the intensity. These peaks are consistent in energy shift and magnitude with previous measurements of QCSE but further measurements are required to be definitive in assigning their cause. These measurements could include CL measurements where luminescence is spatially resolved so that it is possible to determine whether the luminescence signal associated with QCSE comes from regions where QCSE is expected.

7.3 Conclusion

In this chapter we demonstrate the growth of ZnO/ZnMgO heterostructure nanowires and nanobelts in a two-stage process. By STEM-EDS mapping and ensemble photoluminescence we show that at temperatures above 700°C Mg diffuses into ZnO forming homogeneous ZnMgO. We show that by growing at a lower temperature this Mg diffusion does not occur and heterostructures with distinct ZnO and ZnMgO result. We demonstrate the growth of abrupt ZnO/ZnMgO nanowire heterostructures and show that these core-shell structures have improved PL, with sharper, more intense emission across the band gap and a less intense defect peak as compared to plain ZnO nanowires.

We show, for the first time, the growth of heterostructure nanobelts. We demonstrate the growth of nanobelt heterostructures by PL measurements of single nanobelts. At cryogenic temperatures, fine structure is seen in single nanowire PL, indicative of quantum confinement at the heterointerfaces. Future work should include characterisation of these nanobelts by STEM-EDS, an experiment we were unable to perform due to limited access to STEM facilities. Once well characterised, further experiments on these heterostructure nanobelts should focus on performing transport measurements showing a modification of the electron mobility in the nanowire. Further optimizing the growth of these heterostruc-

tures, possibly using patterned catalyst arrays, should decrease the variation in properties between nanobelts.

Chapter 8

Nanoscale Cathodoluminescence Mapping of Single Nanowires

In this chapter we report cathodoluminescence measurements on single nanowires, where CL properties are mapped in a scanning-transmission-electron-microscope (STEM). CL maps are collected on a number of ZnO nanowires. Different luminescence signals are spectrally resolved and spatially mapped showing the spatial dependence of CL signals within single nanostructures and allowing correlation of luminescence features with structural features in a single nanowire. This allows deeper understanding of luminescence data and demonstrates a powerful technique for investigating the properties of semiconductor nanostructures.

There are a number of techniques which may be used in (S)TEM. Many of these techniques may be performed simultaneously as CL is collected. This adds to the power of CL STEM as techniques such as EELS which give information about the local chemistry (i.e. oxidation states) may be correlated to CL signals.

8.1 Experimental Setup

The STEM-CL mapping was performed by Dr. Edward White of Imperial College London using a JEOL2100 field emission gun TEM which has a CL sample holder (Gatan Vulcan) and EELS diffractometer and is located at Brunel University, London. In STEM mode the microscope has a beam diameter of $\sim$2 nm. The electron beam interacts with the sample and excites electron hole pairs as described in section 4.2.5. This set up is shown schematically in Figure 8.1 (b).

Photons are generated by electrons interacting with the sample and are coupled into an

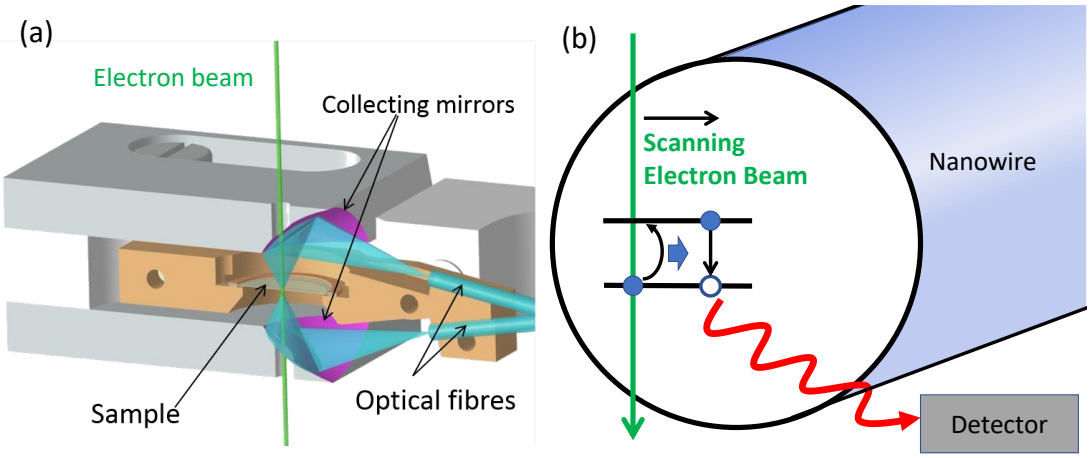

Figure 8.1: Schematic of the experimental setup (a) showing the mirrors coupling the light into optical fibres (figure reproduced from [151]) and (b) showing the excitation of electron hole pairs in the nanowire by the primary electron beam and their subsequent recombination.

optical fibre (Figure 8.1 a). The optical fibre leads out of the microscope to a spectrometer. In order to increase the collection efficiency, a number of mirrors are placed around the sample. A high collection efficiency is necessary in order to collect spatially resolved maps on a nano-scale as the total electron beam dose incident on the nanowires will limit the total measurement time since high doses cause beam damage to the sample.

ZnO nanowires are prepared for TEM as described in chapter 4. The nanowire coated TEM grid is loaded into the microscope where an 80kV primary electron beam with a beam current of 1 nA is used to probe the nanowires. A nanowire is located on the TEM grid. A raster is defined by splitting the area around the nanowire up into a number of pixels. These pixels will be larger than the size of the electron beam and so the electron beam then rasters across these CL pixels just as it rasters a sample in STEM. The beam will be incident on each pixel for a specified amount of time before moving on to the next CL pixel. As the electron beam rasters the pixel, CL data is collected and a CL spectrum for the pixel is recorded.

Despite high quality CL maps nominally requiring a long acquisition time (long exposures giving better signal to noise and high resolution maps containing more CL pixels), there are factors which limit the acquisition time for each CL map. First is a consideration of machine access (and user) time. There is a trade off between the quality of each map and the number of different nanostructures mapped given finite access to the equipment. There are also limits imposed by the measurement and processes occuring to the nanowire as it is exposed to the 80keV electron beam. The electron beam can cause beam damage

to the nanowire and the longer the nanowire is exposed to the electron beam the more damage is caused. Beam damage can either be sputtering of atoms from the surface by the electron beam, atomic displacement due to energy transfer in elastic collisions or structural damage from inelastic scattering [152]. This means there is a maximum dose (charge/unit area) which the nanowire may be exposed to. Given constant beam current this provides a limit to the total time of data acquisition. If this time is exceeded the measurement may cause significant damage to the nanowire and thus change the CL properties and ultimately destroy the nanowire. For each acquisition there is therefore a trade-off between spatial resolution and spectral quality subject to the constraint that the dose is limited to not cause (too much) beam damage to the nanowire being measured.

The stage may be cooled by liquid nitrogen and reaches a temperature of 103K during operation. This reduces the knock-on damage to the sample thereby increasing the maximum time which spectra may be acquired for. Cooling additionally affects the luminescence spectrum, reducing thermal broadening of luminescence peaks allowing different signals to be better distinguished and enhancing radiative recombination. However, inelastic scattering of primary electrons with the sample can cause heating in the sample [152] and the TEM grid has poor thermal conduction meaning it is hard to determine a precise sample temparature.

STEM CL was performed on a number of nanowire samples. In order to confirm that CL signals are robust and present in different samples STEM CL was performed on nanowires grown in two batches and these measurements were performed on different days. The nanowires were both grown with the same growth conditions, a 'normal' recipe where growth occurs using the first sample holder type at 750 °C with BEP Zn pressure of $\sim 3 \times 10^{-7}$ Torr and a 300W oxygen plasma with a flow rate of 3SCCM. A summary of nanowires measured by STEM CL is presented in table 8.1. These nanowires were rastered with different schedules, some optimised for spectral resolution and others for spatial resolution.

8.2 CL on nanowire A

Nanowire A (figure 8.2) is a tapered nanowire from Batch 1. CL maps are collected at the top of this nanowire. The map includes the area where the nanowire has broken off from the substrate (flat edge at the top of Figure 8.2). This is a nanowire grown on c-plane sapphire and as such grows along [0001]. The top broken face of this nanowire is therefore a polar face. Figure 8.2 is a HAADF (high angle annular dark field) image

Name	CL pixel size (nm)	Pixel Acquisition time (s)	Dose ($pAnm^{-2}$)	Batch	Collection date	Results section
Nanowire A	16	16	62.5	1	21/04/15	8.2
Nanowire B	10.2	3	28.8	2	29/05/15	8.3
Nanowire C	7.2	5	96.1	2	29/05/15	8.4

Table 8.1: Summary of nanowires discussed in this thesis. This includes information on the growth-batch of nanowires,and when the data is collected.

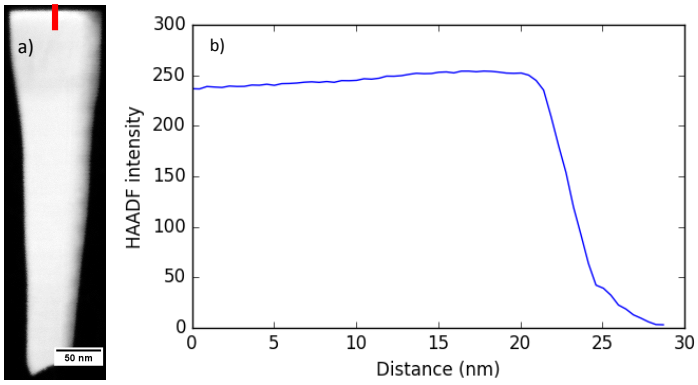

Figure 8.2: (a) HAADF image of nanowire A. The red line indicates where the intensity profile in (b) is taken. (b) HAADF intensity across top face of nanowire in (a).

in which contrast is proportional to thickness (for a constant chemical composition). As shown in Figure 8.2 (b) the HAADF intensity drops from its maximal value to almost zero intensity across ≈ 3 nm. This distance is similar to the dimensions of the electron beam meaning that the polar face is approximately parallel to the electron beam.

The raster for nanowire A is optimized so that CL pixels are comparatively large (16nm) and low noise spectra are collected. Each spectrum on nanowire A is collected for 16s.

8.2.1 CL spectra

CL spectra collected at three points on the nanowire are presented in Figure 8.3. The spectra are collected at a polar nanowire face (blue curve), a non-polar face (green curve) and from the nanowire core (red curve). The same spectra are plotted on a linear axis (Figure 8.3 a) and a logarithmic axis (Figure 8.3 b). Each spectrum is collected for the same time with the same electron beam parameters.

All of the CL spectra in Figure 8.3 have a (typically intense) peak corresponding to photons produced by pair recombination across the band gap of ZnO. In ZnO this

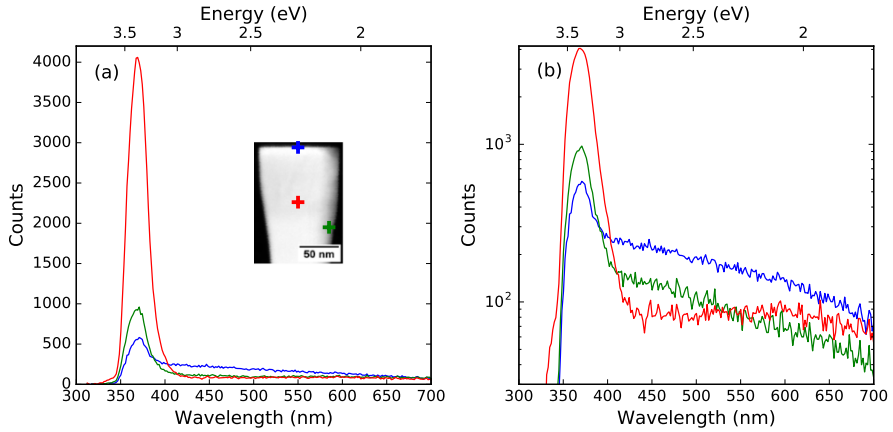

Figure 8.3: CL spectra on (a) linear (b) and logarithmic scales. Spectra collected at three points on nanowire A where the colours of crosses on the HAADF insert to (a) correspond to the plot colours of the CL spectra. The blue cross is at the polar top face of the nanowire, the red cross in the core of the nanowire and the green on a non-polar side. CL is collected at 100K.

recombination is mediated by excitons at room temperature (and below) due to the high exciton energy of ZnO (≈60meV [17]). These transitions are referred to as near band edge (NBE) emission. The NBE component is much stronger in the core of the nanowire than at the surfaces. Additionally the NBE component is stronger at the non-polar face than at the polar face of the nanowire. The naive expectation from the HAADF image (inset to Figure 8.3) is that the NBE should be stronger at the polar face as the HAADF is brighter meaning the nanowire is thicker and there is therefore more material to contribute to NBE emission. There is therefore some difference between the polar and non-polar sides which affects the NBE emission.

There are also counts in the spectra at energies below the band gap of ZnO. This luminescence is due to sub-gap states (defects) which mediate recombination. The sub-gap luminescence is more intense at the non-polar face than in the core of the nanowire despite the less intense HAADF signal at the edge than the centre (meaning there is less ZnO to contribute to this luminescence). This shows that the subgap luminescence is stronger at the surface of the nanowire rather than from the bulk as the CL intensity is not affected by the total volume of ZnO. The subgap luminescence is significantly more intense (greater by a factor of two to three) at the polar face of the nanowire than at the non-polar face. As sub-gap luminescence is stronger at the surface, the increased intensity of subgap luminescence could simply arise from the nanowire geometry. That is, the integrated surface area within the pixel at the polar face could be greater than that at the

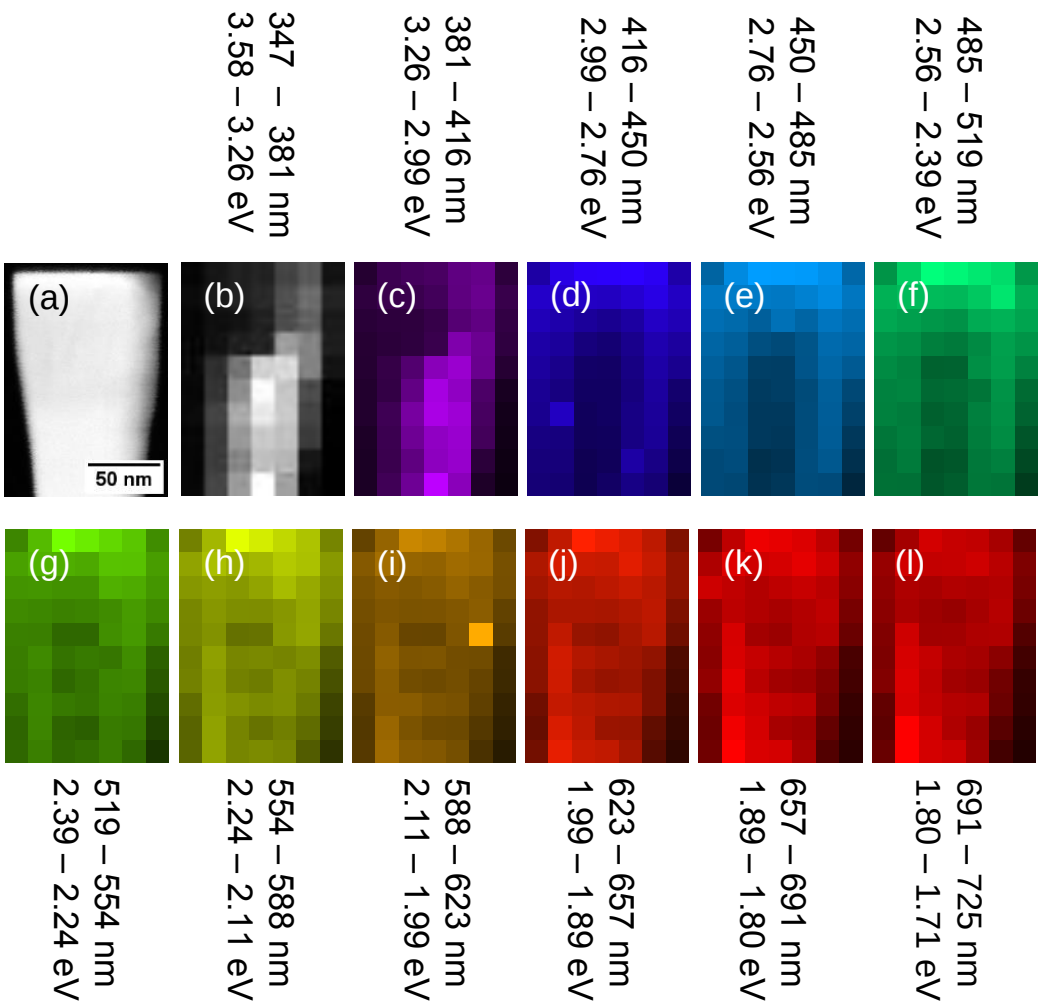

Figure 8.4: (a) HAADF STEM image of region of nanowire A mapped by CL. (b-l) Intensity maps of nanowire A. Each map is integrated over the indicated wavelengths, normalised to the most intense point in the map and colourized to the colour of the central wavelength within the integration range where that is within the visible spectrum and is grey-scale otherwise. Each normalised map is linear in intensity with normalised counts.

non-polar face. Without a 3d model of the nanowire this cannot be precisely determined, however, due to the pixel size being comparatively large compared to the nanowire radius. It is nevertheless unlikely that this discrepancy gives rise to as much as a factor of two. A more likely explanation is that sub-gap CL is stronger at polar faces than non-polar faces. This could be due to a greater amount of surface traps or as carriers excited within the nanowire more often diffuse to the surface due to electric fields caused by the polarization discontinuity at the vacuum interface.

8.2.2 CL intensity maps

In order to further investigate the spatial variation of luminescence in this nanowire we plot CL intensity maps. These maps are generated by integrating intensity across a fixed number of neighbouring wavelength bins at each pixel. Each map is then normalised by the most intense point in the map as shown in Figure 8.4. The CL intensity maps show a trend (repeated in nanowires B, C and others not presented in this thesis) where NBE emission (Figure 8.4 b, c) is most intense at the core of the nanowire and is suppressed at the nanowire edges. There is increased sub-band luminescence(Figure 8.4 d, i) at the surface of the nanowire. And deep-sub-band luminescence (Figure 8.4 j, l) is approximately uniform across the nanowire.

Maps of nanowire A show CL around polar and non-polar surfaces in the same nanowire. We can therefore compare the effects of polar surfaces on CL emission in a nanowire. As observed in individual spectra, subgap CL in the range 2.39 - 2.99 eV is stronger at the polar surface than at the non-polar surface. The NBE emission (Figure 8.4 b, c) is suppressed for approximately three pixels (48nm) in from the polar face, significantly further than suppression from non-polar faces. The sub-gap CL is increased in intensity not only in the top line of CL pixels where the electron beam is incident with the cleaved face, but also for two to three pixels into the nanowire where the electron beam is not incident with significant amounts of nanowire surface. This indicates that carriers excited up to 50 nm into the nanowire diffuse to the surface where they recombine (mediated by surface states). The diffusion in the nanowire seems to occur over longer distances towards the polar face rather than the non-polar face. This may be due to internal fields within the nanowire.

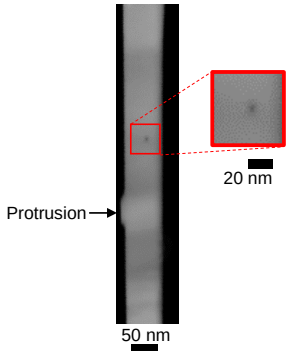

Figure 8.5: HAADF STEM of the section of nanowire B mapped by CL. In the HAADF image intensity is proportional to thickness (assuming constant chemical composition) and so the bright areas are the nanowire and the dark areas the nanowire surrounding/TEM grid. The approximately uniform intensity across the nanowire shows uniform thickness along the nanowire. The zoom shows a region with a 'dark spot' where the electron beam was held causing local beam damage.

8.3 CL on nanowire B

CL is collected with smaller CL pixels for nanowire B which is shown in Figure 8.5. Nanowire B was additionally intentionally damaged using the electron beam and chosen due to a protrusion visible in HAADF likely coincident with some form of defect in the nanowire. This allows us to map the CL variation across a region with increased defects with high spatial resolution. In order to achieve higher spatial resolution the raster has been optimised so that each spectrum is collected in a comparably short time (3 s/pixel). This means that each individual spectrum has a high noise floor.

A HAADF STEM image of nanowire B is shown in Figure 8.5. In order to understand

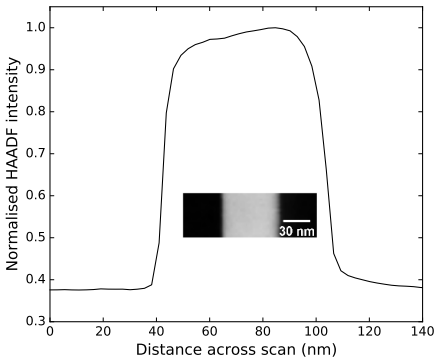

Figure 8.6: linescan of the normalised HAADF intensity in nanowire B. Inset is the HAADF image where these data were collected.

the spatial variation of CL, and relate it to nanowire morphology, it is important to have a clear idea of nanowire geometry. In the HAADF image the contrast corresponds roughly to nanowire thickness. A line-scan of the HAADF intensity across nanowire B is shown in Figure 8.6. Within the core of the nanowire the thickness is approximately uniform with only a slight increase across the direction perpendicular to the nanowire. The edges are comparatively sharp with an increase from minimum to maximum intensity in ≈ 5 nm which is less than a single CL pixel.

There are additional noteworthy features on the nanowire which can be seen in Figure 8.5: a protrusion on the side of the nanowire - likely coincident with some defects in the nanowire - and a dark spot half way down the nanowire which is shown in the zoom in Figure 8.5. The dark spot is where the primary electron beam of the STEM has been held for a $\sim$10 s to intentionally induce vacancies into the ZnO lattice.

Spectra in this map are systematically affected by an automated dark-count correction applied by the software used for data correction. Due to the low signal levels in our spectra this is particularly noticeable when comparing spectra - peaks with similar magnitude to the noise floor occur in all spectra (Figure 8.7 b). The techniques used in the subsequent analysis have therefore been chosen to not be adversely affected by a poor dark count correction and a high signal to noise ratio. The limitations imposed by worse spectra may be circumvented by some general strategies. Integrating across neighbouring energy bins reduces noise but also compromises spectral resolution. So long as the integrated energy range is small compared to the width in energy of CL features then we may improve the SNR and still resolve pertinent spectral features. Comparing the number of counts in different CL pixels at the same energy is not sensitive to poor dark count correction as at each energy the counts have been 'corrected' in the same way. We may also use fitting routines to consolidate high dimensional spectra into lower dimensional, lower noise data which is constrained by counts at a number of energies.

8.3.1 Cathodoluminescence and Photoluminescence spectra

In Figure 8.7 (b) we present CL spectra taken on nanowire B at locations shown by in Figure 8.7 (the colour of squares in (a) corresponds to the colour of lines in (b)). The three spectra are collected at: the core of the nanowire (red), close to the protrusion (green) and with an aloof beam condition (blue). An aloof beam condition is where the primary electron beam passes close to the nanostructure but does not directly impinge upon it [153, 154, 155]. The spectrum taken at the core has intense NBE emission (3.40 eV) and

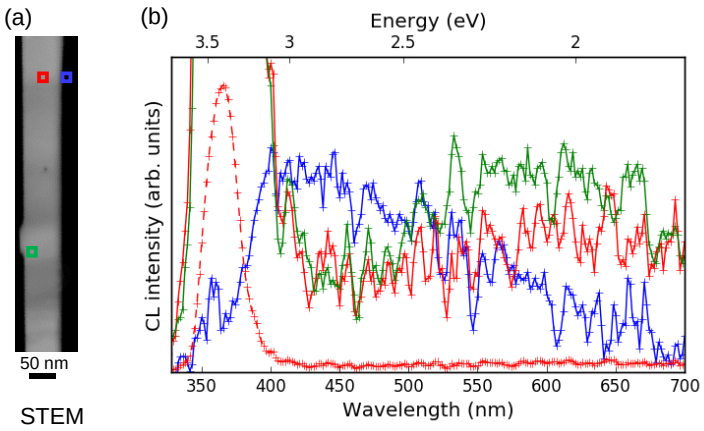

Figure 8.7: (a) Repeat of Figure 8.5 for reference. The location of spectra shown in (b) are indicated by coloured squares. (b) CL spectra on a linear intensity axis collected with electron beam at points indicated by squares of the same colour in (a). The spectrum in red is presented twice (once with a dashed and once with a solid line). The solid line is multiplied by 10 for presentational purposes. A 5 point moving average is applied to this data so that trends in CL spectra are visible and not masked by noise.

small amounts of emission at lower energies. The 3.40 eV NBE emission is consistent with band gaps widely reported for ZnO [156, 157, 158]. The spectrum taken close to the protrusion also has intense NBE emission but additionally has a peak in luminescence at sub-gap energies above the base-line counts. The aloof spectrum has no NBE emission but still contains CL counts at energies below the ZnO band gap. CL is generated in an aloof beam condition by the excitation of surface plasmons which subsequently decay into excitons. These spectra are different from those collected when the beam is incident with the nanowire which we interpret as evidence that electron-hole pairs are recombining at the surface of the nanowire via surface states.

A PL spectrum is collected at room temperature on the as-grown sample from which nanowire B is taken and shown in Figure 8.8. The PL spectrum is collected using a He-Cd excitation laser at 325 nm as described in 4.2.4. Two filters are used to collect data at different wavelengths (326-413 nm and 413-776 nm). The spectra are plotted on the same axis with no further processing (no normalisation/amplitude correction is applied). The PL spectrum provides complementary data to the CL. Intense NBE emission (376 nm/3.30 eV) is present but at slightly lower energy (longer wavelength) than the CL. We attribute this difference to the difference in temperature between the two measurements. CL is performed at 103 K whereas PL is performed at ≈300 K. An increase

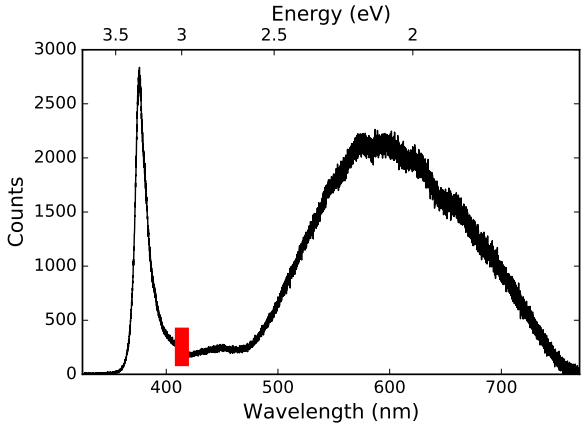

Figure 8.8: Room temperature photoluminescence spectrum collected on the as-grown sample from which nanowire B and C are taken. The spectrum is composed of two separate measurements where the red line indicates the break between the two measurements. This is necessary as different filters are required in order to measure in different parts of the UV/visible spectrum.

in the energy of NBE emission with decreasing temperature has previously been reported for ZnO with shifts in central energy of ≈ 70 meV between room temperature and 100 K [146]. There is also sub-gap luminescence in the PL measurement, an intense broad peak with a maximum at ≈ 600 nm and also a low intensity peak between the NBE emission and 600 nm emission. The 600 nm emission occurs at approximately the same wavelength as the increase in sub-gap CL emission around the protrusion and the low intensity peak is at similar energies to the aloof beam spectra.

The 600 nm emission in the PL is much more intense than the slight increase in sub-gap emission in the spectrum taken at the protrusion. This may be due to temperature dependence of this recombination pathway or due to the fact that CL is taken on a high quality nanowire whereas the PL spectrum spatially averages over high quality nanowires as well as other growth on the substrate which may be more strained (due to epitaxy with the substrate) or lower crystal quality. Alternatively different recombination pathways may be favoured due to the different excitation mechanism (80 keV electrons vs. ≈ 4 eV photons) or local pump fluence (electron beam confined to ≈ 2 nm spot laser spot confined to ≈ 1 μm spot). Differences between PL and STEM-CL spectra have previously been reported for SnO_2 nanowires [159].

8.3.2 Intensity Maps

In order to investigate the spatial dependence of luminescence with high spatial resolution (i.e. small CL pixels), we plot maps of integrated CL intensity (Figure 8.9 (b-k)). These maps show that CL intensity is not homogeneous - there is spatial variation in CL intensity and the spatial variation is energy dependent. NBE emission is stronger in the core of the nanowire but drops at the surface of the nanowire as seen for different nanowires grown and measured on different days (e.g. Figure 8.4). The NBE intensity is suppressed at the point where the electron beam was held at the nanowire inducing knock-on damage and at the base of the protrusion. Emission at energies just below NBE (2.76 - 2.99 eV) are particularly bright at the nanowire surfaces. At lower energies (2.11 - 2.56 eV) the intensity of emission is also increased at the nanowire surface. However, at these energies the base of the protrusion and the dark spot also have more intense emission - precisely where NBE emission drops in intensity. At the lowest energies shown (1.80 - 1.99 eV) there is no increase in intensity at the nanowire surface, although there is some increase in emission at the base of the protrusion and the beam damage. There is also low level uniform emission across the nanowire.

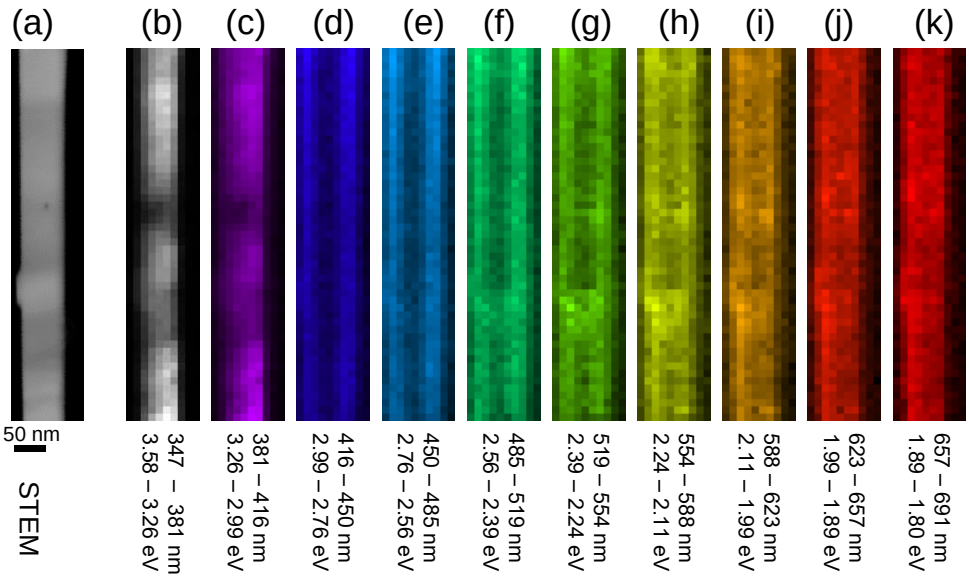

Figure 8.9: (a) HAADF of nanowire for reference repeated from Figure 8.5. (b-k) Integrated CL maps at indicated energy/wavelength windows. Each map is normalised to the most intense pixel within the map and colourised according to the wavelength of light at each bin.

The intensity maps may be qualitatively explained by the presence of four components

of luminescence: NBE emission, a component associated with nanowire surfaces, another component from defects and a final component which is approximately uniformly present across the nanowire and has a low energy. As spectral features are broad in energy each of these raw maps contains components originating from a number of overlapping components. In order to better understand the spatial distribution of luminescence we deconvolve the spectrum into constituent components.

8.3.3 Mapping Luminescence Processes

The deconvolution routine we perform assumes that the spectrum at each CL pixel is composed of a linear sum of different luminescence components. In order deconvolve that spectrum into its constituent components we: identify how many spectral components make up the CL spectrum; characterize the spectrum of each luminescence component and; fit the CL spectrum to a linear sum of the different components where the amplitude of each component is a free fitting parameter. The result of this deconvolution is a spatial map of different luminescence components, meaning we can map the strength of different luminescence processes across a single nanowire.

As mentioned previously, from intensity maps we determine there are four components to the CL spectra. This assumption may be subsequently tested by adding additional components to the deconvolution routine and considering the errors in the subsequent fits. If adding more components increases the total errors in the deconvolved fit parameters, then we are over-fitting the spectra and should use fewer components.

Spectral Characterization

In order to characterize the spectrum of each of the components we fit to both CL and PL spectra. We fit these spectra to Gaussians, this is a minimal model which makes no assumptions about the physical cause of luminescence. The functional form is given by

$$I(E) = I_0 \exp\Big(- \frac{(E - E_0)^2}{2\sigma^2} \Big) \tag{8.1}$$

where E_0 is a central energy and σ is the standard deviation of the Gaussian.

The Gaussian is a function of energy, whereas spectra are intensity counts collected at regular intervals of wavelength. In order to fit a functional form in energy to such a spectrum it is necessary to first perform a Jacobian transformation where

$$I(E) = \frac{\partial \lambda}{\partial E} I(\lambda) = \frac{-hc}{E^2} I(\lambda) \tag{8.2}$$

where the partial derivative of λ with respect to E is the Jacobian, h is Planck's constant and c is the speed of light. The negative prefactor in $I(E)$ can be ignored as it just indicates a direction of integration [160]. As the bins are relatively wide (in particular for CL), rather than applying the Jacobian transformation (strictly valid as $\delta E \to 0$) we instead divide the counts in each bin by the width (in energy) of the bin. This converts the units of the spectrum into counts/unit energy rather than counts/unit wavelength as they are collected. This approach is valid even in the limit that the width in energy of the bin is non-vanishing. Once this transformation is complete the spectra can be fit.

Accurately characterizing all of the spectral components by fitting to the CL spectra can be difficult due to the high signal to noise ratio in the individual spectra and the low intensity, overlapping components which make up each spectrum. However, the relative intensity of components varies across the hyperspectral map. Therefore, by choosing spectra from specific locations on the nanowire we may, in some instances, improve the SNR and reduce the contribution from overlapping components.

NBE is significantly more intense than other luminescence spectra so it is easy to fit to the NBE in the core of the nanowire where it has good signal to noise and is more intense than any other components which may overlap with it. Aloof spectra (where the beam is near the surface but not incident with the nanowire) do not contain overlapping components but have a spectrum which we identify as being characteristic of the nanowire surface. This CL is caused by surface states of the nanowire. This allows us to fit to the aloof spectra despite the comparatively low intensity. We refer to this surface luminescence as S luminescence. These fits are shown in Figure 8.10 (a) for NBE emission and (b) for an aloof spectrum. The fit parameters are given in Table 8.2.

The NBE fits well to a single Gaussian with central energy 3.40 eV. The S luminescence is broad and fit by a Gaussian with central energy of 2.53 eV. Broad signals from surface states have previously been reported from PL measurements with central energies of 2.4-2.54 eV [161, 162, 163] and 2.2 eV [164] as well as from CL measurements with central energies of 2.5 eV [165].

The data become more noisy at lower energies (particularly obvious in Figure 8.10 b) due to the transformation which is applied. In order to transform counts collected at equal wavelength bins are divided by the energy width of each wavelength bin. At lower energies (higher wavelengths) the energy width of each bin becomes smaller. Dividing by smaller numbers makes the adjusted counts larger - this amplifies noise already present in the spectra. The noise in the spectrum results in larger error bars on the spectral

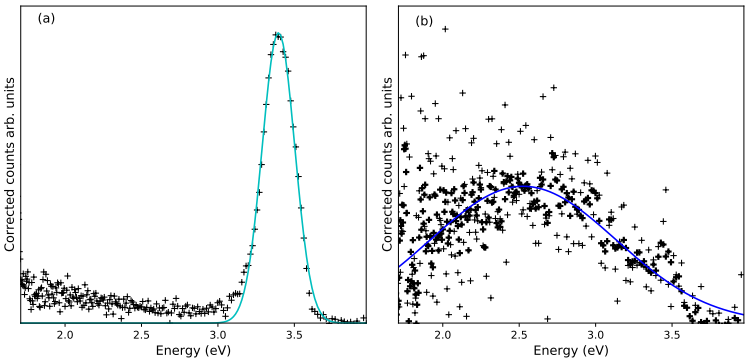

Figure 8.10: Fits to the CL spectra. (a) shows a Gaussian fit to a CL spectrum collected at the core of the nanowire after a Jacobian transformation. (b) A Gaussian curve fit to an aloof spectrum after a Jacobian transformation is applied to the data. Thicker crosses are the same data with a five point moving average applied.

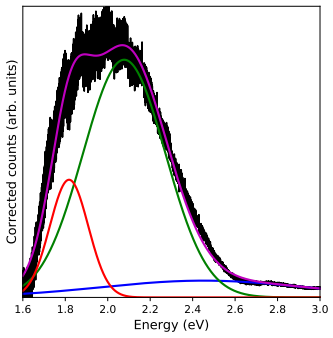

Figure 8.11: PL spectrum transformed into units of counts/eV fit by a linear sum of three Gaussians (blue, red, green lines). The magenta line shows a linear sum of the three Gaussians accurately reproducing the PL spectrum.

characteristics of the aloof spectrum given in Table 8.2.

Close to structural defects (the protrusion and beam damage on nanowire B) there is an increase in sub-gap luminescence around 600nm (similar wavelength to the high wavelength peak in the PL data). This is shown by the green line in Figure 8.7 (b). The peak in the CL has low intensity relative to other spectral features and at sub-gap energies there are several overlapping components. Therefore, in order to get high quality spectral information on these sub-gap peaks we fit to sub-gap luminescence of the PL. Assuming that this luminescence has the same physical origin as the CL spectrum, we can characterize the spectrum of this emission using the intense peak in PL and then use this spectral characteristic when analyzing the CL data.

The PL is fit at energies < 3 eV as shown in Figure 8.11. A number of overlapping

Component	PL/CL	E_0 (eV)	σ (eV)
NBE	CL	3.40 ± 0.01	0.106 ± 0.001
S	CL	2.53 ± 0.05	0.61 ± 0.05
DE1	PL	2.08 ± 0.01	0.194 ± 0.001
DE2	PL	1.82 ± 0.01	0.091 ± 0.001

Table 8.2: Fit parameters of different components which are subsequently used in deconvolution. The data (PL or CL) which is fitted to and the name used to refer to each component are given.

Gaussians are used to fit the PL spectrum. First, a low intensity peak just below the NBE (likely S) is fit in order to remove its contribution to the lower energy peaks. The residual data cannot be fit well by a single Gaussian. We therefore use two Gaussian profiles to fit to this spectrum (green and red curves in Figure 8.11). These two components are referred to as DE1 (green) and DE2 (red) and the fit parameters are listed in table 8.2.

Deconvolution

Having characterized the spectrum of the different luminescence components we can deconvolve the CL spectra into these components. This is done by fitting the CL spectrum at each CL pixel to a linear sum of these different Gaussians (Eq. 8.3) where the amplitude of each component is a fit parameter.

$$I(E) = \sum_i A_i f(E, E_{0,i}, \sigma_i) \tag{8.3}$$

The result of this fit routine is the spatial variation of each of these different components. This allows the spatial variation of these distinct luminescence processes to be mapped. The deconvolved spectra are presented in Figure 8.12 showing how the spectra can be accurately reproduced using the four components which we identify here even at points within the nanowire where the CL spectra differ significantly.

We can map the strength of the different components across the nanowire (Figure 8.13 b-e). These deconvolved CL maps clarify the relationship between the CL components and structural features that is obscured by component mixing in the raw integrated maps of Figure 8.9. The NBE component (Figure 8.13 b) is brightest along the central axis of the nanowire and is suppressed near the nanowire surface and up to ∼50 nm from the protrusion and beam induced defect.

Emission with central energies coincident with S emission (attributed to surface traps)

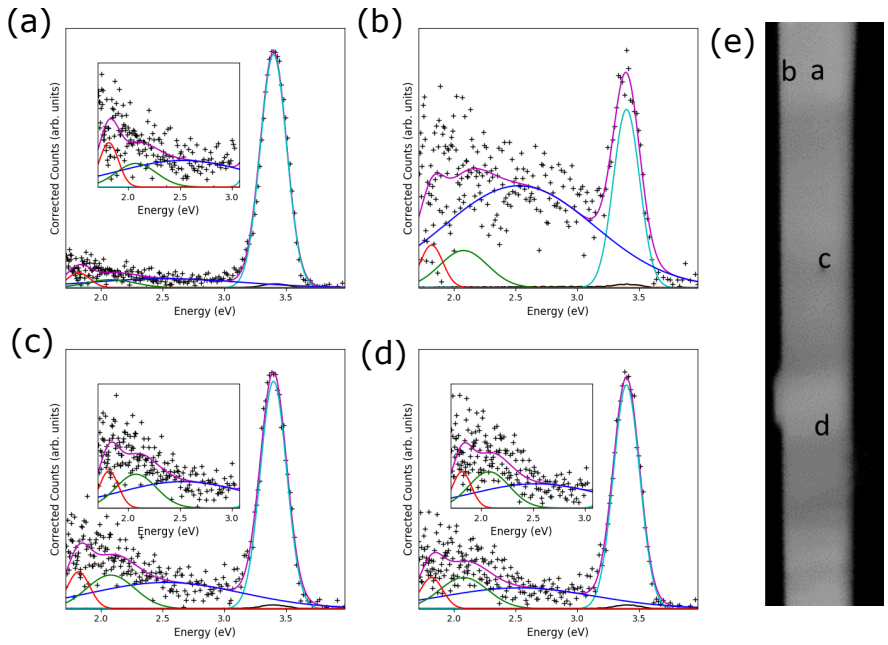

Figure 8.12: (a-d) Example CL spectra (black crosses) and the results of the deconvolution routine (magenta line). Individual components are shown; NBE in cyan, S in blue, DE1 in green and DE2 in red. (e) HAADF image of the nanowire, reproduced from Figure 8.5 with the location where each spectrum (a-d) were collected indicated on the nanowire.

have previously been assigned to adsorbed oxygen [166], Zn vacancies [165] and neutral oxygen vacancies [161]. The significant S intensity when the electron beam is aloof (nearby but not intersecting with the nanowire) is likely due to the excitation of surface plasmons which decay to excitons and subsequently recombine via surface traps in the ZnO. [167]

The yellow/green defect emission, DE1 (Figure 8.13 d), is strongest near the two structural defects in the nanowire, the same regions where NBE is less intense. Far away from structural defects the DE1 emission is non-zero, indicating the trap is likely present throughout the nanowire but at higher concentrations around structural defects. DE1 is centred at 2.08 eV and luminescence at this energy has previously been attributed to oxygen vacancies, consistent with vacancies induced by knock-on damage [168].

The orange/red defect emission, DE2 (Figure 8.13 e), has a central energy of 1.82eV and is approximately uniform across the nanowire with one small peak above the beam-induced knock-on damage region. Luminescence at this energy has been associated with Zn interstitials [169] although other work has questioned the stability of Zn interstitials in ZnO [170].

The suppression of NBE emission around defects is a measure of the exciton diffu-

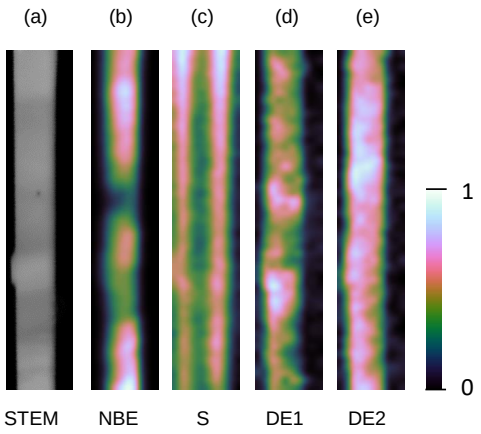

Figure 8.13: (a) STEM HAADF for reference. Maps of (b) NBE (c) S (d) DE1 (e) DE2 amplitude of each component in the deconvolution routine. Intensity in each map is normalised to the largest value in that map and then smoothed by applying a Gaussian blur of pixels with a radius equal to half the CL pixel size (5.1 nm).

sion length in this nanowire as 'dark' regions in NBE emission indicate the region where excitons may diffuse to a defect rich region and recombine via defect states rather than excitonically. Exciton diffusion lengths have previously been measured using a number of e-beam techniques [171]. Previous measurements of exciton diffusion length in single nanowires have shown similar orders of magnitude with a reasonable amount of scatter. 200nm diffusion lengths in 400nm diameter were reported for nanowires at 300 K with a diameter dependence in the diffusion length (shorter diffusion lengths for smaller diameter nanowires) [171] and a diffusion length of $\sim$ 200 nm in a $\sim$ 50 nm nanowire at 5 K [172].

Given the nanowires approximately uniform thickness across the direction perpendicular to the nanowire axis (Figure 8.6), the strong surface suppression of NBE cannot be a thickness effect, and must be related to competing recombination mechanisms. Given that S is brighter across the nanowire surface and NBE is suppressed we infer that the process giving rise to S luminescence (luminescence via surface traps) competes with NBE emission close to nanowire surfaces. Similarly, alternative recombination routes explain the NBE suppression at the defects. The suppression of NBE emission shows that the exciton lifetime is longer than the lifetime associated with recombination across these defects.

Transient absorption spectroscopy (TAS) on ZnO has shown rich recombination dynamics which vary even within single tapered nanowires [173]. In tapered nanowires, trap lifetimes are short at tips and longer in the core, due to the effects of cross section and available surface. Spatial resolution in single nanowires is achieved using confocal mi-

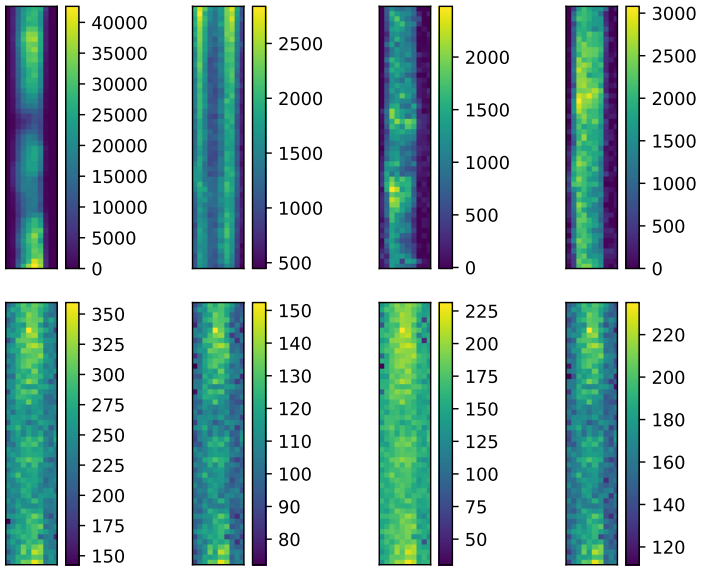

Figure 8.14: Reproduced maps of deconvolved components (top row) with NBE, S, DE1 and DE2 from left to right. The corresponding errors from the fit to Equation 8.3 (bottom row) with NBE, S, DE1 and DE2 from left to right.

croscopy on large nanowires ($\sim 2\mu$m maximum diameter and $> 10\mu$m long). These data are consistent with surface traps having shorter lifetimes than bulk traps as indicated by our measurements. The same work showed the lifetime of NBE emission was much shorter than the lifetime of trap states. Despite this, our measurements show that traps suppress NBE emission which may indicate that although trap lifetimes are long, carrier trapping occurs on short time scales comparable to or faster than NBE emission.

We calculate the errors on the amplitudes of each luminescence process when fitting to Equation 8.3 and plot these in Figure 8.14. The errors in the amplitude are much lower than the absolute amplitude of the signal. Typically, the errors are less than 10% of the signal and are much lower at regions of interest where the amplitude of the signal is high. Adding additional peaks to fit the broad defect peak in the PL increases the errors relative to signal in the deconvolved maps due to over-fitting the spectrum (Figure 8.15). The NBE and S components remain largely unchanged but the magnitude in errors increases from $\sim$225 for each component to >250 for each component due to the addition of an extra component. This further justifies the choice of four components for deconvolution.

8.3.4 Non-radiative recombination

As well as intensity from specific components of CL we can map the total CL intensity produced. By considering the total counts we can understand the degree of non-radiative

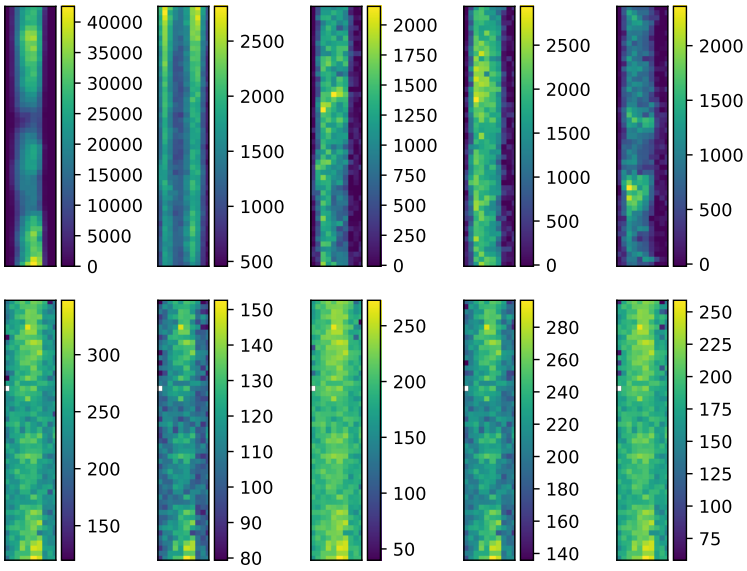

Figure 8.15: Deconvolved maps (rop row) with corresponding errors (bottom row) where the PL peak has been fit to the sum of three Gaussians.

recombination occurring in the nanowire. When the electron beam excites an electron-hole pair in the nanowire, that pair may combine radiatively (resulting in photon emission) or non-radiatively (no photon). Therefore areas with lower total counts are areas where non-radiative recombination is occurring at elevated rates. This assumes that the electron beam is generating electron-hole pairs uniformly across the nanowire. We believe this assumption to be reasonable given the approximately uniform nanowire thickness shown in Figure 8.6.

In Figure 8.16 (b) we plot the integrated CL intensity across all energies (3.97 eV - 1.71 eV) with a HAADF STEM image for reference (Figure 8.16 a). This shows that non-radiative decay is not constant across the nanowire. There is a suppression of total luminescence intensity at nanowire surfaces and around the protrusion. The largest suppression is at the area damaged by the electron beam. These are all areas where there is increased sub-gap luminescence. At surfaces there is an increase in S luminescence whereas at the protrusion and the beam-damaged region there is an increase in DE1. There are therefore other non-radiative recombination mechanisms spatially coincident with sub-gap radiative processes.

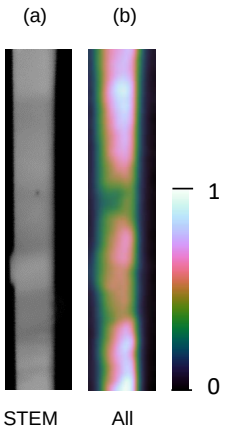

Figure 8.16: (a) HAADF STEM for reference. The nanowire growth direction is vertically upwards. (b) Intensity integrated across all CL energies. The same Gaussian smoothing algorithm as used for deconvolved maps in Figure 8.13 is applied with a radius equal to half the CL pixel size (5.1 nm).

8.4 CL on nanowire C

We also consider CL maps collected on nanowire C which is shown in Figure 8.17 (a). This nanowire has a gold catalyst nanoparticle still attached (the nanoparticle likely fell off in sonication for nanowires A and B). It is also slightly tapered with a thicker base than tip as is quite common for nanowires grown by this technique. This allows us to map the effect of the gold nanoparticle on luminescence. This is pertinent as gold is the most common metal catalyst for VLS nanowire growth [174] and there have been number of experiments where nanowires are decorated with metal nanoparticles affecting band bending at the surface [125, 175].

8.4.1 Intensity Maps

As done for previous nanowires, we show maps of CL intensity at the indicated wavelengths (Figure 8.17) with a CL pixel size of 7.2nm. In the ZnO nanowire far from the gold nanoparticle the trend in luminescence is very similar to that shown in previous nanowires with NBE intensity confined to the core (Figure 8.17 b-c) and sub-gap luminescence at the edges of the nanowire (Figure 8.17 d-g). The gold catalyst nanoparticle on the tip of the nanowire emits at energies below the bandgap of ZnO (Figure 8.17 d-k). This we attribute to surface plasmons of the gold nanoparticle as has previously been observed [176].

Similar trends in luminescence are seen for nanowire C as other nanowires. NBE

emission is confined to the core of the nanowire and suppressed at edges. S luminescence is brightest at nanowire edges and at low energy DE2 is present uniformly across the nanowire. No structural defects are obvious from the HAADF image in nanowire C (Figure 8.17 a) and, as expected if DE1 is caused by defects, no areas of increased DE1 luminescence are present. Nanowire C differs from nanowire A and B by the presence of the gold nanoparticle - therefore it is interesting to compare the CL intensity around the gold nanoparticle. S and DE2 luminescence are unaffected by the gold nanoparticle as far as can be determined from these relatively low intensity maps. However, close to the gold nanoparticle the NBE intensity is significantly suppressed (Figure 8.17 b-c).

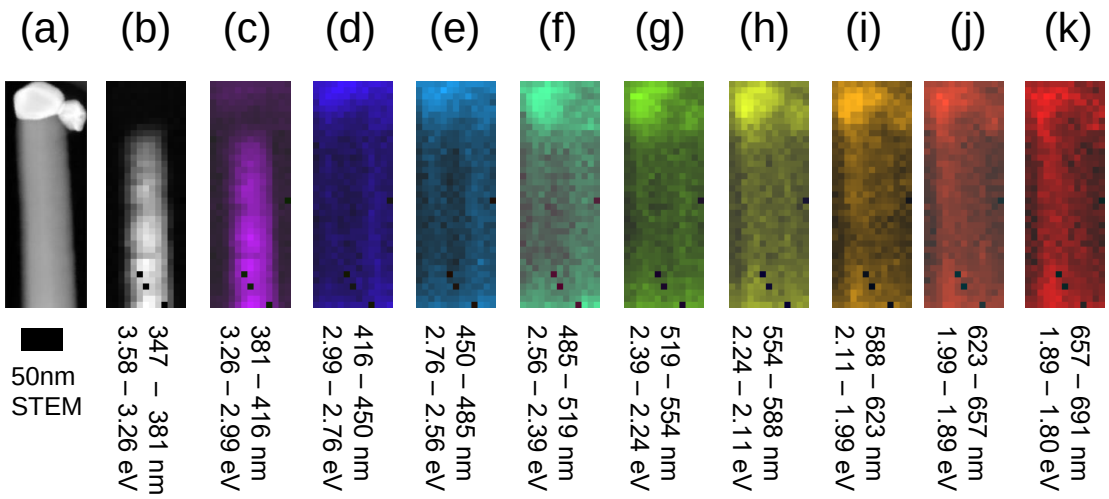

Figure 8.17: (a) STEM HAADF of nanowire. (b-k) Integrated CL maps at indicated energy/wavelength windows. Each map is normalised to the most intense pixel within the map and colourised according to the wavelength of light at each bin where that wavelength falls within the visible spectrum. Otherwise a grey scale is used.

8.4.2 NBE suppression at gold nanoparticle

In order to investigate the suppression of NBE intensity around the gold nanoparticle we integrate the NBE CL intensity (3.10 - 3.65 eV) across the central three CL pixels of the nanowire (Figure 8.18). The core of the nanowire is where NBE emission is strongest and so we may track changes in NBE emission moving away from the gold nanoparticle.

At the gold nanoparticle the NBE intensity is zero. Below the gold nanoparticle (red dashed line Figure 8.18) the NBE intensity starts to increase rapidly. This increase is approximately linear for $\approx$ 30nm (blue dashed line Figure 8.18) before the rate of increase drops to a smaller value which is approximately constant along the nanowire. The small

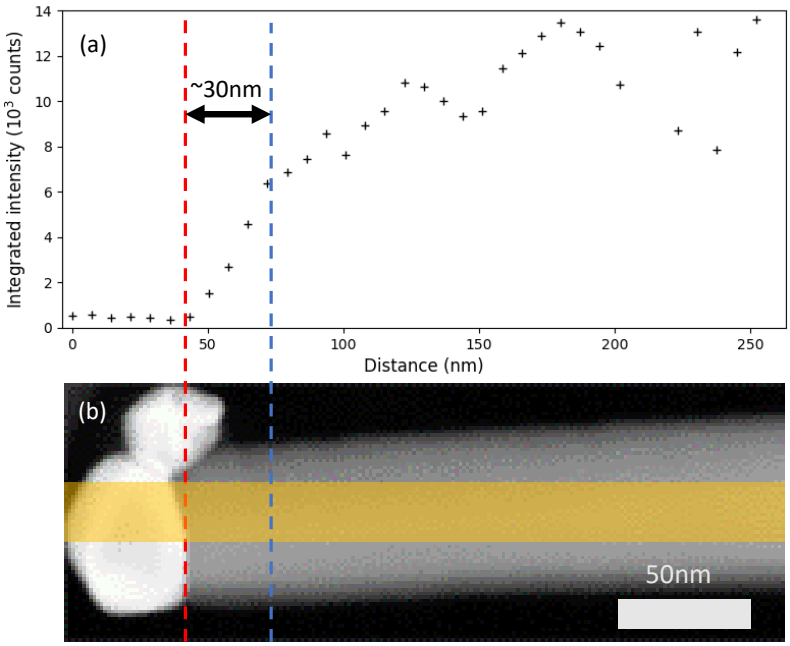

Figure 8.18: (a) CL intensity integrated from 3.65 eV (340nm) to 3.10 eV (400nm) along the axis (central 3 CL pixels) of nanowire C. (b) HAADF image of the nanowire for reference. The red dashed line shows the base of the gold nanoparticle. The blue dashed line shows the kink in CL intensity between nanoparticle limited CL and a gradual increase in CL due to nanowire tapering. The semi-transparent yellow box shows the region where the CL has been integrated.

increase is likely due to the tapering of the nanowire (it is thicker at the bottom and therefore has higher CL emission).

The linear increase in luminescence intensity shows the effect of the gold nanoparticle upon the local NBE CL. For $\approx$ 30nm the NBE CL is suppressed. We attribute this to band bending in the nanowire due to a Schottky contact between the gold and the ZnO [125]. This band bending cause internal fields within the nanowire which causes the separation of electrons and holes in the nanowire. When electrons and holes are separated they may not recombine radiatively and will find alternate recombination paths. The interfaces between ZnO nanowires and gold catalyst nanoparticles have been previously studied by electrical transport. It was shown that gold nanoparticles with lateral dimensions similar to the width of the nanowire, the growth of which they catalysed, act as rectifying contacts [177]. This is consistent with the measurements presented here where band bending at a rectifying contact would cause carrier separation and suppress CL.

8.5 EELS

One of the most powerful things about STEM-CL is that it is possible to perform a number of additional STEM techniques simultaneously. An example is the collection of HAADF maps where thickness information is encoded as has been discussed previously. Energy electron loss spectroscopy (EELS) is a powerful analytical technique where spectroscopy is performed on electrons transmitted through the sample.

Different energy ranges of electrons contain information relating to different physical processes. EELS may either be performed by analysing electrons which have lost a small amount of energy (low loss or valence EELS) or electrons which have lost significant energy (high loss or core-shell EELS).

Low loss EELS contains information about transitions between valence states excited in the sample as well as low energy excitations such as plasmons or inter-band transitions caused by electrons in the primary beam. The low loss spectrum is dominated by a zero-loss peak (ZLP) which is composed of electrons which have lost no energy (i.e. passed through the sample without any inelastic scattering). This intense peak can hide the lowest energy excitations and so the better monochromated the beam, the lower energy the signals which may be observed.

High loss EELS contains information about core-shell transitions excited in the sample and can contain information about the chemical composition of the sample. EELS measurements can in fact be performed with the energy resolution matching (or beating)

that found in synchrotrons [178, 179] and can not only give information about elemental composition but also probe information about the oxidation states of ions within samples.

8.5.1 Low loss EELS - excitation mechanisms

In CL photons produced by electron-hole pair recombination are collected and measured. Electron hole pairs need not be directly excited by the primary electron beam but could be the result of the decay of some other excitation induced by the primary beam. These excitations may be probed using low loss EELS. In EELS we probe the loss of energy of electrons after interacting with the sample. This allows us to probe low energy interactions.

We present a low loss EELS spectrum in figure 8.19. The intense peak centred at 0eV seen in figure 8.19 (a) is the zero loss peak which is caused by electrons passing directly through the sample without interacting and have consequently lost no energy. If the electron beam were directly exciting electron hole pairs then there would be a peak at energies around the band gap of ZnO. The zoom of the low energy loss regime in figure 8.19 (b) shows what might be a low intensity peak (just above the base line) at energies corresponding to these energies (3.4eV). The comparatively low intensity of the peak shows that this is not the dominant excitation mechanism. There are additional peaks at 9.1eV, 18.05eV and 34.5eV including some shoulders to these peaks. The peak at 9.1eV has been correlated to the surface plasmon in ZnO [164], [180]. The most intense peak at 18.05eV is caused by the excitation of bulk plasmons in the nanowire [164]. Additional peaks predominantly seen as shoulders are attributed to transitions of core-shell electrons to the conduction band. We conclude that the primary mechanism of energy transfer from electron beam to sample is by the excitation of plasmons in the ZnO. There is then some decay from plasmons to electron hole pairs which recombine and emit photons.

As well as providing valuable information on excitation mechanisms in STEM CL, this is an important proof of principle experiment for future measurements as we demonstrate the simultaneous collection of STEM CL and STEM EELS spectra. In future experiments high quality EELS data may be correlated with CL data for further materials insights.

8.6 Conclusion

A number of CL maps have been collected on different nanowires. Common to all nanowires mapped is intense NBE emission at the core of the nanowire and an increase in sub-gap luminescence at the nanowire surface. Where defects are present sub-gap luminescence increases around the defect.

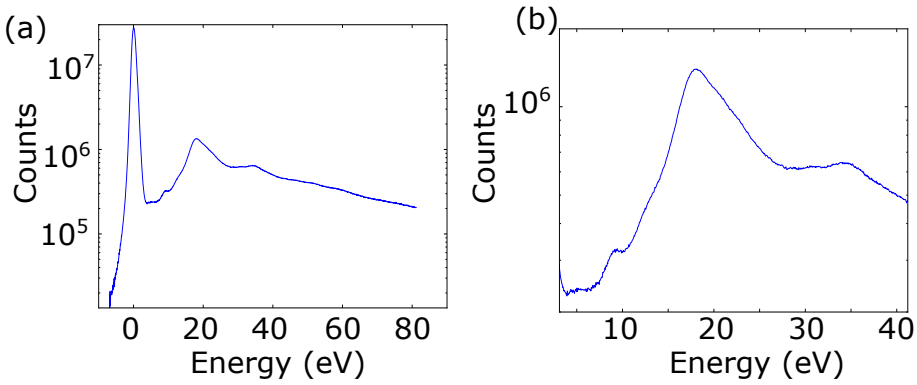

Figure 8.19: Low loss EELS collected simultaneously with CL. In (a) the whole spectrum is shown whilst (b) higher energy transitions (excluding ZLP). At 10 eV is the ZnO surface plasmon and 19 eV is the ZnO bulk plasmon.

Polar and non-polar surfaces can be distinguished by their CL response; polar surfaces have more intense sub-gap luminescence than their non-polar counterparts. Additionally a polar interface between nanowire and vacuum is different from a polar interface between nanowire and gold. At gold/nanowire interfaces no sub-gap CL is emitted, although NBE is suppressed as in the nanowire/vacuum interface.

By fitting to CL and PL spectra CL maps may be deconvolved allowing components of luminescence to be plot across the nanowire. Mapping these components within a single nanowire is in and of itself interesting as we may determine where each component comes from within a nanowire, which physical features correlate to which spectral features and gain a nanoscopic understanding of luminescence in a nanowire. This spatial information may aid future simulations of ZnO nanostructures. For example band structure calculations may help understanding of transport or photocatalytic properties. Furthermore, by examining the relative strengths of components within the nanowire we may infer things about the interplay of different luminescence processes where different recombination mechanisms compete for minority carriers which are mobile within a nanowire.

In Figure 7.7 we show that coating a ZnO nanowire in a ZnMgO shell reduces the intensity of the broad PL peak at lower energies. This is interesting as the CL analysis in this chapter shows that this peak is not directly caused by the surface states of nanowire (which would be passivated by the ZnMgO shell). Therefore, passivating the nanowire effects the defects within the nanowire as well as at the surface. This is likely due to decreased band bending (and corresponding electric fields) within passivated nanowires makin charger defect migration less likely.

EELS spectra are recorded simultaneously as CL is collected and this gives information

about the excitation mechanisms in STEM EELS. In future work EELS signals collected simultaneously with CL signals could be correlated allowing the assignment of CL signals to chemical complexes identified either in low loss or high loss EELS. This will be aided by developments in electron monochromator technology - electron beams with sub 10 meV energy resolution are being developed [181].

Chapter 9

Superconducting Microwave Resonators on Epitaxial ZnO

9.1 Motivation

Hybrid quantum devices which couple different forms of quantum excitation allow fundamental scientific exploration as well as offering attractive technological features in particular for quantum computing applications. A strategy which has had significant success is coupling quantum excitations to superconducting circuits - either superconducting qubits or superconducting resonators. For example superconducting circuits have been coupled to impurity spins in silicon [182] and diamond [127], collective excitations such as magnons in ferrimagnets [183] and, most pertinently for this chapter, phonons or collective mechanical excitations [184].

Many types of mechanical oscillators have been coupled to superconducting circuits such as membranes [185], beams [186] and recently numerous experiments with surface acoustic waves (SAWs) [187, 184, 188]. Surface acoustic waves are attractive collective mechanical oscillations to use in a hybrid circuit as they may be coherently excited at frequencies of several GHz which propagate along the surface of the substrate at the speed of sound in the material. Interdigitated transducers (IDTs) are used to excite SAWs. They are pairs of electrodes with a series of interlocking 'fingers' of electrodes. If IDTs are fabricated on a piezoelectric substrate, applying a potential difference to the two electrodes induces a mechanical deformation in the underlying substrate. If the electrodes are periodic, then the mechanical deformation is also periodic. Therefore, by fabricating IDTs on a piezoelectric substrate it is possible to excited SAWs with a wavelength $\lambda = 2d$ where d is the pitch of fingers in the IDT.

Given the speed of sound in relevant single crystal substrates (typically 2,000-3,000 ms^{-1} [14]), and fabrication limits due to EBL processing (finger pitch $\geq$100 nm) this gives a SAW frequency of $\nu = c/\lambda = c/2d \leq 10$ GHz where c is the speed of propagation of the SAW. This means that the thermal occupation of SAW modes at dilution fridge temperatures is negligible (10-30 mK = 200-600 MHz). SAW cavities therefore only exhibit zero-point fluctuations and experiments in which mechanical oscillations are in the quantum regime are possible. It is important to note that quantum optomechanical experiments have allowed lower frequency mechanical oscillators to reach the quantum regime of only a few phonons by active side-band cooling of the mechanical resonators [185]. For higher frequency SAWs this active side-band cooling is not required.

The necessary components for a SAW device are a smooth piezoelectric substrate which can be used to fabricate electrodes. These requirements are quite simple and thus readily allow piezoelectric-only devices to be fabricated. In [188] a superconducting qubit is fabricated on a piezoelectric substrate and is read out mechanically instead of electronically as is standard practice for superconducting qubits. It is necessary to read the qubit mechanically because the piezoelectric substrate necessary for SAW devices is detrimental to the superconducting architecture conventionally used in circuit quantum electrodynamics (cQED). This is because radio-frequency (RF) superconducting elements couple to the piezoelectric substrate, providing additional loss mechanisms [189]. This means that whilst some experiments where resonators are fabricated onto piezoelectric substrates have been successful [187] no long coherence-time qubits have been demonstrated. For examples, in [187] a relaxation time, $\mathrm{T}_1 = 46$ ns is found which compares poorly to the state of the art which is tens of microseconds. Anecdotal accounts detail how coplanar-waveguide (CPW) resonators have had quality factors of 50 on lithium niobate due to piezoelectric losses.

A strategy to avoid this would be to use epitaxial films of piezoelectric material on a non-piezoelectric substrate. The epitaxial film could be either selectively grown, or selectively etched meaning that piezoelectric zones could be created on the chip. High quality superconducting electronics could be fabricated on non-piezoelectric zones where there is no coupling, and thus loss, between the RF superconducting electronics and mechanical modes of the substrate. Acoustic devices could be fabricated on piezeoelectric regions of the sample with electrodes straddling the two allowing these to be coupled.

Regions of piezoelectric films on non-piezoelectric substrates are used with AlN grown on sapphire in [184]. In [184] the T_1 is 6 μs indicating this strategy may be more suitable for long coherence time qubits. In this work the qubit is only coupled to longitudinal

Fabry-Perot modes of a disk of piezoelectric material which are not suitable for propagating quantum information. Also, the qubit is measured in a 3d cavity which strongly suppresses losses from the qubit and hence increases T_1. This is not compatible with multiplexed qubit geometries where on-chip superconducting microwave resonators act as cavities coupled to the qubits. Indeed recent experiments where superconducting qubits are coupled to surface acoustic waves have used separate chips of sapphire (for qubits) and lithium niobate (for SAWs) with wire-bonds linking the two chips [190].

In future devices quality superconducting electronics could be fabricated on the non-piezoelectric areas, and coupled to SAW devices fabricated on piezoelectric areas. It has been suggested that transmitting quantum information in slowly propagating phonons could be used in order to implement feedback mechanisms [14] where SQUIDs are used to tune qubits in and out of resonance with the propagating quanta based on the outcome of measurements. Superconducting qubits fabricated on non-piezoelectric areas of the substrate could have long coherence times allowing coherence to be maintained as the SAWs propagate. It will take a SAW travelling at 3000 m/s 3 μs to travel 1 cm (a typical chip size). This is much longer than reported coherence times of qubits fabricated on piezoelectric substrates. A sketch is shown in Figure 9.1 where a fast flux line is used to tune a qubit in and out of resonance with a SAW cavity based upon the outcome of measurements either on the first (or other) qubits.

The substrate material used to fabricate superconducting circuits (qubits and resonators) strongly impacts the quality of the subsequent superconducting device. Typically for high quality resonators or long coherence time qubits either intrinsic silicon or sapphire substrates are used. At low power, and low temperatures, as is necessary for qubit operation, the limiting factor for resonator technology is coupling to two level systems (TLS) intrinsic to the sample. Qubits also couple to TLS which introduce noise processes and decoherence and have limited the coherence time of qubits to ~ 100 μs. A full understanding of TLS is still to be developed but recent experiments have started to uncover the chemical nature of some TLS on specific substrates; hydrogen from disassociating water on the surface of sapphire has been identified as a major cause of TLS [191]. The removal of these by thermal annealing has been shown to decrease noise in superconducting resonators [134].

We propose a technology where epitaxial ZnO is grown onto sapphire substrates and subsequently partially etched away. This would allow for piezoelectric zones on sapphire substrates which are compatible with long coherence-time qubits. However, the growth

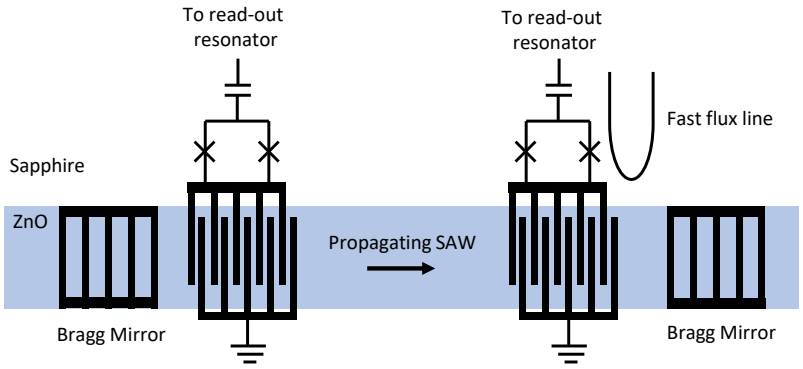

Figure 9.1: Schematic of a possible chip layout allowing the implementation of feedback into a SAW-based quantum circuit. The blue zone indicates the epitaxial ZnO creating piezoelectronic areas. Otherwise the substrate would be sapphire. Bragg mirrors define a SAW cavity on the piezoelectric region of the substrate. The interdigitated fingers galvanically contacted to each of the qubits allows them to interact with SAWs in the cavity. The fast flux line would be used to tune the second qubit in and out of resonance with the SAW cavity based on the results of measurements allowing feedback based on the measurement of the first (or other) qubits.

and subsequent etching of ZnO on sapphire could modify the sapphire or the surface of sapphire, introducing TLS and making the substrate less suitable for long coherence time qubits. It is therefore important to carefully characterize superconducting elements fabricated on such a substrate in order to determine that they can be fabricated without introducing significant additional losses at low r.f. power.

9.2 Materials Growth and Characterization

We grow epitaxial ZnO films on a-plane sapphire since ZnO grows with [0001] normal to this substrate [79]. We characterize these ZnO films by XRD and AFM and use these samples as substrates for further superconducting resonator fabrication. Films are grown at 600°C with a Zn flux of $\approx 3 \times 10^{-7}$ Torr using an oxygen plasma power of 300 W and an oxygen flow of 2 SCCM.

XRD of an example film is shown in Figure 9.2. The $2\Theta/\omega$ scan in Figure 9.2 (a) shows peaks from the film and the substrate. Peaks in ZnO match reflections from (0002) and (0004) showing that the films are growing with [0001] normal to the surface of the substrate as expected for a-plane sapphire.

Shallow angle x-ray reflectometry measurements (Figure 9.2 b) show intensity oscilla-

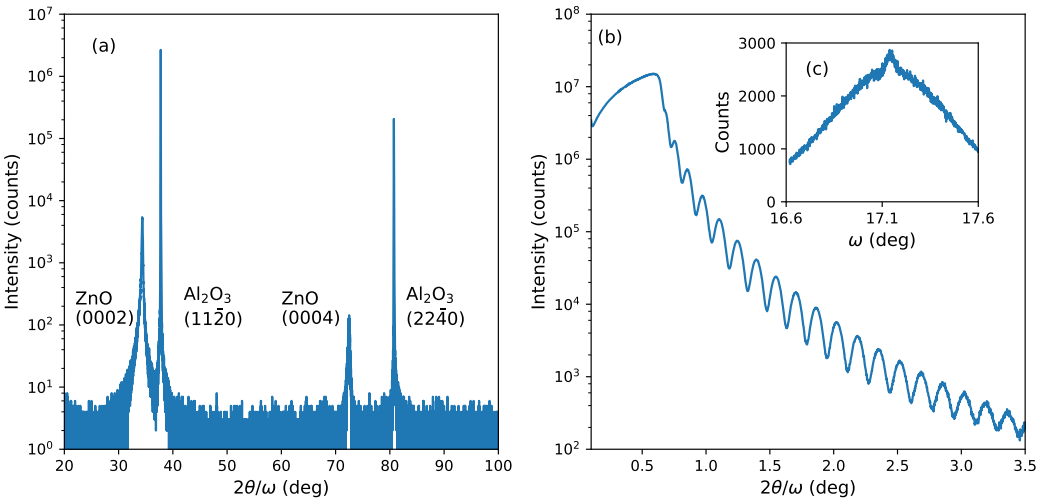

Figure 9.2: XRD of example ZnO film. (a) $2\theta/\omega$ scan of film with XRD peaks of the film and substrate labelled. (b) Shallow angle x-ray reflectance showing thickness oscillations. (c) Rocking curve of ZnO (0002) peak.

tions due to the finite thickness of the film. The period of oscillations show that the film is 52.5 nm thick and the amplitude of oscillations and slope give a roughness of 0.6 nm, i.e. approximately one unit cell. The rocking curve on the (0002) peak (Figure 9.2 c) is broad with a low intensity central peak. This indicates some mosaicity in the film which is likely due to imperfect lattice matching between the ZnO and the a-plane sapphire.

In order to better characterize the surface roughness we take AFM scans on the surface of the ZnO films (Figure 9.3). This allows us to determing the topography of the film and provides a complementary measure of surface roughness. The AFM scans show that there is a very low surface roughness on the films. There are some regions which are slightly elevated ($\approx$ 2 nm above the rest of the film). These islands may also be resist residue as the film was coated with resist as a protective layer prior to dicing the sample before AFM was performed. The films we grow by this technique are low roughness films growing with [0001] normal to the substrate as required for SAW devices. There is some strain from epitaxial mismatch resulting in mosaicity in the ZnO in these films.

9.3 Results

We first fabricate resonators on a series of on substrates which have undergone different treatments. The sequence of material deposition for these four samples is shown in Figure 9.4. These substrates are: untreated sapphire (REF); thin film ZnO (ZNO); sapphire

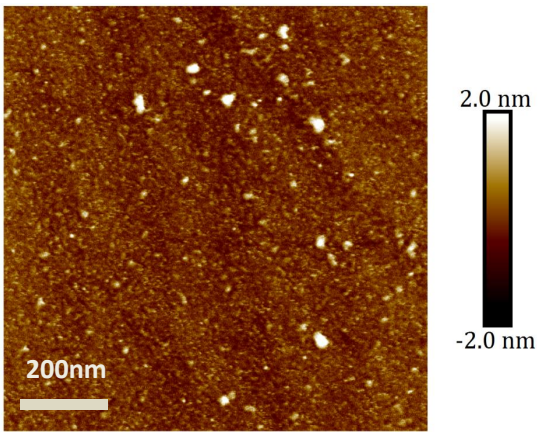

Figure 9.3: AFM of the surface of a ZnO film grown for 1 hour with above conditions. This AFM image was taken by Mr Adrian Hodel of UCL.

where ZnO has been grown and then subsequently etched by HCl (ETCH); and a sample where ZnO is grown and then selectively etched leaving behind some ZnO (ZONE). The ZnO is etched away by immersing the samples in 1:200 HCl for ≈10 s, which is sufficient time to entirely etch any exposed ZnO. 100 nm NbN films are then deposited by DC magnetron sputtering and resonators are etched into the NbN film in accordance with the process outlined in section 5.3.3. We measure these devices at cryogenic temperatures to characterize their performance.

In [192] NbN resonators are fabricated using the same technique and undergo similar characterization and may be compared to results obtained here. Importantly the resonators in [192] are made from thinner films of NbN (which may have some effect on resonator properties) and are fabricated on c-plane sapphire instead of a-plane sapphire which may affect the TLS on the substrate.

9.3.1 Temperature Dependent Transmission

As each device is cooled we measure RF transmission through the feed-line. As the properties of the feedline change with temperature, the transmission through the feed-line also changes. This allows us, for example, to measure the critical temperature of the superconductor. As the NbN undergoes its superconducting transition the attenuation of the feed-line drops significantly, resulting in a sharp increase in transmission through the feed-line. The transmission through the microwave circuitry as a function of temperature is shown for three samples in Figure 9.5. For all transmission measurements the power supplied by the vector network analyzer (VNA) is set to a high power (-20dBm) and frequency

Figure 9.4: Schematic showing the stages in material deposition for resonator fabrication in four samples. These samples are a reference sapphire sample (REF); a sample where ZnO is grown on sapphire and subsequently etched away (ETCH); a sample where resonators are fabricated on ZnO (ZNO); and a sample where zones of ZnO and NbN are deposited separately (ZONE).

is swept in 1001 points from 3 to 8GHz with a 1kHz bandwidth.

In all three samples there is a sharp increase in transmission at $\approx$ 12.2 K. This shows that all films undergo a superconducting transition and that the critical temperature of the superconductor is consistent with widely measured critical temperatures for NbN and consistent between the different samples.

As well as showing that films deposited on all substrates are superconductors, we may compare the transmission as a function of temperature between different samples. For both REF and ETCH transmission rises from an extremely low transmission of -75dB (etched) and -78dB (unprocessed) above T_c to a transmission of -51dB immediately below the superconducting transition. They then slowly increase at the same rate to a maximum transmission of -42dB at $\approx$ 2 K. Sample ZNO shows different behaviour with transmission above T_c of -65dB, an order of magnitude higher than the other samples. DC measurements on similar films deposited in the same equipment are reported in [193] where 100 nm films had a sheet resistance of $\sim$100 $\Omega/\square$ only weakly dependent on temperature. As the feedline is composed of $\sim$130 squares this is a $\sim$13 kΩ resistor. This will have a significant impedance mismatch with the 50Ω wiring and thus most RF energy will be reflected backwards. What little energy is not reflected will be significantly attenuated by the resistive feedline. We therefore neglect transmission through the feedline at temperatures above the critical temperature of the NbN. Instead we attribute this higher transmission to a different transmission mechanism for the sample ZNO.

The VNA provides an RF voltage which is transmitted down the wire bond to the

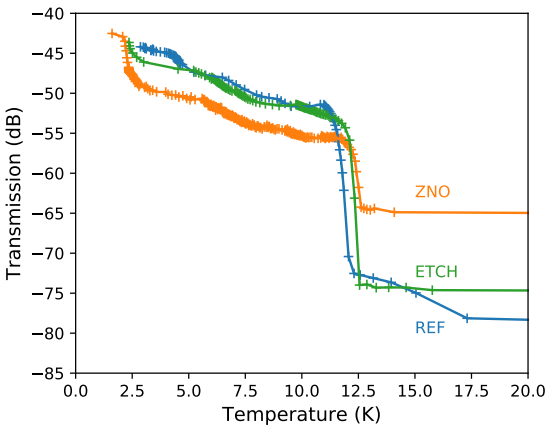

Figure 9.5: Transmission through the feed-line as a function of temperature for REF (blue), ZNO (yellow) and ETCH (green). For all curves an input power of -20dBm is applied by the VNA and the transmission is averaged from 3 to 8 GHz.

bond pad of the transmission line. This bond pad is fabricated on top of ZnO and so the RF voltage from the VNA is applying an RF voltage across the ZnO. Although the electrode is not fabricated into a resonant cavity, SAWs may still be excited incoherently as the RF voltage causes the ZnO to deform. SAWs may the travel outwards from the bond pad and a small fraction of these SAWs will arrive at the other bond wire. This bond wire is also connected to an electrode fabricated on ZnO. As SAWs pass through this ZnO and the ZnO is piezoelectric, there will be a voltage induced at the second bond wire. This allows energy to be transmitted from port 1 to port 2 and results in a larger transmission (value of S_{21}) for the sample ZNO above Tc.

At temperatures below the superconducting transition, the situation is reversed and the transmission in ZNO is -56dB compared to ETCH and REF where it is -51dB. This is clear evidence that the extra transmission above Tc is not due to, for example, connectors on the sample holder, but is a physical effect caused by something happening on the chip.

We attribue the lower transmission in ZNO relative to ETCH and REF to the same incoherently excited SAWs as cause the converse effect above Tc. This is because below Tc the transmission line is superconducting, well impedance matched and a small attenuator. Therefore, a significant fraction of the RF power delivered to port 1 is coupled out of port 2 through the transmission line. As SAWs are incoherently excited by the RF voltage on the transmssion line in ZNO, and not all of these SAWs couple back into the second port, RF energy is lost due to these SAWs. Therefore in this instance the SAWs reduce the transmission below Tc.

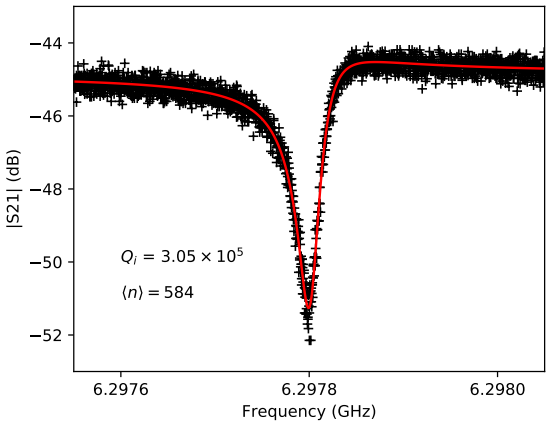

Figure 9.6: The magnitude of S_{21} in dB as a function of the frequency. Data are shown as red-crosses and the fit to the resonance notch is shown in red. The fit is performed using the circle fit routine described in [194]. The resonance notch is collected at a power of -125dBm which corresponds to an average photon number in the resonator of $\langle n \rangle$ ∼600 photons. The internal quality factor of the resonator is $\sim 3 \times 10^5$. This resonance is from a CPW on the ZONE sample.

9.3.2 Low Temperature Resonances

Once the samples are cooled to the base temperature of the cryostat (≈ 300 mK substantially below the 12K critical temperature), we search for resonance features caused by the superconducting CPW resonators. This is done by sweeping the frequency of the VNA and looking for dips in transmission. On both sample REF and ETCH resonance notches were found and characterized. An example resonance notch is shown in Figure 9.6.

For the sample ZNO despite sweeping the VNA frequency from 2-8.5 GHz in 25kHz steps, no evidence of any resonators was seen. To not see resonators with such small frequency steps would indicate a loaded resonator quality factor $\gg 1 \times 10^5$ even at 2GHz. Even if the internal quality factor were significantly larger for resonators fabricated on ZnO, the coupling quality factor is designed to limit the loaded quality factor to values below this. We therefore find it implausible that these resonators are too high quality factor to have been detected by the VNA sweep and conclude that no resonance notches were present.

From the transmission shown in Figure 9.5 we know that the NbN film deposited on the ZnO is a superconductor. We propose two explanations which may plausibly account for the resonators on ZnO not working. Firstly, the piezoelectric substrate introduces a new loss mechanism, i.e. the incoherent excitation of SAWs. This is a sufficiently lossy

process that the quality factor of resonators made on ZnO drops so that no resonance notch can be discerned from the background. For resonators with the same geometry as these devices measured in this setup, resonators with internal quality factor ∼2000 have resonance notches of only a few dB and so a Q_i much lower will not be resolvable. Secondly, the ZnO layer may interfere with device fabrication (particularly the RIE stage) and result in incomplete etching of the NbN in the area surrounding the resonator. This may leave shorts between the central conductor and ground which effectively kill the resonator. We do not see obvious signs of such shorts when inspecting devices under an optical microscope.

For the samples ETCH and REF we measure the resonance notch as a function of power. At each power we can fit to the resonance notch which is done using a traceable fit routine [194] as shown by the red line in Figure 9.6. The fit routine fits to the complex S_{21} transmission as a function of frequency in order to characterize the resonance features.

$$S_{21}(f) = ae^{i\theta}e^{-2\pi i f\tau}\left[1 - \frac{(Q_L/|Q_C|)e^{i\phi}}{1 + 2iQ_L(f/f_0 - 1)}\right] \tag{9.1}$$

where θ is a phase shift of microwaves and τ is the electronic delay, a an amplitude term, Q_L is the loaded quality factor of the resonator, Q_C the coupling quality factor, ϕ is determined by impedance mismatch, f the applied frequency and f_0 the resonance frequency.

The terms in Equation 9.1 before the square brackets are determined by the environment of the resonator. By processing the data we can calibrate out the effects of phase shifts, electronic delays and the amplitude of transmitted microwaves.

The fit routine described in [194] performs this calibration in a number of steps. First, the resonance is plot in the real-imaginary plane. Ideally this should be a circle, but time delays on the cable can result in deformations. By correcting the time delay the S_{21} is transformed to a circle. The circle is then fit. The intersection of the circle with the real axis is 1 far from resonance, the 'off resonant point'. The circle is then translated to have a centre on the real axis and a phase shift is applied to maintain the position of the off resonant point.

Once the calibration is performed, the circle may be fit to. This allows the properties of the resonator to be determined. This then returns the resonant frequency and quality factors. Full details of the fit routine are given in [194].

The fit to comples S_{21} data allows us to determine the internal and coupling quality factors of each resonance as a function of the drive power. As the coupling quality factor describes how energy is coupled between the feedline and the resonator and the internal

Frequency (GHz)	$\langle n \rangle$	Q_i
2.42	29	6.5×10^4
2.50	30	1.9×10^5
3.35	12	1.0×10^5
5.56	22	1.2×10^5
6.36	18	3.0×10^5
7.23	22	2.0×10^5

Table 9.1: Low power quality factors for the sample ETCH recorded at 320 mK.

quality factor of the resonator describes how quickly the resonator loses power to its surroundings we can use these values to determine the energy stored in the resonator at each value of drive power.

The energy stored in the resonator is given by

$$E_{res}(\omega_0) = 2P_{app}S_{min}Q_L/\omega_0 \tag{9.2}$$

where P_{app} is the power applied, S_{min} is the normalised minimum of the resonator magnitude response where normalisation is performed by making the radius of the circle of the resonance response in the real imaginary plane have a radius of 1, Q_L is the loaded quality factor of the resonator and ω_0 is the resonant frequency of the resonator. Once the energy inside the resonator is known then this can be converted into an average number of microwave photons, $\langle n \rangle$ at the resonant frequency since

$$\langle n \rangle = \frac{E_{res}}{\hbar\omega_0} \tag{9.3}$$

The low power (single photon) limit of resonators is of particular interest for technological applications since many circuit QED experiments take place in this limit. At these low powers two level systems (TLS) couple with the resonator and allow energy transfer between the TLS and the resonator – i.e. they act as a loss mechanism. TLS are known to be material dependent and recent experiments have begun to identify different microphysical causes of TLS with physisorbed atomic hydrogen being identified as the main source of TLS on c-axis sapphire [191].

In table 9.1 we show the internal quality factor of all resonances measured from sample ETCH. This shows that at the low power limit of tens of photons the quality factors of these resonators are typically hundreds of thousand with higher quality factors at higher frequencies. The state of the art for internal quality factors at single photon powers at mK

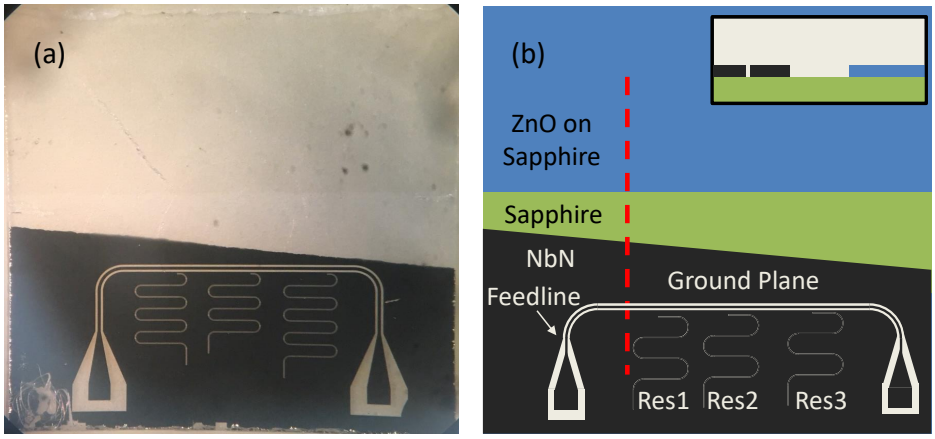

Figure 9.7: (a) Photograph of the device showing a region of patterned superconductor, a region of un-covered sapphire and a region of ZnO where a piezoelectric device may in due course be fabricated. (b) Schematic of the same region showing the different 'zones'. Inset is a cross section of the chip across the red dashed line.

temperatures is $\sim 1 \times 10^6$ [195]. The resonators in ETCH are therefore not state of the art, but have quality factors approaching state of the art. This shows that a-plane sapphire substrates where ZnO is overgrown and subsequently etched are suitable substrates for subsequent resonator fabrication.

9.3.3 Zoned Chips

Having demonstrated that high quality resonators may be fabricated on substrates overgrown by ZnO and subsequently etched away, we fabricated 'zoned' chips as shown schematically in Figure 9.4 using kapton tape to mask regions during HCl etching and NbN deposition. This results in a zoned chip called ZONE with regions of ZnO, exposed sapphire and superconductor such as shown (photograph and schematic) in Figure 9.7. The superconducting layer can then be patterned into devices as has been done in Figure 9.7 (a).

Having fabricated the device we measure the chip in the same manner as for the previous chips. We measure a critical temperature of ~13 K, slightly higher than for previous chips but still within the bounds commonly found for NbN. We then identify resonances. We find five resonance modes, where three are first harmonics and two are second harmonics of the resonators. The second harmonic of the third resonator is at higher frequency than the VNA maximum operating frequency and thus cannot be measured. Of the three first harmonics, only two are reported as due to impedance mismatching the

final resonance notch is not well fit by the same equations making subsequent analysis impossible. The FWHM of the resonator is comparable to the other resonances and therefore has a similar loaded quality factor.

The internal quality factor of the higher frequency resonances are 1.88×10^5 (7.25 GHz) and 2.37×10^5 (6.30 GHz) when 10 photons are stored in the resonator. This is similar to the internal quality factors in the sample ETCH where the substrate has been treated the same up to being masked in kapton tape. The lower frequency resonances have lower quality factors of 5.3×10^3 (2.42 GHz) and 5.2×10^4 (2.11 GHz) at 10 photons. Lower quality factors for lower frequency resonators was also seen in ETCH although the 2.42GHz resonator has a particularly low quality factor.

9.4 Two Level System Loss Fits

We can further characterize the low-power losses in CPW resonators due to the interaction of TLS with the resonators. Models of loss due to interacting TLS and quasiparticles as a function of photon number have been developed [196, 197] and are given by

$$\delta_i \equiv \frac{1}{Q_i} = FP_\gamma\chi \ln\left(\frac{Cn_c}{n} + \delta'_{QP}\right)\tanh\left(\frac{\hbar\omega_0}{2k_BT}\right) \tag{9.4}$$

where F is a geometric filling factor, P_γ depends on the TLS switching rate, χ is a dimensionless TLS parameter, C a (typically large) constant, n_c is the number of photons which saturate TLS effects, and n is the number of photons in the resonator, and δ'_{QP} is the log-scaled quasiparticle loss. $\mathrm{FP}_\gamma\chi$ which characterizes TLS on the substrate is plotted for different resonators in Figure 9.9.

We plot the losses as a function of average photon number in the resonator for samples REF, ETCH and ZONE in Figure 9.8. We fit equation 9.4 to the losses to determine the TLS induced losses. There is a significantly more pronounced up-turn in the losses for REF (Figure 9.8 a) than ETCH and ZONE (Figure 9.8 b, c). This indicates that the ZnO over-growth and subsequent etching actually improves the low-power operation of these resonators over the un-processed substrate. This could be due to the heating during growth desorbing adsorbed gases which removes some TLS species on the substrate.

When fitting the losses to the TLS model given in equation 9.4 we extract a prefactor $FP_\gamma\chi$ which relates to the total TLS losses. We collect this for resonators from the different samples discussed in this chapter as well as those reported in [192] where resonators are fabricated on c-plane sapphire. We then plot these values as a function of resonant frequency in Figure 9.9.

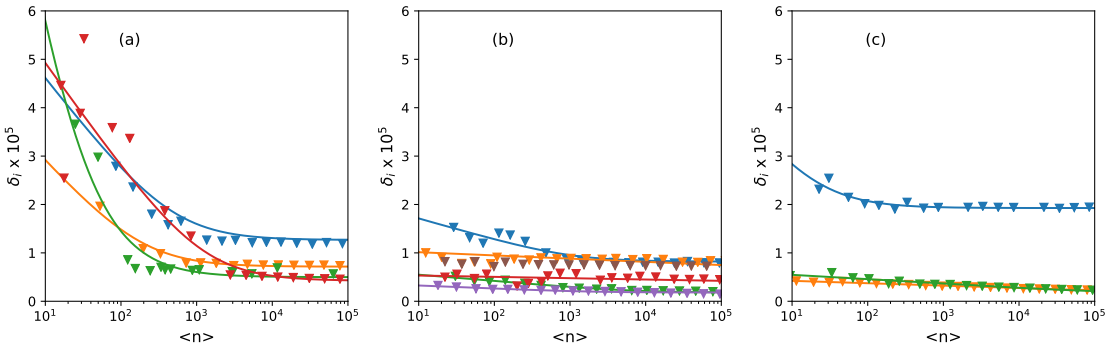

Figure 9.8: Intrinsic resonator losses as a function of the mean photon number stored within the resonators for (a) REF (b) ETCH and (c) ZONE. Fits to the TLS model of equation 9.4 are shown. Due to the almost imperceptible up-turn in losses one resonance in (b) has not been fit. One resonance on the sample ZONE has larger internal losses and thus is not shown on these axes but is shown in Figure 9.9

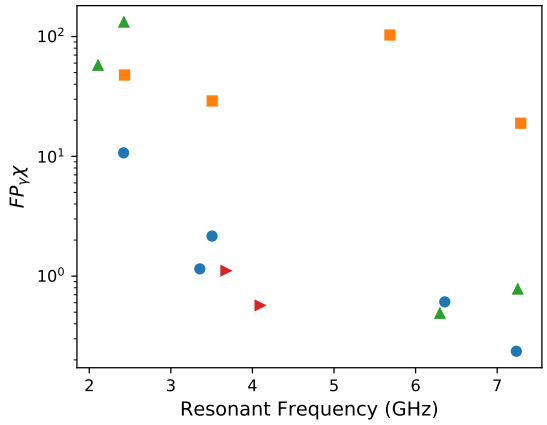

Figure 9.9: $FP_\gamma\chi$ found by fitting losses as a function of mean photon number in the resonator by Equation 9.4 for resonators from different samples: REF (yellow squares), ETCH (blue circles), ZONE (green up-triangles) and resonators reported in [192] (red sideways triangles).

The TLS factor from REF are flat with frequency and systematically higher than those from other samples. The TLS factor for samples ETCH and ZONE show the same frequency dependence with more TLS losses at lower frequencies. This indicates that TLS are not evenly spaced in frequency and that there are greater numbers of TLS on a-plane sapphire at lower frequencies, inducing more losses. The resonators from [192] fall on the line of TLS factors found in ZONE and ETCH. This may indicate that there is similarity between c-plane and a-plane sapphire for TLS densities. To say this conclusively, a more systematic study where identical resonators are fabricated on these different substrates would be required.

9.5 Conclusion

We have fabricated resonators on a-plane sapphire, ZnO thin films on a-plane sapphire, and a-plane sapphire where an over-grown film of ZnO has been etched away. We show that resonators may be fabricated on sapphire but not on ZnO either due to piezoelectric losses or fabrication problems introduced by the ZnO film. Resonators fabricated on both a plane sapphire and overgrown then etched sapphire have high quality factors at high powers. At low powers the quality factor for the untreated sapphire sample decreases significantly faster than for the sample where ZnO is overgrown and etched away.

We made a zoned chip, featuring both ZnO over-grown regions, regions where ZnO has been etched away to leave sapphire and regions of superconductor deposited directly onto sapphire where ZnO has been etched away. On this chip we fabricated superconducting resonators and measured their quality factor as a function of applied RF power. In agreement with the sample where ZnO is uniformly etched we find high quality factor resonances for higher frequency resonances and find lower quality factors at lower frequencies.

By fitting a model motivated by TLS-induced losses to the internal losses of resonators as a function of energy in the resonator, we characterize the TLS-induced losses for the three samples. We find that TLS limited losses are significantly higher for the un-treated sapphire, possibly because adsorbed gases are desorbed during the ZnO growth reducing the TLS density. For the samples where ZnO is etched away we find losses at low photon powers that are comparable to resonators fabricated on c-plane sapphire for high frequency resonances. We also find that losses are significantly increased for lower frequency resonances. This may be evidence that the TLS spectrum is frequency dependent on these substrates and there are more TLS in with energies 2-3 GHz than 5-7 GHz.

Importantly for future applications, we demonstrate superconducting circuits on the

same chip as piezoelectric films. These superconducting circuts can be of extremely high quality, even in the low-power-limit, and couple weakly to TLS. Future experiments are required to fully measure the effects of TLS, likely involving new samples and definitely requiring measurement at dilution fridge temperatures where TLS effects dominate.

In future, lift off processes could be used to fabricate SAW devices on the piezoelectric portion of this chip. The SAW electrodes could extend into the sapphire portion of the chip where they couple, likely via on-chip capacitors, to superconducting elements such as resonators or qubits, for hybrid devices.

Chapter 10

Conclusion and Further Work

In this thesis we present work focusing on the growth by MBE and characterization of ZnO nanowires and nanobelts and ZnO/ZnMgO heterostructures based on these nanostructures. We also present an additional study on epitaxial ZnO films grown on a-plane sapphire used as substrates for RF superconducting circuits as a route to future opto-mechanical experiments coupling mechanical and RF superconducting oscillators on a single chip.

10.1 Conclusions

The growth of ZnO nanobelts by MBE was demonstrated for the first time. These MBE grown nanobelts were characterized structurally by HRTEM and XRD. We demonstrated morphology control of nanobelts where tapering is reduced with increasing growth temperature. We also characterized the electrical properties of the ZnO nanobelts by fabricating field effect transistors showing n-type conductivity. We find a large variation both in donor density and free carrier density between different nanobelts which we ascribe to large numbers of surface states and a large surface-to-volume ratio.

We demonstrate the growth of ZnO/ZnMgO nanowire and nanobelt heterostructures. For nanowires, using STEM-EDS, we demonstrate abrupt heterointerfaces in core-shell nanowires, and show that these core-shell structures give rise to intense luminescence with small defect-related peaks relative to plain ZnO nanowires. These structures may be promising for optical applications such as nanowire lasers. We also show for the first time ZnO/ZnMgO heterostructures embedded within ZnO nanobelts. These heterostructures are particularly interesting since they include polarization-mismatched interfaces which extend along the length of these nanostructures. These interfaces are promising for future

applications where the electron mobility in nanostructures is increased by heterostructuring because 2DEGs form at these polarization mismatched interfaces. We show evidence of the quantum confined Stark effect and quantum well luminescence in cryogenic photoluminescence spectra taken on single nanobelt heterostructures. These phenomena are indicative of the presence of 2DEG interfaces.

We use scanning-transmission-electron-microscopy cathodoluminescence, a new analytical technique, to provide hyperspectral CL maps of ZnO nanowires with record spatial-resolution. These maps allow us to relate the CL spectra to structural features on single ZnO nanowires including luminescence from the surface of the nanowire, luminescence from intrinsic and extrinsic defects and luminescence from the core of the nanowire. We show the interplay of the different luminescence signals and demonstrate that increases in non-radiative recombination are coincident with defect peaks in the nanowire. We develop data processing techniques allowing CL maps to be deconvolved into individual components which we map across nanowires. We also show the effects of gold nanoparticles and polar faces on the CL from nanowires.

We finally present work where we selectively grow and selectively etch ZnO grown on a-plane sapphire and subsequently fabricate RF superconducting circuits on these substrates. We demonstrate that although films deposited on top of ZnO are still superconducting, they do not support resonance modes after being fabricated into quarter wave resonators. We attribute this either to complications in fabrication induced by the ZnO layer or to increased losses due to incoherent mechanical coupling between the resonator and the piezoelectric substrate. We show that RF superconducting resonators with high quality factors can be fabricated on substrates where ZnO has been grown and subsequently etched and that this may also be done with chips where ZnO has been selectively etched. This allows us to develop zoned chips where on part of the chip high quality factor superconducting circuits are fabricated, and another part is overgrown with ZnO and suitable for piezoelectric applications.

10.2 Future work

Further characterization of nanobelt heterostructures by TEM will allow the heterointerface to be better understood. A combination of high resolution imaging and analytical techniques will allow the heterointerface to be precisely characterized, with elemental maps across the interface, imaging of any defects which arise at the heterointerface, and precise determination of the crystallographic orientation of the interface. Fabricating and

measuring nanobelt FETs from heterostructure nanobelts will allow the electron mobility at nanobelt-embedded heterostructures to be determined. These interfaces should have a high electron mobility and remain conductive down to cryogenic temperatures. This experiment would be the first demonstration of a polarity-induced 2DEG embedded along the long axis of a nanostructure modifying the electrical properties in ZnO.

Further STEM CL measurements in which the STEM CL data are combined with other STEM signals or high resolution imaging would be extremely interesting. We attempted to perform high resolution imaging in tandem with STEM CL but found that the HRTEM, if performed before CL, degraded the CL intensity and if performed after CL was not a true measure of the structure of a pristine nanowire. Therefore a good candidate structure for these measurements would be ZnO nanobelts. In ZnO nanobelts extended defects, which are well characterized by HRTEM and found in all nanobelts, can be seen in low resolution TEM. Therefore it should be comparatively straightforward to relate luminescence properties of these well-understood defects to CL spectra. Additionally, CL STEM on heterostructure nanobelts and nanowires would be an interesting study and allow the effects of the heterointerface on optical properties to be mapped locally. This could be correlated with EELS or EDS to allow elemental maps to be simultaneously collected.

The superconducting circuits discussed in this thesis have been measured at $\sim$300 mK due to the availability of cryostats. At these temperatures it is possible to see the effects of two-level fluctuators. These are typically found to limit the low temperature, low power quality factor of superconducting circuits. Performing systematic power dependent measurements on the quality factor of superconducting resonators, fabricated on sapphire with ZnO overgrown and subsequently etched, at $\sim$30mK would allow the suitability of this substrate for quantum applications to be assessed. Future devices, featuring mechanical oscillators fabricated on the ZnO which are coupled to the superconducting architecture to form hybrid quantum devices offer many opportunities for future study.

List of my Publications

[1] Oscar W. Kennedy, Edward R. White, Ashley Howkins, Charlotte K. Williams, Ian W. Boyd, Paul A. Warburton, and Milo S. P. Shaffer. Mapping the Origins of Luminescence in ZnO Nanowires by STEM-CL. *The Journal of Physical Chemistry Letters*, 10(3):386–392, 2019.

[2] Oscar W Kennedy, Maddison L Coke, Edward R White, Milo SP Shaffer, and Paul A Warburton. MBE growth and morphology control of ZnO nanobelts with polar axis perpendicular to growth direction. *Materials Letters*, 212:51–53, 2018.

[3] OW Kennedy, ER White, MSP Shaffer, and PA Warburton. Vapour-liquid-solid growth of ZnO-ZnMgO core–shell nanowires by gold-catalysed molecular beam epitaxy. *Nanotechnology*, 30(19):194001, 2019.

[4] OW Kennedy, J Burnett, JC Fenton, NGN Constantino, PA Warburton, JJL Morton, and E Dupont-Ferrier. Tunable Nb Superconducting Resonator Based on a Constriction Nano-SQUID Fabricated with a Ne Focused Ion Beam. *Physical Review Applied*, 11(1):014006, 2019.

[5] Maddison L Coke, Oscar W Kennedy, James T Sagar, and Paul A Warburton. Electron confinement at diffuse ZnMgO/ZnO interfaces. *APL Materials*, 5(1):016102, 2017.

[6] NGN Constantino, MS Anwar, OW Kennedy, M Dang, PA Warburton, and JC Fenton. Emergence of Quantum Phase-Slip Behaviour in Superconducting NbN Nanowires: DC Electrical Transport and Fabrication Technologies. *Nanomaterials*, 8(6), 2018.

[7] Jonathan Burnett, James Sagar, Oscar W Kennedy, Paul A Warburton, and Jonathan C Fenton. Low-loss superconducting nanowire circuits using a neon focused ion beam. *Physical Review Applied*, 8(1):014039, 2017.

Bibliography

[1] G. E. Moore. Cramming more components onto integrated circuits (Reprinted from Electronics, pg 114-117, April 19, 1965). *Proceedings of The IEEE*, 86(1):82–85, 1965.

[2] John Bardeen and Walter Hauser Brattain. The transistor, a semi-conductor triode. *Physical Review*, 74(2):230, 1948.

[3] Richard P Feynman. Theres plenty of room at the bottom: An invitation to enter a new field of physics. In *Handbook of Nanoscience, Engineering, and Technology, Third Edition*, pages 26–35. CRC Press, 2012.

[4] Andrew B. Greytak, Carl J. Barrelet, Yat Li, and Charles M. Lieber. Semiconductor nanowire laser and nanowire waveguide electro-optic modulators. *Applied Physics Letters*, 87(15):151103, 2005.

[5] R.P. Cowburn. Property variation with shape in magnetic nanoelements. *Journal of Physics D: Applied Physics*, 33(1):R1, 2000.

[6] Jong Hyeok Park, Sungwook Kim, and Allen J Bard. Novel carbon-doped TiO_2 nanotube arrays with high aspect ratios for efficient solar water splitting. *Nano Letters*, 6(1):24–28, 2006.

[7] Mart Graef. More than Moore. Technical report, 2015.

[8] Hadis Morkoç and Ümit Özgür. *Zinc oxide: fundamentals, materials and device technology*. John Wiley & Sons, 2008.

[9] Zhong Lin Wang. Nanostructures of zinc oxide. *Materials Today*, 7(6):26–33, 2004.

[10] Priya Gopal and Nicola A. Spaldin. Polarization, piezoelectric constants, and elastic constants of ZnO, MgO, and CdO. *Journal of Electronic Materials*, 35(4):538–542, 2006.

[11] E. B. Magnusson, B. H. Williams, R. Manenti, M. S. Nam, A. Nersisyan, M. J. Peterer, A. Ardavan, and P. J. Leek. Surface acoustic wave devices on bulk ZnO crystals at low temperature. *Applied Physics Letters*, 106(6):1–4, 2015.

[12] A. Mang, K. Reimann, et al. Band gaps, crystal-field splitting, spin-orbit coupling, and exciton binding energies in ZnO under hydrostatic pressure. *Solid State Communications*, 94(4):251–254, 1995.

[13] Katsumi Maeda, Mitsuru Sato, Ikuo Niikura, and Tsuguo Fukuda. Growth of 2 inch ZnO bulk single crystal by the hydrothermal method. *Semiconductor Science and Technology*, 20(4):S49, 2005.

[14] Thomas Aref, Per Delsing, Maria K Ekström, Anton Frisk Kockum, Martin V Gustafsson, Göran Johansson, Peter J Leek, Einar Magnusson, and Riccardo Manenti. Quantum Acoustics with Surface Acoustic Waves. *Superconducting Devices in Quantum Optics*, pages 217–244, 2016.

[15] Ivan Isakov, Marina Panfilova, Marion JL Sourribes, and Paul A. Warburton. Growth of ZnO and ZnMgO nanowires by Au-catalysed molecular-beam epitaxy. *Physica Status Solidi (c)*, 10(10):1308–1313, 2013.

[16] L. C. Tien, D. P. Norton, S. J. Pearton, Hung Ta Wang, and F. Ren. Nucleation control for ZnO nanorods grown by catalyst-driven molecular beam epitaxy. *Applied Surface Science*, 253(10):4620–4625, 2007.

[17] P. Yang, H. Yan, S. Mao, R. Russo, J. Johnson, R. Saykally, N. Morris, J. Pham, R. He, and H. J. Choi. Controlled growth of ZnO nanowires and their optical properties. *Advanced Functional Materials*, 12(5):323–331, 2002.

[18] Frank Jones, François Léonard, A. Alec Talin, and Nelson S. Bell. Electrical conduction and photoluminescence properties of solution-grown ZnO nanowires. *Journal of Applied Physics*, 102(1):014305, 2007.

[19] B. Q. Cao, J. Zúñiga-Pérez, N. Boukos, C. Czekalla, H. Hilmer, J. Lenzner, A. Travlos, M. Lorenz, and M. Grundmann. Homogeneous core/shell ZnO/ZnMgO quantum well heterostructures on vertical ZnO nanowires. *Nanotechnology*, 20(30):305701, jul 2009.

[20] Zhong Lin Wang and Jinhui Song. Piezoelectric nanogenerators based on zinc oxide nanowire arrays. *Science*, 312(5771):242–246, 2006.

[21] Z. W. Pan, Z. R. Dai, and Z. L. Wang. Nanobelts of semiconducting oxides. *Science*, 291(5510):1947–1949, 2001.

[22] R. S. Wagner, W. C. Ellis, K. A. Jackson, and S. M. Arnold. Study of the Filamentary Growth of Silicon Crystals from the Vapor. *Journal of Applied Physics*, 35(10):2993, 1964.

[23] C. Thelander, P. Agarwal, S. Brongersma, J. Eymery, L. F. Feiner, A. Forchel, M. Scheffler, W. Riess, B. J. Ohlsson, U. Gösele, and L. Samuelson. Nanowire-based one-dimensional electronics. *Materials Today*, 9(10):28–35, 2006.

[24] Wei Lu and Charles M. Lieber. Semiconductor nanowires. *Journal of Physics D: Applied Physics*, 39(21), 2006.

[25] Jonas Johansson and Kimberly A. Dick. Recent advances in semiconductor nanowire heterostructures. *CrystEngComm*, 13:7175, 2011.

[26] Peidong Yang, Ruoxue Yan, and Melissa Fardy. Semiconductor nanowire: Whats Next? *Nano Letters*, 10(5):1529–1536, 2010.

[27] Chunya Geng, Yang Jiang, Yuan Yao, Xiangmin Meng, Juan Antonio Zapien, Chun Sing Lee, Yeshayahu Lifshitz, and Shuit Tong Lee. Well-aligned ZnO nanowire arrays fabricated on Silicon substrates. *Advanced Functional Materials*, 14(6):589–594, 2004.

[28] Babak Nikoobakht, Albert Davydov, and Stephan J. Stranick. Controlling the Growth Direction of ZnO Nanowires on c-Plane Sapphire. *MRS Proceedings*, 818:M8.25.1, 2011.

[29] Jason B. Baxter and Eray S. Aydil. Epitaxial growth of ZnO nanowires on a- and c-plane sapphire. *Journal of Crystal Growth*, 274(3-4):407–411, 2005.

[30] Hou Tee Ng, Bin Chen, Jun Li, Jie Han, M. Meyyappan, J. Wu, S. X. Li, and E. E. Haller. Optical properties of single-crystalline ZnO nanowires on m-sapphire. *Applied Physics Letters*, 82(13):2023–2025, 2003.

[31] Hong Jin Fan, Bodo Fuhrmann, Roland Scholz, Frank Syrowatka, Armin Dadgar, Alois Krost, and Margit Zacharias. Well-ordered ZnO nanowire arrays on GaN substrate fabricated via nanosphere lithography. *Journal of Crystal Growth*, 287:34–38, 2006.

[32] Imran Shakir, Muhammad Shahid, Usman Ali Rana, Inas M. Al Nashef, and Rafaqat Hussain. NickelCobalt Layered Double Hydroxide Anchored Zinc Oxide Nanowires grown on Carbon Fiber Cloth for High-Performance Flexible Pseudocapacitive Energy Storage Devices. *Electrochimica Acta*, 129:28–32, 2014.

[33] Afsal Manekkathodi, Ming-Yen Lu, Chun Wen Wang, and Lih-Juann Chen. Direct growth of aligned zinc oxide nanorods on paper substrates for low-cost flexible electronics. *Advanced Materials*, 22(36):4059–63, 2010.

[34] Fudong Wang, Angang Dong, Jianwei Sun, Rui Tang, Heng Yu, and William E Buhro. Solution - Liquid - Solid Growth of Semiconductor Nanowires. *Inorganic Chemistry*, 45(6):7511–7521, 2006.

[35] Knut Deppert, Jan-Olov Bovin, Jan-Olle Malm, and Lars Samuelson. A new method to fabricate size-selected compound semiconductor nanocrystals: aerotaxy. *Journal of Crystal Growth*, 169(1):13–19, 1996.

[36] Y.-Y. Liu, J. Stehlik, Christopher Eichler, M.J. Gullans, Jacob M. Taylor, and J.R. Petta. Semiconductor double quantum dot micromaser. *Science*, 347(6219):285–287, 2015.

[37] H. Schmid, M. Borg, K. Moselund, L. Gignac, C. M. Breslin, J. Bruley, D. Cutaia, and H. Riel. Template-assisted selective epitaxy of III-V nanoscale devices for coplanar heterogeneous integration with Si. *Applied Physics Letters*, 106(23), 2015.

[38] Deyu Li, Yiying Wu, Philip Kim, Li Shi, Peidong Yang, and Arun Majumdar. Thermal conductivity of individual silicon nanowires. *Applied Physics Letters*, 83(14):2934–2936, 2003.

[39] M. S. Dresselhaus, G. Chen, M. Y. Tang, R. G. Yang, H. Lee, D. Z. Wang, Z. F. Ren, J.-P. Fleurial, and P. Gogna. New Directions for Low-Dimensional Thermoelectric Materials. *Advanced Materials*, 19(8):1043–1053, 2007.

[40] Wu-Xing Zhou, Shihua Tan, Ke-Qiu Chen, and Wenping Hu. Enhancement of thermoelectric performance in InAs nanotubes by tuning quantum confinement effect. *Journal of Applied Physics*, 115(12):124308, 2014.

[41] Q. Wan, Q. H. Li, Y. J. Chen, T. H. Wang, X. L. He, J. P. Li, and C. L. Lin. Fabrication and ethanol sensing characteristics of ZnO nanowire gas sensors. *Applied Physics Letters*, 84(18):3654–3656, 2004.

[42] Hye Seong Jung, Young Joon Hong, Yirui Li, Jeonghui Cho, Yong-Jin Kim, and Gyu-Chul Yi. Photocatalysis using gan nanowires. *ACS Nano*, 2(4):637–642, 2008.

[43] Gongming Wang, Hanyu Wang, Yichuan Ling, Yuechao Tang, Xunyu Yang, Robert C Fitzmorris, Changchun Wang, Jin Z Zhang, and Yat Li. Hydrogen-treated TiO_2 nanowire arrays for photoelectrochemical water splitting. *Nano Letters*, 11(7):3026–3033, 2011.

[44] M H Huang, S Mao, H Feick, H Yan, Y Wu, H Kind, E Weber, R Russo, and P Yang. Room-temperature ultraviolet nanowire nanolasers. *Science (New York, N.Y.)*, 292(5523):1897–1899, 2001.

[45] Xiangfeng Duan, Yu Huang, Ritesh Agarwal, and Charles M. Lieber. Single-nanowire electrically driven lasers. *Nature*, 421:241–245, 2003.

[46] Richard G. Hobbs, Nikolay Petkov, and Justin D. Holmes. Semiconductor nanowire fabrication by bottom-up and top-down paradigms. *Chemistry of Materials*, 24(11):1975–1991, 2012.

[47] Fauzia Jabeen, Vincenzo Grillo, Silvia Rubini, and Faustino Martelli. Self-catalyzed growth of GaAs nanowires on cleaved Si by molecular beam epitaxy. *Nanotechnology*, 19(27):275711, 2008.

[48] Jakub Rybczynski, Debasish Banerjee, Adam Kosiorek, Michael Giersig, and Z.F. Ren. Formation of super arrays of periodic nanoparticles and aligned ZnO nanorods-simulation and experiments. *Nano Letters*, 4(10):2037–2040, 2004.

[49] Yaguang Wei, Wenzhuo Wu, Rui Guo, Dajun Yuan, Suman Das, and Zhong Lin Wang. Wafer-scale high-throughput ordered growth of vertically aligned ZnO nanowire arrays. *Nano letters*, 10(9):3414–3419, 2010.

[50] LJ Lauhon, Mark S Gudiksen, and Charles M Lieber. Semiconductor nanowire heterostructures. *Philosophical Transactions of the Royal Society of London A: Mathematical, Physical and Engineering Sciences*, 362(1819):1247–1260, 2004.

[51] Thomas J Kempa, Bozhi Tian, Dong Rip Kim, Jinsong Hu, Xiaolin Zheng, and Charles M Lieber. Single and tandem axial pin nanowire photovoltaic devices. *Nano Letters*, 8(10):3456–3460, 2008.

[52] Fang Qian, Yat Li, Silvija Gradečak, Hong Gyu Park, Yajie Dong, Yong Ding, Zhong Lin Wang, and Charles M. Lieber. Multi-quantum-well nanowire heterostructures for wavelength-controlled lasers. *Nature Materials*, 7(9):701–706, 2008.

[53] Hyok So, Dong Pan, Lixia Li, and Jianhua Zhao. Foreign-catalyst-free growth of InAs/InSb axial heterostructure nanowires on Si (111) by molecular-beam epitaxy. *Nanotechnology*, 28(13):135704, 2017.

[54] P. Krogstrup, N.L.B. Ziino, W. Chang, S.M. Albrecht, M.H. Madsen, Erik Johnson, Jesper Nygård, C.M. Marcus, and T.S. Jespersen. Epitaxy of semiconductor–superconductor nanowires. *Nature Materials*, 14(4):400, 2015.

[55] C. Colombo, M. Heiß, M. Grätzel, and A. Fontcuberta i Morral. Gallium arsenide p-i-n radial structures for photovoltaic applications. *Applied Physics Letters*, 94(17):173108, 2009.

[56] Erik C. Garnett and Peidong Yang. Silicon nanowire radial p- n junction solar cells. *Journal of the American Chemical Society*, 130(29):9224–9225, 2008.

[57] Jessica L. Boland, Sonia Conesa-Boj, Patrick Parkinson, Gözde Tütüncüoglu, Federico Matteini, Daniel Rüffer, Alberto Casadei, Francesca Amaduzzi, Fauzia Jabeen, Christopher L. Davies, et al. Modulation doping of GaAs/AlGaAs core–shell nanowires with effective defect passivation and high electron mobility. *Nano Letters*, 15(2):1336–1342, 2015.

[58] David C. Dillen, Kyounghwan Kim, En-Shao Liu, and Emanuel Tutuc. Radial modulation doping in core-shell nanowires. *Nature Nanotechnology*, 9(2):116–120, 2014.

[59] Yat Li, Jie Xiang, Fang Qian, Silvija Gradecak, Yue Wu, Hao Yan, Douglas A. Blom, and Charles M. Lieber. Dopant-free GaN/AlN/AlGaN radial nanowire heterostructures as high electron mobility transistors. *Nano Letters*, 6(7):1468–1473, 2006.

[60] A. Ohtomo, M. Kawasaki, T. Koida, K. Masubuchi, H. Koinuma, Y. Sakurai, Yasuda Yoshida, T. Yasuda, and Y. Segawa. $Mg_xZn_{1-x}O$ as a II–VI widegap semiconductor alloy. *Applied Physics Letters*, 72(19):2466–2468, 1998.

[61] S. Sadofev, S. Blumstengel, J. Cui, J. Puls, S. Rogaschewski, P. Schäfer, and F. Henneberger. Visible band-gap ZnCdO heterostructures grown by molecular beam epitaxy. *Applied Physics Letters*, 89(20):201907, 2006.

[62] MB Ullah, V Avrutin, T Nakagawara, S Hafiz, I Altuntaş, Ü Özgür, and H Morkoç. Growth kinetics of O-polar $Be_xMg_yZn_{1-x-y}O$ alloy: Role of Zn to Be and Mg flux ratio as a guide to growth at high temperature. *Journal of Applied Physics*, 121(18):185704, 2017.

[63] Maddison L Coke, Oscar W Kennedy, James T Sagar, and Paul A Warburton. Electron confinement at diffuse ZnMgO/ZnO interfaces. *APL Materials*, 5(1):016102, 2017.

[64] Ivan Isakov. *Semiconductor Nanowires Grown by Molecular Beam Epitaxy for Electronics Applications*. PhD thesis, 2014.

[65] Andrei Malashevich and David Vanderbilt. First-principles study of polarization in $Zn_{1-x}Mg_xO$. *Physical Review B*, 75(4):045106, 2007.

[66] I.-H. Tan, G.L. Snider, L.D. Chang, and E.L. Hu. A self-consistent solution of Schrödinger–Poisson equations using a nonuniform mesh. *Journal of Applied Physics*, 68(8):4071–4076, 1990.

[67] R. Dingle, H.L. Störmer, A.C. Gossard, and W. Wiegmann. Electron mobilities in modulation-doped semiconductor heterojunction superlattices. *Applied Physics Letters*, 33(7):665–667, 1978.

[68] H. Kawai, K. Kaneko, and N. Watanabe. Photoluminescence of AlGaAs/GaAs quantum wells grown by metalorganic chemical vapor deposition. *Journal of Applied Physics*, 56(2):463–467, 1984.

[69] David A.B. Miller, D.S. Chemla, T.C. Damen, A.C. Gossard, W. Wiegmann, T.H. Wood, and C.A. Burrus. Band-edge electroabsorption in quantum well structures: The quantum-confined stark effect. *Physical Review Letters*, 53(22):2173, 1984.

[70] Joseph Falson, Yusuke Kozuka, Masaki Uchida, Jurgen H. Smet, Taka-hisa Arima, Atsushi Tsukazaki, and Masashi Kawasaki. MgZnO/ZnO heterostructures with electron mobility exceeding 1×10^6 cm^2/Vs. *Scientific Reports*, 6:26598, 2016.

[71] Petr Kuznetsov, Valery Lusanov, Galina Yakushcheva, Victor Jitov, Leonid Zakharov, Iosif Kotelyanskii, and Vladimir Kozlovsky. MOVPE growth and study of

ZnO, ZnMgO epilayers and ZnO/ZnMgO MQW structures. *Physica Status Solidi C*, 7(6):1568–1570, 2010.

[72] Toshihiko Maemoto, Nobuyasu Ichiba, Shigehiko Sasa, and Masataka Inoue. Growth of ZnO/$Zn_{1-x}Mg_xO$ films by pulsed laser ablation. *Thin Solid Films*, 486(1-2):174–177, 2005.

[73] Th Gruber, C. Kirchner, R. Kling, F. Reuss, and A. Waag. ZnMgO epilayers and ZnO–ZnMgO quantum wells for optoelectronic applications in the blue and UV spectral region. *Applied Physics Letters*, 84(26):5359–5361, 2004.

[74] H. Tampo, K. Matsubara, A. Yamada, H. Shibata, P. Fons, M. Yamagata, H. Kanie, and S. Niki. High electron mobility Zn polar ZnMgO/ZnO heterostructures grown by molecular beam epitaxy. *Journal of Crystal Growth*, 301:358–361, 2007.

[75] S Sadofev, S Blumstengel, J Cui, J Puls, S Rogaschewski, P Schäfer, Yu G Sadofyev, and F Henneberger. Growth of high-quality ZnMgO epilayers and ZnO/ZnMgO quantum well structures by radical-source molecular-beam epitaxy on sapphire. *Applied Physics Letters*, 87(9):091903, 2005.

[76] A. Ohtomo, K. Tamura, K. Saikusa, K. Takahashi, T. Makino, Y. Segawa, H. Koinuma, and M. Kawasaki. Single crystalline ZnO films grown on lattice-matched ScAlMgO 4 (0001) substrates. *Applied Physics Letters*, 75(17):2635–2637, 1999.

[77] Shunsuke Akasaka, Ken Nakahara, Atsushi Tsukazaki, Akira Ohtomo, and Masashi Kawasaki. $Mg_xZn_{1-x}O$ Films with a Low Residual Donor Concentration ($< 10^{15}$ cm^{-3}) Grown by Molecular Beam Epitaxy. *Applied Physics Express*, 3(7):071101, 2010.

[78] Hiroyuki Kato, Michihiro Sano, Kazuhiro Miyamoto, and Takafumi Yao. Polarity control of ZnO on c-plane sapphire by plasma-assisted MBE. *Journal of Crystal Growth*, 275(1-2):e2459–e2465, 2005.

[79] K. Ogata, K. Koike, T. Tanite, T. Komuro, F. Yan, S. Sasa, M. Inoue, and M. Yano. ZnO and ZnMgO growth on a-plane sapphire by molecular beam epitaxy. *Journal of Crystal Growth*, 251(1-4):623–627, 2003.

[80] J.-M. Chauveau, M. Teisseire, H. Kim-Chauveau, C. Deparis, C. Morhain, and B. Vinter. Benefits of homoepitaxy on the properties of nonpolar (Zn, Mg) O/ZnO

quantum wells on a-plane ZnO substrates. *Applied Physics Letters*, 97(8):081903, 2010.

[81] E. Di Russo, L. Mancini, F. Moyon, S. Moldovan, J. Houard, F.H. Julien, J.-M. Tchernycheva, M .and Chauveau, M. Hugues, G. Da Costa, et al. Three-dimensional atomic-scale investigation of ZnO-$Mg_xZn_{1-x}O$ m-plane heterostructures. *Applied Physics Letters*, 111(3):032108, 2017.

[82] N. Le Biavan, M. Hugues, M. Montes Bajo, J. Tamayo-Arriola, A. Jollivet, D. Lefebvre, Y. Cordier, B. Vinter, F.-H. Julien, A. Hierro, et al. Homoepitaxy of non-polar ZnO/(Zn, Mg) O multi-quantum wells: From a precise growth control to the observation of intersubband transitions. *Applied Physics Letters*, 111(23):231903, 2017.

[83] Sushil Kumar, Chun Wang I Chan, Qing Hu, and John L Reno. A 1.8-THz quantum cascade laser operating significantly above the temperature of $\hbar\omega/k_B$. *Nature Physics*, 7(2):166, 2011.

[84] Zoterac Report Summary. Technical report, 2016.

[85] Kazuto Koike, Kenji Hama, Ippei Nakashima, Gen-you Takada, Masashi Ozaki, Ken-ichi Ogata, Shigehiko Sasa, Masataka Inoue, and Mitsuaki Yano. Piezoelectric carrier confinement by lattice mismatch at $ZnO/Zn_{0.6}Mg_{0.4}O$ heterointerface.

[86] A Tsukazaki, A Ohtomo, T Kita, Y Ohno, H Ohno, and M Kawasaki. Quantum Hall effect in polar oxide heterostructures. *Science*, 315(5817):1388–1391, 2007.

[87] K. Imasaka, J. Falson, Y. Kozuka, A. Tsukazaki, and M. Kawasaki. Spontaneous polarization driven Mg concentration profile reconstruction in MgZnO/ZnO heterostructures. *Applied Physics Letters*, 104(24):242112, 2014.

[88] H. Tampo, H. Shibata, K. Maejima, A. Yamada, K. Matsubara, P. Fons, S. Kashiwaya, S. Niki, Y. Chiba, T. Wakamatsu, and H. Kanie. Polarization-induced two-dimensional electron gases in ZnMgO/ZnO heterostructures. *Applied Physics Letters*, 93(20):1–4, 2008.

[89] Joseph Falson, Denis Maryenko, Yusuke Kozuka, Atsushi Tsukazaki, and Masashi Kawasaki. Magnesium doping controlled density and mobility of two-dimensional electron gas in $Mg_xZn_{1-x}O$/ZnO heterostructures. *Applied Physics Express*, 4(9):091101, 2011.

[90] J. Falson, D. Maryenko, B. Friess, D. Zhang, Y. Kozuka, A. Tsukazaki, and J.H. Smet. Even-denominator fractional quantum Hall physics in ZnO. *Nature Physics*, 11:347–351, 2015.

[91] D. Maryenko, J. Falson, M.S. Bahramy, I.A. Dmitriev, Y. Kozuka, A. Tsukazaki, and M. Kawasaki. Spin-selective electron quantum transport in nonmagnetic MgZnO/ZnO heterostructures. *Physical Review Letters*, 115(19):197601, 2015.

[92] T. Makino, A. Ohtomo, C.H. Chia, Y. Segawa, H. Koinuma, and M. Kawasaki. Internal electric field effect on luminescence properties of ZnO/(Mg, Zn) O quantum wells. *Physica E: Low-dimensional Systems and Nanostructures*, 21(2-4):671–675, 2004.

[93] V.V. Solovyev, A.B. Van'kov, I.V. Kukushkin, J. Falson, D. Zhang, D. Maryenko, Y. Kozuka, A. Tsukazaki, J.H. Smet, and M. Kawasaki. Optical probing of MgZnO/ZnO heterointerface confinement potential energy levels. *Applied Physics Letters*, 106(8):082102, 2015.

[94] Won Il Park, Jinkyoung Yoo, Dong-Wook Kim, Gyu-Chul Yi, and Miyoung Kim. Fabrication and photoluminescent properties of heteroepitaxial ZnO/$Zn_{0.8}Mg_{0.2}O$ coaxial nanorod heterostructures. *The Journal of Physical Chemistry B*, 110(4):1516–1519, 2006.

[95] Won Il Park, G.-C. Yi, M.Y. Kim, and Stephen J. Pennycook. Quantum confinement observed in ZnO/ZnMgO nanorod heterostructures. *Advanced Materials*, 15(6):526–529, 2003.

[96] BQ Cao, J Zúñiga-Pérez, N Boukos, C Czekalla, H Hilmer, J Lenzner, A Travlos, M Lorenz, and M Grundmann. Homogeneous core/shell ZnO/ZnMgO quantum well heterostructures on vertical ZnO nanowires. *Nanotechnology*, 20(30):305701, 2009.

[97] Robin Thierry, Guillaume Perillat-Merceroz, Pierre-Henri Jouneau, Pierre Ferret, and Guy Feuillet. Core–shell multi-quantum wells in ZnO/ZnMgO nanowires with high optical efficiency at room temperature. *Nanotechnology*, 23(8):085705, 2012.

[98] Natalie OV Plank, Henry J. Snaith, Caterina Ducati, James S. Bendall, Lukas Schmidt-Mende, and Mark E. Welland. A simple low temperature synthesis route for ZnO–MgO core–shell nanowires. *Nanotechnology*, 19(46):465603, 2008.

[99] Cheol Hyoun Ahn, Sanjay Kumar Mohanta, Bo Hyun Kong, and Hyung Koun Cho. Enhancement of band-edge emission of ZnO from one-dimensional ZnO/MgZnO core/shell nanostructures. *Journal of Physics D: Applied Physics*, 42(11):115106, 2009.

[100] Noboru Yamazoe, Go Sakai, and Kengo Shimanoe. Oxide semiconductor gas sensors. *Catalysis Surveys from Asia*, 7(1):63–75, 2003.

[101] M Asif Khan, A Bhattarai, JN Kuznia, and DT Olson. High electron mobility transistor based on a GaN-Al_x Ga_{1-x} N heterojunction. *Applied Physics Letters*, 63(9):1214–1215, 1993.

[102] W.S. Lee, G.W. Yoffe, D.G. Schlom, and J.S. Harris Jr. Accurate measurement of MBE substrate temperature. *Journal of Crystal Growth*, 111(1-4):131–135, 1991.

[103] PA Redhead. Modulated Bayard-Alpert Gauge. *Review of Scientific Instruments*, 31(3):343–344, 1960.

[104] Brent A. Wacaser, Kimberly A. Dick, Jonas Johansson, Magnus T. Borgström, Knut Deppert, and Lars Samuelson. Preferential interface nucleation: An expansion of the VLS growth mechanism for nanowires. *Advanced Materials*, 21(2):153–165, 2009.

[105] Frank Glas, Jean Christophe Harmand, and Gilles Patriarche. Why does wurtzite form in nanowires of III-V zinc blende semiconductors? *Physical Review Letters*, 99(14):3–6, 2007.

[106] V. G. Dubrovskii, N. V. Sibirev, J. C. Harmand, and F. Glas. Growth kinetics and crystal structure of semiconductor nanowires. *Physical Review B - Condensed Matter and Materials Physics*, 78(23):1–10, 2008.

[107] David B. Williams and C. Barry Carter. The transmission electron microscope. In *Transmission electron microscopy*, pages 3–17. Springer, 1996.

[108] S. J. Pennycook and D. E. Jesson. High-resolution Z-contrast imaging of crystals. *Ultramicroscopy*, 37(1-4):14–38, 1991.

[109] Ray F. Egerton. *Electron energy-loss spectroscopy in the electron microscope*. Springer Science & Business Media, 2011.

[110] M. Varela, M.P. Oxley, W. Luo, J. Tao, Masashi Watanabe, Andrew R. Lupini, S.T. Pantelides, and S.J. Pennycook. Atomic-resolution imaging of oxidation states in manganites. *Physical Review B*, 79(8):085117, 2009.

[111] Toru Mitsunaga. X-ray thin-film measurement techniques II. Out-of-plane diffraction measurements. *The Rigaku Journal*, 25(1):7–12, 2009.

[112] Takayuki Konya. X-ray thin-film measurement techniques V. X-ray reflectivity measurement. *The Rigaku Journal*, 25(2):1, 2009.

[113] Takayuki Konya. X-ray thin-film measurement techniques III. High resolution X-ray diffractometry. *The Rigaku Journal*, 25(2):1, 2009.

[114] Keigo Nagao and Erina Kagami. X-ray thin film measurement techniques: VII. Pole figure measurement. *The Rigaku Journal*, 27(2):6–14, 2011.

[115] Marion J. L. Sourribes. *Electronic Transport in Indium Arsenide Nanowires Grown on Silicon*. PhD thesis, 2014.

[116] M.J.L. Sourribes, I. Isakov, M. Panfilova, and P.A. Warburton. Minimization of the contact resistance between InAs nanowires and metallic contacts. *Nanotechnology*, 24(4):045703, 2013.

[117] Han-Ki Kim, Sang-Heon Han, Tae-Yeon Seong, and Won-Kook Choi. Low-resistance Ti/Au ohmic contacts to Al-doped ZnO layers. *Applied Physics Letters*, 77(11):1647–1649, 2000.

[118] Hyuck Soo Yang, D.P. Norton, S.J. Pearton, and F. Ren. Ti/ Au n-type Ohmic contacts to bulk ZnO substrates. *Applied Physics Letters*, 87(21):212106, 2005.

[119] William Ralph Smythe. Static and Dynamic Electricity. International Series in Pure and Applied Physics, 1950.

[120] Daryoosh Vashaee, Ali Shakouri, Joshua Goldberger, Tevye Kuykendall, Peter Pauzauskie, and Peidong Yang. Electrostatics of nanowire transistors with triangular cross sections. *Journal of Applied Physics*, 99(5):054310, 2006.

[121] Olaf Wunnicke. Gate capacitance of back-gated nanowire field-effect transistors. *Applied Physics Letters*, 89(8):083102, 2006.

[122] DR Khanal and J Wu. Gate coupling and charge distribution in nanowire field effect transistors. *Nano Letters*, 7(9):2778–2783, 2007.

[123] Shubho Banerjee and Mason Levy. Approximate Capacitance Expressions for Two Equal Sized Conducting Spheres. *Proceedings of the ESA Annual Meeting of Electrostatics*, 2014.

[124] Simon M. Sze and Kwok K. Ng. *Physics of Semiconductor Devices*. John Wiley & sons, 2006.

[125] Cheng Ying Chen, Jose Ramon Duran Retamal, I. Wen Wu, Der Hsien Lien, Ming Wei Chen, Yong Ding, Yu Lun Chueh, Chih I. Wu, and Jr Hau He. Probing surface band bending of surface-engineered metal oxide nanowires. *ACS Nano*, 6(11):9366–9372, 2012.

[126] Andreas Wallraff, David I. Schuster, Alexandre Blais, L. Frunzio, R.-S. Huang, J. Majer, S. Kumar, Steven M. Girvin, and Robert J. Schoelkopf. Strong coupling of a single photon to a superconducting qubit using circuit quantum electrodynamics. *Nature*, 431(7005):162, 2004.

[127] Y. Kubo, F.R. Ong, Patrice Bertet, Denis Vion, V. Jacques, D. Zheng, A. Dréau, J.-F. Roch, Alexia Auffèves, Fedor Jelezko, et al. Strong coupling of a spin ensemble to a superconducting resonator. *Physical Review Letters*, 105(14):140502, 2010.

[128] T Frey, PJ Leek, M Beck, Alexandre Blais, Thomas Ihn, Klaus Ensslin, and Andreas Wallraff. Dipole coupling of a double quantum dot to a microwave resonator. *Physical Review Letters*, 108(4):046807, 2012.

[129] Michael Tinkham. *Introduction to superconductivity*. Courier Corporation, 1996.

[130] James F. Annett. *Superconductivity, superfluids and condensates*, volume 5. Oxford University Press, 2004.

[131] Benjamin A. Mazin. *Thesis by*. PhD thesis, 2007.

[132] Jonathan Burnett. *High Precision Readout of Superconducting Resonators*. PhD thesis, 2013.

[133] John Bardeen, Leon N Cooper, and John Robert Schrieffer. Theory of superconductivity. *Physical Review*, 108(5):1175, 1957.

[134] S.E. de Graaf, L. Faoro, J. Burnett, A.A. Adamyan, A. Ya Tzalenchuk, S.E. Kubatkin, T. Lindström, and A.V. Danilov. Suppression of low-frequency charge noise in superconducting resonators by surface spin desorption. *Nature Communications*, 9(1):1143, 2018.

[135] Xiang Yang Kong and Zhong Lin Wang. Polar-surface dominated ZnO nanobelts and the electrostatic energy induced nanohelixes, nanosprings, and nanospirals. *Applied Physics Letters*, 84(6):975–977, 2004.

[136] Wenzhong Wang, Baoqing Zeng, Jian Yang, Bed Poudel, Jianyu Huang, Michael J. Naughton, and Zhifeng Ren. Aligned ultralong ZnO nanobelts and their enhanced field emission. *Advanced Materials*, 18(24):3275–3278, 2006.

[137] Y. Ding, X. Y. Kong, and Z. L. Wang. Doping and planar defects in the formation of single-crystal ZnO nanorings. *Physical Review B*, 70(23):1–7, 2004.

[138] Yong Ding and Zhong Lin Wang. Structures of planar defects in ZnO nanobelts and nanowires. *Micron*, 40(3):335–342, 2009.

[139] Kazuki Nagashima, Takeshi Yanagida, Keisuke Oka, Hidekazu Tanaka, and Tomoji Kawai. Mechanism and control of sidewall growth and catalyst diffusion on oxide nanowire vapor-liquid-solid growth. *Applied Physics Letters*, 93(15):91–94, 2008.

[140] Sunandan Baruah and Joydeep Dutta. Hydrothermal growth of ZnO nanostructures. *Science and Technology of Advanced Materials*, 10(1):013001, 2009.

[141] Oscar W. Kennedy, Maddison L. Coke, Edward R. White, Milo Shaffer, and Paul A. Warburton. MBE growth and morphology control of ZnO nanobelts with polar axis perpendicular to growth direction. *Materials Letters*, 212:51–53, 2017.

[142] Josh Goldberger, Donald J Sirbuly, Matt Law, and Peidong Yang. Zno nanowire transistors. *The Journal of Physical Chemistry B*, 109(1):9–14, 2005.

[143] Sunghoon Song, Woong Ki Hong, Soon Shin Kwon, and Takhee Lee. Passivation effects on ZnO nanowire field effect transistors under oxygen, ambient, and vacuum environments. *Applied Physics Letters*, 92(26):3–5, 2008.

[144] GZ Xing, XS Fang, Z Zhang, DD Wang, X Huang, J Guo, L Liao, Z Zheng, HR Xu, T Yu, et al. Ultrathin single-crystal ZnO nanobelts: Ag-catalyzed growth and field emission property. *Nanotechnology*, 21(25):255701, 2010.

[145] Zuoming Zhu, Tsung-Liang Chen, Yi Gu, John Warren, and Richard M Osgood. Zinc oxide nanowires grown by vapor-phase transport using selected metal catalysts: a comparative study. *Chemistry of Materials*, 17(16):4227–4234, 2005.

[146] P. Misra, T. K. Sharma, and L. M. Kukreja. Temperature dependent photoluminescence processes in ZnO thin films grown on sapphire by pulsed laser deposition. *Current Applied Physics*, 9(1):179–183, 2009.

[147] Bin Yan, Rui Chen, Weiwei Zhou, Jixuan Zhang, Handong Sun, Hao Gong, and Ting Yu. Localized suppression of longitudinal-optical-phonon–exciton coupling in bent ZnO nanowires. *Nanotechnology*, 21(44):445706, 2010.

[148] H.D. Sun, Y. Segawa, M. Kawasaki, A. Ohtomo, K. Tamura, and H. Koinuma. Phonon replicas in ZnO/ZnMgO multiquantum wells. *Journal of Applied Physics*, 91(10):6457–6460, 2002.

[149] A. Teke, Ü. Özgür, S. Doğan, X. Gu, Hadis Morkoç, B. Nemeth, J. Nause, and H.O. Everitt. Excitonic fine structure and recombination dynamics in single-crystalline ZnO. *Physical Review B*, 70(19):195207, 2004.

[150] Bin Wei, Kun Zheng, Yuan Ji, Yuefei Zhang, Ze Zhang, and Xiaodong Han. Size-dependent bandgap modulation of ZnO nanowires by tensile strain. *Nano letters*, 12(9):4595–4599, 2012.

[151] Cathodoluminescence from insulators, metals, and plasmonics. `http://www.gatan.com/cathodoluminescence-insulators-metals-and-plasmonics`. Accessed: 2018-06-01.

[152] R.F. Egerton, P. Li, and M. Malac. Radiation damage in the TEM and SEM. *Micron*, 35(6):399–409, 2004.

[153] P. E. Batson, A. Reyes-Coronado, R. G. Barrera, A. Rivacoba, P. M. Echenique, and J. Aizpurua. Plasmonic nanobilliards: Controlling nanoparticle movement using forces induced by swift electrons. *Nano Letters*, 11(8):3388–3393, 2011.

[154] R. J. Warmack, R. S. Becker, V. E. Anderson, R. H. Ritchie, Y. T. Chu, J. Little, and T. L. Ferrell. Surface-plasmon excitation during aloof scattering of low-energy electrons in micropores in a thin metal foil. *Physical Review B*, 29(8):4375–4381, 1984.

[155] Brian Zutter, Matthew Mecklenburg, and B C Regan. Aloof Beam Plasmons in Silver Nanoparticles. 22(Suppl 3):1642–1643, 2016.

[156] Y. C. Kong, D. P. Yu, B. Zhang, W. Fang, and S. Q. Feng. Ultraviolet-emitting ZnO nanowires synthesized by a physical vapor deposition approach. *Applied Physics Letters*, 78(4):407, 2001.

[157] Seung Chul, Ye Zhang, Hyun Ruh, Hwack-joo Lee, Hyun-wook Shim, Eun-kyung Suh, and Cheol Jin. Low temperature growth and photoluminescence of well-aligned zinc oxide nanowires. *Chemical Physical Letters*, 363:134–138, 2002.

[158] V. Srikant and D. R. Clarke. On the optical band gap of zinc oxide. *Journal of Applied Physics*, 83(10):5447, 1998.

[159] Derek R. Miller, Robert E. Williams, Sheikh A. Akbar, Pat A. Morris, and David W. McComb. STEM-Cathodoluminescence of SnO_2 nanowires and powders. *Sensors and Actuators, B: Chemical*, 240:193–203, 2017.

[160] Jonathan Mooney and Patanjali Kambhampati. Erratum: Get the basics right: Jacobian conversion of wavelength and energy scales for quantitative analysis of emission spectra (Journal of Physical Chemistry Letters (2013) 4:19 (3316?3318) DOI: 10.1021/jz401508t). *Journal of Physical Chemistry Letters*, 5(20):3497, 2014.

[161] Yinyan Gong, Tamar Andelman, Gertrude F. Neumark, Stephen O'Brien, and Igor L. Kuskovsky. Origin of defect-related green emission from ZnO nanoparticles: Effect of surface modification. *Nanoscale Research Letters*, 2(6):297–302, 2007.

[162] N. E. Hsu, W. K. Hung, and Y. F. Chen. Origin of defect emission identified by polarized luminescence from aligned ZnO nanorods. *Journal of Applied Physics*, 96(8):4671–4673, 2004.

[163] Ketaki Sarkar, Souvik Mukherjee, Gary Wiederrecht, Richard D. Schaller, David J. Gosztola, Michael A. Stroscio, and Mitra Dutta. Ultrafast carrier dynamics and optical pumping of lasing from Ar-plasma treated ZnO nanoribbons. *Nanotechnology*, 29(9), 2018.

[164] Juan Wang, Xipo An, Quan Li, and R. F. Egerton. Size-dependent electronic structures of ZnO nanowires. *Applied Physics Letters*, 86(20):1–3, 2005.

[165] F. Fabbri, M. Villani, A. Catellani, A. Calzolari, G. Cicero, D. Calestani, G. Calestani, A. Zappettini, B. Dierre, T. Sekiguchi, and G. Salviati. Zn vacancy induced green luminescence on non-polar surfaces in ZnO nanostructures. *Scientific Reports*, 4(1):5158, 2015.

[166] Yanhong Lin, Dejun Wang, Qidong Zhao, Ziheng Li, Yudan Ma, and Min Yang. Influence of adsorbed oxygen on the surface photovoltage and photoluminescence of ZnO nanorods. *Nanotechnology*, 17(9):2110–2115, 2006.

[167] Jiake Wei, Nan Jiang, Jia Xu, Xuedong Bai, and Jingyue Liu. Strong Coupling between ZnO Excitons and Localized Surface Plasmons of Silver Nanoparticles Studied by STEM-EELS. *Nano Letters*, 15(9):5926–5931, 2015.

[168] Zhi-Min Liao, Hong-Zhou Zhang, Yang-Bo Zhou, Jun Xu, Jing-Min Zhang, and Da-Peng Yu. Surface effects on photoluminescence of single ZnO nanowires. *Physics Letters A*, 372(24):4505–4509, jun 2008.

[169] D. N. Montenegro, V. Hortelano, O. Martínez, M. C. Martínez-Tomas, V. Sallet, V. Muñoz-Sanjosé, and J. Jiménez. Non-radiative recombination centres in catalyst-free ZnO nanorods grown by atmospheric-metal organic chemical vapour deposition. *Journal of Physics D: Applied Physics*, 46(23), 2013.

[170] M. D. McCluskey and S. J. Jokela. Defects in ZnO. *Journal of Applied Physics*, 106(7):10, 2009.

[171] F. Donatini, Andres de Luna Bugallo, Pierre Tchoulfian, Gauthier Chicot, Corinne Sartel, Vincent Sallet, and Julien Pernot. Comparison of three e-beam techniques for electric field imaging and carrier diffusion length measurement on the same nanowires. *Nano Letters*, 16(5):2938–2944, 2016.

[172] Jun Seok Hwang, Fabrice Donatini, Julien Pernot, Robin Thierry, Pierre Ferret, and Le Si Dang. Carrier depletion and exciton diffusion in a single ZnO nanowire. *Nanotechnology*, 22(47), 2011.

[173] Brian P. Mehl, Justin R. Kirschbrown, Michelle M. Gabriel, Ralph L. House, and John M. Papanikolas. Pump - Probe Microscopy : Spatially Resolved Carrier Dynamics in ZnO Rods and the Influence of Optical Cavity Resonator Modes. *Physical Chenistry B*, 117(16):4390–4398, 2013.

[174] Hong Jin Fan, Peter Werner, and Margit Zacharias. Semiconductor nanowires: from self-organization to patterned growth. *Small*, 2(6):700–17, jun 2006.

[175] C. W. Cheng, E. J. Sie, B. Liu, C. H A Huan, T. C. Sum, H. D. Sun, and H. J. Fan. Surface plasmon enhanced band edge luminescence of ZnO nanorods by capping Au nanoparticles. *Applied Physics Letters*, 96(7):2008–2011, 2010.

[176] Giovanni Bertoni, Filippo Fabbri, Marco Villani, Laura Lazzarini, Stuart Turner, Gustaaf Van Tendeloo, Davide Calestani, Silvija Gradečak, Andrea Zappettini, and

Giancarlo Salviati. Nanoscale mapping of plasmon and exciton in ZnO tetrapods coupled with Au nanoparticles. *Scientific Reports*, 6:1–8, 2016.

[177] Alex M. Lord, Thierry G. Maffeis, Olga Kryvchenkova, Richard J. Cobley, Karol Kalna, Despoina M. Kepaptsoglou, Quentin M. Ramasse, Alex S. Walton, Michael B. Ward, Jürgen Köble, et al. Controlling the electrical transport properties of nanocontacts to nanowires. *Nano Letters*, 15(7):4248–4254, 2015.

[178] Jessica A. Alexander, Frank J. Scheltens, Lawrence F. Drummy, Michael F. Durstock, Fredrik S. Hage, Quentin M. Ramasse, and David W. McComb. High-resolution monochromated electron energy-loss spectroscopy of organic photovoltaic materials. *Ultramicroscopy*, 180:125–132, 2017.

[179] Ondrej L. Krivanek, Tracy C. Lovejoy, Niklas Dellby, Toshihiro Aoki, R. W. Carpenter, Peter Rez, Emmanuel Soignard, Jiangtao Zhu, Philip E. Batson, Maureen J. Lagos, Ray F. Egerton, and Peter A. Crozier. Vibrational spectroscopy in the electron microscope. *Nature*, 514(7521):209–212, 2014.

[180] Yong Ding and Zhong Lin Wang. Electron energy-loss spectroscopy study of ZnO nanobelts. *Journal of Electron Microscopy*, 54(3):287–291, 2005.

[181] Ondrej L. Krivanek, Tracy C. Lovejoy, Matthew F. Murfitt, Gwyn Skone, Philip E. Batson, and Niklas Dellby. Towards sub-10 meV energy resolution STEM-EELS. *Journal of Physics: Conference Series*, 522(1), 2014.

[182] Audrey Bienfait, J.J. Pla, Yuimaru Kubo, Xin Zhou, Michael Stern, C.C. Lo, C.D. Weis, Thomas Schenkel, Denis Vion, Daniel Esteve, et al. Controlling spin relaxation with a cavity. *Nature*, 531(7592):74, 2016.

[183] Hans Huebl, Christoph W. Zollitsch, Johannes Lotze, Fredrik Hocke, Moritz Greifenstein, Achim Marx, Rudolf Gross, and Sebastian TB Goennenwein. High cooperativity in coupled microwave resonator ferrimagnetic insulator hybrids. *Physical Review Letters*, 111(12):127003, 2013.

[184] Yiwen Chu, Prashanta Kharel, William H Renninger, Luke D Burkhart, Luigi Frunzio, Peter T Rakich, and Robert J Schoelkopf. Quantum acoustics with superconducting qubits. *Science*, page 1511, 2017.

[185] J.D. Teufel, Tobias Donner, Dale Li, J.W. Harlow, M.S. Allman, Katarina Cicak, A.J. Sirois, Jed D. Whittaker, K.W. Lehnert, and Raymond W. Simmonds. Side-

band cooling of micromechanical motion to the quantum ground state. *Nature*, 475(7356):359, 2011.

[186] J.D. Teufel, J.W. Harlow, C.A. Regal, and K.W. Lehnert. Dynamical backaction of microwave fields on a nanomechanical oscillator. *Physical Review Letters*, 101(19):197203, 2008.

[187] Riccardo Manenti, Anton F. Kockum, Andrew Patterson, Tanja Behrle, Joseph Rahamim, Giovanna Tancredi, Franco Nori, and Peter J. Leek. Circuit quantum acoustodynamics with surface acoustic waves. *Nature Communications*, 8(1):975, 2017.

[188] Martin V. Gustafsson, Thomas Aref, Anton Frisk Kockum, Maria K. Ekström, Göran Johansson, and Per Delsing. Propagating phonons coupled to an artificial atom. *Science*, 346(6206):207–211, 2014.

[189] Marco Scigliuzzo, Laure Bruhat, Andreas Bengtsson, Jonathan Burnett, and Per Delsing. Phononic Losses in Superconducting Coplanar Waveguide Resonators on Piezoelectric Substrates. *Bulletin of the American Physical Society*, 2019.

[190] K.J. Satzinger, Y.P. Zhong, H-S. Chang, G.A. Peairs, A. Bienfait, Ming-Han Chou, A.Y. Cleland, C.R. Conner, É. Dumur, J. Grebel, et al. Quantum control of surface acoustic-wave phonons. *Nature*, 563(7733):661, 2018.

[191] S.E. de Graaf, A.A. Adamyan, T. Lindström, D. Erts, S.E. Kubatkin, A. Ya Tzalenchuk, and A.V. Danilov. Direct Identification of Dilute Surface Spins on Al_2O_3: Origin of Flux Noise in Quantum Circuits. *Physical Review Letters*, 118(5):057703, 2017.

[192] Jonathan Burnett, James Sagar, Oscar W Kennedy, Paul A Warburton, and Jonathan C Fenton. Low-loss superconducting nanowire circuits using a neon focused ion beam. *Physical Review Applied*, 8(1):014039, 2017.

[193] Nicolas GN Constantino, Muhammad Shahbaz Anwar, Oscar W Kennedy, Manyu Dang, Paul A Warburton, and Jonathan C Fenton. Emergence of Quantum Phase-Slip Behaviour in Superconducting NbN Nanowires: DC Electrical Transport and Fabrication Technologies. *arXiv preprint arXiv:1806.07708*, 2018.

[194] S. Probst, F.B. Song, P.A. Bushev, A.V. Ustinov, and M. Weides. Efficient and robust analysis of complex scattering data under noise in microwave resonators. *Review of Scientific Instruments*, 86(2):024706, 2015.

[195] Jonathan Burnett, Andreas Bengtsson, David Niepce, and Jonas Bylander. Noise and loss of superconducting aluminium resonators at single photon energies. In *Journal of Physics: Conference Series*, volume 969, page 012131, 2018.

[196] Lara Faoro and Lev B. Ioffe. Internal loss of superconducting resonators induced by interacting two-level systems. *Physical Review Letters*, 109(15):157005, 2012.

[197] Lara Faoro and Lev B. Ioffe. Interacting tunneling model for two-level systems in amorphous materials and its predictions for their dephasing and noise in superconducting microresonators. *Physical Review B*, 91(1):014201, 2015.